Optimization of a Transition Radiation Detector for the Compressed Baryonic Matter Experiment

Andreas Arend

Optimization of a Transition Radiation Detector for the Compressed Baryonic Matter Experiment

Dissertation

zur Erlangung des Doktorgrades
der Naturwissenschaften

vorgelegt beim Fachbereich 13
der Johann Wolfgang Goethe-Universität
in Frankfurt am Main

von

Andreas Arend
aus Mühlhausen (Thüringen)

Frankfurt am Main, 2014

(D30)

vom Fachbereich 13
der Johann Wolfgang Goethe - Universität
als Dissertation angenommen.

Dekan: Prof. Dr. Joachim Stroth

Gutachter: Prof. Dr. Harald Appelshäuser, Prof. Dr. Christoph Blume

Datum der Disputation:

Zusammenfassung

Die Zusammensetzung und der Aufbau der sichtbaren Kernmaterie ist Teil aktueller Grundlagenforschung. Die Quarks als fundamentale Bausteine unterliegen der starken Wechselwirkung. Als Austauschteilchen dient dabei das Gluon. Der gebundene Zustand eines Quarks mit einem Antiquark wird als Meson bezeichnet, die Verbindung von drei Quarks als Baryon. Die Ladung der starken Wechselwirkung ist die Farbe. Aufgrund der linearen Charakteristik des Potentials der starken Wechselwirkung bei großen Abständen können nur farbneutrale Zustände beobachtet werden. Die Farbladung ist innerhalb des Zustandes eingeschlossen, was als Confinement bezeichnet wird. Die Quantenchromodynamik ist die beschreibende Quantenfeldtheorie der starken Wechselwirkung.

Mithilfe der Kollisionen von schweren Ionen ist es möglich, Kernmaterie in einem Zustand sehr hoher Dichte und Temperatur zu erzeugen. Bei den dabei ablaufenden Prozessen werden sehr hohe Impulse zwischen den Konstituenten übertragen, die groß genug sind, um Quarks und Gluonen in diesem neuen und exotischen Zustand der Materie quasi frei beobachten zu können. Dieser Zustand des Deconfinements wird als Quark-Gluon-Plasma bezeichnet. Die Untersuchung des Phasenübergangs zum Zustand des Quark-Gluon-Plasmas und die damit einhergehende Untersuchung des Phasendiagrammes der Quantenchromodynamik ist mit Hilfe geeigneter Observablen möglich. Dazu eignen sich seltene Sonden, die in den unterschiedlichsten Phasen einer Schwerionenkollision entstehen. So lassen sich z.B. aus der Messung thermischer Photonen Rückschlüsse auf die Temperatur des Quark-Gluon-Plasmas ziehen, oder aus dem Vergleich der gemessenen Produktionsraten bei Proton-Kern-Kollisionen mit Kern-Kern-Kollisionen Rückschlüsse auf die Beschaffenheit des Quark-Gluon-Plasmas ziehen. Eine dieser seltenen Sonden ist das J/ψ und seine angeregten Zustände, die über ihre Zerfallsprodukte nachgewiesen werden können.

Zum Nachweis der im Verlauf der Kollisionen entstehenden Teilchen wird die Wechselwirkung der Teilchen mit ihrer umgebenden Materie ausgenutzt. Geladene Teilchen, die einen Detektor durchfliegen, ionisieren das sie umgebende Material. Die so frei werdenden Elektronen und Ionen können nachgewiesen werden. Ebenso können Teilchen Energie durch die Emission von Photonen verlieren. Diese Photonen können über den Cherenkov-Effekt oder über die Entstehung von Übergangsstrahlung entsendet werden. Die Wahrscheinlichkeit zur Aussendung eines Übergangsstrahlungsphotons ist dabei abhängig vom γ Faktor. Somit ist es mit Hilfe dieses Effektes möglich Elektronen und Pionen zu unterscheiden. Die Ionisationsspur und ein möglicherweise entstandenes Übergangsstrahlungsphoton werden in einer Vieldrahtproportionalkammer (MWPC) nachge-

wiesen. Da die Erzeugung des Übergangsstrahlungsphotons ein statistischer Prozess an einer Grenzschicht zweier Materialien unterschiedlicher Dielektrizitätskonstanten ist, wird zu ihrer Erzeugung ein Radiator verwendet. Dieser Radiator stellt viele Grenzschichten zwischen je zwei Materialien bereit. Es wird dabei zwischen regelmäßigen Radiatoren, z.B. Stapel von Folien mit definiertem Abstand, und unregelmäßigen Radiatoren, z.B. Schäume aus Polyethylen, unterschieden. Der Radiator ist direkt an eine Vieldrahtproportionalkammer angebracht. Die MWPC besteht dabei aus den begrenzenden Kathoden und einer Anodendrahtebene im Inneren und ist mit dem Detektorgas gefüllt. Das zu detektierende Teilchen durchfliegt Radiator und MWPC. Das Übergangsstrahlungsphoton wird innerhalb der MWPC absorbiert. Zusammen mit Elektronen, die beim Durchfliegen durch Ionisation entstehen, driften Elektronen entlang des elektrischen Feldes zu den Anodendrähten. Nah an den Drähten entsteht aufgrund des erhöhten Feldes eine Elektronenlawine (Gasverstärkung) die an den Anodendrähten absorbiert wird. Dabei wird auf den Kathoden eine Spiegelladung induziert. Die entsprechend entstehenden Ionen erzeugen ein auslesbares Signal, das durch die Ausleseelektronik weiter verarbeitet wird.

Die zukünftige Facility for Antiproton and Ion Research (FAIR) wird mit es mit ihren Beschleunigerkomplexen SIS 100 und SIS 300 ermöglichen, Kollisionen von schweren Ionen mit einer nie vorher dagewesenen hohen Ereignisrate zu erzeugen, um so seltene Sonden des Quark-Gluon-Plasmas mit ausreichender Präzision in den angeschlossenen Experimenten nachzuweisen.

Das Compressed Baryonic Matter (CBM) Experiment ist ein fixed target Experiment am SIS100/300. Es ist modular aufgebaut und ermöglicht es, dedizierte Messungen durch geeignete Kombination unterschiedlicher Detektorsysteme durchzuführen. Insbesondere kann der Aufbau wahlweise für die Messung von Elektronen oder Myonen optimiert werden. Je nach Ausbau der Beschleunigeranlagen sind Ausbaustufen für SIS100 und SIS300 vorgesehen. Die beteiligten Detektorsysteme sind dabei ein Micro-Vertex-Detektor und ein Silizium-Streifen-Zähler, die innerhalb eines supraleitenden Magneten angebracht sind. Außerhalb des Magneten befinden sich ein Ring-Imaging Cherenkov Detektor (RICH), der Übergangsstrahlungszähler (TRD), der Gegenstand dieser Arbeit ist, sowie die Komponenten der Teilchenflugzeitmessung. Im Myon-Messszenario befindet sich anstelle des RICH ein Myon-Detektionssystem. Aufgrund der hohen zu erwartenden Teilchenraten wird das CBM Experiment für eine kontinuierliche Datenauslese ausgelegt.

Der Übergangsstrahlungszähler des CBM Experimentes wird zur Identifikation geladener Teilchen, speziell zur Unterscheidung von Elektronen und Pionen, dienen. Auch wird der TRD über die Messung von Spurpunkten zur Rekonstruktion der Teilchentrajektorien beitragen. Die angestrebten Messungen seltener Proben und die experimentelle Umgebung definieren dabei die Anforderungen an den TRD. So muss der TRD es ermöglichen, Pionen um einen Faktor 100 zu unterdrücken, bei einer geforderten Effizienz von 90% für Elektronen. Die Ortsauflösung des TRD muss genauer als 1 mm sein, um ein ausreichend gutes Signal zu Untergrund Verhältnis z.B. für die Zerfallsprodukte des J/ψ zu erreichen. Basierend auf den zu erwartenden hohen Ereignisrate und den unterschiedlichen Positionen innerhalb der gegebenen Messszenarien wurden die ortsabhängigen Teilchenraten innerhalb des TRD abgeschätzt. Um den TRD in die Messszenarien des CBM Experimentes zu integrieren wird der TRD in drei separaten Stationen mit je 4+4+2 Detektorlagen aufgebaut. Somit ist es möglich, den TRD in die verschiedenen Aufbauten und bei verschiedenen Strahlenergien optimal einzusetzen.

Zur Realisierung eines Übergangsstrahlungszählers für das Compressed Baryonic Matter Experiment werden unterschiedliche Ansätze verfolgt. Im Rahmen dieser Arbeit werden dünne, symmetrische Vieldrahtproportionalkammern vorgeschlagen. Im Hinblick auf die hohen Teilchenraten innerhalb des TRD sollen mit Hilfe des schmalen Verstärkungsbereiches Signale hinreichend schnell erzeugt werden. Die vorgeschlagenen Prototypen werden mit einem dünnen folienbasierten Eintrittsfenster versehen, um das zusätzliche Materialbudget zwischen Radiator und MWPC so gering wie möglich zu halten. Unterschiedliche Ansätze werden von den kollaborierenden Arbeitsgruppen in Münster und Bukarest untersucht. Hierbei kommt insbesondere ein zusätzlicher Driftbereich zum Einsatz, der jedoch zu einer langsameren Signalerzeugung führt.

Basierend auf dem Konzept symmetrischer Vieldrahtproportionalkammern ohne Driftbereich wurden verschiedene Prototypgenerationen angefertigt. Die Prototypen der ersten Generation wurden als Machbarkeitsstudien angefertigt und getestet. In den Generationen II und III wurden die Geometrien der Draht- und der Kathodenebenen auf 4+4 mm und 5+5 mm festgelegt sowie unterschiedliche Rahmenmaterialen verwendet. Die Prototypen der Generation II und III weisen eine aktive Fläche von $15 \times 15\,\mathrm{cm}^2$ auf. Basierend auf den Erfahrungen und den Ergebnissen einer Teststrahlzeit mit den Generation II und III Prototypen wurden die Prototypen der IV. Generation in einer Größe von $60 \times 60\,\mathrm{cm}^2$ angefertigt. Dies entspricht der realen Größe von Detektormodulen im inneren Bereich des CBM TRD. Zur Fertigung des folienbasierten Eintrittsfensters wurde ein speziell entwickeltes thermisches Spannverfahren entwickelt. Alle hergestellten Prototypen weisen eine einfache Bauart auf, die es ermöglicht, einzelne Komponenten auszutauschen.

Zu den entwickelten Vieldrahtproportionalkammerprototypen wurden entsprechende Prototypen von Radiatoren entwickelt. Neben regelmäßigen Folienradiatoren in unterschiedlichen Konfigurationen von Foliendicke und Abständen, wurden Radiatoren aus Polyethylenschäumen verwendet. Es wurden ebenfalls Radiatoren in Sandwichbauweise entwickelt, die, begrenzt von soliden Schaumschichten, ein Fasermaterial als Radiator benutzen.

Zur Auslese der Prototypen wurde der SPADIC Chip in der Version 0.3 verwendet. Die Pad-Ebene der Generation IV Prototypen ermöglichen es ebenfalls, die Weiterentwicklung (SPADIC v1.0) sowie andere Front-End-Elektronik zu benutzen.

Zu den Prototypen ohne Driftbereich wurden Simulationen bezüglich ihrer elektrostatischen und mechanischen Eigenschaften durchgeführt. Mit Hilfe des Software-Paketes Garfield wurden das elektrische Feld und die daraus resultierenden Driftlinien der entstehenden Elektronen berechnet. Die mittlere Gasverstärkung in Abhängigkeit vom verwendeten Detektorgas sowie in Abhängigkeit von der angelegten Anodendrahtspannung wurde simuliert. Die geometrische Homogenität der Gasverstärkung wurde ebenfalls betrachtet.

Da bei der Verwendung eines folienbasierten Eintrittsfensters eine Deformation aufgrund von differentiellem Überdruck zu erwarten ist, wurde die Variation der Gasverstärkung in Abhängigkeit der Ausdehnung des Eintrittsfensters besonders untersucht. Ebenso wurden Simulationen der mechanischen Stabilität des Eintrittsfensters mit Hilfe einer Finite-Elemente-Methode angefertigt, um die Variationen der Gasverstärkung abzuschätzen. Die zu erwartenden Driftzeiten und die resultierenden Signale wurden ebenfalls mit Hilfe des Softwarepaketes Garfield simuliert.

Die angefertigten Prototypen wurden mit weiterführenden Messungen im Labor untersucht. Die simulierte Ausdehnung des folienbasierten Eintrittsfensters wurde mit Überdrucktests verifiziert. Die absolute Gasverstärkung wurde in einem Aufbau bestimmt, in der die Prototypen einer ionisierenden Strahlung ausgesetzt waren. Die Homogenität der relativen Gasverstärkung der Generation IV Prototypen wurde bei einer gegebenen Verformung des Eintrittsfensters gemessen. Ebenso wurde mit Hilfe einer ^{55}Fe-Quelle die Energieauflösung der Vieldrahtproportionalkammern bestimmt.

Die Elektron-Pion-Separation der Prototypen der Generationen II, III und IV wurden in zwei Teststrahlzeitkampagnen 2011 und 2012 am CERN PS bestimmt. Diese Strahlzeiten wurden gemeinsam mit den Instituten aus Münster und Bukarest sowie den Detektorsystemen RICH und TOF im Experimentierbereich T9 durchgeführt. Dabei lieferte das CERN PS einen Teilchenstrahl aus Elektronen und Pionen mit einem Impuls von 2 GeV/c bis zu 10 GeV/c. Für diese Teststrahlzeiten wurde ein auf dem Go4-System basiertes Echtzeitanalysesystem entwickelt und die benutzten SPADIC v0.3 Ausleseelektronik in das Datenerfassungssystem integriert. Während der Teststrahlzeit 2012 wurden zusätzlich externe Parameter für eine mögliche Kalibration der Gasverstärkung aufgenommen.

Die während der Teststrahlzeiten aufgezeichneten Daten wurden ausgewertet. Zur Bestimmung der Teilchenidentifizierung wurde eine Kombination aus zwei Cherenkov-Detektoren und einem Bleiglas-Kalorimeter als Referenz benutzt. Mithilfe eines Separationsverfahrens wurde die Reinheit der Referenz-Teilchenidentifizierung und somit ein Beitrag zum systematischen Fehler der anschließenden Messungen bestimmt. Die aufgenommenen Rohdaten wurden mit einem mehrstufigen Korrekturalgorithmus von Störeinflüssen befreit. Dieser Korrekturalgorithmus benutzt Ereignisse ohne Teilchen in den zu testenden Detektoren, um die Variation der Impulsböden der Ausleseelektronik zu korrigieren. Weiterhin wurden aus den Signalen die korrelierten Störeinflüsse mit Hilfe eines auf der Kovarianz-Matrix basierenden Verfahrens isoliert und entfernt. Diese Signale wurden weiter in einem Algorithmus zur Cluster-Bestimmung verarbeitet. Dabei wurde aus den Signalen sowohl die Amplitudeninformation als auch das integrierte Gesamtsignal verwendet. Mit den so aufbereitete Signalen und der externen Teilchenidentifizierung ist es möglich Spektren der deponierten Ladung für Elektronen und Pionen zu erzeugen. Diese Spektren wurden mit einem multiplikativen Verfahren bezüglich der Gasverstärkung kalibriert.

Basierend auf den Ladungsspektren lässt sich die Leistungsfähigkeit der benutzten Radiatorprototypen bezüglich ihrer Elektron-Pion-Separation bestimmen. Dabei wird sowohl

ein Verfahren verwendet, welches ausschließlich eine Detektorlage verwendet, als auch Extrapolationsverfahren angewendet. Die Extrapolationsverfahren basieren auf den Berechnungen einer klassischen und logarithmischen Likelihood-Methode. Die Leistungsfähigkeit verschiedener Radiator-MWPC-Kombinationen wurde miteinander verglichen. Dabei stellte sich heraus, dass die Leistungsfähigkeit der schaumbasierte Radiatoren mit den theoretisch gut verstandenen regelmäßigen Folienradiatoren vergleichbar sind und eine ähnlich gute Trennung von Elektronen und Pionen zulassen. Sie stellen daher eine einfach zu handhabende und kostengünstige Alternative zu regelmäßigen Radiatoren dar. Die Leistungsfähigkeit bezüglich der Elektron-Pion-Trennung wurde abhängig vom Impuls der durchquerenden Teilchen analysiert.

Mit Hilfe der Informationen aus dem Algorithmus zur Cluster-Bestimmung wurde die Pad-Response-Funktion bestimmt. Aus einer Anpassung der theoretischen Beschreibung wurde daraus die tatsächliche Ausdehnung, welche sich auf Grund des differentiellen Überdruckes ergibt, für die Prototypen der Generation IV während der Teststrahlzeit 2012 bestimmt.

Aus den Ergebnissen lässt sich schließen, dass dünne, symmetrische Vieldrahtproportionalkammern nur mit Verstärkungsbereich kombiniert mit einem schaumbasierten Radiator die Anforderungen des CBM Experimentes an einen Übergangsstrahlungszähler erfüllen.

Untersuchungen bezüglich der Ratenfestigkeit der vorgeschlagenen Prototypen befinden sich in der Vorbereitungsphase. Weiterentwicklungen des MWPC-Designs basierend auf einer alternierenden Anodendrahtgeometrie zur Minimierung der Variationen der Gasverstärkung sowie die mechanische Unterstützung und Stabilisierung des Eintrittsfensters mit Hilfe eines Radiatormaterials werden ebenfalls untersucht.

Contents

1 Introduction

The genesis and the evolution of our observable universe is a topic in which many scientists are interested in. It is assumed that matter and anti-matter were created at the *Big Bang* and a hot and dense state of matter called *Quark Gluon Plasma* (QGP) has been developed. High-energy heavy-ion collisions are a tool to investigate and analyze the properties of this exotic state of matter in the laboratory. First experiments exploring the properties of the quantum-chromodynamic's phase diagram were performed at *BEVALAC* [BF11] at Lawrence Berkeley Laboratory and the *SIS18* at GSI in Darmstadt at collision energies of 1-2 AGeV. These energies were too low to reach the area of *deconfinement* in the phase diagram. In experiments at the Alternating Gradient Synchrotron (AGS) at Brookhaven National Laboratory (BNL), where gold nuclei at energies of 2 and 11 AGeV, and at the CERN Super Proton Synchrotron (SPS) where lead ions of 10 to 160 AGeV were collided with a fixed target, first signatures for the QGP [PRSZ08] were observed. The Relativistic Heavy-Ion Collider (RHIC) at BNL investigated Au-Au collisions at top center of mass energy of $\sqrt{s_{NN}} = 200\,\mathrm{GeV}$. The Large Hardon Collider at CERN currently collides Pb ions at $\sqrt{s_{NN}} = 2.76\,\mathrm{TeV}$. At these energies the ratio of matter to anti-matter is roughly unity in the region of a lower baryonic density.

The future Compressed Baryonic Matter (CBM) experiment [BF11] at the Facility for Antiproton and Ion Research (FAIR) in Darmstadt (Germany) is designed to explore the unknown area at lower to moderate temperatures and at high baryonic densities in the QCD phase diagram by utilizing heavy-ion collisions of different ion species with a fixed-target energy of up to 44 AGeV at an unprecedented high particle flux of up to $5 \cdot 10^{11}$ particles per bunch. The analysis of these collisions allows to characterize the properties of the generated state of matter during the collision. The reaction products and the subsequently generated decay products are tracked and identified inside the CBM experiment.

The identification and tracking of electrons are the supreme disciplines of a Transition Radiation Detector (TRD). Its working principle is based on the characteristic of energy loss due to photon emission of traversing particles. Multi-Wire Proportional Chambers (MWPC) are utilized to detect the generated signals of these particles.

This work describes the development, construction and characterization of a Transition Radiation Detector prototype for the future Compressed Baryonic Matter experiment on the basis of simulation and test beam campaigns. The proposed prototypes employ a low-absorption foil-based entrance window, a driftless MWPC for signal generation and a rectangular readout-pad geometry.

2 Physics Motivation

The questions about the properties of the material in our environment is one of the oldest questions of mankind. The properties of the smallest particles and the properties of the interaction of these particles are one part of this fundamental question.

The CBM experiment will explore these particles and their interaction. The following chapter will briefly depict the current state of research and summarize the contribution of the CBM experiment to this topic.

2.1 The Standard Model of Particle Physics

Matter consists of atoms. Protons and neutrons form the nucleus of an atom, which is orbited by electrons, see figure 2.1. But protons and neutrons are not fundamental particles, they are composed of quarks and gluons. The properties of these fundamental particles as well as their interaction are descried in the socalled Standard Model.

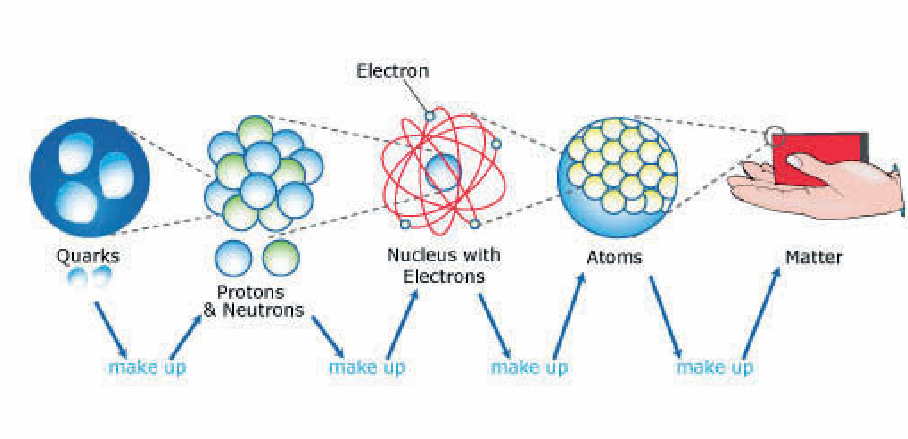

Figure 2.1: Illustration of the composition of our visible matter [Uni].

2.1.1 Quarks, Gluons and the Strong Interaction

In the 1960's Murray Gell-Mann postulated the existence of quarks as fundamental particles with half-integer spin and a 1/3 electric charge [GM64]. Up to that proposal hardonic particles were described with their quantum numbers Isospin and Strangeness. Based on both origins todays standard model of particle physics has been developed containing six quark species, six kinds of leptons and their corresponding anti particles. This is completed by the gauge bosons and the recently discovered Higgs boson [AC12]. Quarks and leptons are categorized as fermions, particles with spin 1/2. Figure 2.2 shows a schematic view on this classification. Quarks and leptons can additionally be categorized in three generations, so called *families*, represented by the vertical ordering of the columns in figure 2.2.

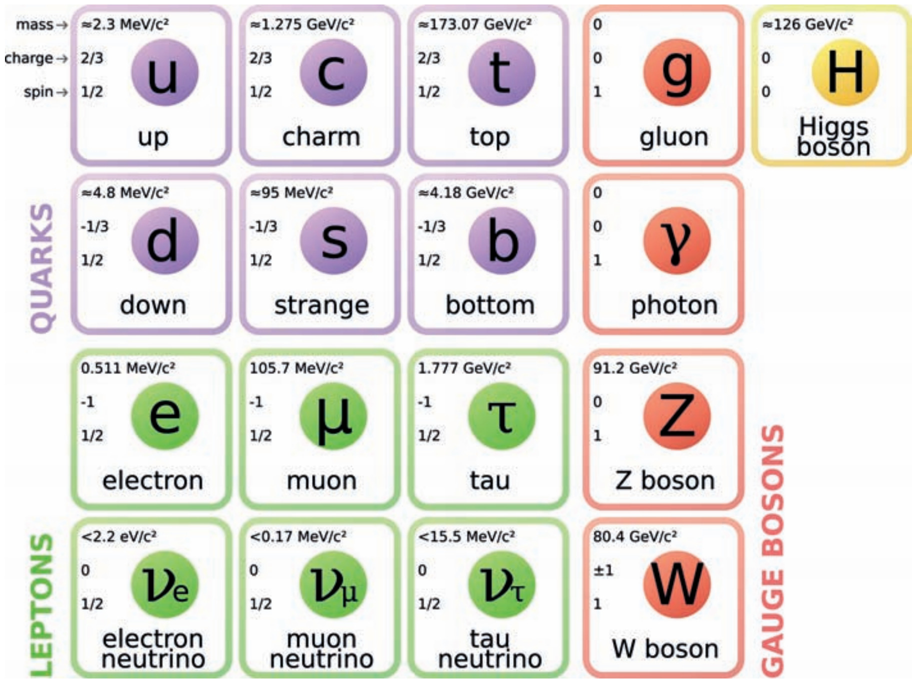

Figure 2.2: Particles of the standard model with their mass, charge and spin properties, including the Higgs Boson.[SMw].

The four fundamental forces represented by their exchange particles are also listed in figure 2.2. The standard model of particle physics utilizes the concept of a virtual transmitter for the effect of the forces. These four forces are the strong, weak and electromagnetic interactions and the gravitation. The masses of the gauge bosons are correlated strongly to their range which has been proven experimentally. Quarks and gluons are interacting strongly, bound states are called hadrons. Hadrons are subdivided in baryons and mesons according to their baryon number B. Quarks carry $B = 1/3$, Antiquarks $B = -1/3$. Hadrons with $B = \pm 1$ are assigned as baryons, hadrons with $B = 0$ are assigned to mesons [Gro10].

Nuclear processes are dominated by the strong interaction. The model of choice to describe this force is the Quantum Chromo Dynamics (QCD). Similar to the electric charge in the Quantum Electro Dynamics (QED), strongly interacting matter is attached with a *color charge* in QCD where *red*, *green* and *blue*, *anti-red*, *anti-green* and *anti-blue* are the states of this color charge. Quarks carry one single color, anti-Quarks one anti-color. Gluons are charged with a color and a anti-color at the same time. The fact, that gluons are color charged leads to the phenomenon that they can self interact, which is one fundamental difference to QED, where the photons do not carry an electric charge. The coupling constant is strongly depending on the momentum transfer Q^2, the QED coupling constant α_{em} is almost independent from Q^2. For the strong interaction based on QCD, the coupling constant α_s shows a clear dependence on Q^2. It also shows a $\approx \frac{1}{r^2}$ behavior on the distance of the constituents. The functional dependency of α_{em} and αs is shown in figure 2.3.

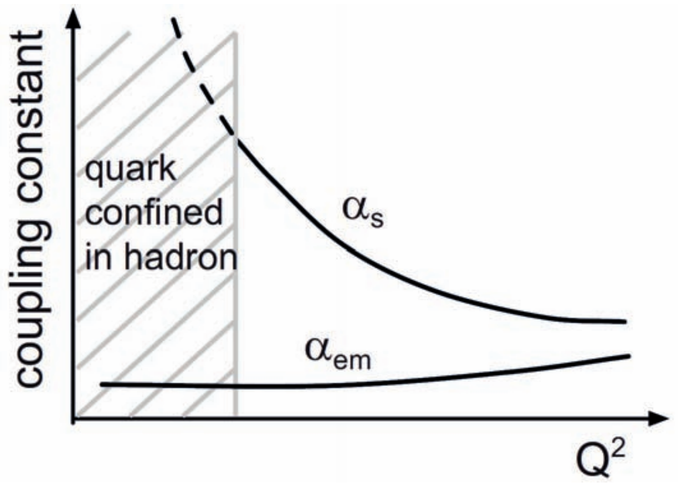

Figure 2.3: α_s and α_{em} depending on Q^2 [PRSZ08].

The potential of the strong interaction is given by the following formula:

$$V = -\frac{4}{3} \cdot \frac{\alpha_s(r)hc}{r} + kr. \tag{2.1}$$

The potential of the strong interaction has been explored according to the coulomb potential via energy level schemata. The analogy of a Positronium (bound state of electron and positron) to the Charmonium (bound state of a charm quark and an anti-charm quark) revealed differences at very small and also at very large distances [Kön86]. The larger the distance of two quarks gets, the larger the linear component of the potential $k \cdot r$ gets. This potential grows until enough energy is stored it to create a new colorless quark - anti-quark pair. This phenomenon of the strong interaction is called string breaking. According to this, only color neutral particles can exist and they are subject to the condition of confinement. However at very small distances or at very large momentum transfers the potential vanishes, because the coupling constant α_s converges to zero. Quarks and gluons are then asymptotically free. This state is called deconfinement, the constituents can be observed as quasi-free.

2.1.2 The Quark Gluon Plasma and the Phase Diagram

Heavy-ion collisions provide such high energy densities that the state of deconfinement can be reached, which is attended by a phase transition of the medium [BF11]. The involved hadron gas crosses over into a hot and dense state called Quark Gluon Plasma. This phase transition can be compared with a *classical* change of the aggregate state. The characterization and quantification of such a state of matter and its phase diagram are the objectives of the CBM experiment.

According to the potential of the strong interaction (see equation 2.1) the bounding of two quarks at very small distances vanishes. In heavy-ion collisions the energy density ϵ of the observed system, depending on temperature and the net baryonic density, is increased. The critical value of the energy density for the phase transition is $\epsilon_c \approx 1\,\mathrm{GeV/fm^3}$. If this value is exceeded the hadron gas goes over into the state of a Quark Gluon Plasma [PRSZ08].

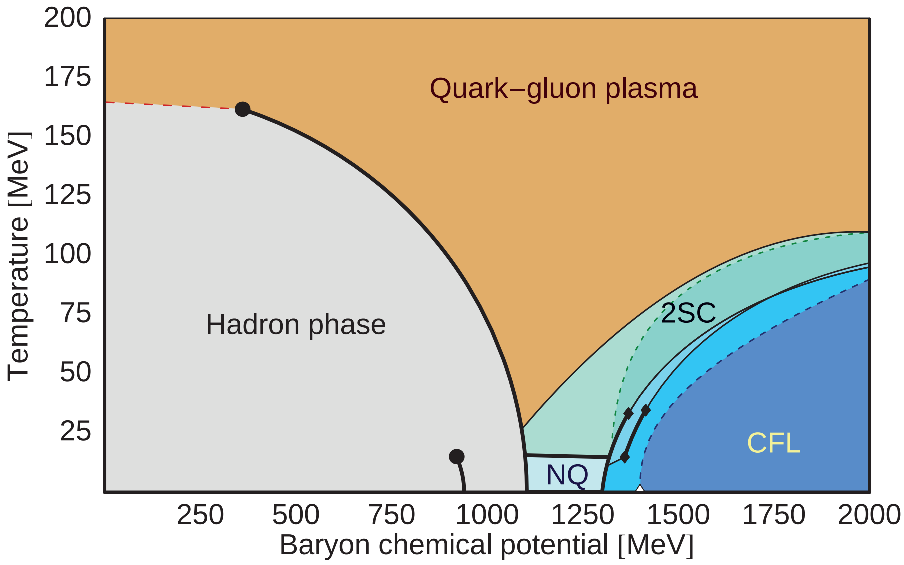

Figure 2.4: Schematic view on the QCD phase diagram [SBRR].

Figure 2.4 shows the simplified version of the quantum chromodynamics phase diagram. The temperature (energy of the observed medium) is depicted as function of the baryo-chemical potential μ_B. At low values of $\mu_B < 350\,\mathrm{MeV}$ a smooth transition from hadron gas and quark gluon plasma is expected (*crossover*). For higher values of $\mu_B > 500\,\mathrm{MeV}$ a first or second order phase transition is predicted.

One of the main intentions of the current heavy-ion research is the examination of the Quark Gluon Plasma (QGP) and the comparison with theoretical models and their predictions. The left part of figure 2.5 shows three different thermal models of the QGP. The right part of figure 2.5 shows trajectories of Pb-Pb collisions at different energies. Starting at low temperature and nominal values of hardronic matter the system reaches higher values in temperature. At the future *Schwerionensynchroton-300* (SIS-300) at the Gesellschaft für Schwerionenforschung in Darmstadt high baryon densities will be reached.

Measurements at moderate beam energies were performed at the CERN Super Proton Synchrotron (SPS) and at the Relativistic Heavy-Ion Collider (RHIC) at Brookhaven National Laboratory. These measurements cover a wide range of energy but the collected statistics did not allow a sufficiently precise measurement of for example the Charmonium, which is a bound state of a charm-anticharm pair. Besides other key measurements CBM

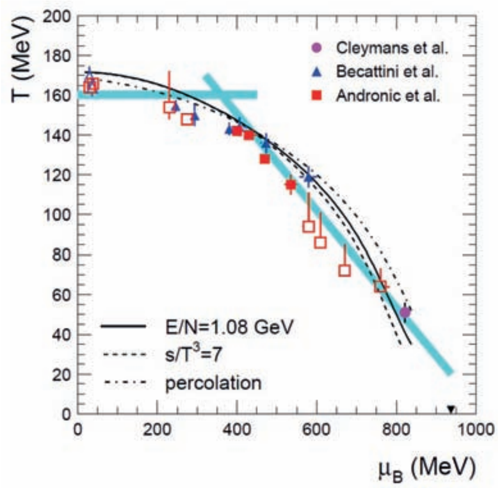

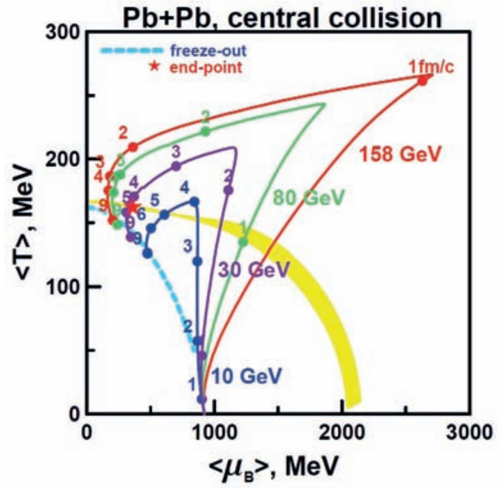

Figure 2.5: Thermal models of the QCD phase diagram [AA]. Right: trajectories of the heavy ion collision [col05].

at SIS-300 aim to provide these data in order to complete the knowledge about the QGP.

To generate a quark gluon plasma, heavy-ions are collided using modern accelerator techniques. Lead or gold ions are accelerated to ultra-relativistic velocities and than brought to collision where two different kinds of techniques are distinguished: collider experiments, where the two colliding ions are both accelerated and than brought to collision, and fixed-target experiments, where one accelerated ion collides with a non moving target. In collider experiments a larger center of mass energy $\sqrt{s}$ than in fixed target experiments can be achieved. However in fixed target experiments the luminosity is higher than in collider experiments.

The CBM Experiment requires very high statistics for its high precision measurements, which will be achieved with the help of high luminosities delivered by the future SIS-300 for a fixed-target setup. The key measurements will be the analysis of particles which include a charm quark like D^0, J/ψ and$\Psi\ '$. The expected production rates in a Au-Au collision at a given energy are shown in figure 2.6. These calculations were done using the HSD model (version 2.4) with an *impact parameter* $b = 0.5$ fm [col05]. The comparison of the exception to the measured production rate of such particles is one possibility to test the agreement of the properties of the observed medium with the assumed model.

2.2 Observables of the CBM Experiment

In case of the QGP many observables that could enable the probing of its properties were discussed. The production rate of particles containing a strange or charm quark or the suppression or enhancement compared to model predictions of the J/ψ are considered to serve as such signatures. There is not one single observable or signature which can prove the existence of the QGP, but the combination of multiple observables or signatures could

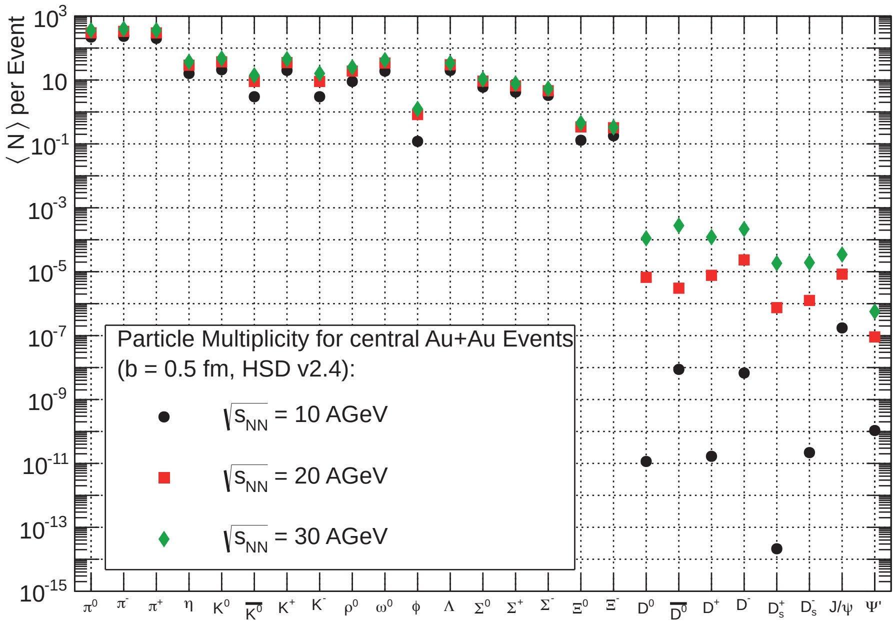

Figure 2.6: Mean number ($\langle N \rangle$) of particles per average event in a Au-Au - collision at $\sqrt{s_{NN}} = 10$, 20 and 30 AGeV calculated using HSD v2.4 model [col05].

---

reveal the nature of the QGP and its phase transitions.

The supreme discipline of a Transition Radiation Detector is the precise discrimination of electrons/positrons and pions. Almost all particles listed in figure 2.6 have at least one decay channel involving electrons, positrons or pions. The measurement of dilepton pairs and in particular the measurement of the J/ψ are described exemplarily in greater detail.

2.2.1 Dileptons

Dileptons are lepton - antilepton pairs which are generated in decay processes. They do not interact strongly, which enables them to traverse the strongly coupled medium without being affected. Dileptons transmit informations of all stages of the heavy-ion collision. The effect of electromagnetic interaction can be neglected in that case because the mean free path of photons and leptons is larger than the expected size of the generated medium.

Dilepton pairs are generated in decay processes which happen frequently enough in heavy ion collisions. According to the production channels of dileptons a variety of initial particles can be observed in a invariant mass spectrum. Since $e^- + e^+$ pairs have the smallest rest mass, the phase space to generate such pairs is largest for all lepton-antilepton pairs. Therefore $e^- + e^+$ pairs are the dominating contributers to the dilepton invariant mass spectrum. Figure 2.7 shows an invariant mass spectrum only for $e^- + e^+$ pairs.

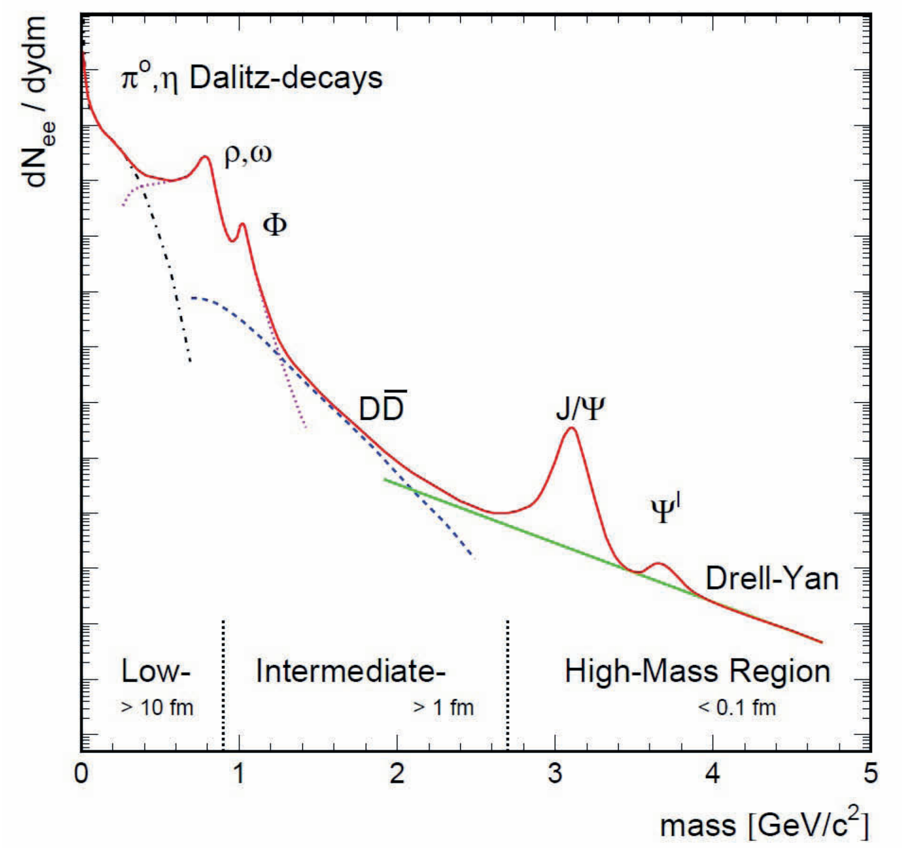

Figure 2.7: Expected sources of $e^- + e^+$ production as function of invariant mass in ultra-relativistic heavy ion collisions [Dah08].

The measured dileptons are assigned to different production mechanisms according to their invariant mass. In the low mass region up to $\approx 0.9\,\mathrm{GeV}/c^2$ the decay products of light vector mesons like the ρ, ω and ϕ are expected. Within this mass region, a variation of heavy-ion collisions compared to proton-nucleus collisions may serve as a signature for the QGP [Rap11].

In the intermediate mass region, from $\approx 0.9\,\mathrm{GeV}/c^2$ up to $\approx 2.7\,\mathrm{GeV}/c^2$, semileptonic decays of charm and anticharm quarks are considered the main contributing processes. The source of these processes are considered to be from hard scattering [Col10].

At high masses ($>2.7\,\mathrm{GeV}/c^2$) Drell-Yan-Processes and the quark-antiquark annihilation of heavier quarks like charm - anticharm and bottom-antibottom are relevant processes. Inside the generated medium, the collision of such quark-antiquark ($q\bar{q}$) pairs result in a virtual photon which decays immediately into a lepton-antilepton pair of the corresponding invariant mass.

2.2.2 J/ψ Suppression

The measurement of the production rate of the J/ψ meson is considered to be one of the *smoking gun* signatures of the quark gluon plasma. The J/ψ is the lightest vector meson of the charmonia. It is a state of a bound charm - anticharm ($c\bar{c}$) quark pair. It has a long lifetime resulting in a narrow peak in the invariant mass spectrum because the strong decay channel into two D-Mesons is impossible due to energy conservation. Because of this the electromagnetic decay channel into dileptons has a significant branching ratio [Gro10].

Due to the high mass of the $c\bar{c}$ pair these bound states are formed in the early phase of the heavy-ion collision based on hard scattering processes. However, if a QGP is formed, the color charge of charm quarks is shielded due to the color charge of the other quarks and gluons inside this medium. This phenomenon is called *Debye-Screening*, which is known from electromagnetic plasmas. Additionally to the restricted production processes, it is considered that the existing $c\bar{c}$ pairs brake up due to scattering processes inside the QGP. These so-called cold nuclear matter effects can be studied in proton-nucleus collisions. Finally, a comparison of pp, p–A and A–A collisions will shed light on the question of deconfinement at FAIR energies.

3 Principle of Operation of a Transition Radiation Detector

A Transition Radiation Detector provides the possibility to detect and identify charged particles passing the active area of the detector. With the help of its generated signals an accurate position determination of the puncture can be accomplished. The first part of this chapter describes the interactions of a charged particle with its surrounding medium. The second part lays out the working principle of the TRD and denotes the function of the detector parts. [BRR08]

3.1 Interaction of Charged Particles with Matter

Every interaction of a particle with matter causes a loss of energy of this particle. Mostly this energy loss is caused by an electro-magnetic process. The characteristic of this process can be used to identify and/or track the charged particle in the detector. There are three different processes relevant for state-of-the-art detector concepts:

- atoms of the active detector volume can be excited or ionized
- a charged particle passing through the medium emits Cherenkov light
- a charged particle can emit a transition radiation photon which is taken advantage of in a TRD.

3.1.1 Energy Loss: Ionisation

The dominant process for energy loss of a charged particle in a medium is the specific energy loss caused by ionization and excitation of surrounding atoms. It is described by the Bethe-Bloch-formula [GS08]:

$$-\frac{dE}{dx} = 4\pi N_A r_e^2 m_e c^2 z^2 \frac{A}{Z}\frac{1}{\beta^2}\left(\ln\frac{E_{kin}^{max}}{I} - \beta^2 - \frac{\delta}{2}\right) \tag{3.1}$$

with N_A as Avogadro constant, r_e and m_e as radius and mass of an electron, Z and A as atomic and mass number of the medium and I as its ionization potential and the density parameter δ. The maximum transferable kinetic energy of a particle to the atomic shell is E_{kin}^{max}. It can be approximated for particles with $m_0 \ll m_e$ and moderate energies ($2\gamma m_e \ll 1$ which is true for pions with a momentum smaller than $18\,GeV/c$) with

$$E_{kin}^{max} \approx 2m_e c^2\beta^2\gamma^2. \tag{3.2}$$

The specific energy loss is independent of the mass of a charged particle. It only depends on the velocity $\beta = v/c$ and the charge of the ionizing particle. As function of velocity the specific energy loss decreases with $1/\beta^2$ until a broad minimum is reached at $\beta\gamma \approx 4$. Particles in this region are called *Minimum Ionizing Particles* (MIPs). Starting at the minimum of $\beta \simeq 1$ the relativistic rise is proportional to $\ln(\beta^2\gamma^2 = 2\ln(\gamma))$. This rise is founded in the relativistic expansion of the transverse field of the particle. With increasing range of the field, the shielding of the electrons of the medium also increases. The energy loss saturates earlier in the so called Fermi-plateau the more dense the surrounding medium is. This effect is described with the density parameter δ. For noble gases the relativistic rise can reach values of 50 - 70%, in solid materials only around 10% [GS08, Kle05].

3.1.2 Energy Loss: Emission of Photons

Cherenkov Effect

According to quantum electrodynamics all electromagnetic processes are based on photon exchange. Which of the initially mentioned (section 3.1) phenomena actually happens, depends on the energy and the dielectric constant of the medium $\epsilon = \epsilon_1 + i\epsilon_2$, where $\epsilon_1 = n^2$ is given by the refractive index n and ϵ_2. The different cases are described by the photon absorption and ionization model [WJ80]: The emission angle θ_C of a photon with energy $\hbar\omega \ll \gamma_0 c^2$ in the direction of movement of the particle can be approximated by the four-vector conservation and the dispersion equation

$$\cos\theta_C = \frac{1}{\beta\sqrt{\epsilon}} = \frac{1}{v}\frac{c}{\sqrt{\epsilon}}. \tag{3.3}$$

Is the energy of the photon above the lowest excitation energy of the surrounding medium ($\epsilon_2 > 0$), only virtual photons can be exchanged which may cause excitation or, if carrying enough energy, ionization. This excange can not happen if the energy is below this excitation energy ($\epsilon_2 = 0$). There the dielectric constant is real and with $\epsilon_1 > 1$ the angle θ_c also gets real according to equation 3.3 if the particle is faster than the speed if light in this particular medium ($v > c/\sqrt{\epsilon}$). This allows the emission of a real photon with a wavelength in the optical band. This phenomenon is called Cherenkov radiation.

Transition Radiation

The energy loss of a particle through the exchange of a virtual photon can loom up the region of several MeV, but the interoperability decreases with $1/E^2$. When $\epsilon_2 \to 0$ the absorption region is shifted to the x-ray area. This transition is done at energies of $\approx$ 5 keV [Kle05]. Then ϵ_1 gets almost real and the emission of real photons gets in principle possible again. But then $\epsilon_1 < 1$ so that the necessary speed of the particle is $v < c$. According to this, the emittance of cherenkov radiation within the medium is not possible. But, if the dielectric constant changes at the transition from one medium to an other, transition radiation can be generated at the boundary of the two media.

The charged particle develops a dipole with the induced mirror charge when approaching the boundary of the media. The field intensity varies when the particle gets closer to the boundary and collapses completely when the particle penetrates the second medium. This temporally change of the field intensity can lead to the emission of a real photon with a wavelength in the x-ray region.

The amount of this radiation, also denoted as intensity in this frequency region, is given by [Kle05]:

$$\frac{dn}{d\omega} \propto \frac{2\alpha}{\pi\omega} \ln\left(\frac{\gamma\omega_p}{\omega}\right) \tag{3.4}$$

with α as the fine structure constant and the plasma frequency ω_p. The probability of emitting a photon the boundary of two media is at the order of $\alpha = 1/137$ [GS08]. While the intensity of the radiation only rises with $\ln \gamma$, the energy flow rises proportional to γ according to

$$S = \frac{1}{3} \alpha z^2 \hbar \omega_p \gamma \tag{3.5}$$

A particle with larger Lorentz factor is only producing slightly more transition radiation photons than a particle with a lower Lorentz factor, but, on average, this TR-Photon has a higher energy. The direction of emission of the TR-Photon is laying on a cone around the particle trajectory with an opening angle of $\theta = 1/\gamma$ [GS08].

For a sufficiently high TR yield several hundred transitions of different media are required due to the low production probability. In practice this is often realized with regular reoccurring structures like stacks of foils with a defined air gap in between. This type of radiators is called regular radiator. The energy spectrum of the TR photons of such a regular radiator can be described by a theoretical model which considers interference effects [CW75]. This interference effects appear due to coherent overlays of radiation fields on both surfaces of the bordering media as well as from different layers of a medium.

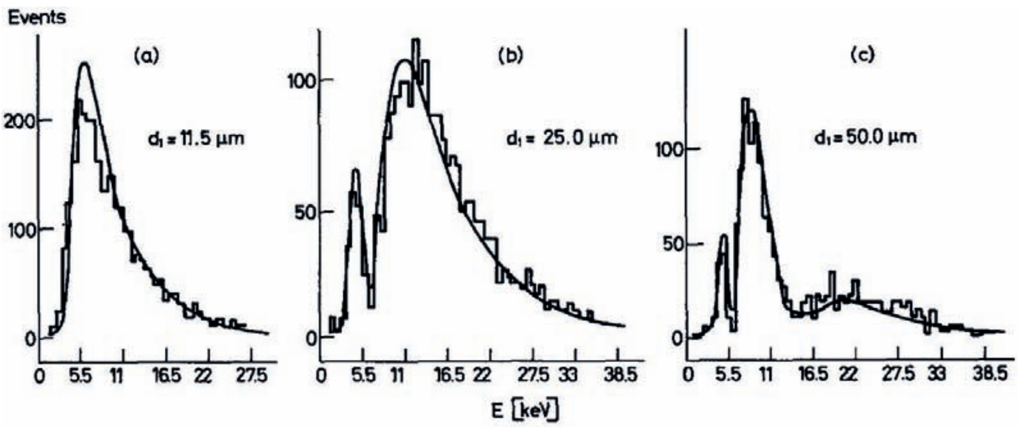

Figure 3.1: Measured energy spectra of TR-Photons produced in regular foil radiators of variable width d_1 shown together with simulations (smooth line) [CW75].

The measured TR photon spectra of three regular radiators with different foil widths are shown in figure 3.1. The interference effect increases significantly from (a) to (c). This can be described very well by a model from [CW75].

3.2 Working Principle of a TRD

In heavy-ion collision experiments the main task of a transition radiation detector is the separation of electrons and pions of momenta $p \gtrsim 1\,\mathrm{GeV/c}$. This results from the fact that electrons (and positrons) are the only particle which are ultra relativistic ($\gamma \gtrsim 2000$) and are thus able to produce TR-Photons at these momenta.

A Multi-Wire Proportional Chamber (MWPC) consists essentially of a set of thin, parallel, and equally spaced anode wires, symmetrically sandwiched between two cathode planes. Depending on the experimental requirements one usually chooses a detector gas mixture consisting of a quenching gas like CO_2 and a noble gas like Xe or Ar. When a negative potential is applied to the cathodes and the anode is grounded or a positive potential is applied to the wires and the cathodes are grounded, respectively, an electric field develops as sketched in figure 3.2.

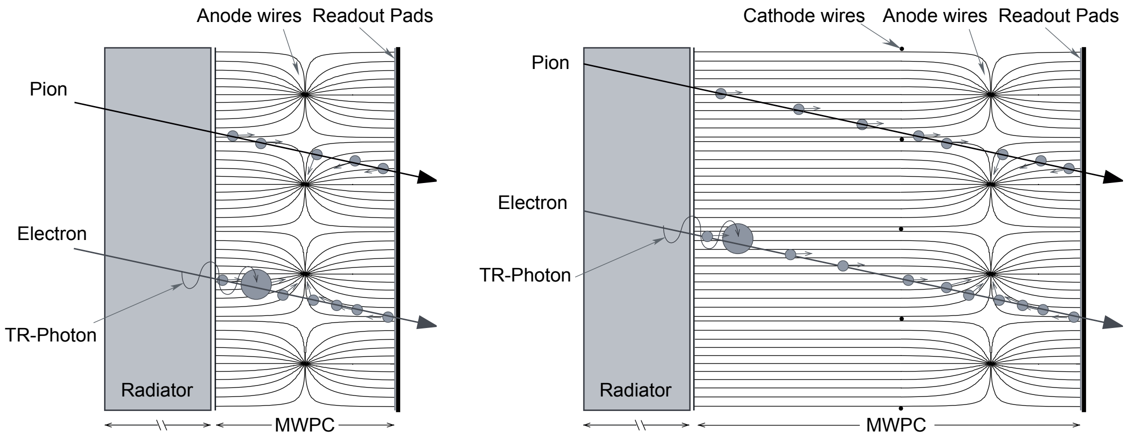

Figure 3.2: Schematic layout of a MWPC without (left) and with additional drift region (right).

3.2.1 Radiator

The production of transition radiation takes place when an ultrarelativistic particle crosses multiple layers of different materials. The typical energy of the TR-photon is within the range of 1-30 keV (see figure 3.1). To lower the potential re-absorption, radiator materials with low atomic numbers are used. The photo- and the Compton effect act as absorption processes. The photo effect has a larger cross section in the relevant energy range which can be described in Born approximation:

$$\sigma^K_{photon} = \left(\frac{32}{\epsilon^7}\right)^{\frac{1}{2}} \alpha^4 Z^5 \cdot \frac{8}{3}\pi r_e^2 \tag{3.6}$$

where $\epsilon = E_\gamma/m_e c^2$ is the reduced photon energy [GS08]. Because of the proportionality of equation 3.6 to the fifth power of the atomic number, materials with low Z should be preferred. Foils made of lithium could serve as an optimal solution, but also foils consisting of polypropylene (PP) or polyethylene (PE) could be used. For the construction of a new detector not only performance matters, but also stability and long term reliability may influence the choice of radiator material. In fact, also foam and fiber materials provide a good compromise between performance and stability. The TRD of the ALICE experiment at CERN LHC consists of a sandwich type radiator of ROHACELL foam and fibers [ALI01].

3.2.2 Multi Wire Proportional Chamber

The actual detection device is directly connected to the radiator. It catches the emitted photons and generates traces along the traversing particle. Gas detectors of various kinds, which are constructable in suiting sizes, are suitable for this. A Multi-Wire Proportional Chamber (MWPC) is one of these detectors featuring high efficiency and a relatively low material budget. Such MWPCs have already been employed for the ALICE-TRD and are the primary attempt for the CBM TRD [Ber09].

In the simplest case, a MWPC consists of two parallel grounded layers, which serve as entrance and exit window. Centered between this layers the anode wire plane is mounted and supplied with a positiv potential. If a traversing particle ionizes the gas the generated electrons will be attracted by the positive potential and travel to the anode wires. The potential is chosen such, that the multiplication is located in the area of proportional counters of figure 3.3.

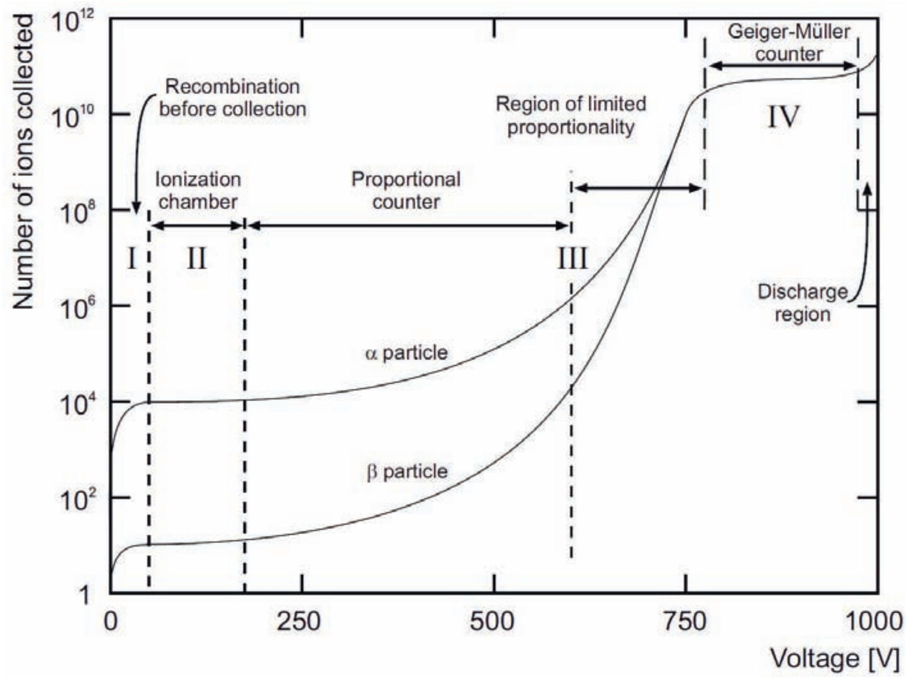

Figure 3.3: Number of ions collected versus the potential on the anode wire [Ber09].

The multiplication of the ionization electrons is called *gas amplification* or *gas gain*. The development of this gas gain and its avalanche characteristics is depicted in figure 3.4. According to the linearity of the proportional area the charge collected on the wire can be used to reconstruct the total deposited energy inside the MWPC.

To obtain a two dimensional position information of the incident particle the exit plane is divided in segmented electrodes (*pads*). The signal is split and collected by these pads (see figure 3.5), which are connected to the read out electronics. The position information

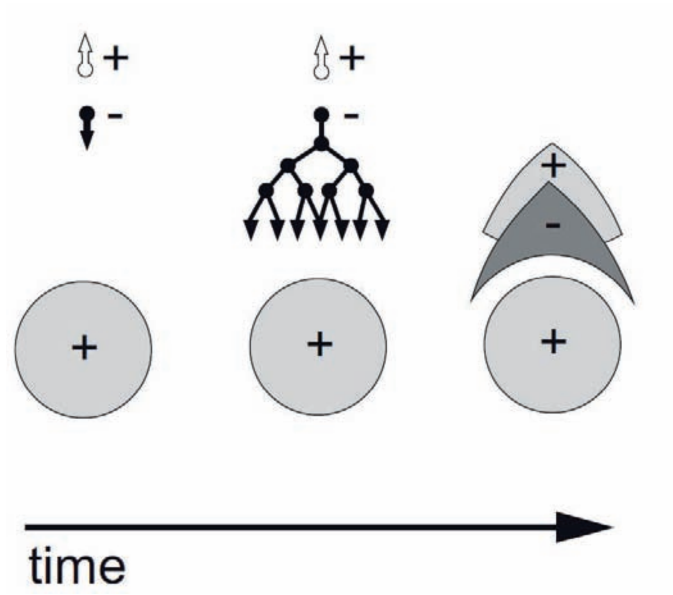

Figure 3.4: Illustration of the development of an avalanche of electrons near the anode wire [Ber09].

is reconstructed by the relative hight (*center of gravity*) of the signals of the involved pads.

During the amplification process the produced electrons move quickly towards the anode wires and induce time-dependent mirror charges in both cathodes, which again generate a short signal on the pads. As soon as the electrons are absorbed by the anode wire, the produced ions produce also a signal in a similar way, but more slowly. These signals are distributed over the segmented pads on the exit plane and are read out by the electronics.

Additional Drift Region attached to a MWPC

Additionally to the described symmetric MWPCs (see chapter 3.2.2) a further drift region can be attached to decouple the generated signals from the size of the gas volume. Both types are shown in figure 3.2. With a drift region the generated signal is higher and extended in time, which simplifies the signal collection for the read-out electronics. The additional gas volume increases also the probability of the TR photon being absorbed in the gas volume. The construction of a MWPC with drift region requires an additional wire plane and the signal generation is slower compared to a symmetric MWPC. This may be a drawback at the high collision rates in the CBM experiment (see chapter 5). Both alternatives of MWPCs were investigated for the CBM TRD.

Selection of Gas

The efficiency of the electron - pion separation is directly connected to the absorption of the produced transition radiation. In contrast to the radiator material, the employed gas should have a very high atomic number according to equation 3.6. The heaviest non-radioactive gas is xenon (Xe) with $Z = 54$. The advantage of noble gases to complex

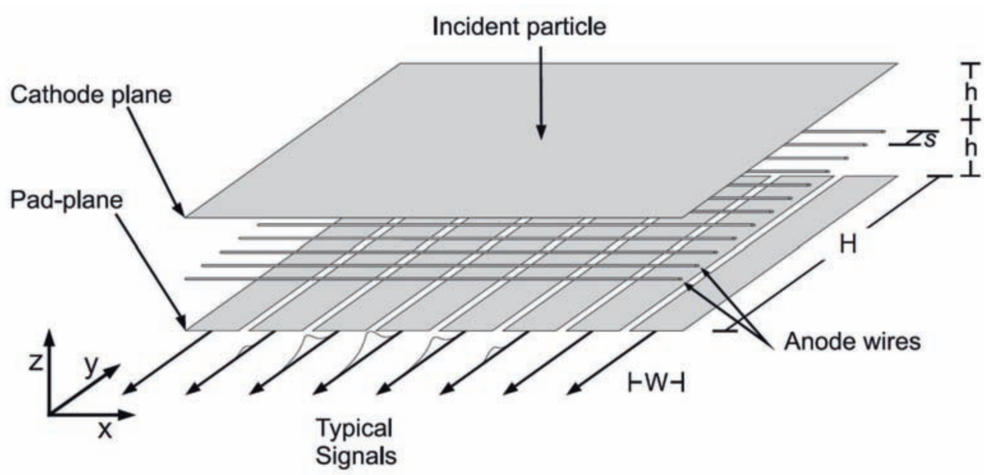

Figure 3.5: Read-out pads collect generated signal [Ber09].

molecules is that a large fraction of the deposited energy by the incident particle leads to ionization, whereas molecules tent to get excited by the energy deposited in the gas volume.

However, a small fraction of the utilized gas has to be a so called *quenching gas*, e.g. CO_2. Secondary photons emitted by excited xenon atoms should be absorbed locally by the quencher. These secondary photons may be absorbed by any material with low work function (e.g. metal in the surrounding frame) and may release an electron which leads to an avalanche and thus in a fake signal. If a xenon atom is stronger excited than the ionization energy of a CO_2 molecule, this energy can be transfered and contributes to the wanted gas amplification. This process is called *penning transfer* [Gar].

The absorption of a photon inside a medium can be described as follows: The intensity I of a monoenergetic photon beam of energy E after passing trough a material of thickness d is given by

$$I(d) = I_0 \cdot e^{-\frac{\mu}{\rho}(E)\cdot\rho\cdot d} \tag{3.7}$$

It depends on the mass attenuation coefficient $\frac{\mu}{\rho}(E)$ of the crossed material and the density ρ [RJ74]. The mass attenuation coefficient for Xe/CO_2 of a mixture of $85:15$ versus the photon energy E is shown in figure 3.6 [Para, Parb]. The shape of the function in figure 3.6 is dominated by the photo effect and is influenced by the $L-$ and $K-$shell binding energy of xenon up to $E \approx 300\,\mathrm{keV}$. Subsequently the Compton effect is dominating and is followed by pair production at $E \approx 6\,\mathrm{MeV}$. Both effects are depending differently on the atomic number which causes a strong dependency on the material. Only the photo effect is relevant in the energy regime of transition radiation [GS08] .

Gas Amplification

The process of avalanche formation based on ionization in the proportional area of a MWPC is called gas gain. It is defined with the first Townsend coefficient α, the excitation-

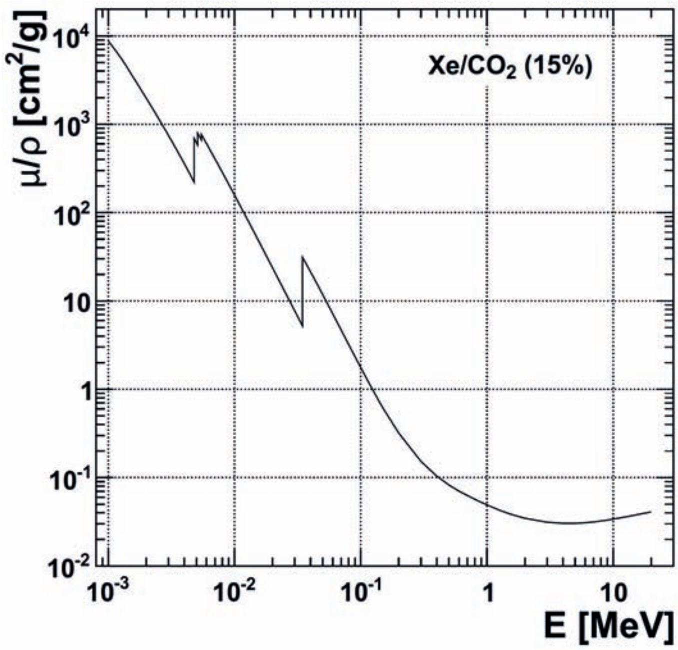

Figure 3.6: Mass attenuation coefficient of Xe/CO_2 in a mixture of $85 : 15$.

and ionization cross section of electrons, the ionizing gas and its density as well as the electric field strength. The first Townsend coefficient specifies the number of generated electron - ion pairs per path length. It has to be measured for every gas because it can not be calculated analytically. Integrated over the total drift length, the gas gain is the ratio of number of electrons N inside an avalanche with respect to the initial number of electrons N_0:

$$\frac{N}{N_0} = \exp \int_{s_{min}}^{\alpha} \alpha(s) ds = \exp \int_{E_{min}}^{E(a)} \frac{\alpha(E)}{dE/ds} dE \tag{3.8}$$

where E_{min} is the electric field strength, which is needed to cause multiple ionization, a is the radius of the wire and dE/ds is the gradient of the electric field. The wire radius a has to be small compared to the wire pitch. The electric field in the environment of the wire is given as a function of the distance r and with λ as charge per unit length on the wire:

$$E(r) = \frac{\lambda}{2\pi\epsilon_0 r} \tag{3.9}$$

This results in the gas gain of:

$$\frac{N}{N_0} = \exp \int_{E_{min}}^{E(a)} \frac{\lambda\alpha(E)}{2\pi\epsilon_0 E^2} dE \tag{3.10}$$

The charge per unit path length can be described with the capacity C and the anode voltage U via

$$\lambda = \frac{Q}{L} = \frac{C \cdot U}{L} \tag{3.11}$$

The capacity of a MWPC can be characterized in two different ways. The first method approximates the anode wires as one anode plane and the MWPC as a parallel-plate capacitor. For this approximation the distance between anode and cathode has to be much larger than the anode wire pitch, which is not correct for the CBM TRD prototypes. The second way is the approximation of every single anode wire as a cylindrical capacitor, which would take the comparable large wire pitch into account. In this case the capacity is given as:

$$C = 2\pi\epsilon_0 \cdot \frac{L}{\ln\left(\frac{R}{\alpha}\right)} \tag{3.12}$$

with L as the length of the anode wire and the distance of anode to cathode as R. Applying this to equation 3.11 the gas gain can be expressed by:

$$\frac{N}{N_0} = \exp \int_{E_{min}}^{E(a)} \frac{U}{\ln\left(\frac{R}{\alpha}\right)} \cdot \frac{\alpha(E)}{e^2} dE. \tag{3.13}$$

According to this approximation the gas gain is depending on the distance R of the anode wires to the cathode plane and decreases at a given anode voltage U and with increasing distances [BRR08, Rei08].

4 The FAIR Complex

The future Compressed Baryonic Matter experiment will be set up at the Facility for Antiproton and Ion Research (FAIR). The FAIR accelerator complex together with its experiments will be located at the *Gesellschaft für Schwerionenforschung* (GSI) near Darmstadt in the State of Hesse, Germany. The existing research facilities of the GSI will be extended and the necessary infrastructure for the upcoming experiments will be provided. The civil construction has started and according to the current planning it will be finished by 2018 [ROS13].

In addition to the CBM experiment, a variety of other experiments with a wide range of research fields will use the FAIR accelerator complex. The planned layout of FAIR including its experiments is shown in figure 4.1. The new facilities will be built in two phases. The accelerators and the CBM experiment are part of the first of these two stages of construction [ROS13].

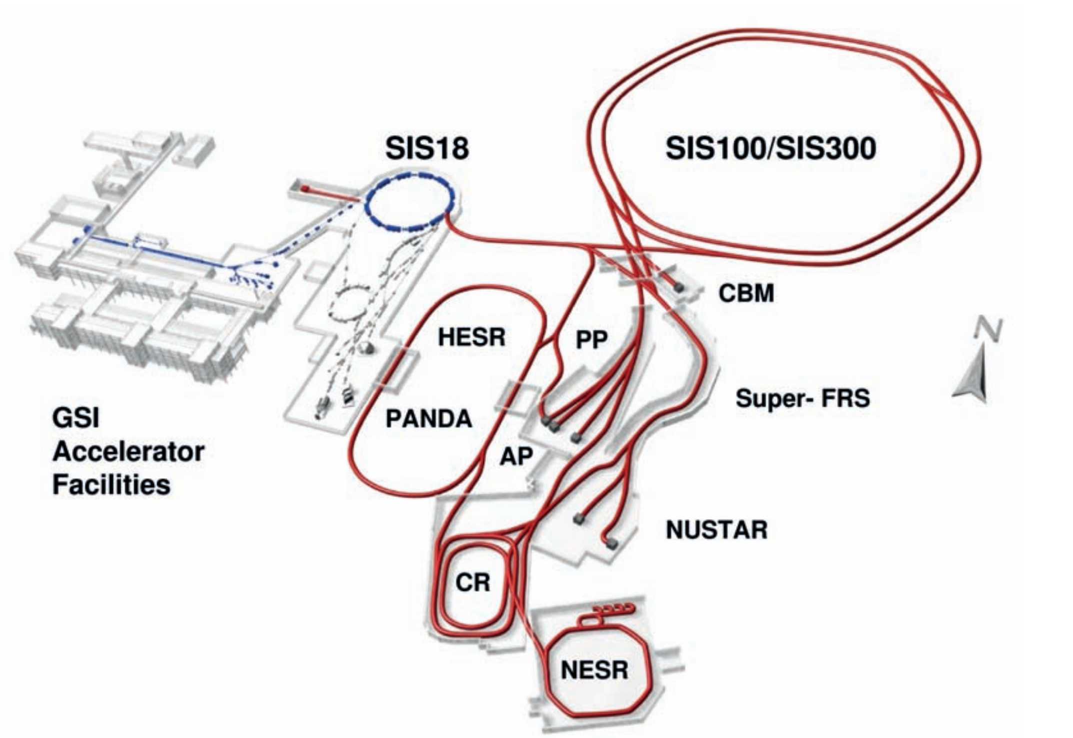

Figure 4.1: Layout of the future FAIR accelerator complex. The existing accelerators (SIS18) are shown as blue lines, the additional new FAIR complex is shown as red lines [FAI].

In figure 4.1 the accelerator complex is shown as blue and red lines. The main particle accelerator is the *Schwerionen-Synchrotron* SIS100/300 which is attached to the existing SIS18. SIS18 will inject the preaccelerated particles into SIS100/300, which will boost them to their maximal energy. SIS100 is part of the first stage of construction, SIS300 will be set up as an upgrade to SIS100 according to the current planning. The difference in the accelerator settings are the highest achievable magnetic rigidity R of the used magnets. The maximum values are $R_{SIS100} = 100\,\mathrm{Tm}$ and $R_{SIS300} = 300\,\mathrm{Tm}$ for SIS100 and SIS300, respectively. SIS300 will deliver particles at a beam energy of $\sqrt{s_{NN}} = 34\,\mathrm{GeV/c}$ with $5 \cdot 10^{11}$ particles per bunch. This high number of projectiles results in an outstanding luminosity which is necessary for the precision measurements of CBM and the other experiments hosted by FAIR.

SIS100/300 delivers its beam also to other devices and experiments. Directly connected to SIS100/300, the Fragment-Separator Super-FRS produces and separates rare isotopes which are investigated by the Nu-STAR experiments. The storage rings HESR, NESR and RESR host additional experiments like PANDA. The APPA collaboration aims to measure the effects of irradiation to biological cells and material structures. PANDA, Nu-STAR and APPA as well as their storage rings are part of the second construction stage of FAIR [AR09]. Figure 4.2 shows an artits view of the finished FAIR complex. As the CBM experiment is the main topic of this thesis it will be described in detail in chapter 5.

Figure 4.2: Artists view of the FAIR complex. The SIS100/300 is surrounded with forest [Off14].

5 The Compressed Baryonic Matter Experiment

The Compressed Baryonic Matter experiment at the future FAIR complex is a dedicated heavy-ion experiment which will explore the QCD phase diagram. For this purpose, rare probes will be investigated, which requires very large statistics. This will be achieved with the outstanding luminosity the FAIR accelerator complex provides. The high interaction rate requires a very fast detector design. At the same time, the detector systems have to be precise enough to resolve the physics observables CBM aims for. Both aspects determine the design of the future CBM experiment.

A modular design of the CBM experiment allows for the exchange of separate detector systems. The first setup is dedicated to identify electrons, it is shown in figure 5.1. The second setup enables the CBM experiment to measure muons, the corresponding setup is shown in figure 5.2.

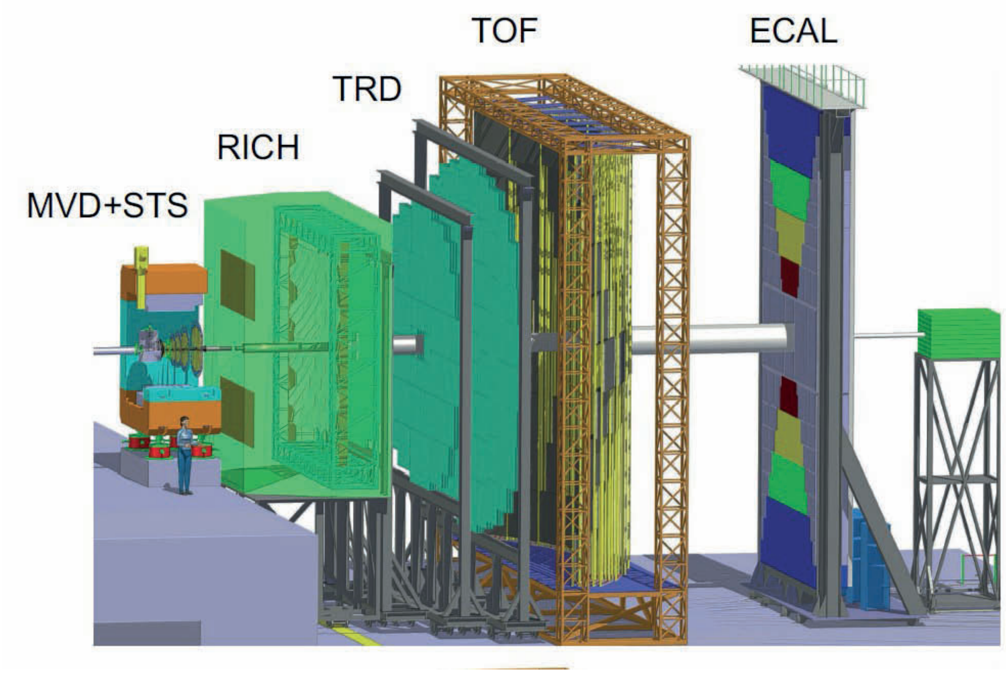

Figure 5.1: Illustration of the electron identification setup of the CBM experiment [BF11].

The Micro Vertex Detector (MVD) and the Silicon Tracking System (STS) are placed directly around the collision vertex enclosed by a superconducting dipole magnet. This first section of CBM is part of both setups.

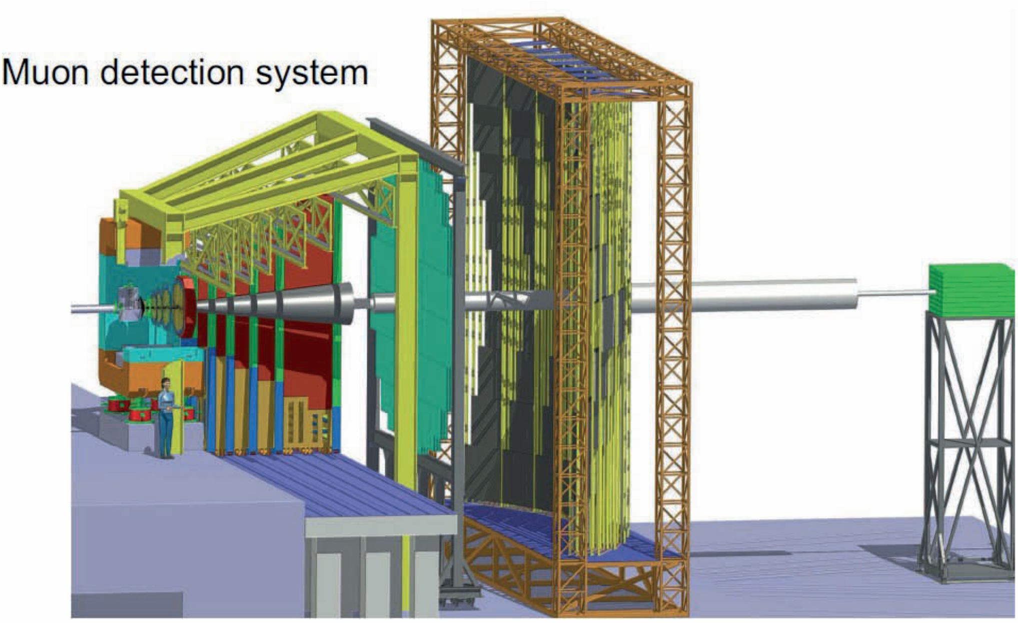

Figure 5.2: Illustration of the muon identification setup of the CBM experiment [BF11].

For the electron identification setup the first section is supplemented by the Ring Imaging Cherenkov Detector (RICH) and the Transition Radiation Detector (TRD). The TRD is divided into three stations. The first two consists of four layers each and the third station completes the setup with two additional detector layers. These TRD stations and the RICH can be moved for the muon identification setup. The Moun Detection System (MUCH) is inserted for this setup. The last station of the TRD completes the muon setup with additional spacial hit information.

The Time Of Flight (TOF) wall is part of both setups, the Electromagnetic Calorimeter (ECAL) is only included in the electron identification setup. The Projectile Spectator Detector (PSD) completes the setup in both cases.

An overview of the experimental area is depicted in figure 5.3. The CBM experiment is hosted in the same cave as the HADES experiment and uses the same beam line.

5.1 Superconducting Dipole Magnet

The superconducting dipole magnet of the CBM experiment is of `H-type` with circular superconducting coils and with two cryostats. It is shown in figure 5.4. It has a large aperture (gap height 140 cm, gap width 260 cm) in order to host the Silicon Tracking System. The field integral is 1 Tm [FS13].

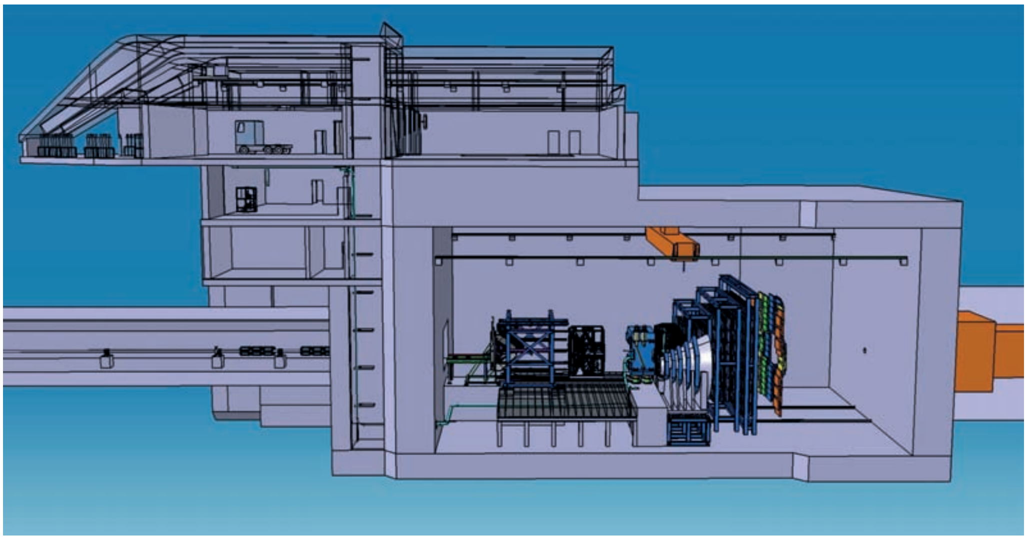

Figure 5.3: Overview of the CBM experimental area. The HADES experiment is placed in front of CBM in the same beam line [Nie13].

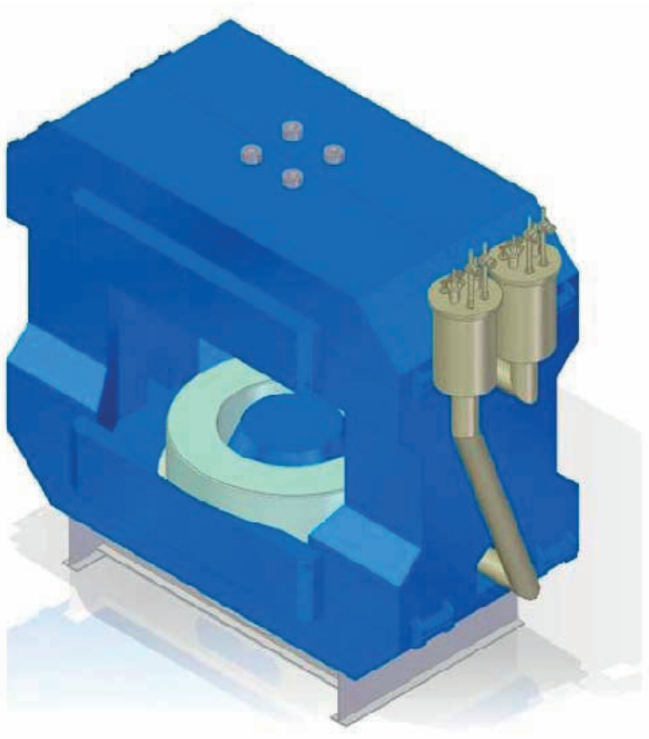

Figure 5.4: Schematic drawing of the CBM superconducting Magnet [FS13].

5.2 Detector Systems

In this section, the most important detector systems of the CBM experiment are briefly introduced. The TRD will be discussed separately in chapter 6.

5.2.1 Micro Vertex Detector

The Micro Vertex Detector (MVD) aims for precise determination of weak decay vertices in CBM. This measurement requires a highly-granulated, fast, radiation-hard, and low-mass detector system. Based on this requirements, ultra-thin Monolithic Active Pixel Sensors (MAPS) will be used in the MVD. These sensors have been developed to exhibit a high signal-to-noise ratio even after an integrated neutron dose of $10^{13}\,\mathrm{neq/cm^2}$ [FS13].

5.2.2 Silicon Tracking System

The CBM Silicon Tracking System (STS) is based on double-sided micro-strip sensors with outer dimensions of $6.2 \times 2.2\,\mathrm{cm^2}$, $6.2 \times 4.2\,\mathrm{cm^2}$, and $6.2 \times 6.2\,\mathrm{cm^2}$. The front-side strips are inclined by a stereo angle of $7.5\,^\circ$. Short strips in the sensor corners will be interconnected to a strip in the opposite corner either via a second metallization layer or via an additional micro cable. Both options are under investigation. Each sensor (2048 strips) is read out via 16 low-mass micro cables (128 wires each) by 8 free-streaming ASICs (2 channels each). The cables will be tab-bonded at both ends. Several of these modules consisting of a sensor, the cables and the front-end board carrying 8 ASICs will be mounted on a light-weight carbon ladder. Up to 16 of these ladders will be integrated into a detector station. The STS consists of 8 stations of increasing size with larger distance from the target (see figure 5.5). The STS will be operated in a thermal enclosure at about -10 °C [FS13].

5.2.3 Ring Imaging Cherenkov Detector

Figure 5.6 presents the Ring Imaging Cherenkov (RICH) Detector which exhibits an active area of $2.4\,\mathrm{m^2}$ and 55000 individual readout channels. In 2012, two options for photo sensors have been investigated as possible alternatives to the *Hamamatsu H8500* baseline solution: the *Hamamatsu R11265* with enhanced quantum efficiency due to Super-Bialkali cathode and a Micro Channel Plate (MCP) sensor from *Photonis*, *XP85012*, which is immune against magnetic stray fields. All three sensors have been tested in parallel during a RICH test beam at CERN PS (see chapter 11). In the beginning of 2012, the development of a new FPGA-TDC based readout concept for the RICH was started at the GSI electronic department. First prototype modules have been successfully tested at CERN together with the previously used n-XYTER readout, allowing for a direct comparison of the two different concepts [FS13]. The RICH will contribute to the electron-pion separation in the momentum range of up to $8\,GeV/c$, see figure 5.7.

5.2.4 Time Of Flight Detector

An array of Multi-gap Resistive Plate Chambers (MRPCs) will be used for hadron identification via Time-Of-Flight (TOF) measurements. The TOF wall covers an active area of about $120\,\mathrm{m^2}$ and is located about 6 m downstream of the target for measurements at SIS-100, and at 10 m at SIS-300. The required time resolution is of the order of 80 ps. For 10 MHz minimum bias Au+Au collisions, the innermost part of the detector has to

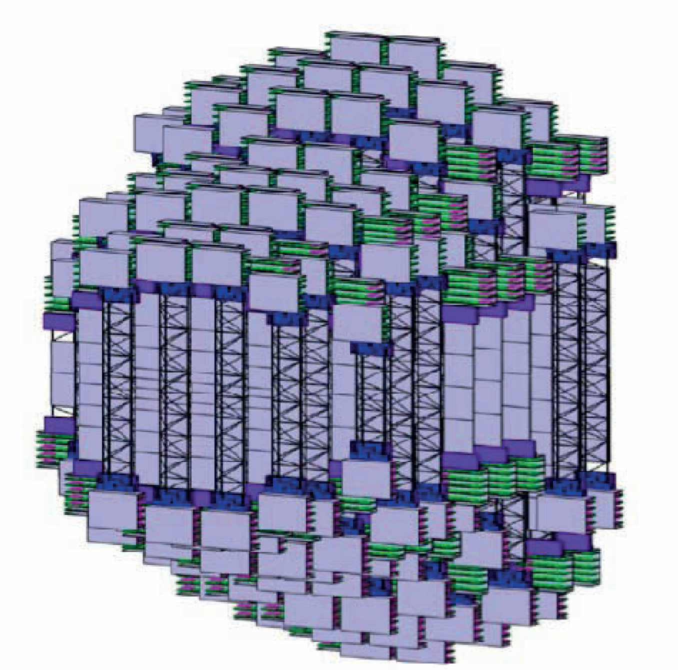

Figure 5.5: Layout of the CBM STS. [FS13]

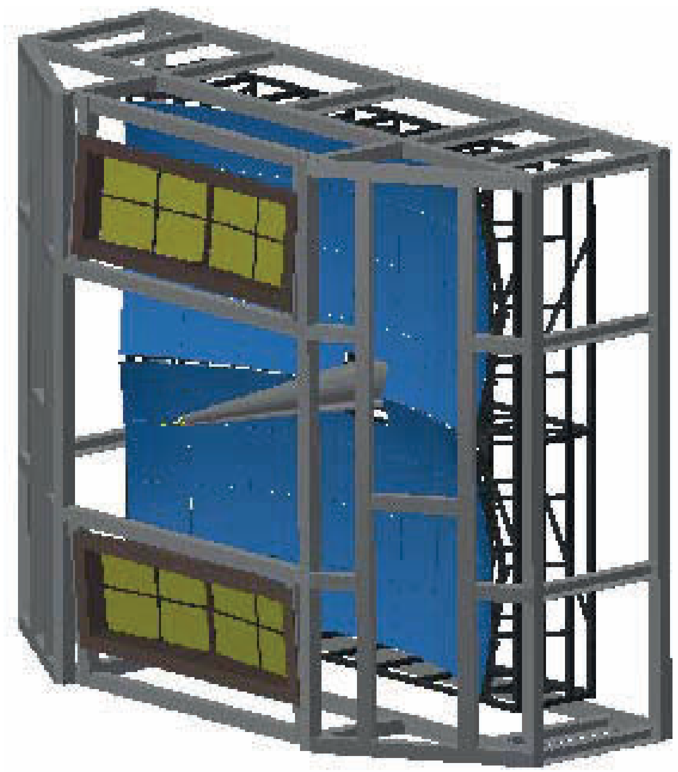

Figure 5.6: Technical drawing of the CBM RICH detector system [FS13].

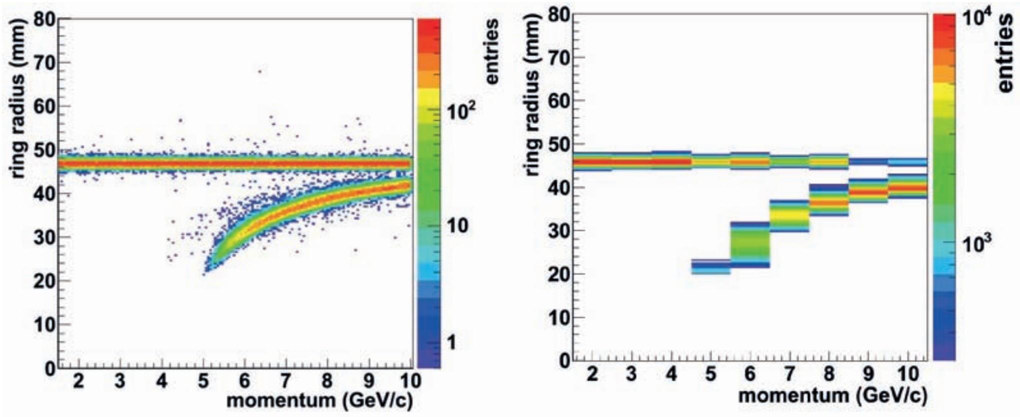

Figure 5.7: Ring radius in the RICH depending on initial particle momentum. The left panel shows a simulation, right panel depicts the measurement. Electrons show up as a constant band whereas the pions exhibit a dependency on momentum which approaches asymptotically to the electron value at high momenta [FS13].

---

work at rates up to 20 kHz/cm^2. Prototype MRPCs built with low resistivity glass have been tested with a time resolution of σ = 40 - 60 ps at 20 kHz/cm^2. At small deflection angles the pad size is about 5 cm^2, corresponding to an occupancy of below 5% for central Au+Au collisions at $\sqrt{s_{NN}}$ = 25 AGeV. In order to optimize the number of gaps, the pad layout, and the read-out electronics, several prototype MRPCs have been tested with particle beams at CERN. At large polar emission angles, i.e. in most of the active area of the CBM TOF detector, the hit rate is of the order of 1 kHz/cm^2. At these low rates, a conventional MRPC in multi-strip configuration with thin standard float glass can be used [FS13].

5.2.5 MUCH System

In order to identify muons from vector meson decays in a large hardronic background, CBM will use an instrumented hadron absorber. The detection system comprises 6 iron slabs of varying thickness from 20 cm to 100 cm, with detector triplets behind each iron absorber. The technology of the gaseous muon tracking detectors is matched to the hit density and rate: behind the first and second hadron absorber (particle density up to 50 kHz/cm^2) Gas Electron Multiplier (GEM) detectors will be installed. Prototype GEM detectors with single-mask foils have been successfully tested with particle beams at CERN. Further downstream, where the hit density is reduced, straw-tube detectors will be used [FS13].

5.3 The Free Streaming Data Readout Concept

One of the challenges in the design and development of the CBM experiment is the high event rate and the resulting unprecedented high particle density. A triggered and event-based data read-out would be too slow or cause loss of rare and interesting events. For that reason the data read-out of the CBM experiment will be taken continuously. The reconstruction of events will be based on a `time-slice procedure` which utilizes a global time stamp of the read out data. The continuous data readout generates an enormous amount of raw data.

Measurements with high event rates require online event selection algorithms on specialized hardware which reject the background events (which contain no signal) by a factor of 100 or more. The event selection system will be based on a fast online event reconstruction running on a high-performance computer farm equipped with many-core CPUs and graphics cards (*GSI GreenIT cube*) [FS13].

6 Transition Radiation Detectors for CBM

The Transition Radiation Detector (TRD) is, together with the RICH-Detector, the main electron identification device. With its capability to resolve a traversing particle in x-y-plane, the TRD additionally contributes to the experiment-wide tracking of charged particles. For this purpose multiple the x-y-layers of segmented read-out pads are utilized.

6.1 Requirements for the CBM TRD

According to the physics goals of CBM (see chapter 2.2) and the currently planned CBM setups three main requirements for the TRD can be derived:

- A *rate capability* of more than 10^5 traversing charged particles per cm^2 per second at an interaction rate of 10 MHz [BF11].
- A *pion rejection factor* of better than 100 at an electron efficiency of 90% [BF11]. This translates into a misidentification probability of less then 1% for a pion to be an electron.
- A *position resolution* of better than 1 mm to achieve a signal over background ratio of ≈ 30 for the J/ψ [WYH10].
- A gas gain variation of less then 10% and/or a calibration scheme to compensate for it.

6.2 TRD inside CBM

The TRD of the CBM experiment is constructed out of multiple layers of separate detectors. One station of the TRD is made up of several layers. For the current design three stations are foreseen. The first and second station are out of four layers each. The third station is constructed out of two layers, which results in 10 detector layers in total. The configuration of the separate detector modules depends on station, layer and position with respect to the beam pipe in x-y-plane. Figure 6.1 shows one of the possible setups. The final design of the TRD depends on the performance of the developed detector modules and the global experimental layout.

According to the different setups of the CBM experiment at SIS100 and SIS300, with electron identification and muon identification setup, the position in beam direction z of each is shown in table 6.1 and 6.2. For SIS100 an additional hadron identification setup is planned [Mue13]. A visualization of the resulting setups are shown in figure 6.2, 6.3, 6.4 for SIS100 and figure 6.5 and 6.6 for SIS300.

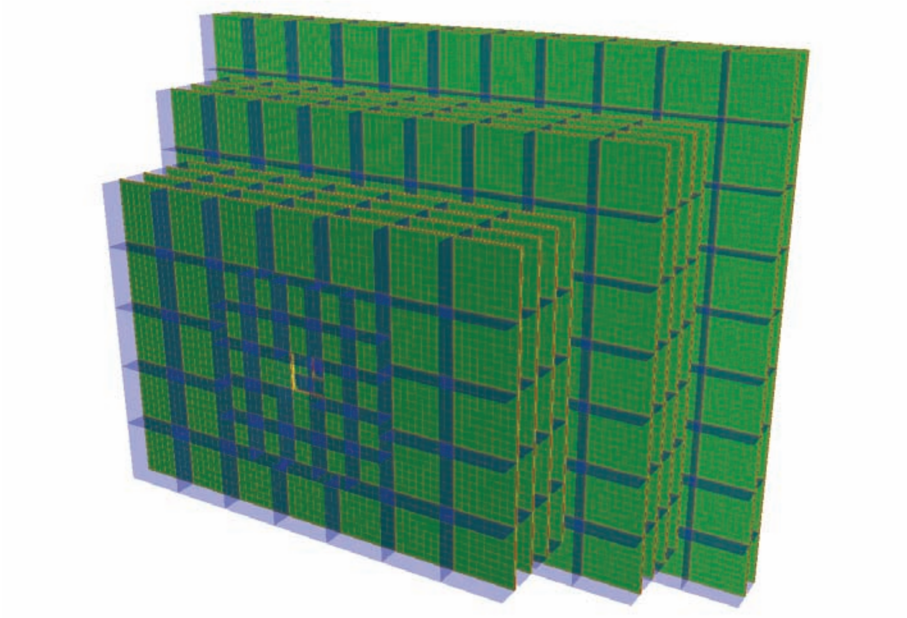

Figure 6.1: Current schematic setup of the complete TRD. This setup consists of three stations with four, four and two detector layers. The inner-most detector modules in station one and two are smaller than the outside ones [Ems13a].

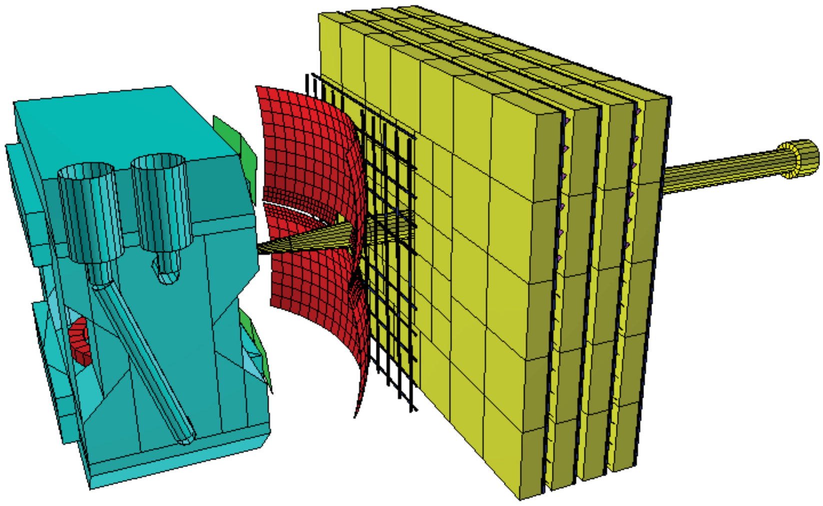

Figure 6.2: Electron identification setup of CBM at SIS100 (v13k). The four layers of the TRD are shown in yellow. [Ems13a].

		Part	z-position start [mm]	z-position end [mm]
Electron identification setup	TRD v13k	STS-Box	0	1200
		Magnet	0	1600
		Clearance	1600	1800
		RICH	1800	4000
		Clearance	4000	4100
		TRD station 1	4100	5900
		Clearance	5900	6000
		ToF	6000	7200
		Clearance	7200	7500
		PSD	7500	9000
		Cave End		20050
Muon identification setup	TRD v13l	STS-Box	0	1200
		Clearance	1200	1250
		Absorber 1	1250	1850
		Much Detector station 1	1850	2150
		Absorber 2	2150	4200
		Clearance	4200	4300
		TRD station 1	4300	6100
		Clearance	6100	6200
		ToF	6200	7400
		Clearance	7400	7700
		PSD	7700	9200
		Cave End		20050
Hadron setup	TRD v13h	STS-Box	0	1200
		TRD station 1	2600	4400
		Clearance	4400	4500
		ToF	4500	5700
		Clearance	5700	6000
		PSD	6000	7500
		Cave End		20050

Table 6.1: Positioning of subsystems and detectors at SIS100.

		Part	z-position start [mm]	z-position end [mm]
Electron identification setup	TRD v13g	STS-Box	0	1200
		Magnet	0	1600
		Clearance	1600	1800
		RICH	1800	4000
		Clearance	4000	4100
		TRD station 1	4100	5900
		Clearance	5900	5950
		TRD station 2	5950	7750
		Clearance	7750	7800
		TRD station 3	7800	8700
		Clearance	8700	8800
		ToF	8800	10000
		Clearance	10000	10300
		PSD	10300	11800
		Cave End		20050
Muon identification setup	TRD v13m	STS-Box	0	1200
		Clearance	1200	1250
		Absorber 1	1250	1850
		Much Detector station 1	1850	2150
		Absorber 2	2150	2350
		Much Detector station 2	2350	2650
		Absorber 3	2650	2850
		Much Detector station 3	2850	3150
		Absorber 4	3150	3450
		Much Detector station 4	3450	3750
		Absorber 5	3750	4100
		Much Detector station 5	4100	4400
		Absorber 6	4400	5400
		Clearance	5400	5500
		TRD station 1	5500	7300
		Clearance	7300	7350
		TRD station 2	7350	9150
		Clearance	9150	9200
		TRD station 3	9200	10100
		Clearance	10100	10200
		ToF	10200	11400
		Clearance	11400	11700
		PSD	11700	13200
		Cave End		20050

Table 6.2: Positioning of subsystems and detectors at SIS300.

Geometry	# channels	active area	# detector modules	channel per area
CBM TRD v13h,k,l	258560	$125\,m^2$	200	$2163\,/m^2$
CBM TRD v13g,m	807424	$528\,m^2$	708	$1597\,/m^2$
ALICE TRD	1181952	$694\,m^2$	540	$1703\,/m^2$

Table 6.3: Characteristic quantities of the described CBM TRD [Ems13a] compared to the ALICE TRD [ALI01].

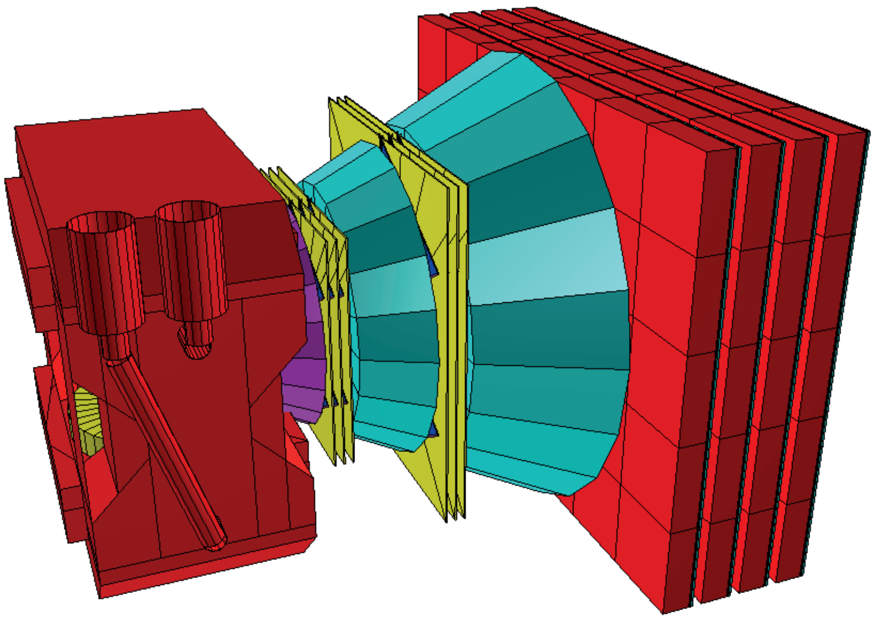

Figure 6.3: Muon identification setup of CBM at SIS100 (v13l). The four layers of the TRD are shown in red. [Ems13a].

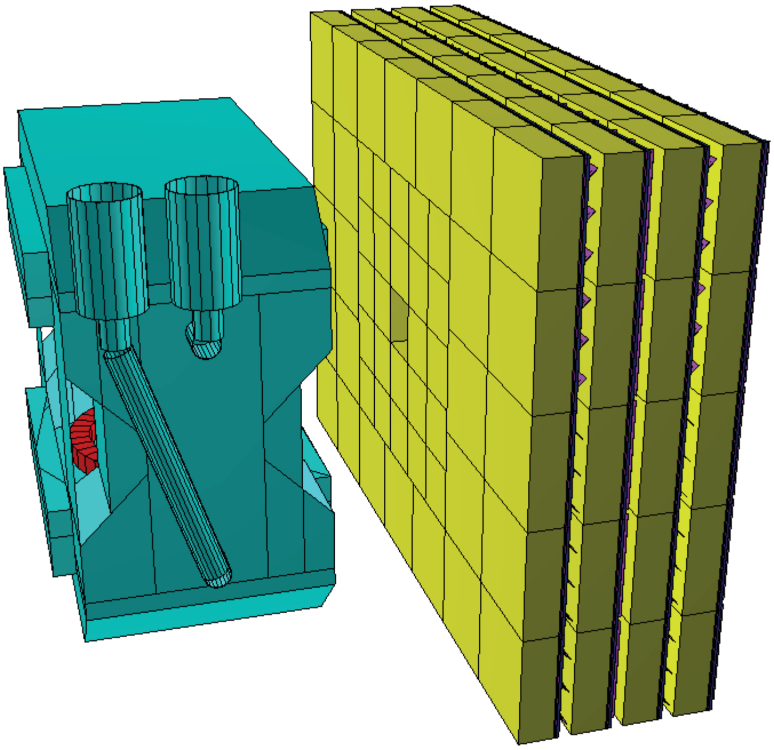

Figure 6.4: Hadron setup of CBM at SIS100 (v13h). The four layers of the TRD are shown in yellow. [Ems13a].

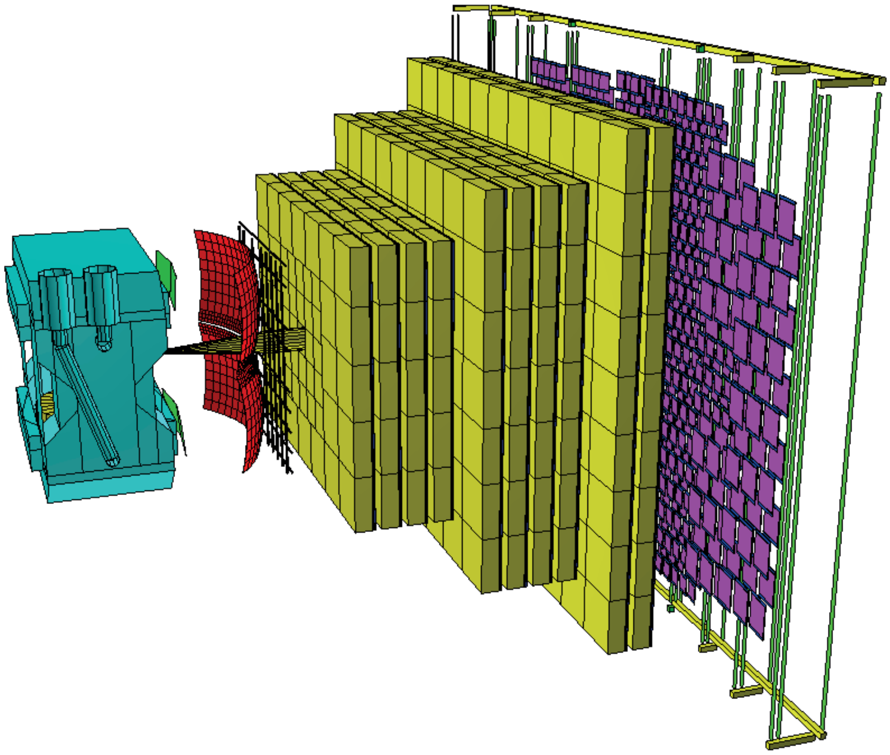

Figure 6.5: Electron identification setup of CBM at SIS300 (v13g). The three stations (10 layers in total) of the TRD are shown in yellow. [Ems13a].

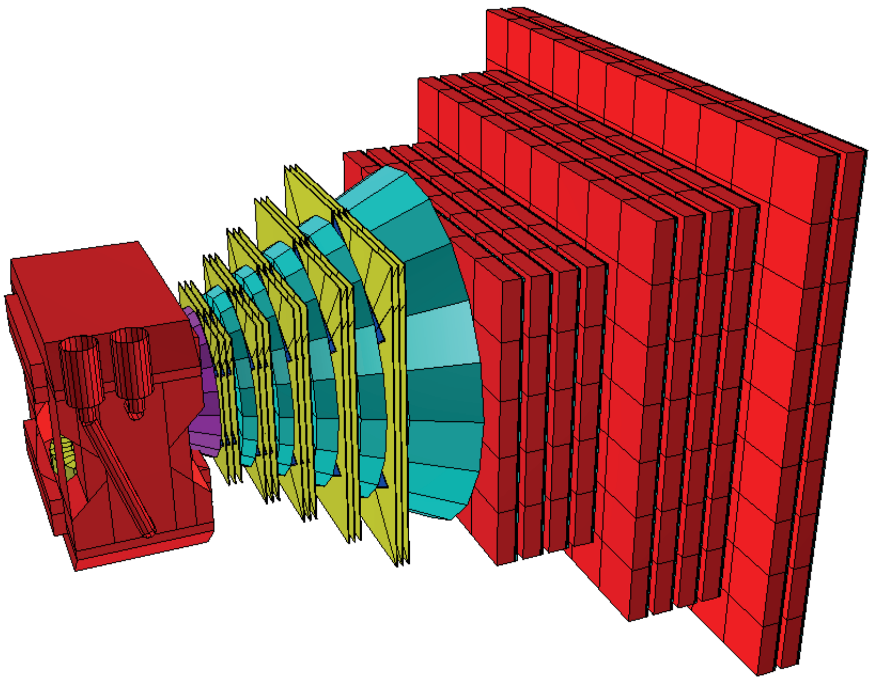

Figure 6.6: Muon identification setup of CBM at SIS300 (v13m). The three stations (10 layers in total) of the TRD are shown in red. [Ems13a].

6.3 Hit Rates of the TRD

The FAIR accelerator facility will provide a heavy-ion beam on a fixed target in the CBM experiment. The evolution of the collision has been calculated with UrQMD [MBG99] and transported through the detector material using GEANT [S. 03]. To obtain an upper limit of the load for the TRD, only central collisions are assumed. Furthermore, δ-electrons are neglected in this simulation as well as any influence of a magnetic stray field. Taking the currently proposed positioning and layout of the TRD into account the resulting hit rates in the TRD can be simulated. The results for the TRD Geometry version *v12f* are shown in figure 6.7, 6.8 and 6.9 [Ber13]. The simulation uses a pad width of 7.125 mm for all pads. The length are integer multiples of 6.75 mm in the inner part and 7.11 mm in the outer part. With this partitioning it is possible to achieve a hit rate of less than 10^5 per pad in all areas of the detector.

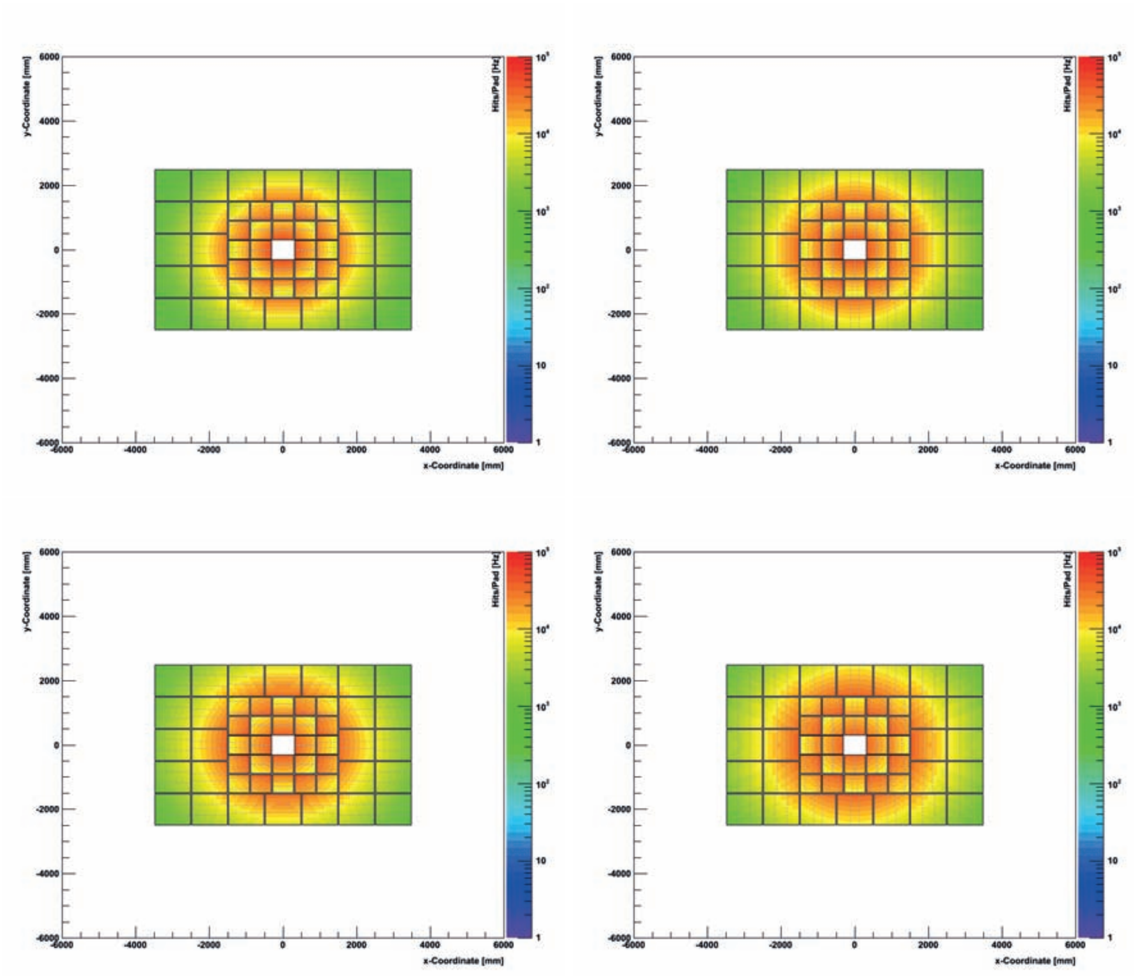

Figure 6.7: Simulated hit rates TRD Station 1. Layer 1 is shown upper left, layer 2 upper right, 3 lower left, 4 lower right [Ber13].

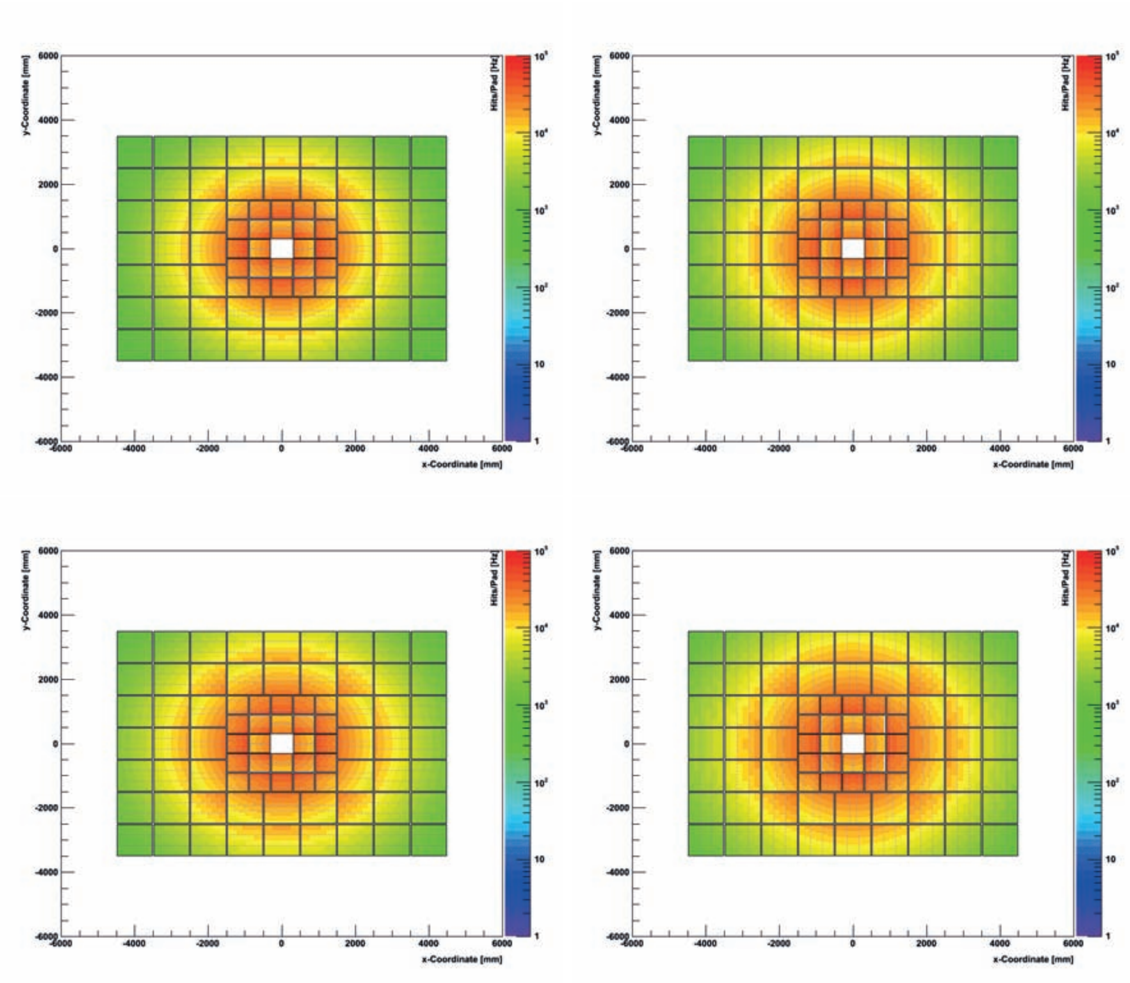

Figure 6.8: Simulated hit rates TRD Station 2. Layer 5 is shown upper left, layer 6 upper right, 7 lower left, 8 lower right [Ber13].

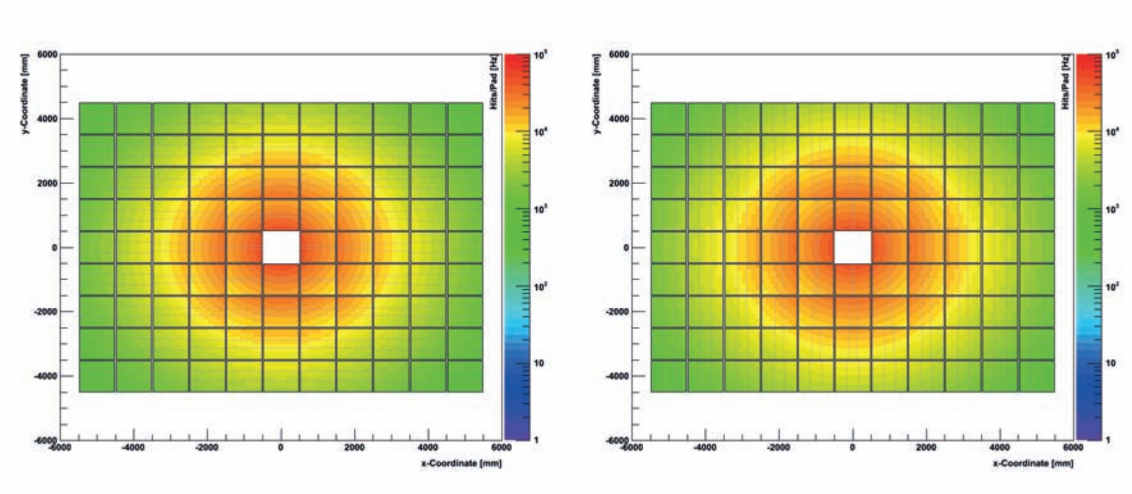

Figure 6.9: Simulated hit rates TRD Station 3. Layer 9 is shown left, layer 10 right [Ber13].

6.4 Modularized Layout of the TRD

The development and optimization of the subsequent layout of the TRD is an iterative process. Global experimental properties like hit-rate distributions, positioning inside the experiment, as well as the performance of the detector prototypes and the necessary read-out electronics have to be taken into account. The current layout of four TRD stations with a segmentation into $4 + 4 + 2$ layers is planned to consist of an inner and an outer sector. The hit rate and hit density decreases with larger distance from the beam pipe. This allows a lower granularity (larger read-out pads) in the more peripheral regions. Detector modules of the inner part are planned with a size of $60 \times 60\,\mathrm{cm}^2$, modules of the outer part with a size of $100 \times 100\,\mathrm{cm}^2$.

The front-end electronics (FEE) which will be utilized in the final experimental setup is designed with 32 read-out channels. The possibility to increase the number of channels to 64 is under investigation. Since the number of read out channels is fixed, the decreasing hit density can be compensated by an adapted read-out pad design. The upper part of figure 6.10 shows a drawing of a prototype with high read-out density and a small read out pads, while the lower part shows a prototype with large pads and accordingly lower density of read-out electronics. [Ems13a]

6.5 Design Options

Three different approaches were followed to develop prototypes, that fulfills the experimental requirements.

6.5.1 Prototypes built in Münster

The prototype built at the Institut für Kernphysik of the Westfälische Wilhelms-Universität Münster follows closely the design concept of the ALICE TRD [ALI01] (see figure 3.2 right). Introducing a dedicated drift and conversion gap makes it possible to decouple

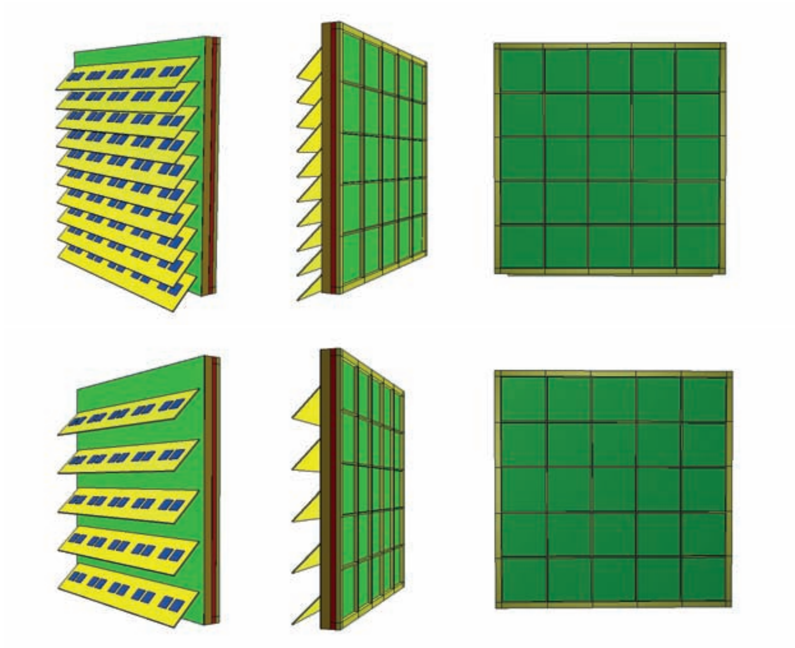

Figure 6.10: A detector model with small read out pads (high front end electronics density) in the upper part, and one detector with large pads and low read out density in the lower part [Ems13a].

the signal size (deposited charge inside the MWPC) from the size of the gas volume inside the MWPC. Within this approach the pad size can be small whereas the absorption probability of the generated Transition Radiation Photon can be increased by enlarging the gas volume (distance between entrance window and read out pads). The efficiency for the signal generation and particle identification will be optimized. Due to the additional drift region the signal generation is smaller with respect to a MWPC without drift region. The Münster style prototypes utilized the SPADIC front-end electronic connected to rectangular read out pads during the test beam campaigns described in chapter 8.

6.5.2 Prototypes developed in Bucharest

The prototype built at the National Institute for Physics and Nuclear Engineering in Bucharest is a symmetric double-sided approach with a centered read out-pad plane. The read out pads are shaped triangular which improves the position resolution. The double-sided design increases the efficiency due to the enlarged absorption volume. The Bucharest prototypes use the FASP front end electronic for data read out (see chapter 8).

6.5.3 Prototypes designed in Frankfurt

The prototype built at the Institut für Kernphysik of the Johann Wolfgang Goethe - Universität Frankfurt am Main uses a symmetric Multi-Wire Proportional Chamber without additional drift region (see figure 3.2 left). This design concept provides a faster signal generation and is more robust at the expected high particle fluxes with respect to prototypes with dedicated drift region. It requires only one plane of anode wires. This simplifies the construction of the detector. The pads have a rectangular shape and are read out via the SPADIC front end electronic.

In addition to the basic symmetric design concept, the Frankfurt-style prototypes employs a thin foil-based entrance window without any support structure to reduce the material budget of the prototypes. Since the entrance window has a size of at least $60 \times 60\,\mathrm{cm}^2$, a special stretching technique has been developed to reduce deformations due to pressure gradients. These prototypes are subject of this thesis. A detailed description on the prototype construction is given in chapter 7.

7 Prototype Design and Construction

The development of the CBM TRD prototypes at the *Institut für Kernphysik Frankfurt* are the subjects of the thesis. These prototypes are symmetric Multi-Wire Proportional Chambers (MWPC) with a thin foil-based entrance window following the principles layed out in chapter 3.2. Based on early studies of small-size demonstrators [Rei11] full size prototypes were developed, built and tested in test beam campaigns at the CERN PS. In total four generations of MWPC prototypes as shown in table 7.1 have been developed and tested. The prototypes are divided in three categories:

1. small proof-of-concept studies with an active area of $8{\times}6\,\mathrm{cm}^2$.
2. small-size demonstrators with an active area of $15{\times}15\,\mathrm{cm}^2$.
3. full-size prototypes of $59{\times}59\,\mathrm{cm}^2$ active area.

The full-size prototypes are of the size currently proposed for the inner region of the CBM TRD.

Serial #	Generation	Active Area	Pad Size	Gas Gap
FFM-p1 [1]	I	$8{\times}6\,\mathrm{cm}^2$	$7.5{\times}16\,\mathrm{mm}^2$	4+4 mm
FFM-p2	I	$8{\times}6\,\mathrm{cm}^2$	$7.5{\times}16\,\mathrm{mm}^2$	5+5 mm
FFM-001 [1]	II	$15{\times}15\,\mathrm{cm}^2$	$4.7{\times}49.7\,\mathrm{mm}^2$	4+4 mm
FFM-002	II	$15{\times}15\,\mathrm{cm}^2$	$4.7{\times}49.7\,\mathrm{mm}^2$	5+5 mm
FFM-003 [1]	II	$15{\times}15\,\mathrm{cm}^2$	$4.7{\times}49.7\,\mathrm{mm}^2$	6+6 mm
FFM-004	III	$15{\times}15\,\mathrm{cm}^2$	$4.7{\times}49.7\,\mathrm{mm}^2$	5+5 mm
FFM-005	III	$15{\times}15\,\mathrm{cm}^2$	$4.7{\times}49.7\,\mathrm{mm}^2$	6+6 mm
FFM-006	III	$15{\times}15\,\mathrm{cm}^2$	$4.7{\times}49.7\,\mathrm{mm}^2$	4+4 mm
FFM-007 [1] [2]	III	$15{\times}15\,\mathrm{cm}^2$	$4.7{\times}49.7\,\mathrm{mm}^2$	5+5 mm
FFM-010	IV	$59{\times}59\,\mathrm{cm}^2$	$15/45/75 \times 7.125\,\mathrm{mm}^2$	4+4 mm
FFM-011	IV	$59{\times}59\,\mathrm{cm}^2$	$15/45/75 \times 7.125\,\mathrm{mm}^2$	5+5 mm

Table 7.1: Dimensions quantities of all constructed symmetric MWPC prototypes.

The expected high particle rates at SIS300 require fast and rate-capable detectors. In this approach thin MWPCs are proposed. According to the short drift times a fast signal generation and less effects due to space charge can be expected.

The gas gap devotes the size of the distance between the entrance window and the read-out plane. In the used symmetric setup the anode wire plane divides this distance into

[1] not used in this work
[2] not used in beam time campaigns due to high current at applied high voltage for anode wires

half. The nomenclature of a geometry with $A + A$ mm dimensions refers to the distances of the read-out pads to the anode wires, and from the anode wires to the entrance window respectively. The gas gap defines the corresponding absorption volume for the generated transition radiation photon and the volume of energy loss for traversing charged particles. The chosen size of gas volume follows simulations of the energy loss and absorption probabilities [Rei11].

The wire pitch describes the distance of the anode wires. This distance influences the size of the generated avalance, which generates the read-out signal. By this the anode wire pitch defines an upper limit of the position resolution of a MWPC obtained via the pad response function.

Technical details and the mechanical setup of these demonstrators and prototypes are described in this chapter. The required simulations of this prototypes are carried out in chapter 9, the measurements in lab in chapter 10 and the conducting of the test beam campaigns in chapter 11. Results of the test beam campaigns are shown in chapter 12.

7.1 Small Demonstrators

The small size demonstrators with an active area of 15×15 cm have been built in the prototype generation II and III. A technical drawing of the basic features is shown in figure 7.1.

The anode wires used for all prototypes are made of gold plated tungsten wires with a diameter of 20 μm. The entrance window, which serves as the second cathode plane, is made out of 20 μm thick, aluminized Mylar foil.

A prototype of generation II separated in its components is shown in figure 7.2. A frame out of hardened fiberglass (*G10/Vetronit*) holds the pad plane with segmented read-out pads, connectors for gas in/out feed-through and high voltage for the anode wires. Distance ledges also made out of hardened fiberglass are glued on to the pad plane and provide a fixed distance of the pad plane to the anode wires. The anode wires are tensioned with 0.5 N and placed onto these distance ledges. A cap defining the overall high of the gas volume and housing the entrance window is covering the anode wires. The cap is sealed with an O-Ring to the main frame. A close up of the technical drawing to illustrate the distances of the anode wires and the distances of the entrance window to the read-out pad plane is shown in figure 7.3

The basic features of generation II and III prototypes are identical. The evolution from II to III only affects the support structure and a minor change in the anode wire setup. Additionally to the 20 μm thick gold tungsten wires, two ≈80 μm thick copper beryllium wires are added peripheral to the anode wires to restrict disturbances of the electric field inside the MWPC. The main frame of the generation III prototypes is made out of aluminum. It provides the possibility to mount a reference radiator directly on the entrance window as well as an improved grounding scheme to shield the inner MWPC from external electric disturbances. A summary of the main mechanical values is shown in table 7.2. A photo of a generation III prototype is shown in figure 7.5

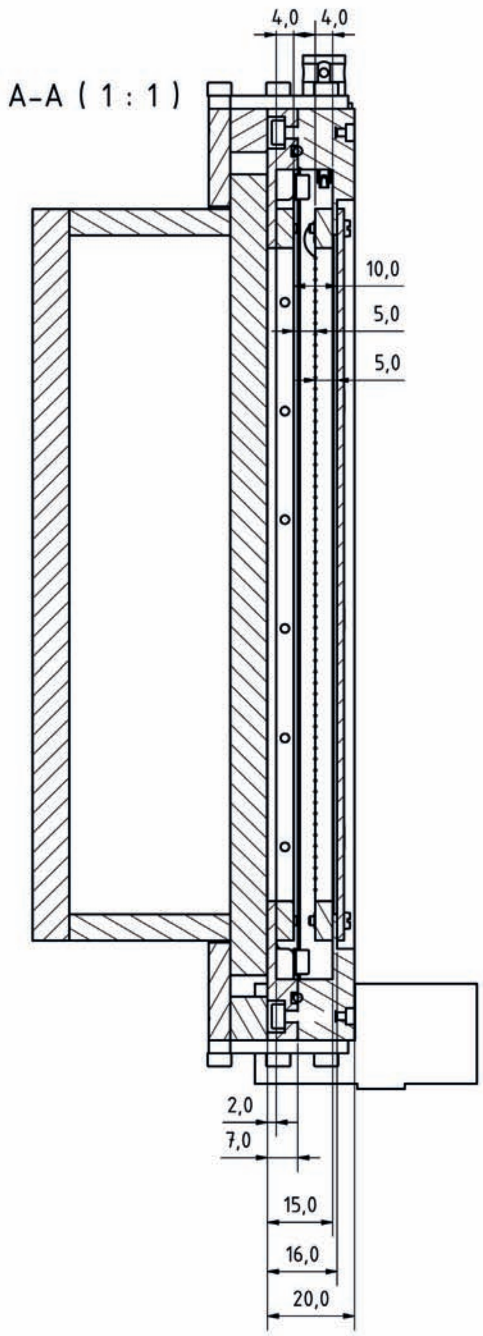

Figure 7.1: Technical blueprint of the small demonstrators. The shown prototype of generation III features the additional possibility to attach a radiator directly to the entrance window. The MWPC setup is identical to generation II prototypes.

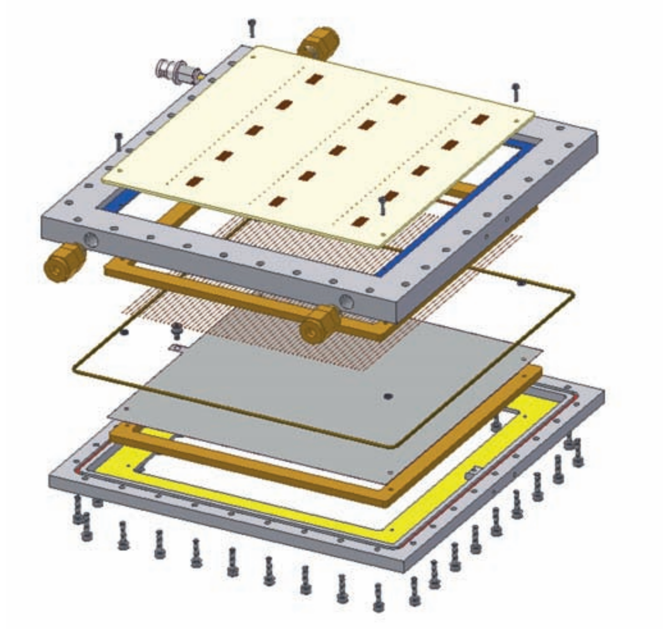

Figure 7.2: Small size demonstrator (generation II) split into its components.

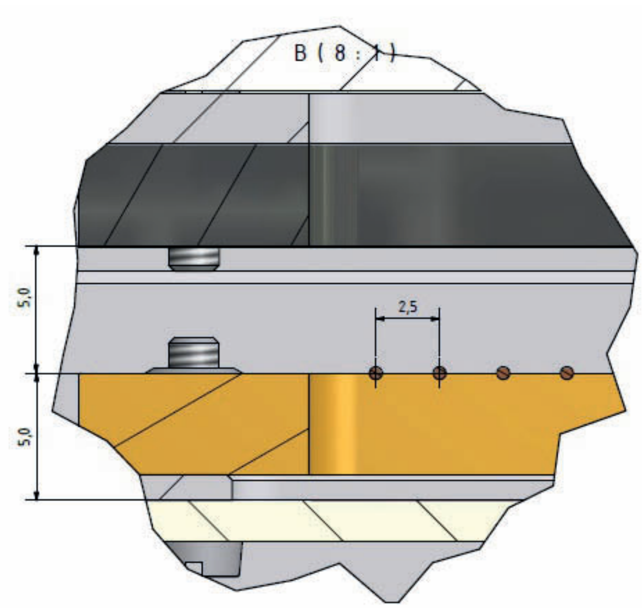

Figure 7.3: Close-up of the technical drawing for generation II and III prototypes illustrating the distances of the entrance window to the anode wires and to the read-out plane.

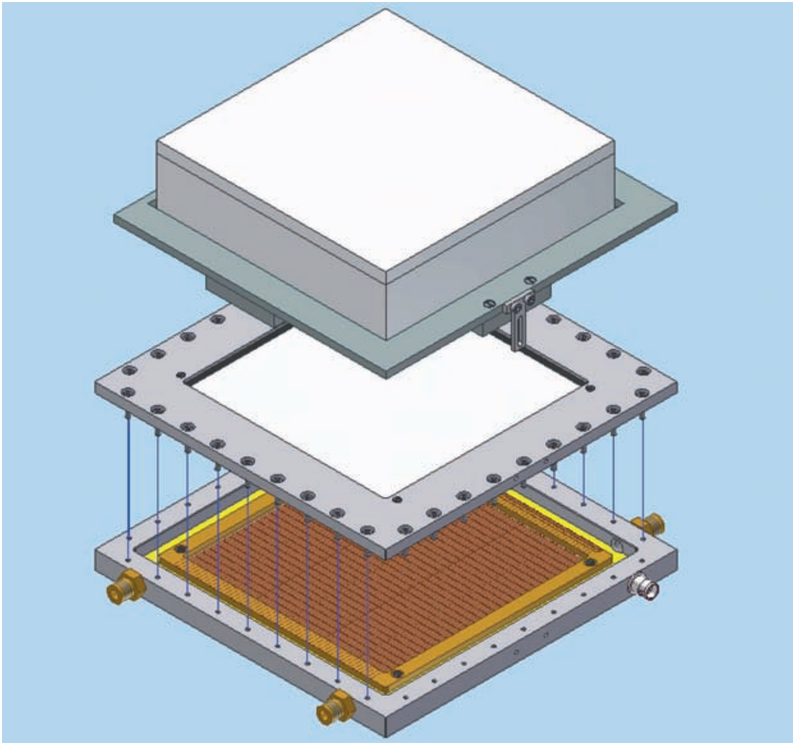

Figure 7.4: Small size demonstrator of generation III separated into its components illustrating the additional attachment mechanism for the reference radiator.

Serial #	Generation	Pad Size	Connector	Gas Gap	Frame Material
FFM-002	II	$4.7{\times}49.7\,\mathrm{mm}^2$	8 Channels	5+5 mm	*Vetronit*
FFM-004	III	$4.7{\times}49.7\,\mathrm{mm}^2$	8 Channels	5+5 mm	Aluminum
FFM-005	III	$4.7{\times}49.7\,\mathrm{mm}^2$	8 Channels	6+6 mm	Aluminum
FFM-006	III	$4.7{\times}49.7\,\mathrm{mm}^2$	8 Channels	4+4 mm	Aluminum

Table 7.2: Key quantities of the constructed small-size demonstrators.

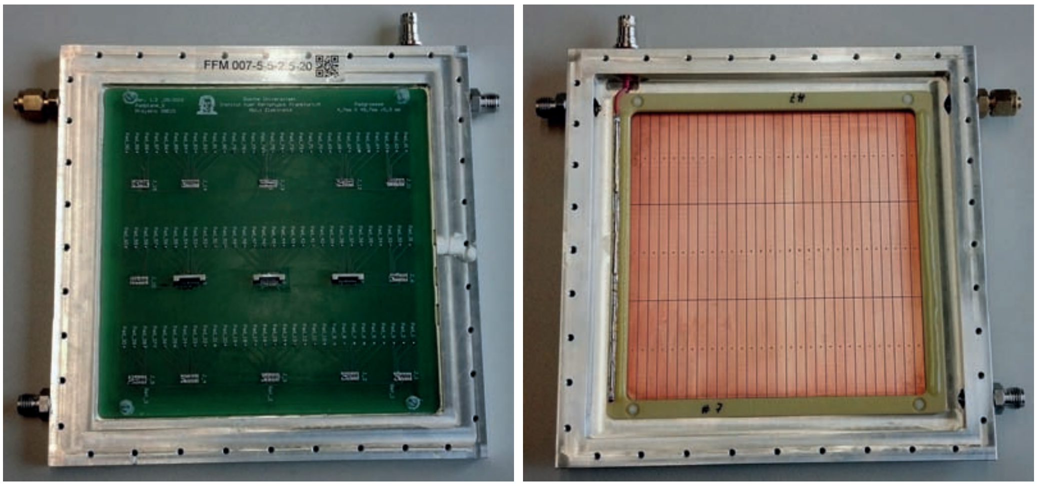

Figure 7.5: Photo of a generation III small-size demonstrator. The back side (left picture) shows the read-out plane with its connectors mounted to the aluminum frame, which also holds gas in- and outlets and the high-voltage connectors. In the inner part (right picture) the segmented read-out plane and the wire grid attached to the distance ledges is shown.

7.2 Full size Prototypes

The Frankfurt-style full-size prototypes match the size of the detector modules in the inner part of the CBM TRD (see chapter 6). These prototypes of generation IV feature a modular layout to enable an adaption for multiple measurement scenarios and simplify the construction of these prototypes. The conceptual design of the MWPC is kept identical to the generation III prototypes, the dimensions of the MWPC have been enlarged to an active area of $59 \times 59\,\mathrm{cm}^2$.

The modular design of the full-size prototypes is shown in figure 7.6. It consists of the main back panel frame, which holds the pad plane and the anode wires, an intermediate frame to define the distance of the entrance window to the pad plane and a cap, which holds the stretched foil of the entrance window. The production of the entrance window is described in chapter 7.2.1.

The back panel frame is made of aluminum. The pad plane with the segmented read-out pads is glued to it. A light-weight honeycomb structure is inserted to support the pad plane and covered with an *FR4* plate. The aluminum frame also houses gas in- and outlets and the high-voltage connectors, as shown in the left part of figure 7.7. A pad plane is designed to provide read-out pads of three different sizes of $15/45/75 \times 7.125\,\mathrm{mm}^2$ [Ems13b]. The connectors of the read-out pads are selected such that the 32 channel-based SPADIC 1.0 (see chapter 8) can be used for read-out. The wire grid is made of gold-plated tungsten wires with a diameter of $20\,\mu$m terminated with $\approx$80$\,\mu$m thick copper beryllium wires. The wire pitch is 2.5 mm. The single wires of the wire grid are stretched with 0.5 N. The wire grid is mounted on the distance ledges which are placed on the back panel frame as shown in figure 7.8. The intermediate frame defines the distance from the read-out plane to the entrance window. It also contains connectors for a sophisticated grounding scheme.

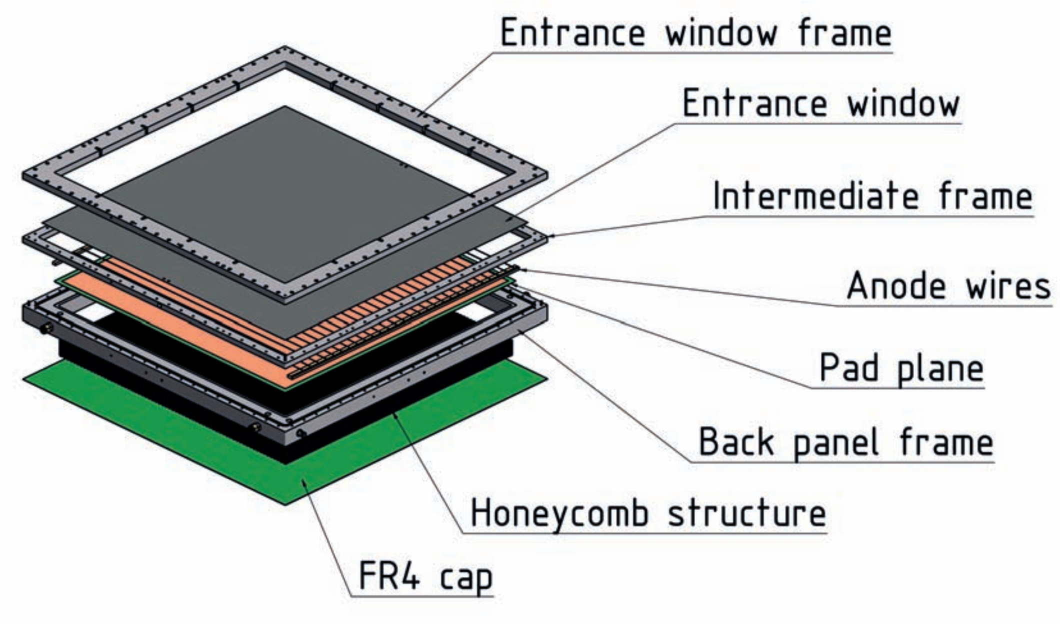

Figure 7.6: Technical drawing of the full-size generation IV prototype.

The entrance window cap holds the stretched foil and provides prepared mounting frames for a potential support structure. An aluminized Mylar foil of 20 μm thickness is used. The aluminized side of the foil is connected to the frame material (see figure 7.7 right) to avoid electrostatic charging up and to provide the possibility to include the entrance foil into the grounding scheme. All three modular components of the generation IV prototypes are mounted with screws and sealed with O-rings. The characteristics of the generation IV prototypes are summarized in table 7.3.

Serial #	Generation	Pad Size	Connector	Gas Gap	Frame Material
FFM-010	IV	15/45/75 $\times$ 7.125 mm^2	32 Channels	4+4 mm	Aluminum
FFM-011	IV	15/45/75 $\times$ 7.125 mm^2	32 Channels	5+5 mm	Aluminum

Table 7.3: Key quantities of the constructed full size prototypes.

7.2.1 Stretching Procedure for the Entrance Window Construction

The entrance window serves as cathode plane in the utilized symmetric MWPC setup. The foil experiences deformations due to pressure gradients, which will lead to a variation of the gas gain of the MWPC (see chapter 9.2.1). To minimize this variation, the entrance foil is mechanically stretched prior to mounting.

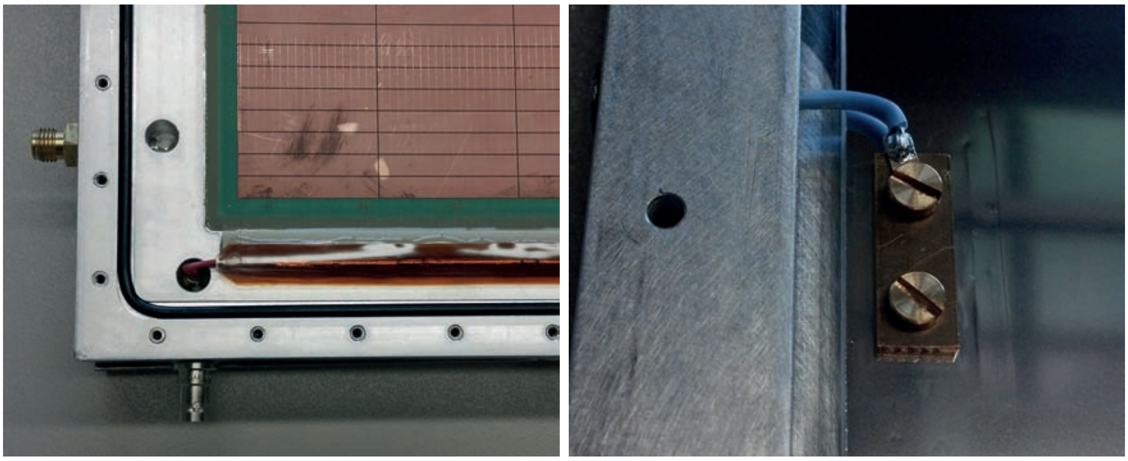

Figure 7.7: Left: detailed view on the main frame of the generation IV prototype. This frame holds gas in- and outlets and the high voltage connectors. The wire grid is placed on *Vetronit* distance ledges. The connection of the wire grid to the high voltage is covered by a capton foil. Right: grounding connection of the aluminized Mylar foil and the cap frame to the intermediate frame.

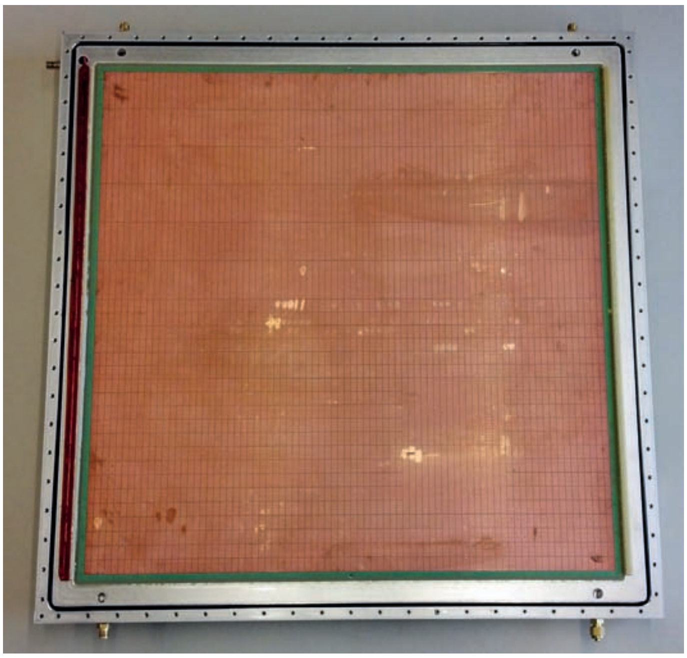

Figure 7.8: Photo of the main frame of a full-size prototype. The segmented read-out plane features multiple pad sizes. The distance ledges hold the wire grid.

The stretching procedure of the foil-based entrance window uses a technique based on thermal expansion. The originating idea was developed for stretching large area *GEM foils* and uses infrared light bulbs [Mic11]. This procedure has been adopted for the construction of the entrance window of the generation IV prototypes [Reu13].

The non-tensioned aluminized Mylar foil is fixed into an acrylic glass frame. This frame is warmed up to a temperature of 55 °C using heating elements sticked on aluminum plates covering the acrylic glass frame whereas the Mylar foil itself remains at ambient temperature. The acrylic glass frame evenly expands according to its material constants in all directions and stretches the fixed Mylar foil. The temperature of the acrylic glass frame is kept constant using a simple control circuit including the power supplies of the heating elements as well and a measurement of the frame temperature at four different positions. A photo of this setup is shown in figure 7.9. A comparison of the non-tensioned and tensioned Mylar foil is shown in figure 7.10.

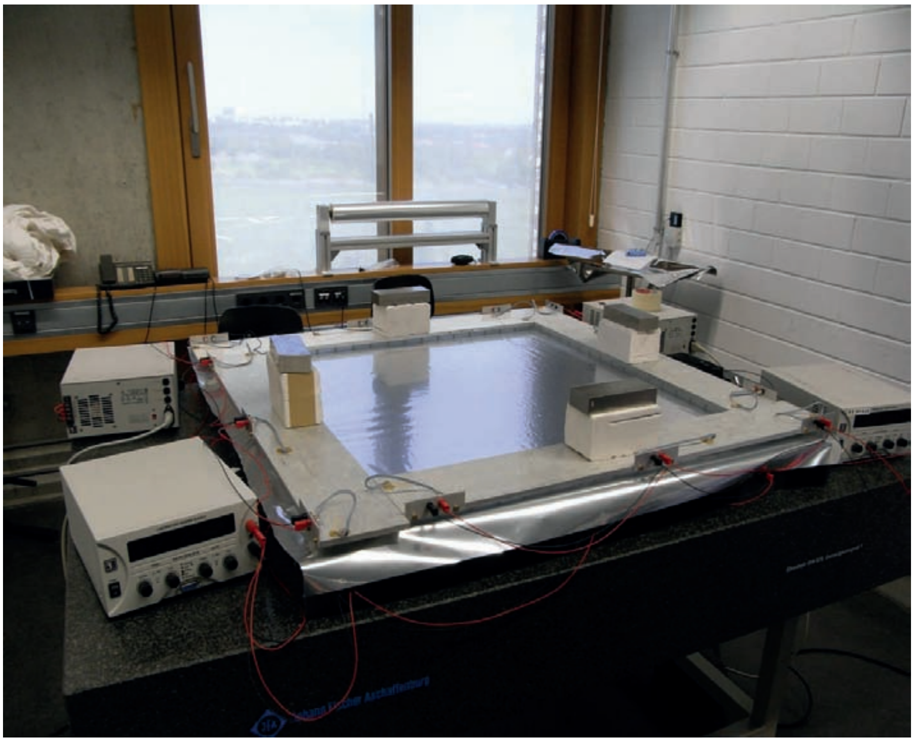

Figure 7.9: Setup of the foil-stretching device. The non-tensioned foil is fixed into the acrylic glass frame covered by the heating elements.

7.3 Radiator Development

The transition radiation (TR) which is necessary for an efficient electron-pion separation is generated in the radiator material. This efficiency depends on the intensity and the energy of the transition radiation. Both quantities are determined by the choice of the radiator material and structure. Radiators can be classified in regular and irregular radiators. Regular radiators are made of periodic structures of different materials, e.g. multiple

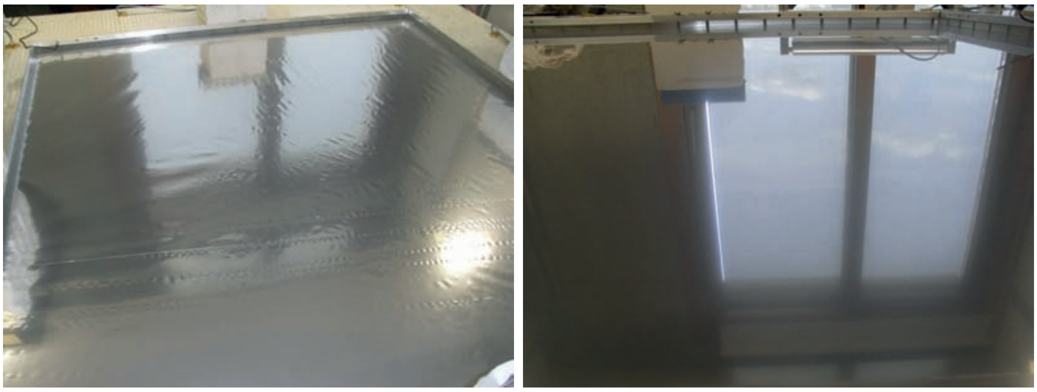

Figure 7.10: Mylar foil for the entrance window before (left) and after (right) the stretching procedure. The tension of the foil is suggested by the reflections on the foil.

layers of a foil with a fixed clearance. In irregular radiators these structures and distances vary around a mean value. Such radiators are for example foam materials or bundles of a fiber material. Regular radiators can be calculated using an extrapolation of one single transition. The dependencies of the TR intensity and the spectra of a given radiator can be extracted by [AW11, CW75]:

$$\frac{dW}{d\omega} = \frac{4\alpha}{\sigma(\kappa+1)}(1-\exp(-N_f\sigma))\times\sum_n \theta_n \left(\frac{1}{\rho_A+\theta_n} - \frac{1}{\rho_B+\theta_n}\right)^2 [1-\cos(\rho_A+\theta_n)] \tag{7.1}$$

$$\rho_i = \frac{\omega l_1}{2\beta c\left(\gamma^{-2}+\frac{\omega_i^2}{\omega^2}\right)} \quad , \quad \kappa = \frac{l_2}{l_1} \tag{7.2}$$

$$\theta_n = \frac{2\pi n + (\rho_A+\kappa\rho_B)}{\kappa+1} > 0 \tag{7.3}$$

In equation 7.1 N_f represents the number of used foil layers, l_1 is the thickness of one foil layer and l_2 is the distance between two foils or the thickness of a secondary material respectively, whereas l_1 and l_2 are chosen such that

$$l_1 < l_2 \tag{7.4}$$

Figure 7.11 shows the yield of TR photon production as a function on the photon energy depending on the Lorentz factor and the thickness of the utilized materials. The rise of the TR yield in the upper panel is expected due to equation 3.6. A similar behavior can be observed when varying the distance of the foils l_2 (lower panel in figure 7.11), where this dependency only slightly influences the peak position of the TR spectra. The enhancement of this distance saturates for higher values of l_2. The shape of the spectrum is mostly defined by the thickness of the foils l_1. A thicker foil results in a higher peak position in the (resulting harder) TR spectra, a thinner foil results in a softer TR spectra (central panel of figure 7.11).

These physical principles are also valid for irregular radiators, but, due to the variations in l_1 and l_2 they are not analytically calculable. The main advantage of irregular radiator

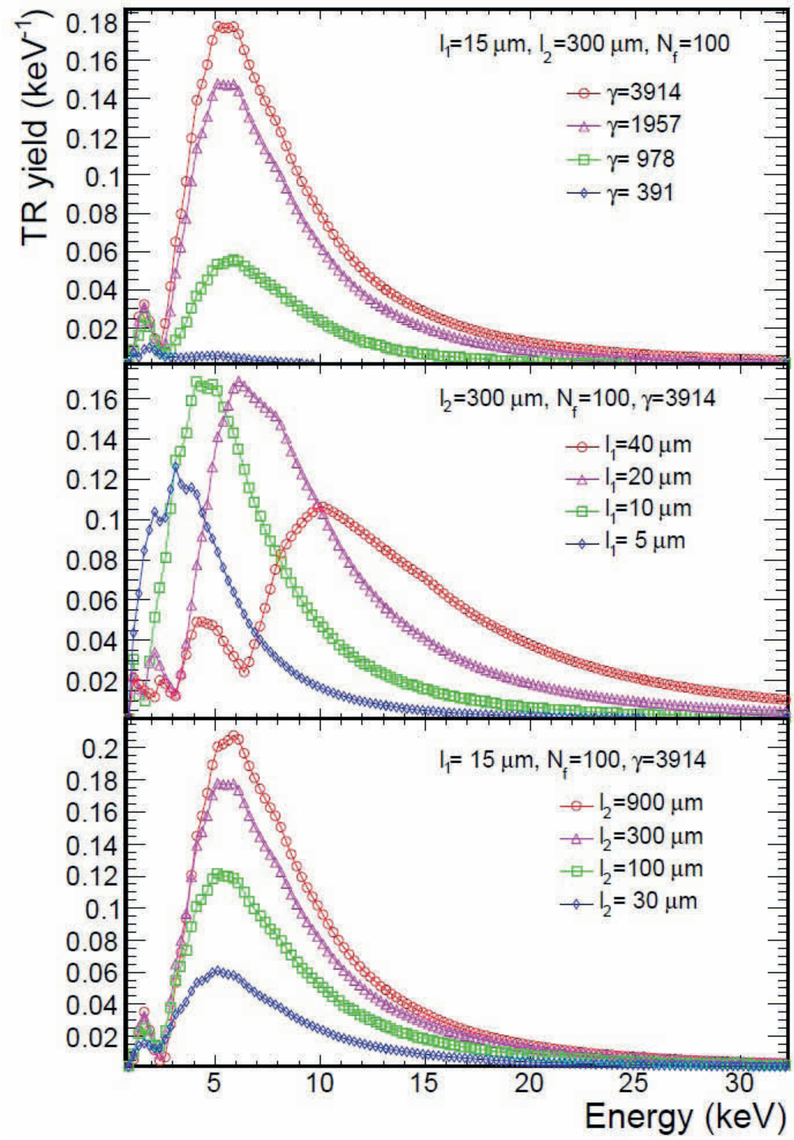

Figure 7.11: Yield of TR production depending on TR photon energy [AW11]. In the three panels the Lorentz factor γ, and the distances l_1 and l_2 are varied.

are their mechanical and economical properties: foam-based materials are self-supporting, fiber and foam materials are commonly used in industry and therefore cost-effective and easy to purchase. The TR efficiency and the energy spectra of the TR photons can only be determined experimentally which only allows an empirical optimization of an irregular radiator material for the CBM TRD.

The optimization of the radiator for a future experiment can only be done in combination of radiator and read-out detector. The configuration and geometry of the MWPC determine the peak position in the TR photon spectra which can be absorbed most efficiently TR absorption, whereas the maximum TR yield in a TR spectrum should be most efficiently absorbed by the MWPC. Both facts result in an iterative process. Further simulations on this can be found in [Ber13]. The selection of a radiator not only depends on its TR efficiency, but also on parameters like technical feasibility.

For the Frankfurt prototypes a set of radiators has been developed and tested during two test-beam campaigns. The key properties are shown in table 7.4. The ALICE-type radiator (figure 7.12 top left) is a sandwich structure of *ROHACELL HF71* as enclosure and polypropylene fiber mats. The radiators R005 and R003 are set up similarly but with different materials and dimensions. Regular radiators have been built in piles of 50 foil layers each resulting in stacks of 150 to 350 transitions (figure 7.12 top right) with varying l_2, a radiator prototype with a self-supporting foil structure (pushed in deformations) tries to mimic this regular configuration with the trade of with local irregularities giving mechanical support to the radiator (figure 7.12 lower panel). Solid foam material radiators with different spacing conditions (figure 7.13) are also constructed and tested during the test-beam campaigns. Microscopic close-ups of selected materials are shown in figure 7.14 and 7.15.

Radiator	Configuration	Material	$\langle l_1 \rangle$ [μm]	$\langle l_2 \rangle$ [μm]	Thickness [mm]	Transitions
ALICE-type	Sandwich	reinforced HF71	8	75	2×8	2×96
		Polypropylene fibers	17	50	30	448
R005	Sandwich	HF71	8	75	2×8	2×96
		Polyethylene Fibers	15	120	103	760
R003	Sandwich	HF71	8	75	2×8	2×96
		Organic Fibers	13	40	226	4200
Foil Radiators	Regular	Polyethylene Foils	20	500	78-182	150-350
Foil Radiators	Regular	Polyethylene Foils	20	700	108-252	150-350
Foil Radiators	Regular	Polyethylene Foils	20	1200	183-247	150-350
Micro-structured Foil	Irregular	POKALON N470	24	700	250	350
Type N	Foam	Polyethylene (*Cell-Aire*)	12	600	260	425
R002	Foam	Polyethylene (hard)	12	600	260	424
R007	Foam	Polyethylene (soft)	12	1000	118	116
HF 110	Foam	Rohacell HF 110	15	75	30	333
Type H	Foam	Polyethylene (*Cell-Aire*)	12	900	177	388

Table 7.4: Properties of the constructed radiators.

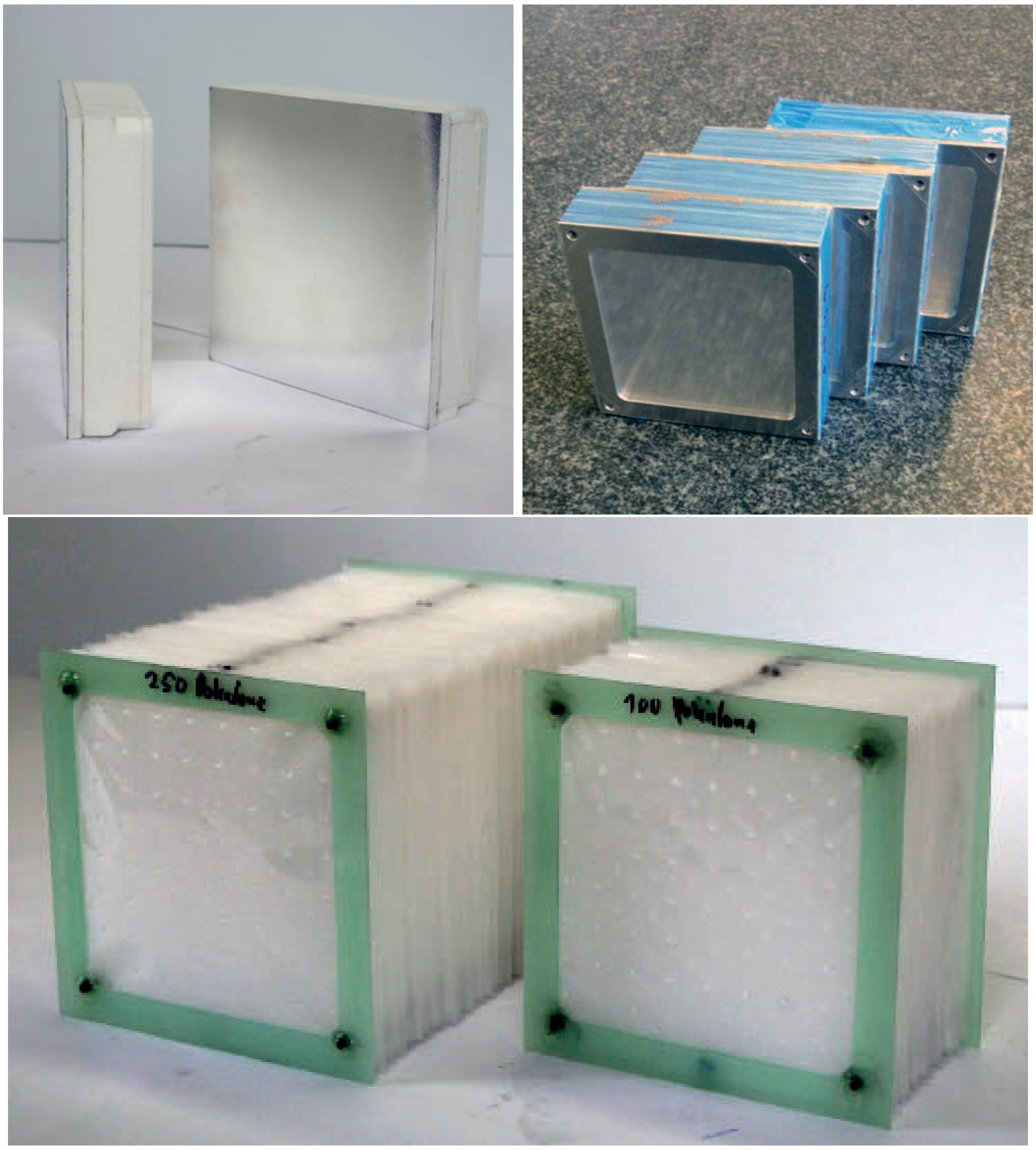

Figure 7.12: Photo of the ALICE-type reference radiator (top left), stacks of the regular foil radiator (top right) and the irregular (micro-structured) foil radiator (bottom).

Figure 7.13: Photo of foam radiators type R002 (hard PE foam) top left and R007 (soft PE foam) top right. Type H lower left, Type N lower right.

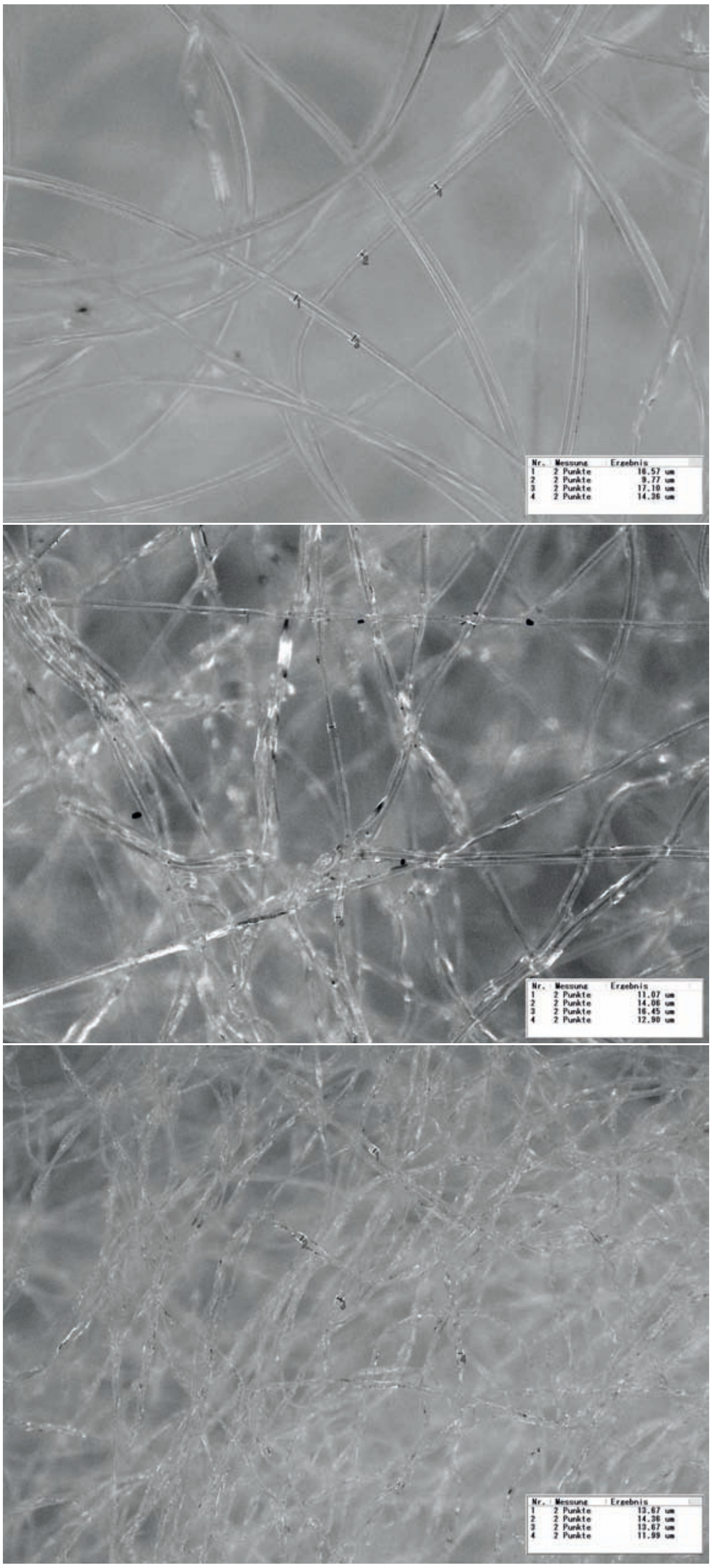

Figure 7.14: Microscopic photo of the used fiber materials. Top: PE fiber as used in R005, middle: PE fiber mate used for the ALICE-type radiator, bottom: organic fibers used in R003.

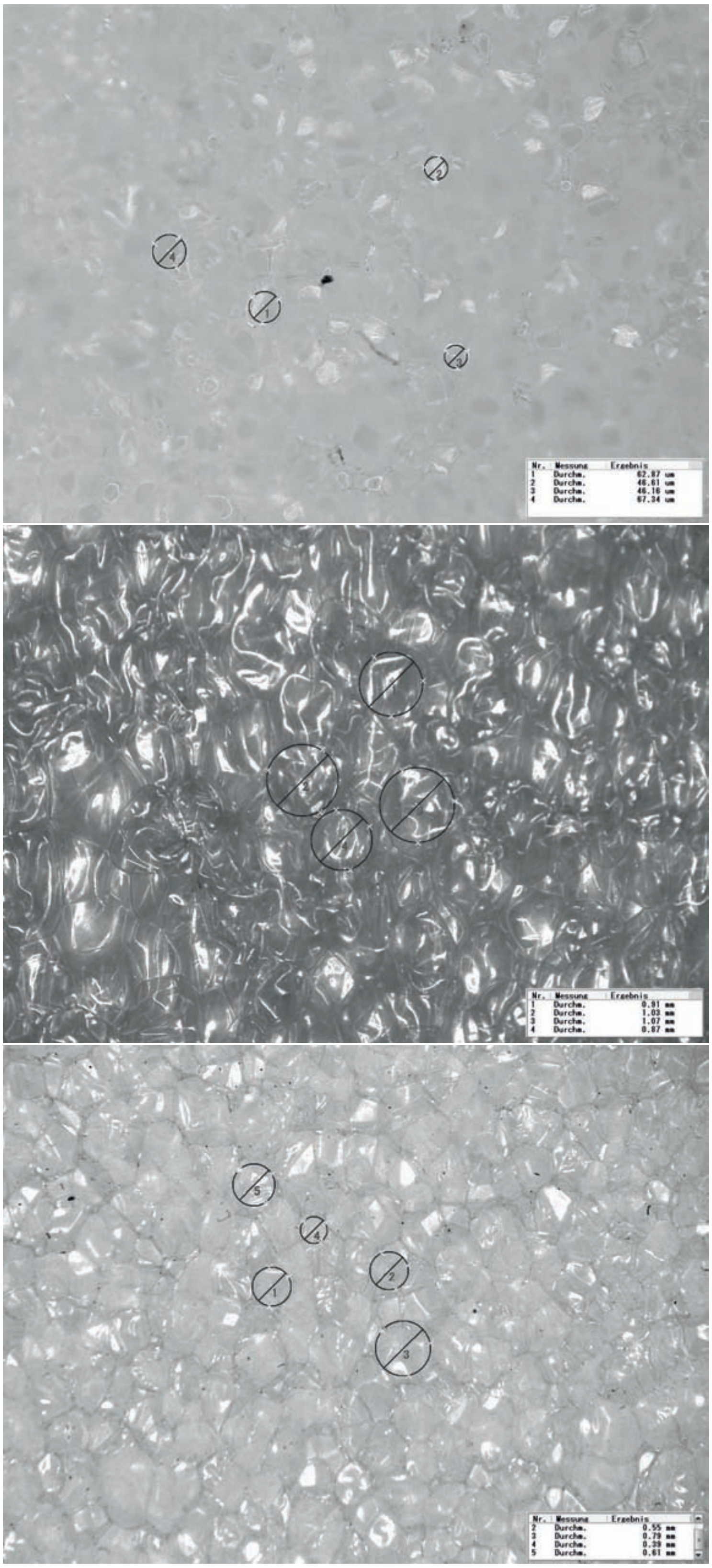

Figure 7.15: Microscopic photo of the used foam materials. Top: Rohacell HF71, middle: soft PE foam (R007), bottom: Hard PE foam used in R002.

8 Read-Out Electronics

Regarding the large hit rates within the TRD that are expected from simulations, not only the detector itself has to be capable and fast enough to measure the particle trajectories and particle identification information, but also the read-out electronics has to be able to process all informations. The generated small signals (see chapter 9.4) have to be amplified and digitized. According to the expected event and hit rates the resulting high numbers of read-out cycles the produced amount of raw data has to be as small as possible. However, this data reduction must not effect the electron identification capabilities. Current approaches for the read-out electronics are the SPADIC and the FASP chips.

8.1 SPADIC 0.3 Prototype

The *Self-triggered Pulse Amplification and Digitization asIC* (SPADIC) in its revision 0.3 is the read-out device which has been utilized for the Frankfurt CBM TRD prototypes. It is the first front-end electronics especially developed for the CBM experiment. For the analysis of the multi-wire proportional chambers the deposited charge inside the chamber has been read out with a SPADIC - *SUSIBO* read out chain. The SUSIBO serves as communication interface between the SPADIC and the data acquisition and configuration system. [AFP09]

The used SPADIC 0.3 consists of an analog preamplifier and a pulse shaper combined with an 8 bit analog-digital-converter (ADC). Its intrinsic white noise is at a level of 800 electrons, which includes a noise of 200 electrons from the shaper unit. It is capable to handle input signals of 0. . .40 fC. The pulse shaper has a shaping time of 90 ns whereas the analog-digital-converter provides a digitization rate of 25 MHz. The ADC converts analog signals into 45 time bins which results in a single event duration of 1.8 μs. The SPADIC in its revision 0.3 provides eight read-out channels. The read-out cycle is event-based. Further important key characteristics are listed in table 8.1.

The SPADIC chip is hosted on a Xilinx Spartan FPGA evaluation board (shown in figure 8.1) which is connected to a SUSIBO read-out board. The SUSIBO connects via USB to the data acquisition system and provides the ability to read out the digitized data as well as configuration and debugging utilities for the SPADIC.

The controlling and configuration software for the SPADIC v0.3 is the *Hitclient*, which was developed specially for this chip. The *Hitclient* is standalone and enables the user to configure and read out the SPADIC. It is possible to set trigger thresholds for each of the eight channel individually, and to adjust the read-out delays between the fired trigger and starting of the digitalization cycle. A screenshot of the *Hitclient* software user interface is depicted in figure 8.2. It consists of a quasi online event display, an online spectrum of amplitude values and the display of a fast Fourier analysis of the input signals.

Characteristic	Quantity
Chip Technology	UMC 0.18 μm, 1P6M, MiMCaps
Chip Area	$1.5 \times 3.2\,\mathrm{mm}^2$
Channel / ADC Area	40×540 / $130 \times 120\,\mu\mathrm{m}^2$
Number of Channels / ADCs	26 / 8
Power per Channel / ADC	3.8 / 4.5 mW
Shaper Noise (ENC)	200 e + 20 e / pF
Shaper Peaking-Time	95 ns
ADC Resolution	7-8 bit effective
ADC Speed	24 MSamples / s

Table 8.1: Characteristic quantities of the SPADIC 0.3 [AFP09].

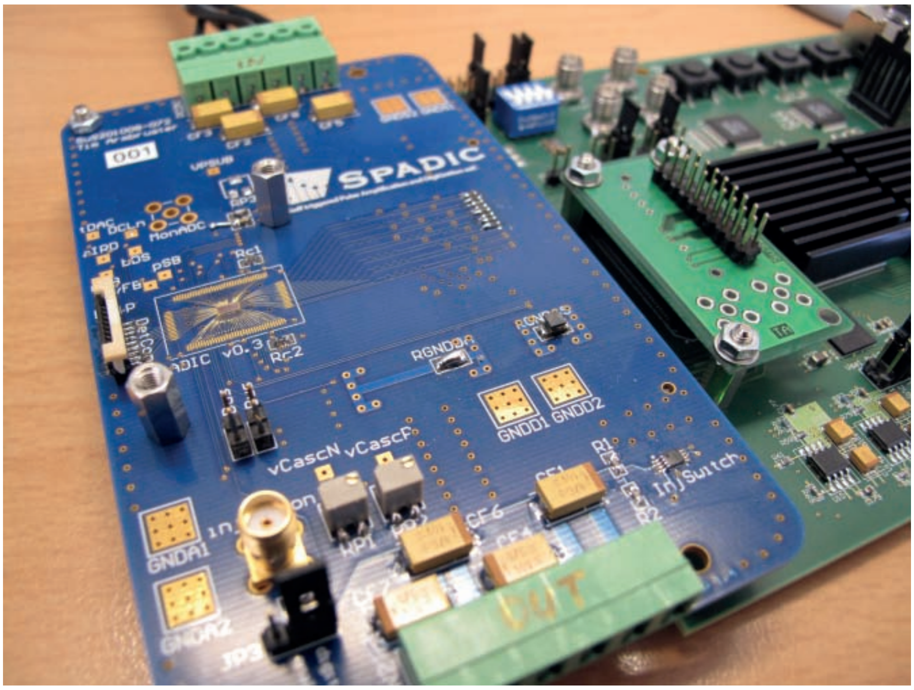

Figure 8.1: Photo of the SPADIC v0.3 on a Xilinx Spartan FPGA evaluation board.

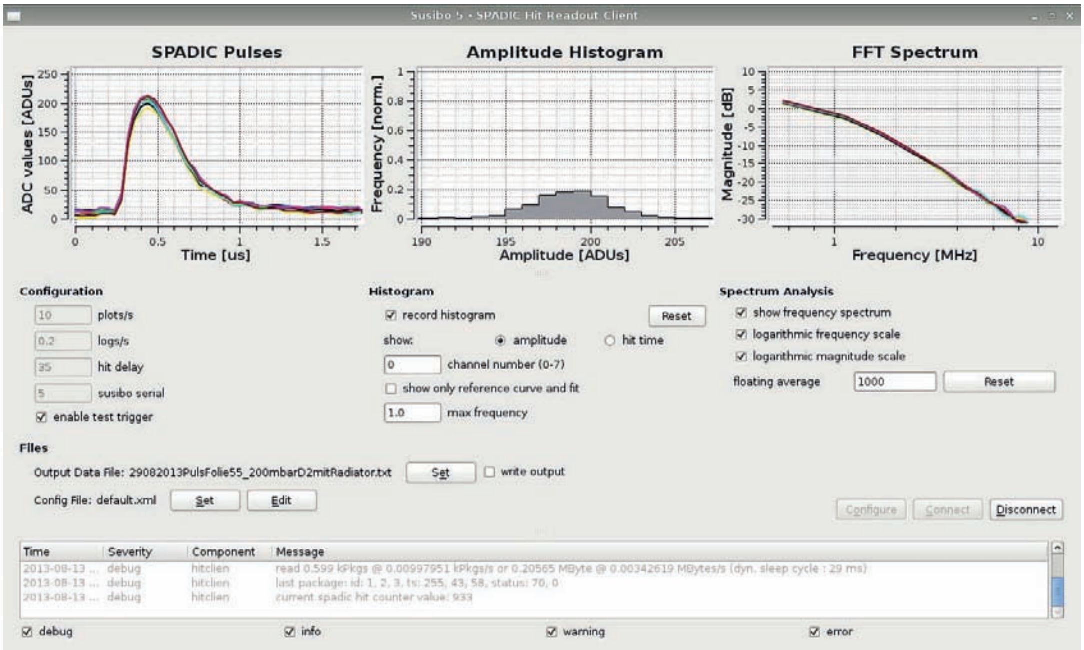

Figure 8.2: Screenshot of the Hitclient software.

8.1.1 Further Development: SPADIC 1.0

The SPADIC revision 1.0 is the continued development on the SPADIC v0.3. Compared with revision 0.3, version 1.0 provides 32 read-out channels [AK12] and an improved grounding scheme, which increases the robustness against external noise. Attached to its carrier board, the SPADIC 1.0 is compatible with the CBMnet protocol, which will be used in the final experimental setup for data acquisition. CBMnet and SPADIC 1.0 are capable of free streaming and self-triggered data read-out. The read-out of the data is implemented through a standardized HDMI connector. The SPADIC 1.0 with its carrier board and the read-out interface is shown in figure 8.3. First successful attempts to connect the SPADIC 1.0 to a Münster-type MWPC have been performed during the test beam campaign 2012.

8.2 Fast Analog Signal Processor

The Fast Analog Signal Processor (FASP) is a front-end electronics device for a high counting-rate TRD. It is based on a ASIC chip which is designed in AMS CMOS 0.35 μm *N-well* manufacturing technology. It has eight identical analog channels, each with two outputs: a fast semi-Gaussian output and a peak-sense output. All channels have a self-trigger capability with variable threshold. For an easy interconnection with a data acquisition system the chip implements an Input/Output interface working on a request/grant basis. There are also some specific features for high counting requirements: fast recovery from overload, good response to double pulses and high rate pulses, base line restoration due to leakage current and/or high counting rate [WV10]. The FASP read out chip has been utilized in test beam campaingns on Bucharest-type TRD prototypes [FS13, FS12].

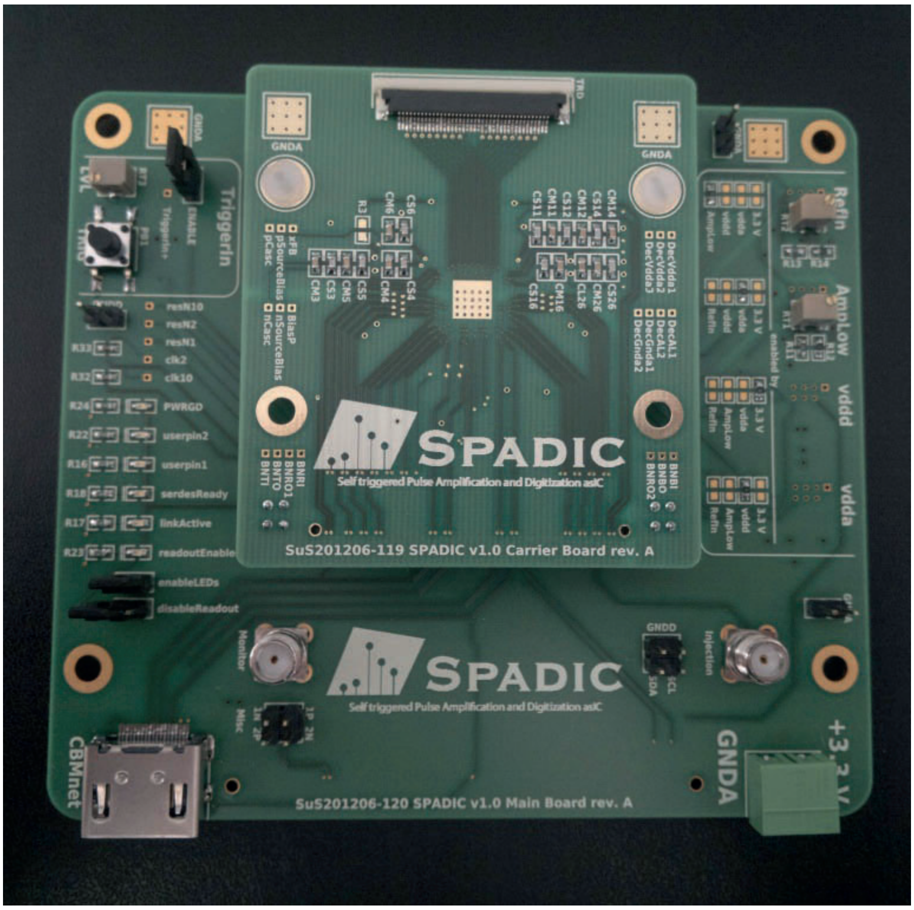

Figure 8.3: Photo of the SPADIC 1.0 on a carrier board with HDMI connector.

9 Simulations of the TRD Prototype

The setup of the electric field of a MWPC and the resulting electron and ion drift times, as well as the gas gain which is directly connected to the read out signal, are key characteristics of a MWPC. To achieve reproducible and comparable results and to study effects on mechanical variations and deformations, the electric field, the gas gain, and the mechanical stability of the foil-based entrance window have been simulated.

The entrance window of the full size $60\times60\,\text{cm}^2$ Frankfurt-type MWPC prototype is based on a thin Mylar foil which is attached to the cap (see chapter 7.2). Nevertheless the entrance window gets deformed due to differences of the internal to the ambient pressure. The global experiment-wide gas system in the CBM experiment is going to compensate for this, but the reaction might be slow compared to external pressure variations (e.g. related to weather changes) which results in pressure differences in the order of millibars. The magnitude of the bulging has been simulated with the Abaqus finite element analysis framework [FEA]. The calculation of the gas gain as well as its variation due to pressure differences, the electron and ion drift times, and the raw generated signal of the MWPC have been done with the GARFIELD software package [Vee].

9.1 Simulation of the Electric Field

To consider the available prototypes as specified in chapter 7, the simulation of the electric field has been done for the three different MWPC geometries of 4+4 mm, 5+5 mm and 6+6 mm. The entrance window and the read-out plane have been approximated with two continuous cathode planes in y-direction (perpendicular to the beam axis x) of the simulation. For each simulation 399 anode wires with a diameter of $20\,\mu$m at a spacing of 2.5 mm have been utilized, which results in a total detector height of 100 cm. In the simulation the detector is treated as open in y-direction which results in deformations of the electric field in the border areas. This is the reason, why only a center part of the electric field is shown in figure 9.1 (left part).

The anode wire voltage is directly connected to the gas gain and has to be adjusted individually for each of the used geometries. The references for this adjustment are the values obtained in direct operation of these prototypes in the test beam campaigns (see chapter 11), which have been modified slightly to result in a common gas gain.

The gas mixture used in this simulation consists of xenon (Xe) and carbon dioxide (CO_2) in a default mixing ratio of Xe/CO_2 (80/20). For studies on gas variations a mixing ratio of Xe/CO_2 (90/10) has also been simulated. Ambient pressure and temperature have been kept constant at values of p =1 atm and T =300 K.

In figure 9.1, the equipotential lines and the electron drift lines are shown for a central area in the 4+4 mm MWPC geometry at an anode wire voltage of 1940 V. The electron

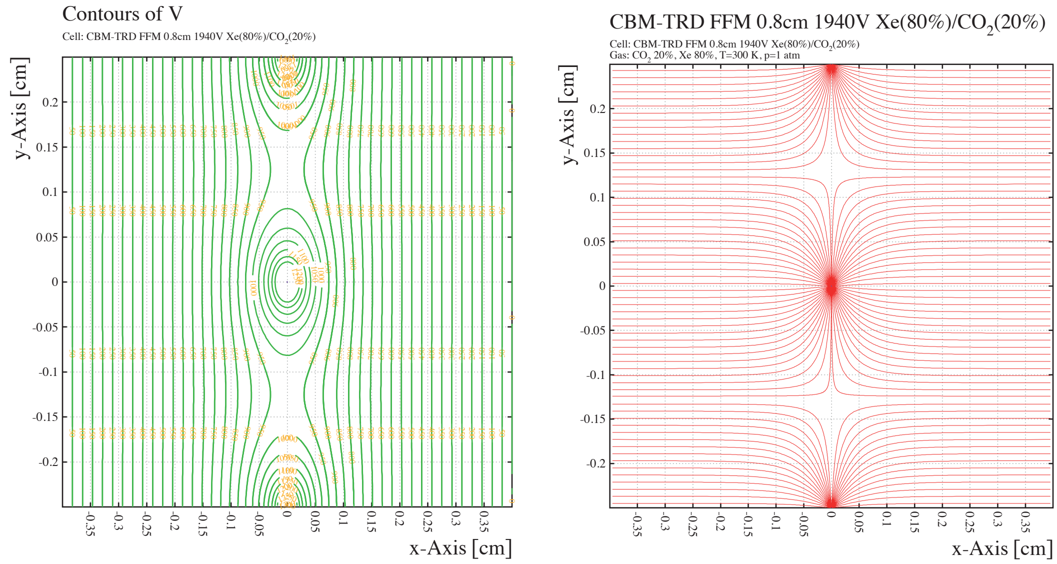

Figure 9.1: Electric field (left) and electron drift lines (right) of a central cell in a 4+4 mm MWPC geometry [Hel13b].

drift lines indicate the path of the generated ionization electrons. This structure (*cell*) recurs which results in a regular structure of the electric field. This allows that the following simulations of the gas gain and the electron/ion drift times are reduced to one non-border cell.

9.2 Simulation of the Gas Gain

The simulation of the gas gain has been performed for two different mixtures of Xe/CO_2 (80/20 and 90/10) for all three detector geometries (4+4 mm, 5+5 mm and 6+6 mm) at three different anode wire voltage settings. In this simulation the area of the central cell of the detector has been filled evenly with ionization electrons which are accelerated by the electric field along the drift lines. The statistical mean of the gas gain generated by the avalanche is calculated via integration of the first Townsend coefficient determined by the *Magboltz* software, over drift length. With this calculation the mean of the gas gain $\langle gain \rangle$ of each wire is obtained.

In figure 9.2, the spatial distribution of the gas gain in the central cell of the MWPC is depicted. The anode voltages have been selected such that the values for the gas gain are comparable for all used layouts. A small drop of the gas gain at the borders of the cell is visible for all geometries. For electrons generated at the edge of a cell, the drift length in areas of large field strength (proportional area) is shorter compared to electrons generated perpendicular to the wire. Because the dominant part in gas gain generation happens in the proportional area, spatial differences in the absolute values of the gas gain generation occur.

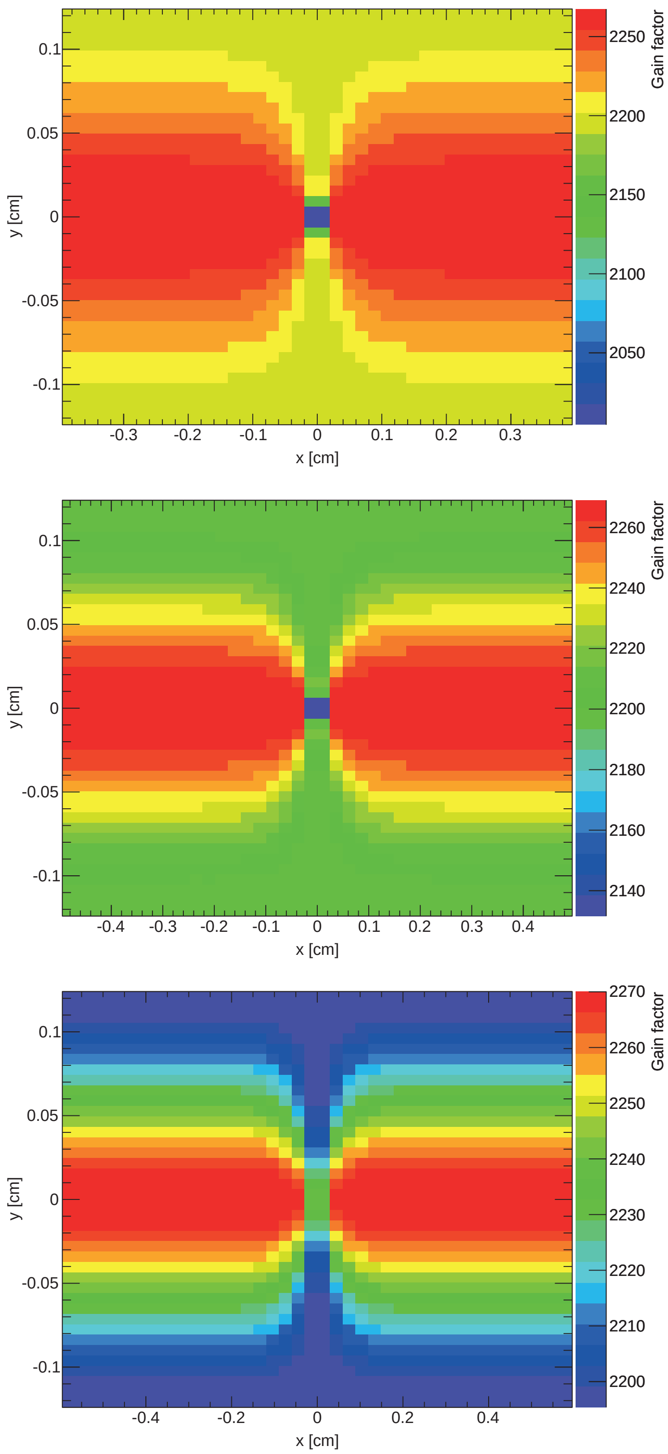

Figure 9.2: Spatial distribution of the mean gas gain for all three geometries using Xe/CO_2 (80/20). Top: 4+4 mm at 1940 V anode wire voltage, middle: 5+5 mm at 2220 V anode wire voltage, bottom: 6+6 mm at 2500 V anode wire voltage [Hel13b].

In table 9.1 the mean values of the gas gain for all three detector geometries and for the gas mixtures of Xe/CO_2 (80/20) and Xe/CO_2 (90/10) are shown. The standard deviation is given as error, which is about 2% for all given values. Following this deviation the spatial variations of the gas gain are negligible for central cells. Besides the cells on the border of the MWPC the gain uniformity is flat for the complete detector area.

Geometry	Xe/CO_2 (80/20)		Xe/CO_2 (90/10)	
	Anode Voltage	$\langle gain \rangle$	Anode Voltage	$\langle gain \rangle$
4+4mm	1820 V	1003±21	1770 V	1027±22
	1890 V	1592±36	1830 V	1545±36
	1940 V	2224±53	1880 V	2181±53
5+5mm	2090 V	1047±20	2020 V	995±20
	2160 V	1568±33	2100 V	1602±34
	2220 V	2227±49	2150 V	2166±49
6+6mm	2350 V	1029±19	2280 V	1024±19
	2440 V	1632±32	2360 V	1562±31
	2500 V	2229±46	2420 V	2154±46

Table 9.1: Mean gas gain for all three geometries using Xe/CO_2 (80/20) and Xe/CO_2 (90/10) at different anode voltages [Hel13b].

The comparison of the three simulated geometries according to the utilized gas mixture shows that the anode wire voltage which is required to generate a desired value of the gas gain is lower for Xe/CO_2 (90/10) than for Xe/CO_2 (80/20). In other words, for a fixed anode voltage the gas gain is higher for Xe/CO_2 (90/10). The higher amount of xenon in the gas mixture goes along with a higher ionization cross section, but the dominant source for the larger gas gains are the different Penning-transfer rates. The Penning effect describes an ionization process in which an excited gas atom ionizes another atom of the gas. If an energy level of an atom or molecule is higher than the ionization energy, the excited atom can return into its ground state via photon emission or direct collision with another gas atom which is then ionized. In a gas mixture of xenon and carbon dioxide, the CO_2 molecules have three excitation states with energy levels of 12.2 eV, 13.2 eV and 15.0 eV. These are all higher than the minimal ionization energy of 12.13 eV for a xenon atom [Gar]. The Penning transfer rate characterizes the fraction of excited CO_2 molecules with a larger excitation energy than the minimal ionization energy of xenon, which contribute to the ionization of the xenon. This fraction is severely different in both gas mixtures: for Xe/CO_2 (80/20) the Penning transfer rate is about 11%, where as for Xe/CO_2 90/10 it is about 44%. This causes the mean gas gain to be larger for the Xe/CO_2 90/10 mixture at a fix anode voltage.

Figure 9.3 depicts the mean gas gain factor for the three used geometries depending on the applied anode voltage for both gas mixtures. According to the almost linear shape in this logarithmic representation, the exponential character of the gas gain (see equation 3.10) can be verified. The difference for both gas mixtures can be clearly seen. For the 4+4 mm MWPC the values of the gas gain of Xe/CO_2 (90/10) at the lowest anode voltage of 1800 V are almost a factor 1.44 larger than for the 80/20 mixture, which increases for

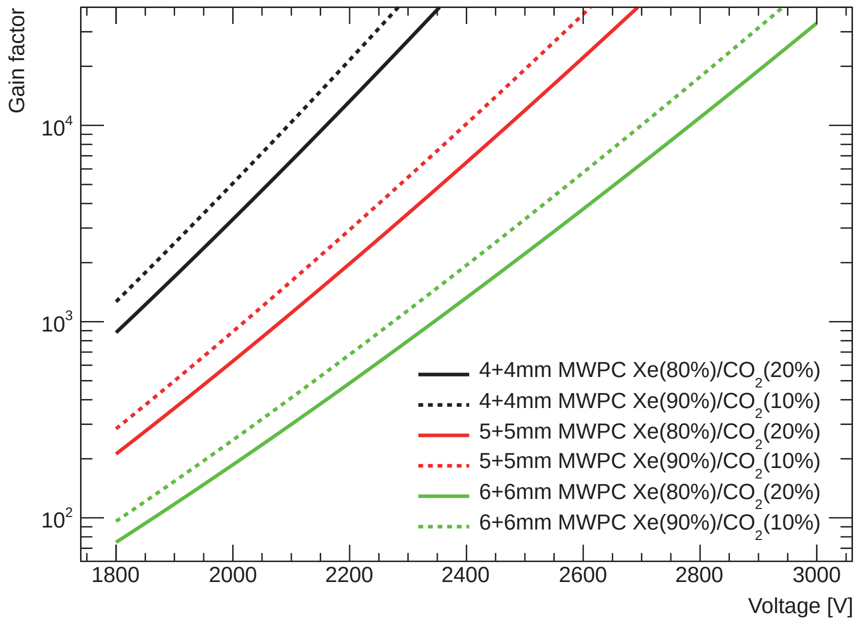

Figure 9.3: Mean gas gain factor depending on the applied anode voltage for Xe/CO_2 (90/10) and Xe/CO_2 (80/20) for all three used MWPC geometries [Hel13b].

---

the highest anode voltages of 3000 V up to a factor of 2.12. Such large anode voltages will most likely not be applied to a MWPC due to possible damage caused by sparks. The mean of the gas gain factor for the 4+4 mm MWPC filled with Xe/CO_2 (90/10) is a factor 1.75±0.2 larger. The resulting values for the 5+5 mm geometries are at a mean of 1.58±0.15 and for the 6+6 mm at a mean of 1.47±0.12. The divergence at large voltages can be explained with the first Townsend coefficient, which is different for both gas mixtures but additionally shows a dependency of the applied electric field, which varies with the applied anode voltage [Hel13b].

9.2.1 Gas Gain Variation due to Expansion

The Frankfurt type MWPC prototype uses a thin foil-based entrance as one of the cathode planes. This foil will experience deformations due to unavoidable differences in the inner and the ambient pressure. These pressure differences lead to a bulging of the foil. To simulate the effects on the gas gain, the distance of the left cathode (entrance window) is varied in steps of$\Delta\ d = 5\,\mu$m and the mean gas gain factor $Gain(d)$ is calculated. The relative gain change $\frac{Gain(d)}{Gain(0)}$ is determined with the help of the gas gain factor at no distance variation $Gain(0)$. In figure 9.4, this relative gain is shown for different anode voltages depending on the distance variation d for each detector geometry filled with Xe/CO_2 (80/20). The anode voltage has been chosen such that the base value of $Gain(0)$ is equal for the three geometries at a given voltage. All three geometries show the same behavior with changing distance d. The increase for smaller anode-cathode distances ($d < 0$) and the decrease for larger anode-cathode distances ($d > 0$) are expected according to equation 3.13. The relative gain change of the 4+4 mm is more sensitive to a distance variation while the 6+6 mm MWPC shows the smallest changes and is thus more robust against these variations. Such behavior can be explained by the fraction of the distance variation with respect to the total dimensions of the MWPC: a variation of $d/4$ mm is larger than the $d/6$ mm which results in larger variation in the gas gain.

According to chapter 6.1 one of the experimental requirements for the TRD is a gas gain uniformity with variations of less than$\Delta\ Gain_{max} = \pm\ 10\%$ for the total gas gain factor. Applying this limit to the calculation of the gas gain with distance variation, it results in a lower ($\Delta Gain_{max} = -\ 10\%$) and an upper ($\Delta\ Gain_{max} = +\ 10\%$) limit for the position of the thin foil-based entrance window. Figure 9.5 shows the gain variation for each geometry type. These values have been used to calculate the resulting positioning limits shown in table 9.2.

MWPC	Anode Voltage	$\langle gain \rangle$	d_{min}	d_{max}	$\langle d_{min} \rangle$	$\langle d_{max} \rangle$
4+4 mm	1820 V	1003±21	-109 μm	126 μm	-104±4 μm	120±5 μm
	1890 V	1592±36	-103 μm	119 μm		
	1940 V	2224±53	-99 μm	115 μm		
5+5 mm	2090 V	1047±20	-124 μm	143 μm	-118±4 μm	137±5 μm
	2160 V	1568±33	-118 μm	136 μm		
	2220 V	2227±49	-114 μm	131 μm		
6+6 mm	2350 V	1029±19	-140 μm	161 μm	-133±5 μm	154±6 μm
	2440 V	1632±32	-132 μm	153 μm		
	2500 V	2229±46	-128 μm	147 μm		

Table 9.2: Limits of maximal distance variations for$\Delta\ Gain_{max} = \pm\ 10\%$ [Hel13b].

The values of the deformation limits d_{min} and d_{max} for the 4+4 mm are between 99 and 126 μm, the same values are up to 128-161 μm for the 6+6 mm MWPC. Comparing each separate detector geometry with its different anode voltage settings to each other only a small spread of the values is observed. Here the gas gain only exhibits small changes due to voltage variations. This behavior can be seen in figure 9.5 for all used geometries. Due to the small changes according to voltage variations the mean value for the minimum and maximum deformation $\langle d_{min} \rangle$ and $\langle d_{max} \rangle$ can be calculated giving the range of values for a gain stability of$\Delta\ Gain_{max} = \pm\ 10\%$. These values are also listed in table 9.2 [Hel13b].

Following equation 3.13 the variation of the anode-cathode distance is not influenced by the change of the gas mixing ratio. The used gas mixture is accounted for by the use of the first Townsend coefficient. When selecting comparable base value of $Gain(0)$ the changing of the gain according to distance variations are equivalent. Figure 9.6 shows the simulated gas gain variation for the 4+4 mm MWPC depending on d for an anode voltage of 1770 V for Xe/CO_2 (90/10) and 1820 V for Xe/CO_2 (80/20). Both curves are lying on top of each other. This is explained by the independence of the gain variation by the gas mixture.

Following the results of the gas gain simulation, a set of criteria for the usage of the foil based entrance window can be derived under the requirement of a gain uniformity

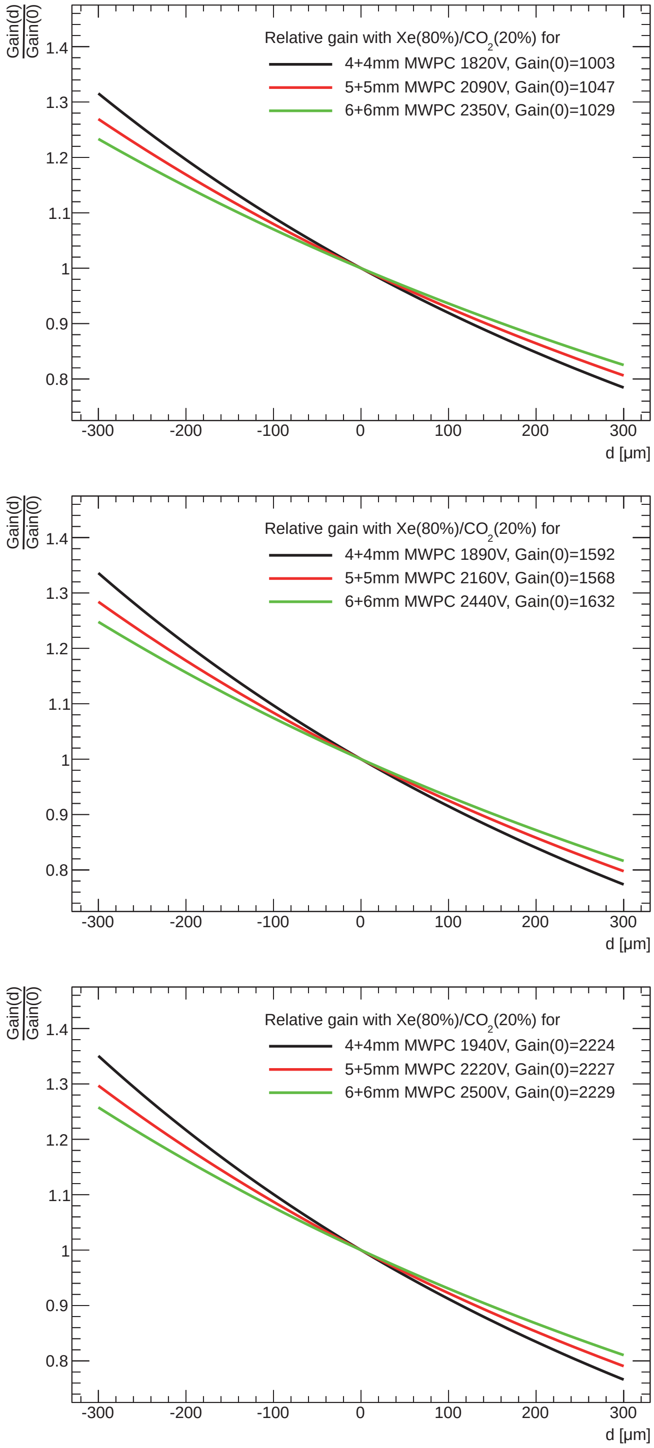

Figure 9.4: Gain variation $\frac{Gain(d)}{Gain(0)}$ depending on the distance modification d. Top figure: low anode wire voltage, middle figure: approximated running condition anode voltage, bottom figure: high anode wire voltage [Hel13b].

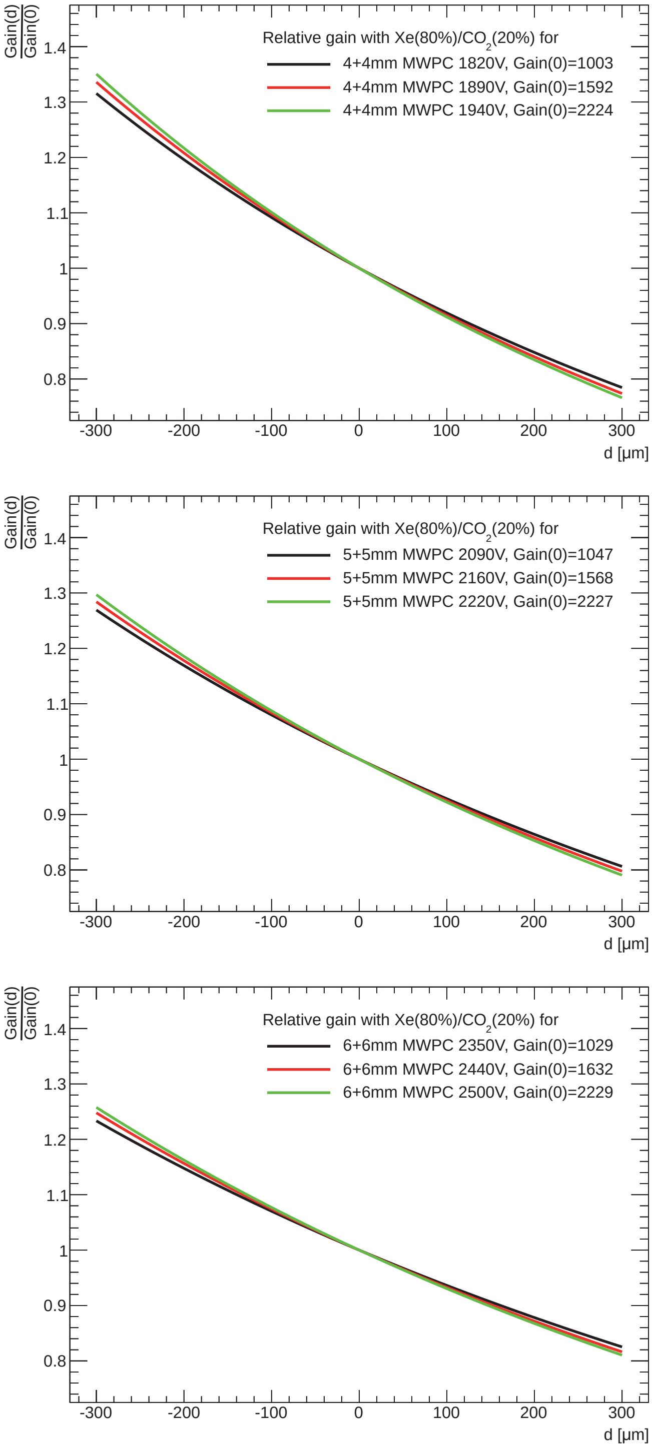

Figure 9.5: Gain variation $\frac{Gain(d)}{Gain(0)}$ depending on the distance modification d. The plots from top to bottom show the three different geometries of 4+4 mm, 5+5 mm and 6+6 mm [Hel13b].

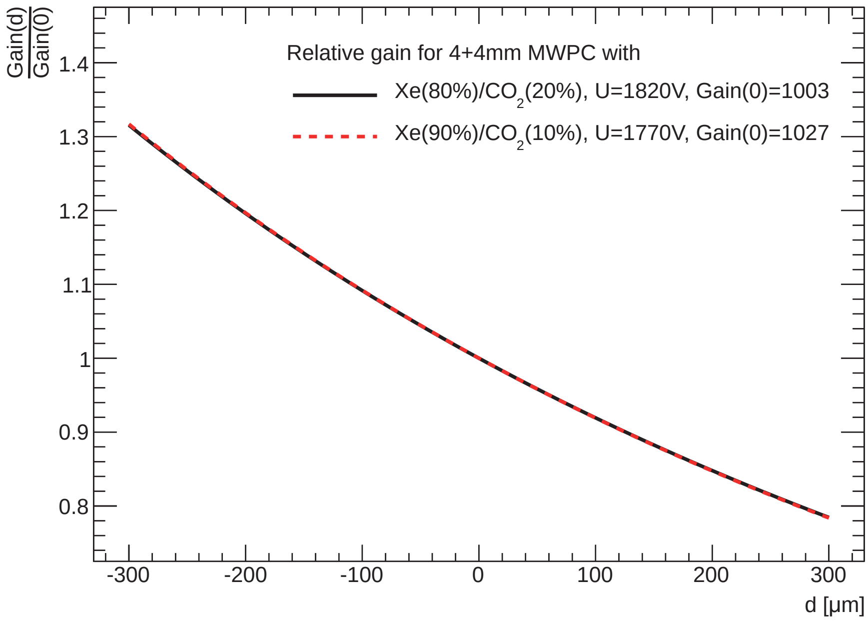

Figure 9.6: Gas gain variation of the 4+4 mm MWPC for Xe/CO_2 (80/20) and Xe/CO_2 (90/10) [Hel13b].

of $\frac{Gain(d)}{Gain(0)} = \pm 10\%$. Due to the overpressure during operational conditions a dent of the entrance foil towards the anode wires can be prevented. This overpressure results in an appropriate bulging of the foil, which will vary with respect to the ambient pressure. When requesting a gain uniformity of 10% the maximal acceptable bulging of the entrance window is 120±5 μm for the 4+4 mm MWPC and 154±6 μm for the 6+6 mm MWPC. The calculations of the corresponding pressure differences with a mechanical simulation of the MWPCs are shown in chapter 9.5.

9.3 Electron and Ion Drift Times

Since the CBM experiment will be operated at event rates of ≈10 MHz, fast detectors are required. Apart of read-out electronics and data acquisition capabilities, the read-out time of gas detectors like the TRDs is dominated by the drift time during the signal generation. The drift time describes the temporal interval in which the generated electrons and ions move with the drift velocity v_D towards the anode wire or cathode planes and induce the signal. If the drift times are too large, the signal generation decelerates, and signals from two different events overlay and can not be separated anymore (*pile-up effects*). The time resolution of such events depends on the difference in time if the initial electrons of the first avalanche which is determined with via the electron drift time [Leo94]. The ionization happens along the complete path of the traversing particle. For the drift time determination the first electron arriving at the anode wire is decisive. The distance to the anode wire of this first electron can not be larger than half of the wire pitch due to geometrical reasons. An uncertainty of the drift time of the initial electron occurs due to this distance. To simulate the time resolution$\Delta\ t$ of the three used detector geometries, electrons are distributed evenly inside the central cell (analog to chapter 9.2) and the drift times for electrons and ions are calculated. The ion mobility has been implemented into the simulation by using single ionized xenon (Xe^+) [RT00].

The electron drift times for the three used MWPC geometries for a gas mixture of Xe/CO_2 (80/20) are shown in figure 9.7, figure 9.8 depicts the results for Xe/CO_2 (90/10). The ion arrival times on the cathodes are shown in figure 9.9. The electron and ion drift times along the y-axis are homogeneous. Close to the anode wire, the electron drift times are only a few nanoseconds which leads to a time divergence of$\Delta\ t \approx$30 ns. On the edges of the cell, the drift times rise significantly. Table 9.3 summarizes drift times for Xe/CO_2 (80/20) as well as for Xe/CO_2 (90/10).

MWPC	Xe/CO_2	Anode Voltage	$\langle T_D \rangle$	$\langle T_{D,max} \rangle$	Δt
4+4 mm		1940 V	0,054±0,028 μs	0,098±0,010 μs	
5+5 mm	80/20	2220 V	0,065±0,034 μs	0,122±0,010 μs	≈30 ns
6+6 mm		2500 V	0,077±0,041 μs	0,145±0,010 μs	
4+4 mm		1880 V	0,077±0,040 μs	0,145±0,010 μs	
5+5 mm	90/10	2150 V	0,095±0,050 μs	0,181±0,010 μs	≈40 ns
6+6 mm		2420 V	0,112±0,060 μs	0,216±0,010 μs	

Table 9.3: Summary of drift times for both gas mixtures and all three used MWPC geometries [Hel13b].

The maximum drift times at the edge of a cell can be translated into an average maximum hit rate of 10.2 MHz for the 4+4 mm MWPC, 8.2 MHz for the 5+5 mm MWPC, and 6.9 MHz for the 6+6 mm MWPC. Compared with the hit rate simulation in chapter 6.3 all MWPC prototypes with Xe/CO_2 (80/20) are per design fast enough to handle the expected hit rates of ≈0.1 MHz. The comparison of Xe/CO_2 (80/20) to Xe/CO_2 (90/10) results in a longer electron drift time for all MWPC prototypes. The achieved time resolution is$\Delta\ t \approx$40 ns. The 6+6 mm MWPC as the slowest detector only reaches a hit rate of 4.6 MHz, which is still 46× faster than the hit rate simulation requires. The benefit of a higher TR photon absorption probability when increasing the fraction of xenon in the detector gas can excepted because the drawbacks concerning the drift time are still above the simulation which defines the requirements.

9.4 Signal Simulation

The induced raw signals of the utilized MWPC prototypes have been simulated by using electron and ion drift information. For this simulation, electron/ion pairs have been distributed according to the avalanche topology obtained by figure 9.10. This topology has been approximated by the following conditions:

- The opening angle α of the avalanche is 90°.

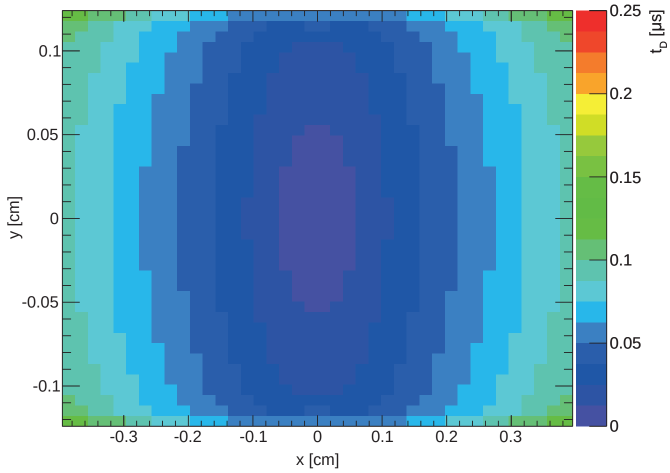

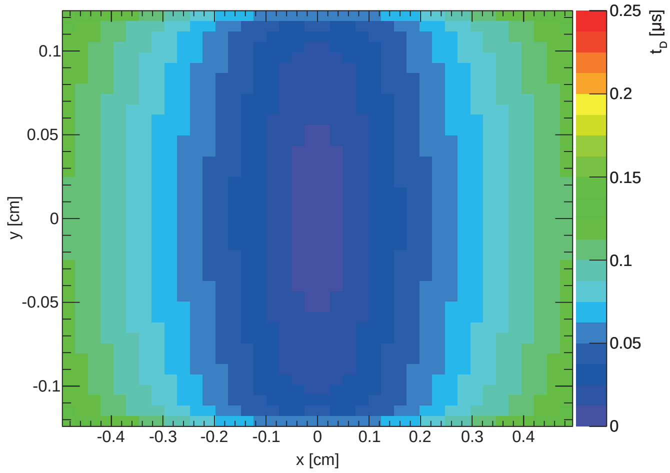

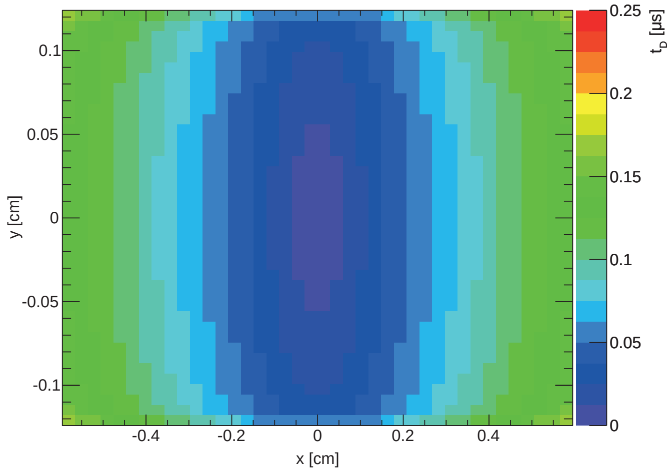

Figure 9.7: Electron drift times for Xe/CO_2 (80/20) for the 4+4 mm, 5+5 mm and 6+6 mm MWPC (top to bottom) [Hel13b].

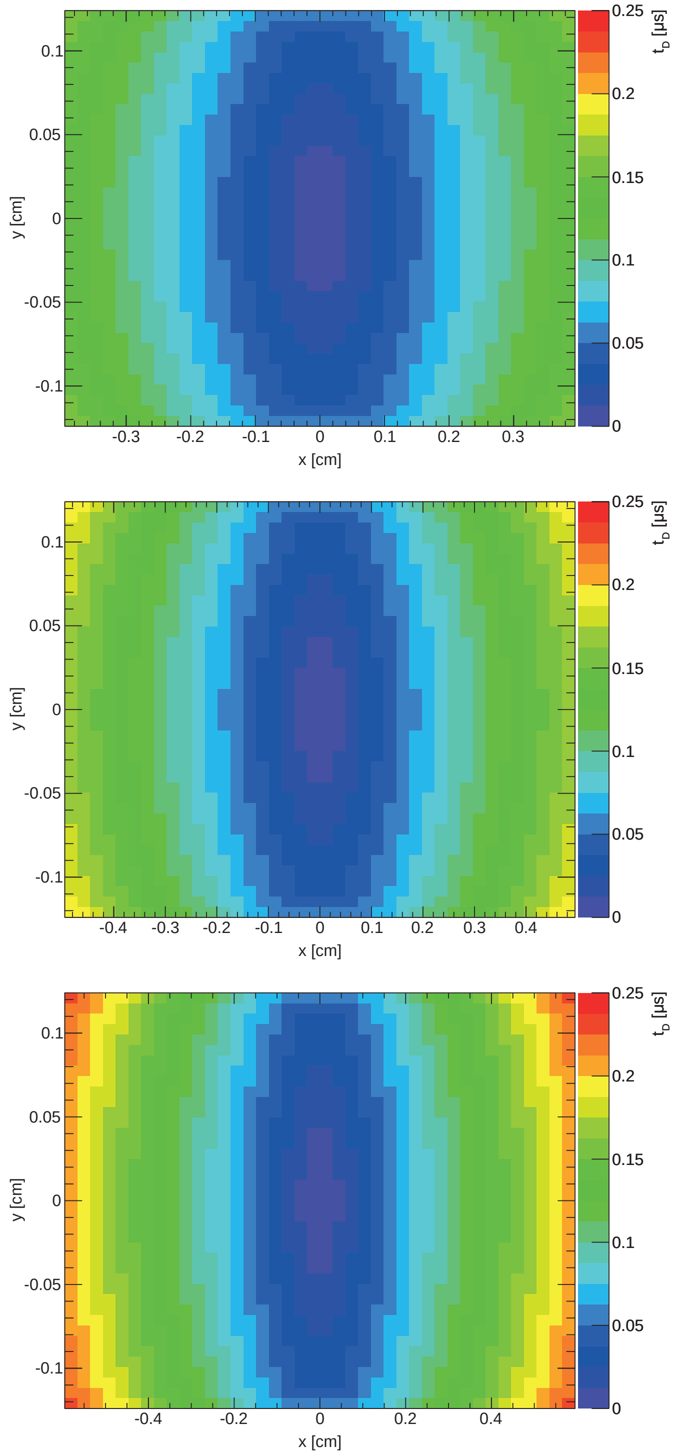

Figure 9.8: Electron drift times for Xe/CO_2 (90/10) for the 4+4 mm, 5+5 mm and 6+6 mm MWPC (top to bottom) [Hel13b].

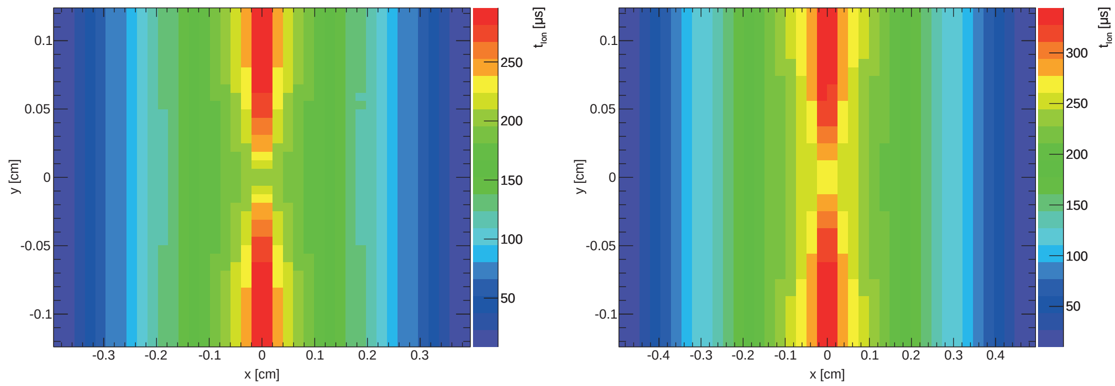

Figure 9.9: Ion arrival times for the 4+4 mm MWPC at an anode voltage of 1940 V on the left, and for the 5+5 mm MWPC at 2220 V on the right side [Hel13c].

- The longitudinal distribution (along the beam axis z perpendicular to the simulated cell) is a half Gaussian distribution.
- The distribution along the wire axis is a full Gaussian.

The actual values of the utilized distributions are selected to mimic the given topology and dimensions according to figure 9.10. Following these distributions 1000 electron/ion pairs have been placed randomly inside the avalanche. The ions are propagated towards the read-out pad plane and the induced signals have been added. The resulting raw signal on the read-out pads of the 4+4 mm MWPC filled with Xe/CO_2 (80/20) is shown exemplary in figure 9.11.

The simulated signal features a very fast rising edge according to the implied ion distribution. The falling edge of the signal shows the expected asymptotic decrease. The absolute height of the signal is created by the number of ions placed in the cell.

9.5 Mechanical Simulation of the Entrance Window

The Frankfurt type MWPC prototype utilizes a thin foil based entrance window which will be deformed when it experiences pressure differences of its inner gas volume to the ambient pressure. To quantify the expansion due to this pressure differences, mechanical simulations are performed. The *finite-element* software package *Abaqus* [FEA] has been used for this simulation in which the production and stretching procedure of the entrance window (see 7.2.1) has been emulated. Abaqus uses a tight-knit lattice to determine mechanical properties of simulated objects. The expansion of the tensioned foil has been calculated for a set of different pressure values [Reu13].

Within the simulation two acrylic glass frames are generated and the Mylar foil is fixed between the frames. The temperature of the acrylic glass frames is set to 55 °C, while the mylar foil keeps room temperature (20 °C). The deformation and the resulting tension applied to the foil is calculated according to the expansion coefficients, Poisson's ratio and

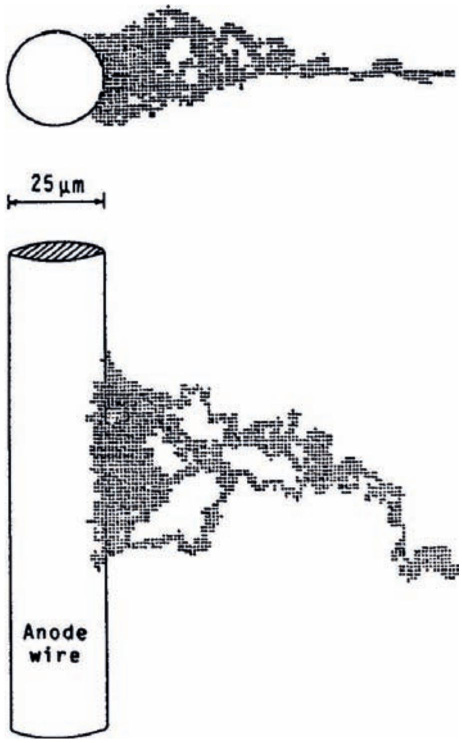

Figure 9.10: Two-dimensional displays of the electron density in an avalanche [BRR08].

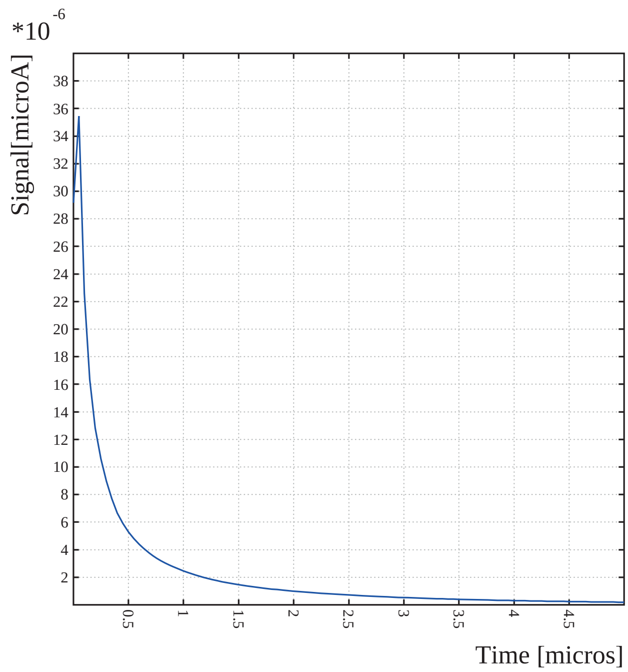

Figure 9.11: Simulation of the induced signal on the read-out pads for the 4+4 mm MWPC filled with Xe/CO_2 (80/20) [Hel13c].

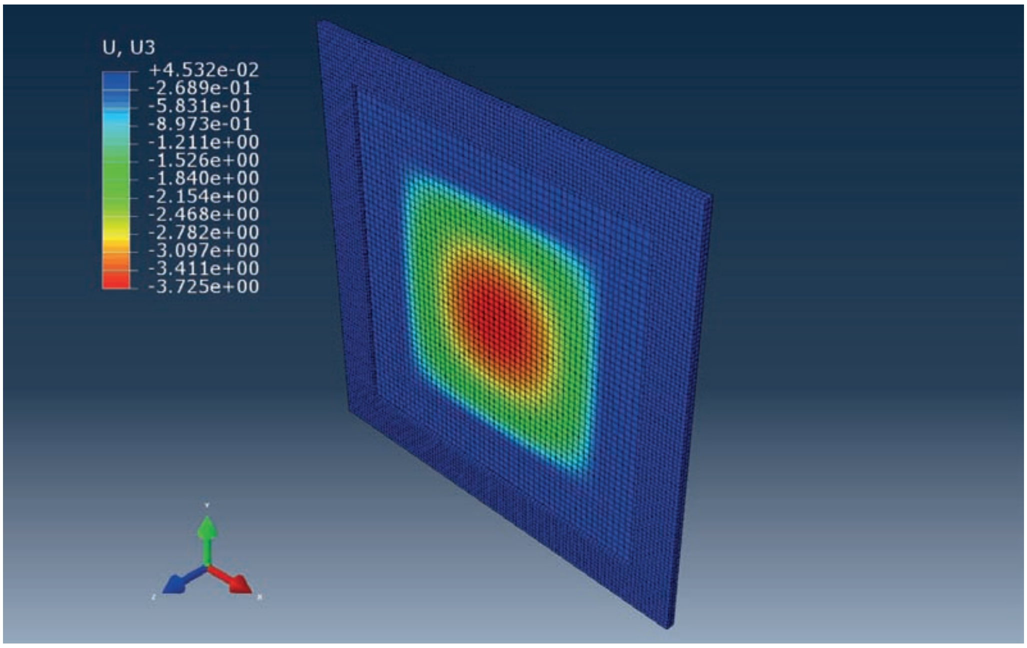

Figure 9.12: Mechanical simulation of expansion of the entrance window. The deformation is color coded, the tight-knit lattice of the Abaqus simulation framework are visible [Reu13].

elastic modulus of the used materials. After stretching the foil, an additional volume with a base area of $59\times59\,\mathrm{cm}^2$ and the required overpressure is attached to the foil and the expansion is calculated in a second simulation step. A screen shot of the resulting object is shown in figure 9.12.

The resulting expansions are displayed in figure 9.13 as a function on the applied overpressure, the error bars shown in this plot are given by the Abaqus software. According to the simulation of the gain variation (see chapter 9.2.1), the limit of deformation for the largest 6+6 mm MWPC geometry is $154\pm6\,\mu$m. This value is exceeded already at an overpressure of $20\,\mu$bar. For comparison, the ALICE TRD with a reinforced and self-supporting radiator directly placed as entrance window deviates from a flat surface by 3.25 mm at an overpressure of 1 mbar [ALI01].

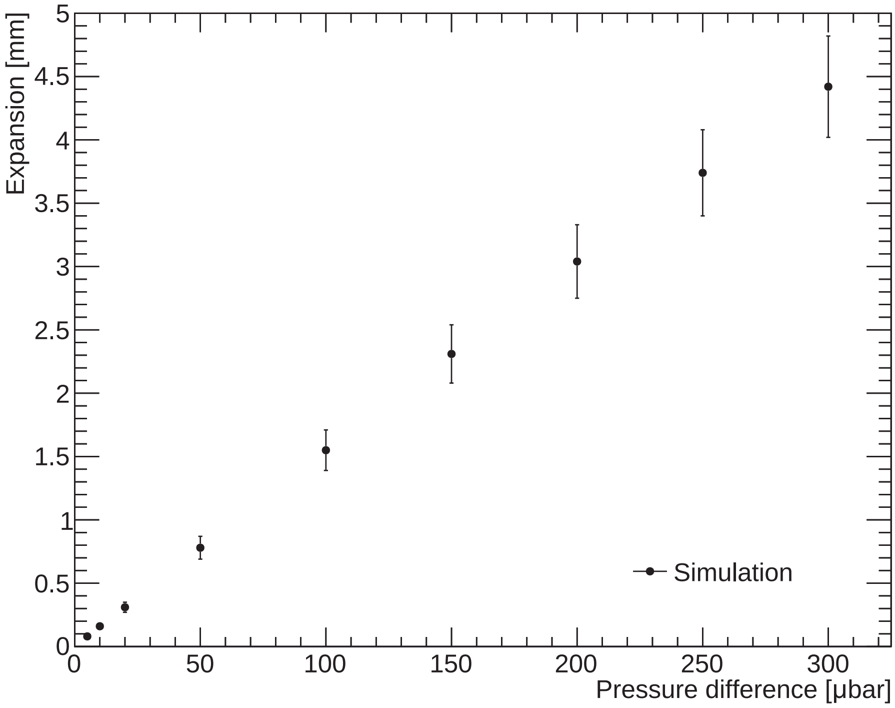

Figure 9.13: Expansion of the foil based entrance window depending on the allied overpressure [Reu13].

10 Validation of Prototype Characteristics

In a set of test measurements, the constructed prototypes were characterized with respect to the mechanical stability of the entrance window, absolute gain factors, gain homogeneity and the energy resolution.

10.1 Mechanical Stability of the Entrance Window

For the mechanical stability tests of the full-size prototypes thin foil-based entrance window, a mock-up frame with the exact same dimensions has been used. A stretched and tensioned Mylar foil (see 7.2.1) has been glued on a wooden frame. The mock-up frame was covered with a *G10* plate on the backside. Two gas inlet and outlet as well as a connection pipe to a differential pressure sensor have been attached. The gas outlet was connected to a *pig tail*. The mock-up setup has been proven to be sufficiently gas tight for this tests. A photo of the setup is shown on figure 10.1.

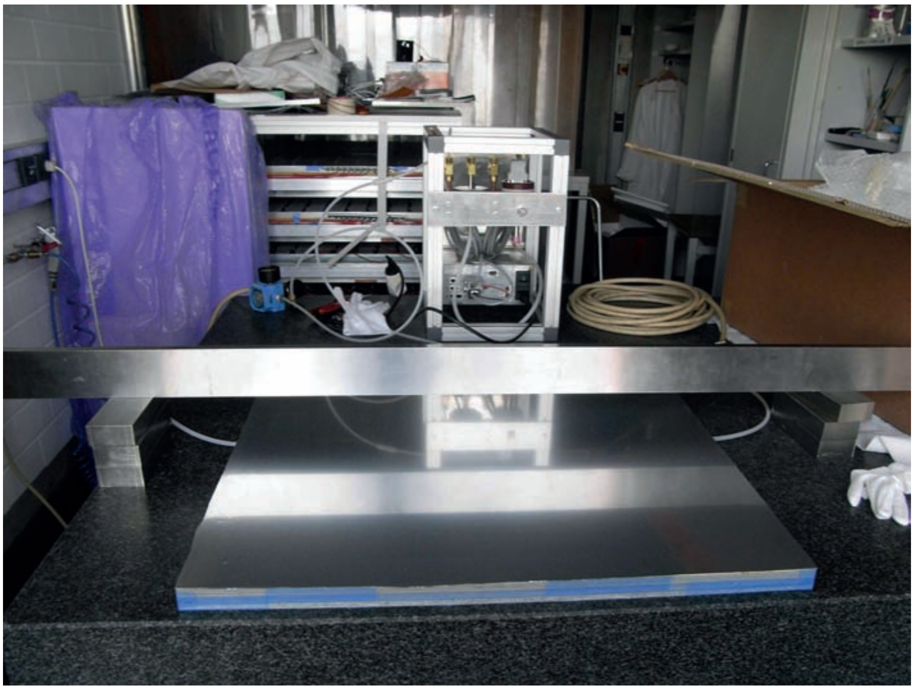

Figure 10.1: Setup for the expansion tests of the foil-based entrance window [Reu13].

The mock-up has been filled with compressed air via a pressure regulator. The gas flow and the attached *pig tail* with its intrinsic resistivity generate an overpressure inside the mock-up. The differential pressure (overpressure over ambient pressure) was measured and the resulting expansion of the foil could be directly observed using a caliper rule centered on the middle of the foil based entrance window. The gas flow has been regulated to generate different values of overpressure inside the mock-up, the resulting expansion has been recorded and displayed in figure 10.2 in comparison to the simulated expansion [Reu13].

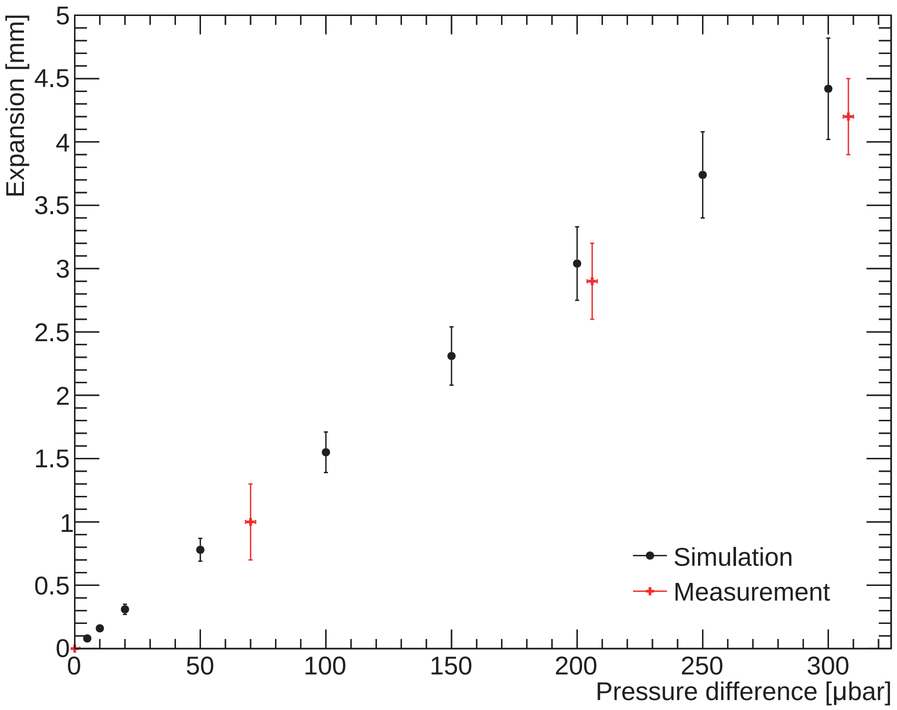

Figure 10.2: Measured expansion in comparison to simulation [Reu13].

The depicted measured values in figure 10.2 include approximated systematic errors of 0.2 mm for the expansion and 20 μbar for the differential pressure measurement. The error which is introduced to a non-centered expansion measurement can be neglected. Even if the off-center variation is more than 5 cm the corresponding variation in expansion is less than 0.15 mm on the highest simulated overpressure of 450 μbar, which is due to the large area of 60×60 cm^2 of the utilized foil.

The measured and the simulated values for the expansion of the foil are in very good agreement for small pressure differences (<100 μbar). For larger values a deviation is visible but measurement and simulation are still in agreement within the error bars. This measurement validates the simulation and the conclusions for the gain variation deduced on that.

10.2 Gas Gain Measurements

The gas gain of a Multi Wire Proportional Chamber (MWPC) can be measured via the current at the anode wires, which is generated if the MWPC is exposed to ionizing radiation. To determine the gas gain G the generated current at the anode wire I_A is compared to the primary current I_P, which is generated by the utilized source:

$$G = \frac{I_A}{I_P} \tag{10.1}$$

This allows a measurement of the absolute gas gain as well as a relative measurement of the gas gain. The relative gas enables a fast measurement when varying parameters of the MWPC with a simple experimental setup only measuring the anode current assuming a fixed primary current. The absolute gas gain requires a more sophisticated setup, but allows the direct comparison to the simulations and serves as input for additional studies.

10.2.1 Absolute Gas Gain

Equation 10.1 can be adopted by replacing the primary and anode currents by measurable quantities:

$$G = \frac{I_A}{I_P} = \frac{I_M - I_D}{R \cdot N_P \cdot e} \tag{10.2}$$

The anode current is composed of the actually measured current I_M and the dark current I_D. The dark current can be determined by measuring without an ionizing source and has to be subtracted. The primary current I_P can be composed by the rate R of absorbed photons and electrons released per primary ionization N_P multiplied with the elementary charge e . The rate of photons corresponds to the measured signal rate and the number of released electrons per ionization is determined via the energy of the utilized radiation and the ionization potential of the used gas mixture:

$$N_P = \frac{E_\gamma}{E_I} \tag{10.3}$$

For the measurement of the absolute gas gain a mix of Ar/CO_2 (80/20) has been used with $E_I =$ 27.6 eV. The spectrum of the utilized ionizing ^{55}Fe source is composed of the ^{55}Fe-K_α line at $E =$ 5.9 keV and the argon escape line for the full size generation IV MWPC prototypes. Therefor a combined average primary energy of $E =$5.6 keV, which results as the weighted mean value of both energies. The rate is composed of a directly counted rate with correction factors:

$$R = \frac{R_M}{1 - R_M \cdot \tau} - R_D \tag{10.4}$$

Where R_M is the measured ionizing radiation, R_D was measured without source and has been used for correction of background and noise. Additionally the dead time τ of the used electronics has to be taken into account for each measurement. It has been approximated with $\tau =$15 ns [Dil13].

Figure 10.3 schematically shows the experimental setup of the absolute gas gain measurement. High voltage connections towards the prototype are shown as black lines, red lines depict the directly decoupled analogue signals through a preamplifier and green lines represent *NIM* signal transmission from a discriminator to a counter if a given trigger

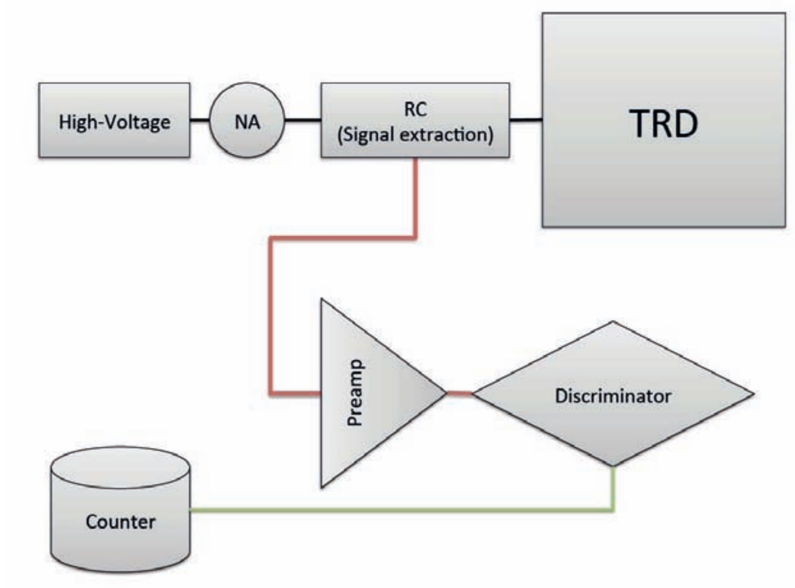

Figure 10.3: Schematic overview of the absolute gas gain measurement setup: high voltage connections are shown as black lines, red lines depict the directly decoupled analog signals and green lines represent *NIM* signal transmission [Dil13].

threshold is exceeded. For ionization measurements a ^{55}Fe source has been used.

The measurement of the primary ionization is the dominant source of measurement errors in this given setup. It is sensitive to the choice of the trigger setup, which has to be set low enough, such that all primary ionization particles are counted and above a given noise level, that the background noise does not lead to miscounting, which can not be corrected by R_D. Diminutive variations of this trigger thresholds already lead to variations of $\pm 10\%$ which substantiates an error approximation of the measured rate of $\pm 10\%$ which is propagated. According to the dominance of this error, the uncertainty of the resulting gas gain has also been approximated with $\frac{\Delta G}{G} = \pm 10\%$. All other potential sources of measurement errors have been found to be negligible.

In figure 10.4 and 10.5 the measured absolute gas gain depending on the applied anode voltage is shown together with simulated values [Hel13a] for a gas mixture of Ar/CO_2 (80/20). The simulations use a Penning transfer rate of 37% at normal atmospheric pressure [Hel13a], although the measurement has been performed at an differential overpressure of 600 μbar and 610 μbar over atmospheric pressure. As shown in chapter 3.2 the MWPC has to be operated in the proportional region. Regarding the functional dependency of the gas gain on the high voltage an exponential behavior should be seen, which could be verified with an exponential fit to the data (red line). As expected due to the smaller gas volume and the smaller absorption length the 4+4 mm prototype shows a comparable gas gain already at 1925 V (2300 V for the 5+5 mm MWPC). The discrepancy between measurement and simulation can be explained with the sensitive rate measurement and the differences in pressure for both scenarios. Taking this into account the simulated and the measured values are in good agreement, which indicates the correctness of the further depicted electro static simulations in chapter 9. According to the exponential fit and the

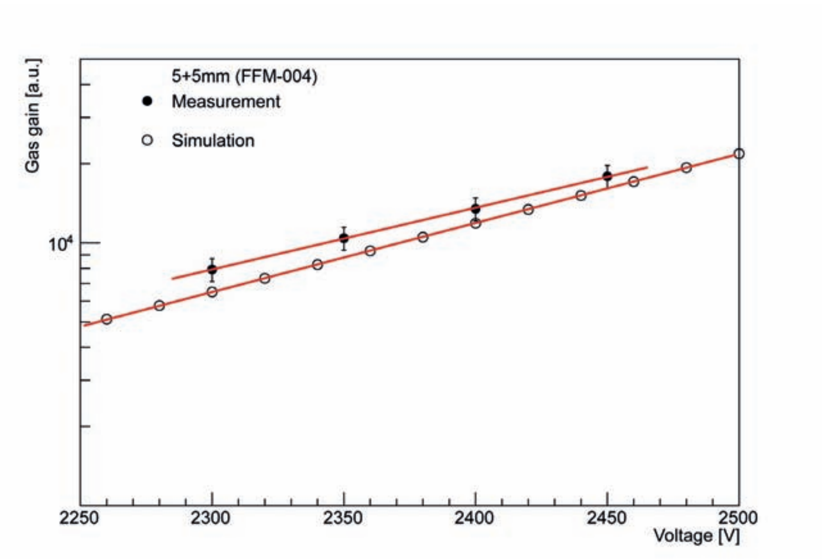

Figure 10.4: Measurement [Dil13] and simulation [Hel13a] of the absolute gas gain for the generation III 5+5 mm prototype (FFM-004) depending on the applied high voltage. The measurement has been performed with a gas mixture of Ar/CO_2 (80/20) at an differential overpressure of 600 μbar. The simulation utilizes a penning transfer rate of 37% without overpressure [Hel13a]. The red lines indicate exponential fits to the data [Dil13].

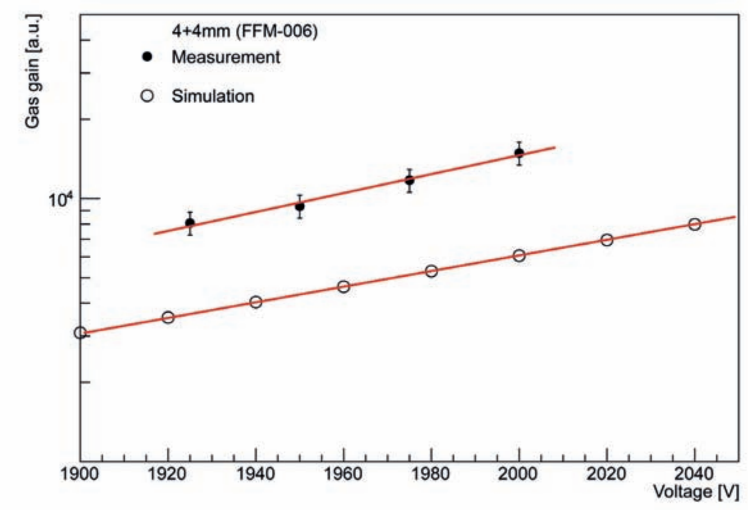

Figure 10.5: Measurement [Dil13] and simulation [Hel13a] of the absolute gas gain for the generation III 4+4 mm prototype (FFM-006) depending on the applied high voltage. The measurement has been performed with a gas mixture of Ar/CO_2 (80/20) at an overpressure of 610 μbar. The simulation utilizes a penning transfer rate of 37% without overpressure [Hel13a]. The red lines indicate exponential fits to the data [Dil13].

properties of the further used SPADIC read out device (see chapter 8) a high voltage setting can be derived to use the dynamic range of the SPADIC in an optimal way.

10.2.2 Uniformity of the Relative Gas Gain with Full Size Prototypes

To verify the homogeneity of the gas gain taking the bulging of the entrance window into account a position dependent scan of the relative gas gain has been carried out. By assuming a constant primary current I_P in equation 10.1 the measured anode voltage directly represents the relative gas gain only modified by a constant factor. Figure 10.6 depicts the measured anode wire current of the full-size generation IV prototype with the 4+4 mm geometry being irradiated with the ^{55}Fe source. The used gas mixture is Ar/CO_2 (80/20). The x- and y-axis represent the position of the ^{55}Fe source in front of the prototype, the color-coded z-axis depict the measured current in nA at a given position. The applied high voltage was set to 1600 V and the differential overpressure has been set to 43±1 μbar [Bal13].

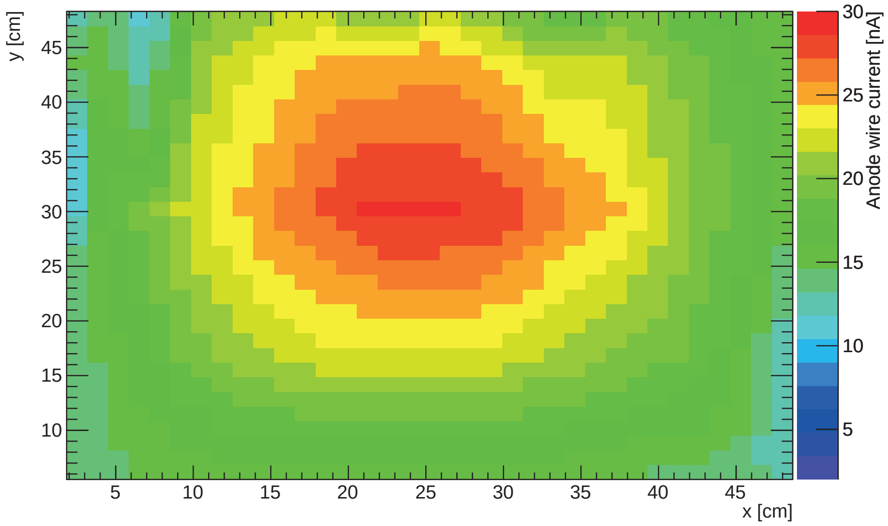

Figure 10.6: Measured anode wire current (color coded) on the full size 4+4 mm (FFM011) at 43±1 μbar differential overpressure and 1600 V applied high voltage [Bal13].

The shape of the distribution shown in 10.6 reflects roughly the inverse shape of the mechanical simulation when overpressure is applied (see chapter 9.5 especially figure 9.12). This measurement procedure is sensitive to any change in the absolute gas gain which enables it to be utilized to check any prototype or later final MWPCs for anomalies [Kra06]. During the construction of the FFM010 prototype three contiguous anode wires have been damaged and need to be repaired. The left part of figure 10.7 depicts the resulting scan on this prototype. The area of the damaged wires modify the electric field configuration and lead to the visible inhomogeneities (red band). The right part of 10.7 shows the scan after the anode wires have been repaired.

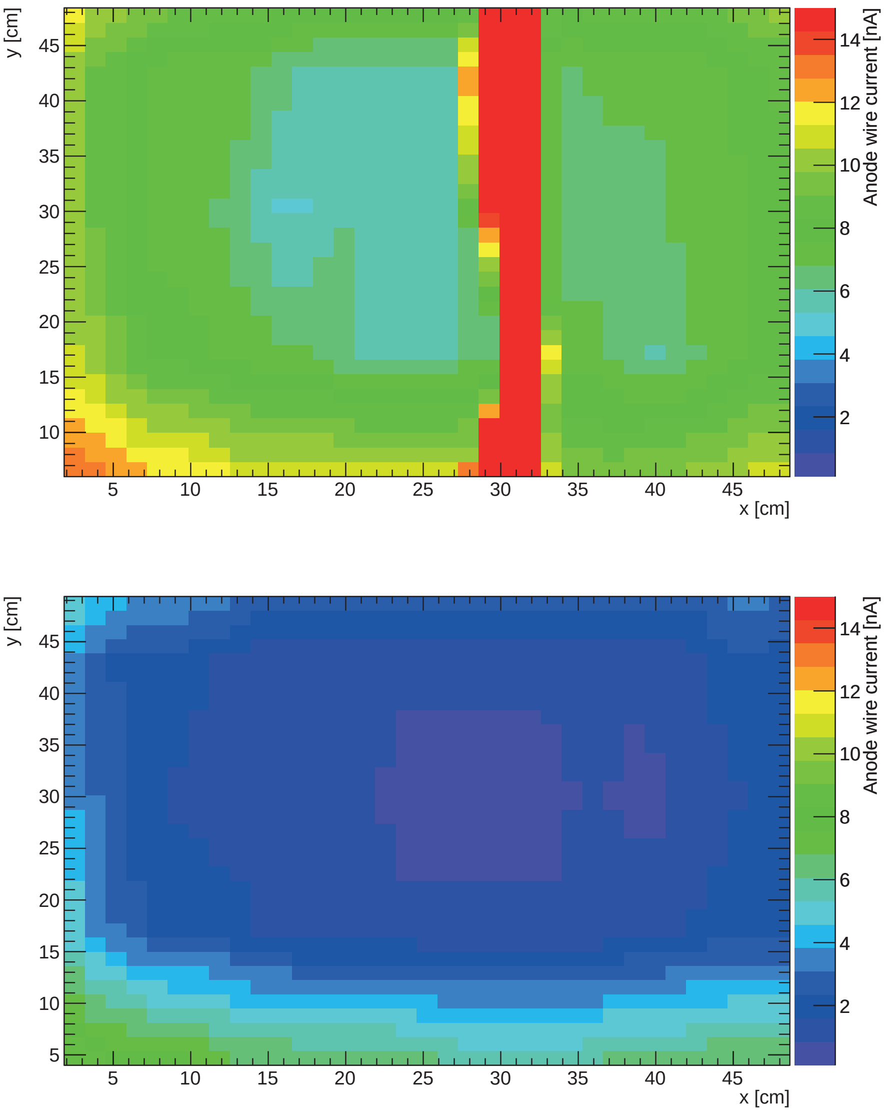

Figure 10.7: Position-dependent scan of the relative gas gain of the FFM-010 prototype at ≈400 μbar and 2000 V anode wire voltage. In the top figure the damaged anode wires show up as a resulting band of higher gas gain. The lower plot depicts the same prototype with same conditions and repaired anode wires [Bal13].

10.3 Energy Resolution

The characteristics of the total deposited charge inside the MWPC is essential for the purpose of particle identification (see chapter 12.4) in a TRD. Therefore the energy spectrum of a ^{55}Fe source has been recorded in lab measurements. According to the width of the measured spectrum conclusions on the energy resolution of the used MWPC prototype can be drawn [Dil13].

The generation III prototypes FFM-004 and FFM-006 have been equipped with a SPADIC read-out chain and irradiated with a ^{55}Fe source. The raw signal digitized by the SPADIC has been noise corrected with a covariance matrix based algorithm (see chapter 12.2 and especially 12.2.1).

The signal amplitudes of the time bin with the maximal value in the noise corrected SPADIC v0.3 signal have been summed up and filled into a histogram, so that one entry in the energy spectrum is represented by this value. According to the efficient performance of the correction algorithm and the very low electric noise in the used laboratory environment no further cluster finding is necessary to obtain this energy spectrum. This measurement has been performed at different high voltage settings to identify the optimal conditions for the energy resolution of the MWPC prototype. The limiting factor in this procedure is the dynamic range of the SPADIC v0.3 read out chip. The high voltage settings have been sufficiently large to generate processable raw signals and small enough to not generate overshoots and overflows in the SPADIC.

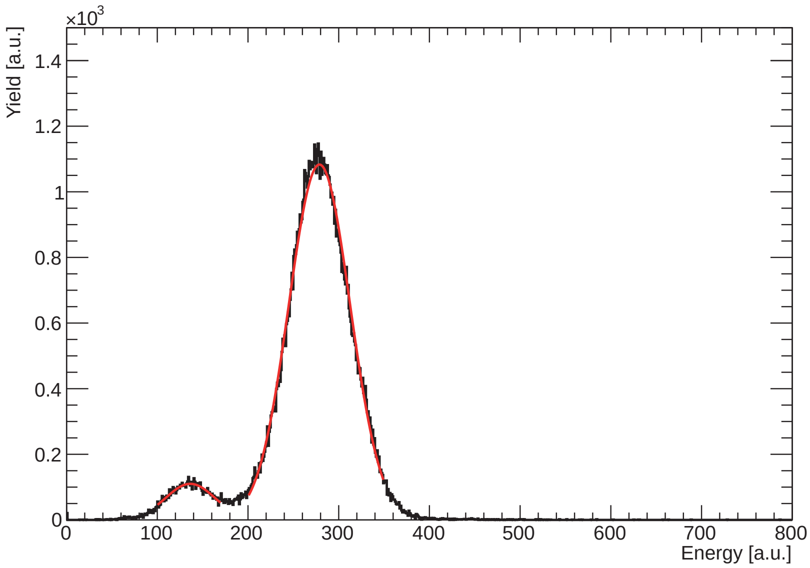

Figure 10.8: Unscaled energy spectra (deposited charge) measured with the 4+4 mm geometry generation III prototype FFM-006 irradiated with a ^{55}Fe source. The fit of the two Gauss functions to the argon escape and ^{55}Fe-K_α is shown as red line [Dil10].

The spectra obtained with the described method is shown in 10.8 based on ≈100.000 recorded events. The sum of the signal amplitudes are shown on the x-axis representing the total deposited charge, which is directly correlated with the initial energy. At a value of ≈ 130 [a.u.] the maximum of the argon escape distribution is located, at ≈ 280 [a.u.] the distribution for the Fe-K_α can be found. The lines are broadened with a Gaussian shape according to the energy resolution of the utilized MWPC. The two peaks are fitted with two separate gauss distributions and the corresponding parameters amplitude, σ and mean position of the gauss function are extracted. Figure 10.8 also contains the two Gaussian fits drawn as red lines. With the parameters mean and σ the relative energy resolution can be calculated via:

$$\Delta E_{relative} = \frac{\sigma}{Mean} \tag{10.5}$$

Table 10.1 shows the parameters of the measurement shown in figure 10.8 and the resulting energy resolution. The given errors are the statistical errors obtained via the fitting procedure.

Spectral line	Fit Parameter			Energy resolution
	Amplitude	σ	Mean	
argon escape	110.02±1.99	27.31±0.80	136.40±0.53	20.02%±0.51%
Fe-K_α	1083.21±4,76	33.75±0.11	278.78±0.12	12.11±0.03%

Table 10.1: Fitted parameters of the Gauss function and the resulting relative energy resolution of the 4+4 mm geometry generation III prototype FFM-006 [Dil13].

The relative energy resolution is translated in an absolute energy resolution by multiplying with the actual value of the regarded energy of the spectral line:

$$\Delta E_{absolute} = \Delta E_{relative} \cdot E_{spectral} \tag{10.6}$$

The position of the Fe-K_α spectral line is 5.9 keV, which leads to an absolute energy resolution of:

$$\Delta E_{absolute} = 12.11\% \cdot 5.9\,\text{keV} = 0.71\,\text{keV} \tag{10.7}$$

For scaling and calibration of the energy spectra are weighted with their actual energies:

$$\alpha_{scaling} = \frac{E_{^{55}Fe-K_\alpha} - E_{argonescape}}{\mu_{^{55}Fe-K_\alpha} - \mu_{argonescape}} \tag{10.8}$$

The position of the argon escape peak is at 2.9 keV, which finally leads to a scaling factor for the given setup:

$$\alpha_{scaling} = \frac{5.9\,\text{keV} - 2.9\,\text{keV}}{278.78 - 136.4} = 0.021 \tag{10.9}$$

This value is only valid for the used setup of the presented measurement. This takes voltage setting, used gas mixture, signal extraction and clustering algorithm into account.

This procedure has to be redone for any change in the used setting.

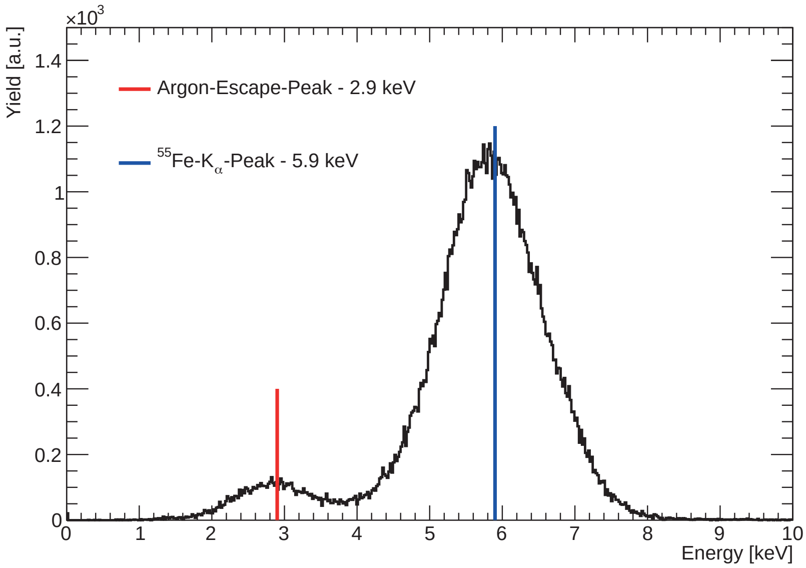

Figure 10.9: Energy calibrated spectrum of the 4+4 mm geometry generation III prototype FFM-006. The Fe-K_α (blue) and argon escape (red) positions are marked with lines [Dil10].

Figure 10.9 shows the energy calibrated (scaled) spectrum for the 4+4 mm geometry generation III prototype FFM-006. The fitted position of the spectral lines are marked as red and blue lines. To study the energy resolution for different high voltage settings, multiple measurements have been performed and the relative energy resolution has been derived with the described procedure, where all examined prototypes showed comparable results.

Figure 10.10 depicts the resulting relative resolutions for the energy using the Fe-K_α spectral line for the 4+4 mm and 5+5 mm generation III prototypes using a gas mixture of Ar/CO_2 (85/15) and Ar/CO_2 (80/20) with different applied high voltage settings. The obtained values for the resolutions are, depending on the utilized prototype, between 8% and 12%. The propagated statistical errors are smaller than the used markers inside the plot. Studies on the systematical errors will be available with modified setups using the SPADIC 1.0. According to the limited dynamic range of the SPADIC v0.3 and due to the resulting limited possible configurations on the high voltage and the gas gain respectively only the presented amount of measurements could be performed. The resolution also depends on the choice of the gas mixture. For this in lab measurements only a mix of argon and carbon dioxide could be used, although the future experiment will use xenon instead of argon.

The presented measurements concerning the energy resolution have been done in a setup that fixes the position in x and y of the measurement. According to the expected bulging of the entrance window of the full size generation IV prototypes a position dependent

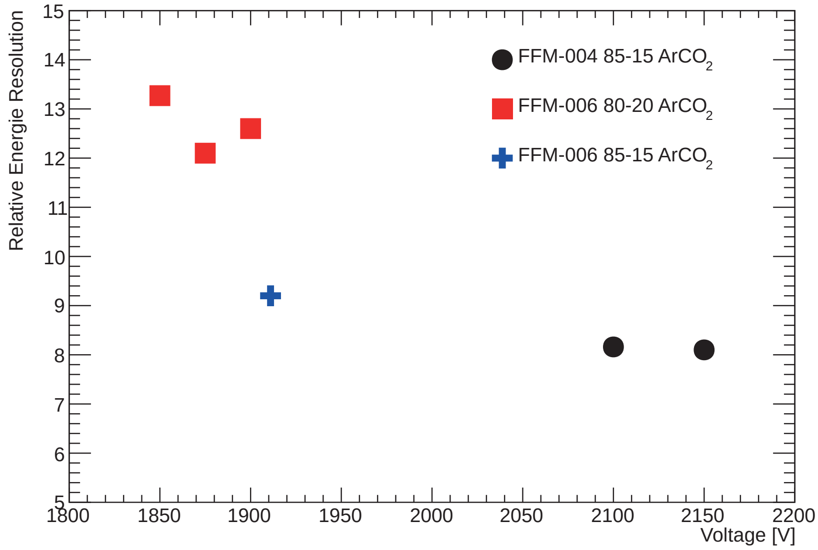

Figure 10.10: Resulting energy resolution for the 4+4 mm and 5+5 mm generation III prototypes using a gas mixture of Ar/CO_2 (85/15) and Ar/CO_2 (80/20) depending on the applied high voltage [Dil10].

---

determination of the energy resolution has to be performed additionally.

11 Test Beam Campaigns

To test the performance of the generation III and IV prototypes two campaigns at the experimental area T9 of the CERN Proton Synchrotron (PS) have been accomplished. The CERN PS delivers a secondary particle beam of mixed electrons and pions at momenta of 2 GeV/c up to 15 GeV/c [DFH+98]. This allows a simultaneous measurement of these particles for the quantification of the electron / pion separation capabilities for the employed prototypes. The generation III prototypes have been tested in the 2011 test beam campaign, whereas the generation IV prototypes were studied in beam in 2012.

11.1 Test Beam Campaign 2011

The 2011 test beam campaign took place from 17.10.2011 until 30.10.2011 with the aim of testing the small size prototypes for their electron-pion separation capabilities in combination with a variety of radiator prototypes. Furthermore their pad response function was investigated. The generation III prototypes FFM004, FFM005 and FFM006, together with the prototype FFM002 of the generation II for comparison, have been read out with the SPADIC v0.3. In total ≈244 GB of raw data have been recorded with overall ≈27,913,600 events in 204 runs corresponding to a 153h 24min 25s of data taking time. The campaign has been performed in cooperation with prototypes for the RICH and the TOF CBM detector subsystem and together with TRD development groups from Münster, Bucharest and Dubna. The schematic layout of the test beam setup is presented in figure 11.1, a photo from top is illustrated in figure 11.2 and a detailed photo of the prototypes from IKF Frankfurt are shown in figure 11.3.

In beam direction, the first detectors are two Cherenkov counters (*Cherenkov 1+2*) which are used for reference particle identification in conjunction with the Pb-glass calorimeter (see chapter 12.1) at the end of the beam line. Subsequent to the Cherenkov counters a plastic scintillator (*Sc 1*) and a fiber tracker (*FT*) used as trigger detectors have been placed, followed by the RICH prototype. In total 12 TRD prototypes have been placed downstream of the RICH prototype. Two of them are with dedicated drift region read out via FASP and MADC from the Bucharest group followed by four prototypes with also drift and SPADIC v0.3 read out provided by the IKP Münster. The four prototypes without drift by the IKF Frankfurt follow up in the mentioned sequence. Two prototypes of the Dubna group are most downstream and read out with a PASA chip and the MADC system. After the TRD prototypes two resistive plate chambers (*RPCs*) complete the line up of to be tested prototypes. In the end of the beam line a second plastic scintillator for triggering and the Pb-glass calorimeter for reference PID are placed.

All tested TRD prototypes have been served by a common gas system. The used gas mixture for all measurements was Xe/CO_2 (80/20). For initial flushing pure Argon has been used. The monitored contamination with oxygen inside the gas system was in the order of less than 100 ppm.

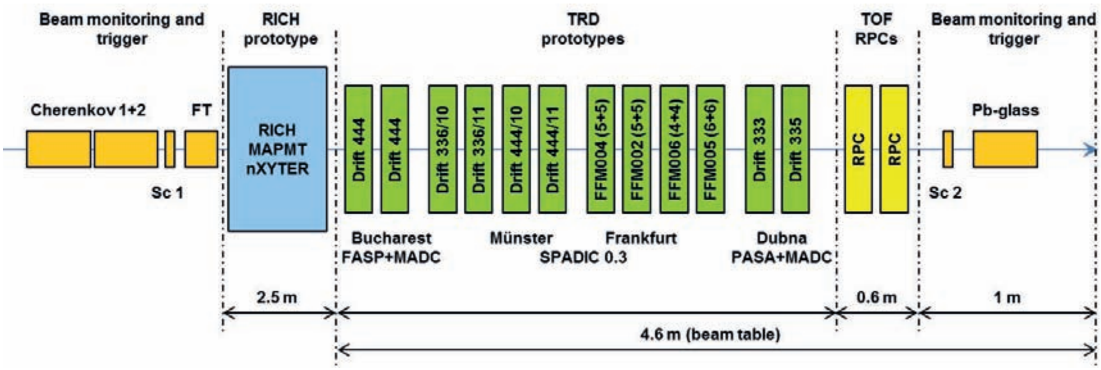

Figure 11.1: Schematic drawing of the setup during the test beam campaign 2011 (not to scale) [FS12].

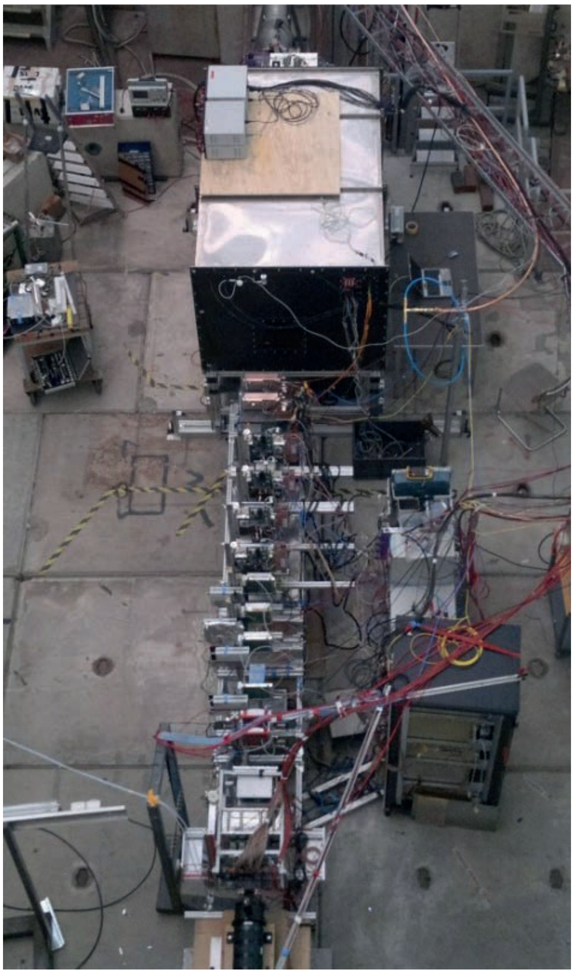

Figure 11.2: Bird's-eye view photo of the setup 2011 [FS12].

Figure 11.3: Photo of the generation II and III Frankfurt prototypes equipped with the ALICE type radiator.

A schematic overview of the used data acquisition (DAQ) system is shown in figure 11.4. The investigated prototypes have been read out with SPADIC rev 0.3 chips connected with SUSIBO boards to the DAQ system. Informations from trigger and particle identification detectors have been packed and synchronized in a multi-branch system (MBS) [R. 00]. Data storage and publishing to the online monitoring system has been handled by the Data Acquisition Backbone Core (DABC) [J.A09].

The ROOT based [R. 97] *GSI Object Oriented On-line Off-line system Go4* [J.A13] has been used for online monitoring. A simple noise cancellation algorithm based on the assumption that the two lowest channels are not hit and carry no signal has been used to average the noise and subtract it from all channels. With this cleaned signals further basic monitoring has been performed. A simple overlay of all signals has been used to monitor the raw and cleaned signal. A screenshot of one of the first events of the 2011 beam time in the Go4 online monitoring system is shown in figure 11.5. By correlating the maximum amplitude of each MWPC to the others a rough alignment could be achieved. In the last analysis step of the online monitoring all information of all other detectors in the DAQ system is available, which allows already for electron-pion separated spectra of deposited charge using the pre-cleaned raw data and a simple three-pad fixed clustering algorithm.

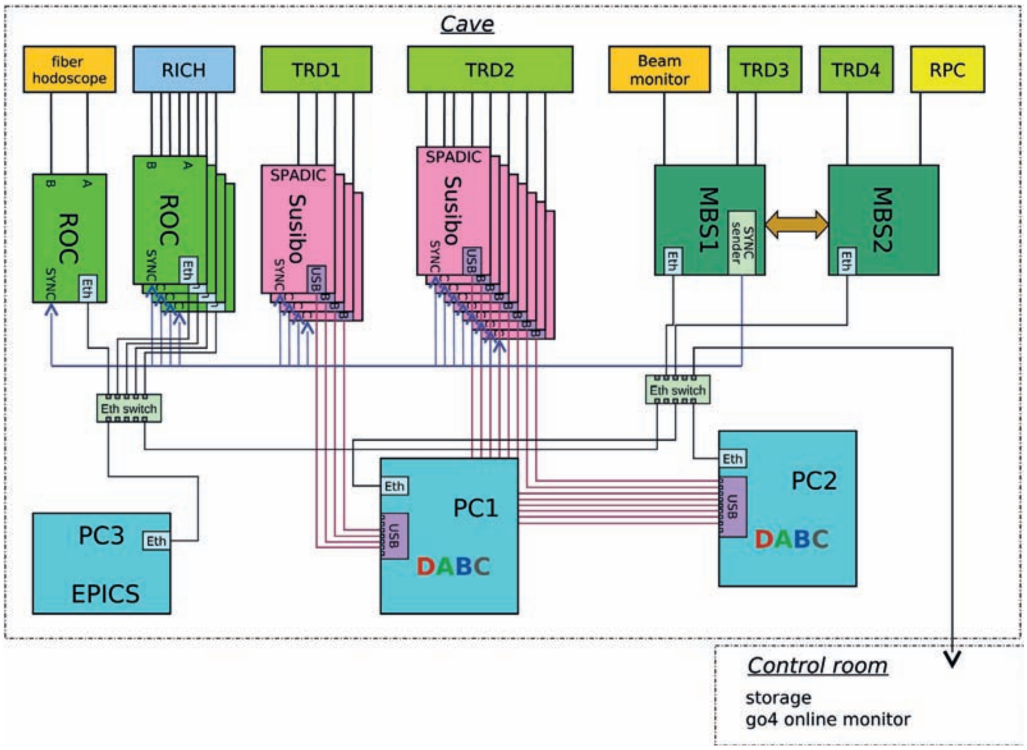

Figure 11.4: Schematic layout of the data acquisition system used at the 2011 test beam campaign [Lin12]

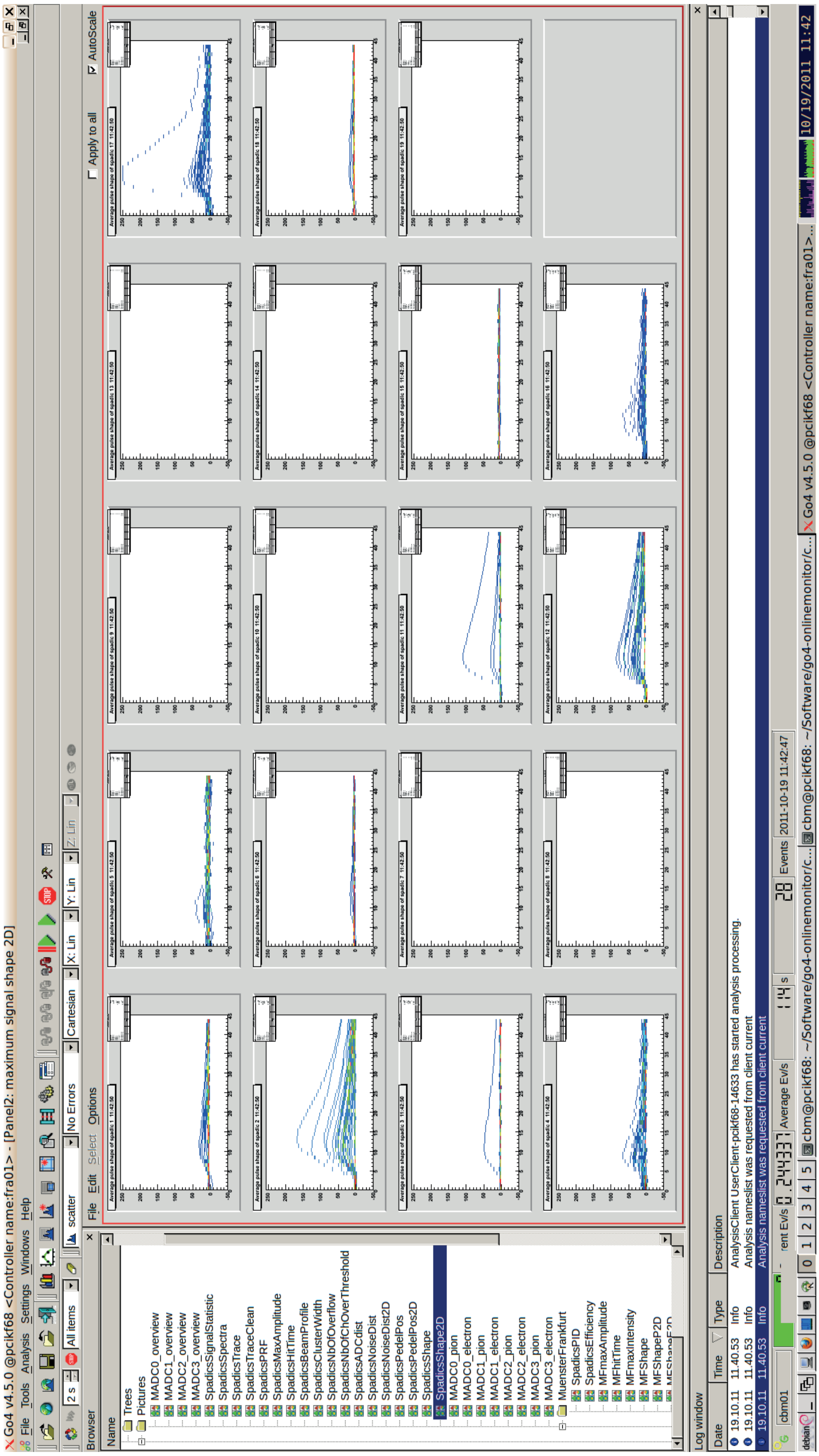

Figure 11.5: Screenshot of the raw signal of the first real events taken with the TRD prototypes in the Go4 online monitoring system at the test beam campaign 2011.

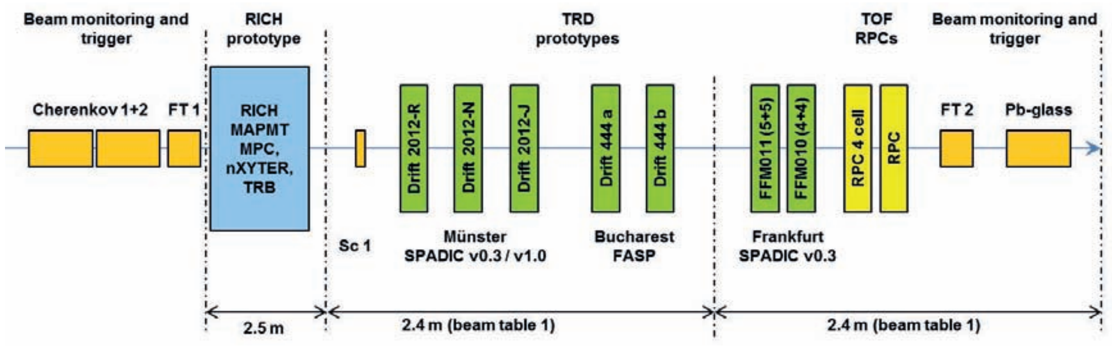

Figure 11.6: Schematic drawing of the setup during the test beam campaign 2012 (not to scale) [FS13]

During the 2011 test beam campaign a variety of trigger setups have been used. All trigger configurations sensitive to particles passing through the beam line require at least a signal over a given threshold in the plastic scintillators. Additionally to these triggers sensitive to particles, a periodic trigger in the PS spill pause has been applied to record empty events, which is used for baseline and noise subtraction in the analysis.

After setting up all required systems the TRD prototypes have been tested with developed radiator prototypes at a fixed beam energy of 3 GeV followed by an energy scan with the ALICE type reference radiator at energies of 2, 4, 6, 8, and 10 GeV. The observed noise level in the online monitoring was low although a small break down of the baseline at later time bins of the used SPADIC v0.3 has been recorded, which could be compensated in the offline analysis with the used noise cancellation algorithm (see chapter 12.2.1).

11.2 Test Beam Campaign 2012

The 2012 test beam campaign took place from 28.10.2012 to 11.11.2012 with the aim of testing the full size generation IV prototypes with a set of potential radiator candidates for the final experimental setup. The prototypes FFM010 and FFM011 have been integrated in a common setup at CERN T9 together with a prototype of the RICH detector system, two prototypes of the TOF RPC and in total seven TRD prototypes (three from the Münster group, two from Bucharest, and two from IKF). The setup of the participating detector systems is similar to the one used in 2011. The schematic layout is presented in figure 11.6, a photo of the setup is shown in figure 11.7 and a detailed photo of the full size prototypes from IKF Frankfurt is shown in figure 11.8.

The sequence of detectors in the beam line starts with two Chernenkov counters (*Cherenkov 1+2*) for reference particle identification (PID) followed by a fiber tracker (*FT 1*) which determines a position information of the passing particle. A second fiber tracker (*FT 2*) is placed at the end of the beam line. With both fiber trackers it was assumed to get an information on the particle trajectory and so on the exact point of transition. Unfortunately this was not possible due to a malfunction of *FT 2*. A plastic scintillator (*Sc 1*) was placed between the RICH prototypes and the first TRD prototype as a trigger detector. In total seven TRD prototypes have been tested: three prototypes with drift region, support

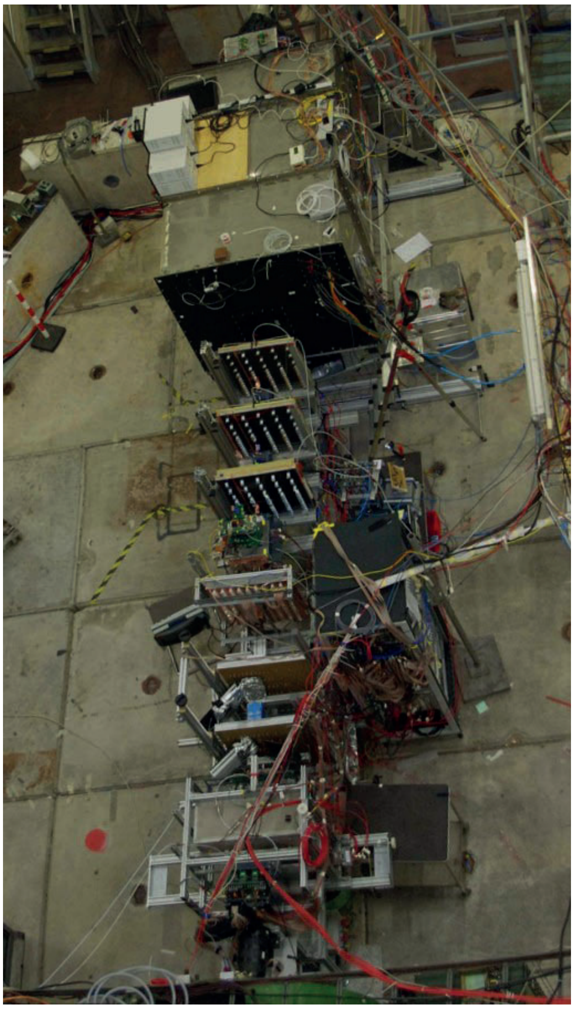

Figure 11.7: Bird's-eye view photo of the setup 2012 [Ber12].

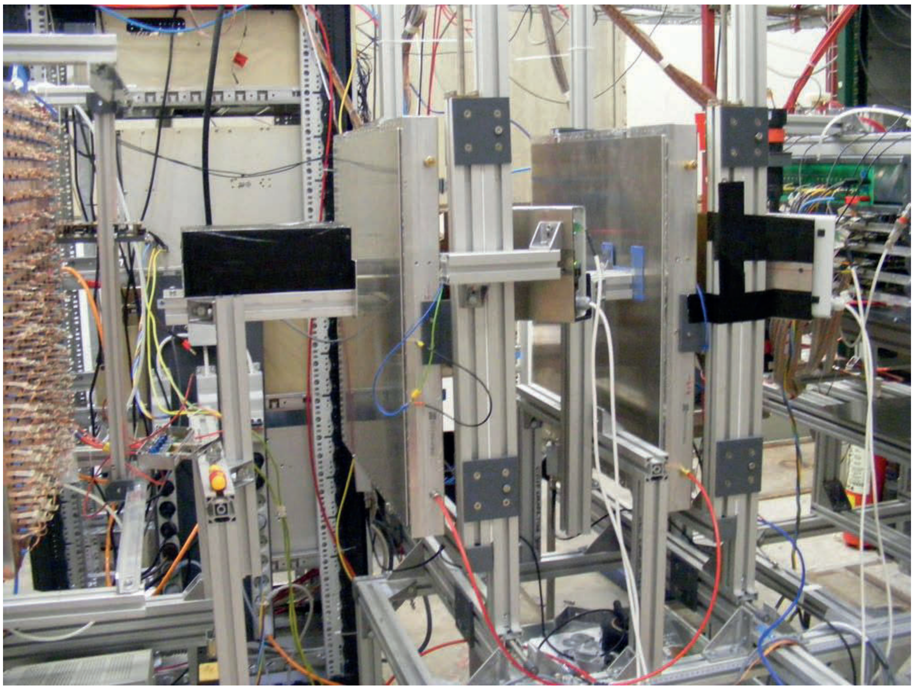

Figure 11.8: Photo of the full size generation IV prototypes in the beam line (still with protection shield in front of the fragile foil based entrance window).

structure for the entrance window and SPADIC based read out by the IKP Münster, two prototypes with FASP by the Group from Bucharest, and the two prototypes of the IKF Frankfurt also based on SPADIC read-out. Two RPC prototypes closed the sequence of prototypes. The last detector in the beam line was a lead glass calorimeter for reference PID as in 2011.

As in the previous test beam campaign all tested TRD prototypes have been supplied by a common gas system. The gas mixture in all measurements was Xe/CO_2 (80/20). For initial flushing pure argon has been used. The contamination with oxygen has been monitored.

A schematic overview of the data acquisition (DAQ) system in the 2012 test beam campaign is shown in figure 11.9. Data from the fiber tracker and the RICH detectors are read-out with read out reciver cards (ROC). It was planed to read out the SPADIC based TRD prototypes with the SPADIC v1.0, but due to the lag of functional hardware it was only possible to read out one of the Münster detectors for prove of principle test in a small number of runs. For the majority of runs and for the Frankfurt prototypes the SPADIC v0.3 read-out chain has been used. For the beam monitoring and trigger detectors, the FASP based TRDs and the RPC prototypes the data have been packed and shipped via an MBS system.

Connected to the DAQ system the Go4 online monitoring system used in the 2011 campaign has been extended and improved. A noise cancellation scheme based on the covariance calculation (see chapter 12.2.1) has been implemented as well as an adapted

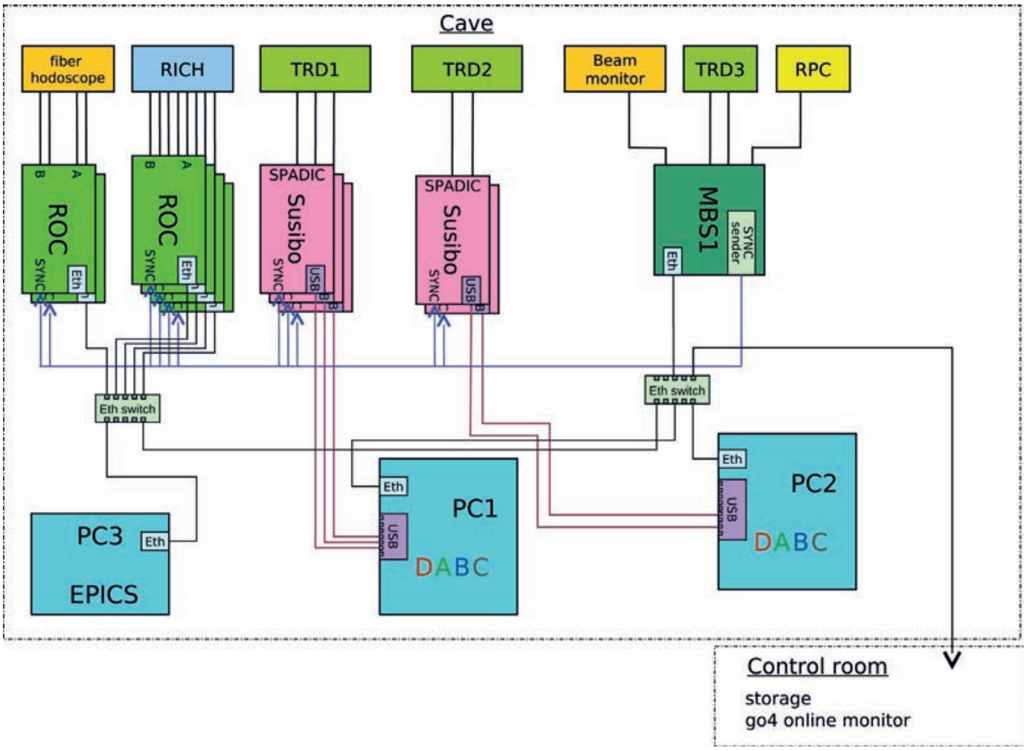

Figure 11.9: Schematic layout of the data acquisition system used at the 2012 test beam campaign [LB13].

alignment scheme. A screenshot of one of the first taken events is shown in figure 11.11.

The accomplishment of the 2012 test beam campaign was driven by a systematic radiator studies. Additionally the particle momentum dependencies have been studied at beam energies of 2, 4, 6 and 8 GeV. Compared to the campaign in 2011 an enhanced noise level was observed, which can be seen in a broader base line band in 11.11.

11.2.1 External conditions 2012

One of the aims of the 2012 test beam campaign was to prove the functionality and controllability of a thin foil-based entrance window. During the test beam a set of external conditions have been recorded using the EPICS [PSK13] system as well as a log book. Figure 11.10 depicts the temperature, the absolute ambient pressure, the humidity and the differential overpressure inside the FFM011 prototype. These values have been obtained by measuring stations directly inside the T9 experimental area as well as at the gas area outside the experimental area but inside the east area hall.

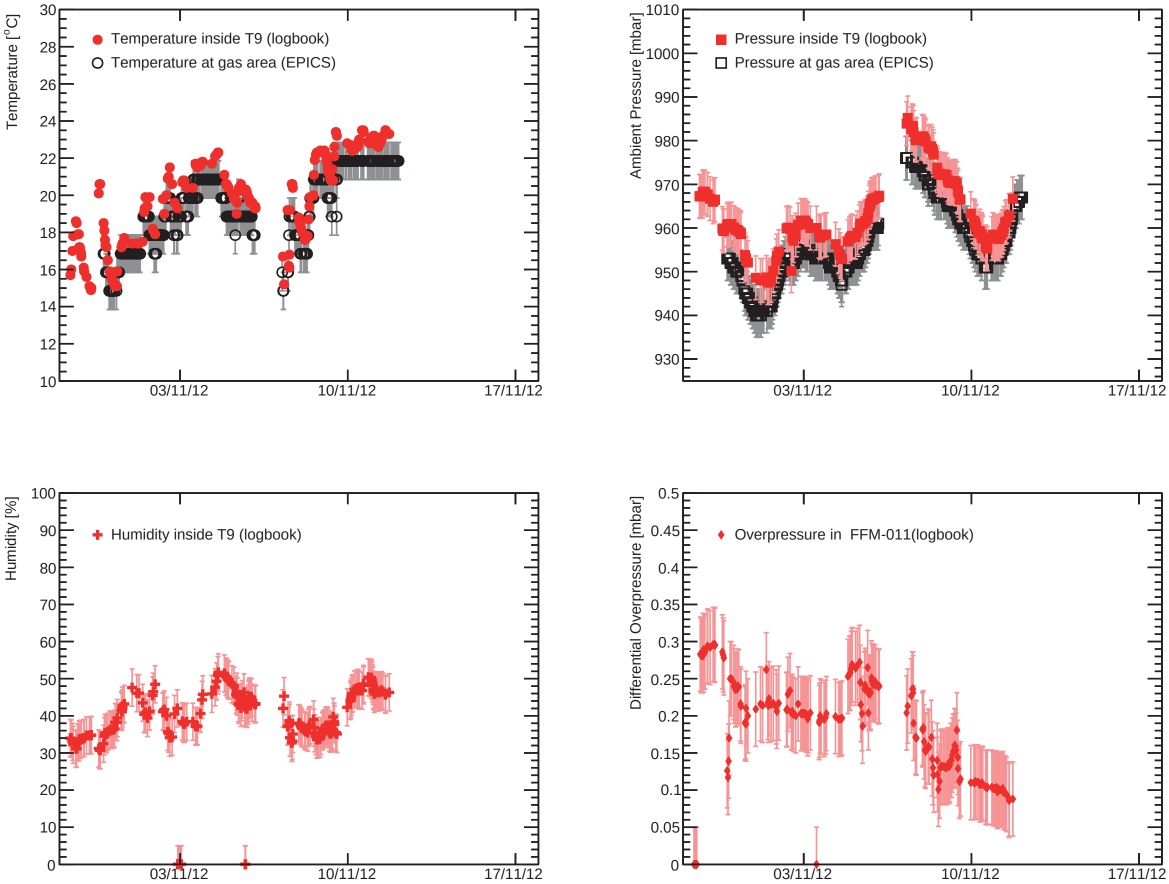

Figure 11.10: Trending ambient conditions during the time of the 2012 test beam campaign: temperature (top left), ambient pressure (top right), humidity (lower left), differential overpressure (lower right) in the gas line of FFM011.

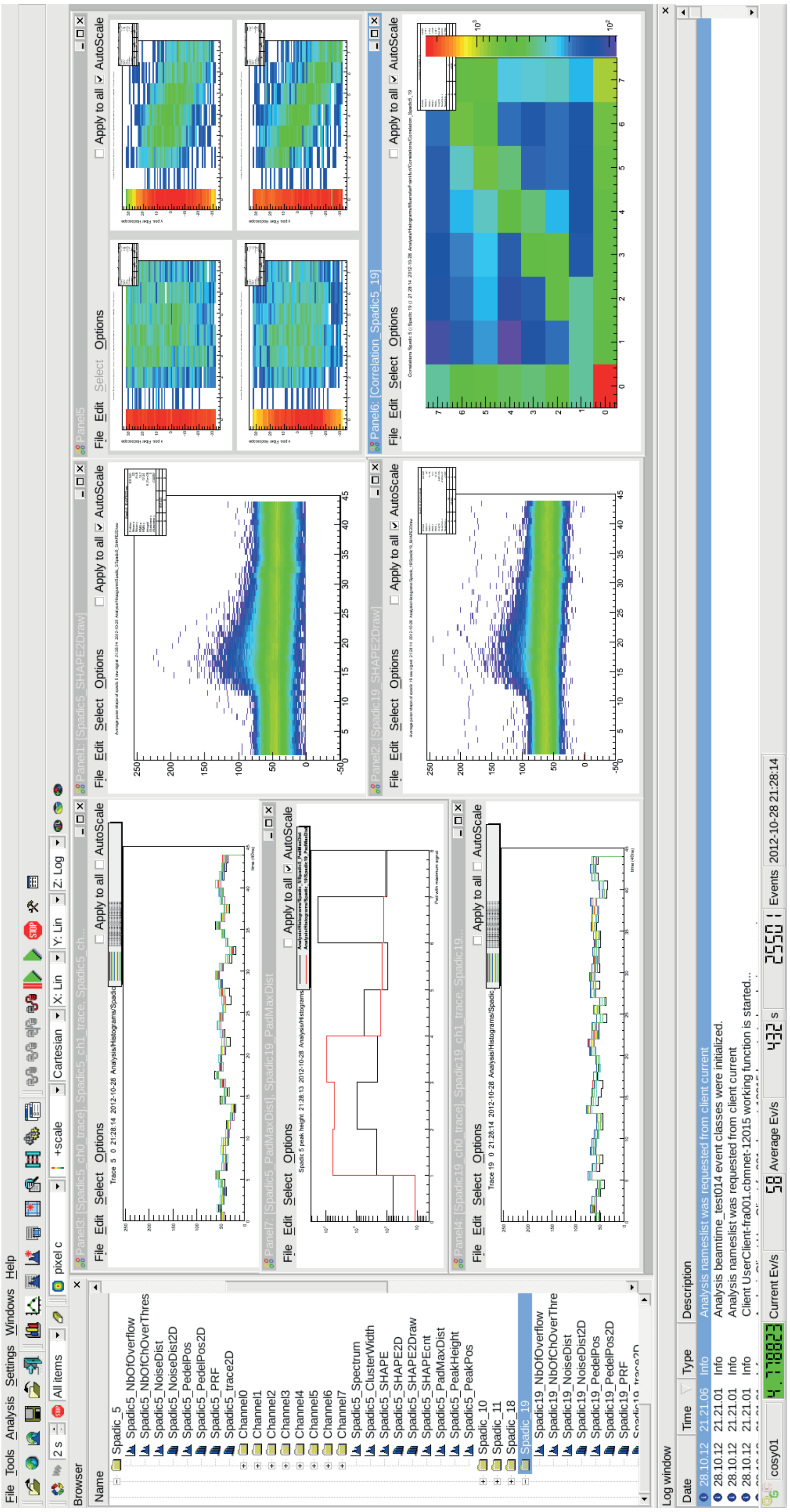

Figure 11.11: Screenshot of the first events in the Go4 online monitoring at the 2012 test beam campaign.

12 Results from the Test Beam Campaigns

In this chapter the analysis performed to quantify the performance of the prototypes and the radiators during the two test beam campaigns in 2011 and 2012 is described. To emphasize the development and the evolution of the examined prototypes the analysis procedures are done equally for all prototypes and reference detectors. In all plots of the following chapter electron and electron related-data is shown in red, pion and pion-related data is shown in black.

12.1 External Particle Identification

Particle identification from independent reference detectors is essential to characterize the performance the prototype detectors. During both test beam campaigns the information from two Cherenkov counters (*Cherenkov 1* and *Cherenkov 2*) and a lead glass calorimeter (*Lead Glass*) combined have been used to distinguish between electrons and pions (see chapter 11.1 and 11.2). This analysis has been performed for all runs of both test beam campaigns.

The raw signals of the three reference detectors are shown in figure 12.1 for run *2110015* of the 2011 campaign exemplary. To perform the particle identification a set of thresholds (*cuts*) has been used to select signal candidates of electrons and pions. Regions in the spectra have been selected for each individual detector where signals of electrons and pions are expected. The red lines in 12.1 indicate the region of expected electrons, the black lines for pions respectively. These thresholds have been chosen such, that the selected samples of electrons and pions are as pure as possible (by giving enough statistics for the present analysis) and to enable the following procedure of quantifying the purity of the samples defined by these cuts.

By making use of all three reference detectors it is possible to determine a particle identification with two of these detectors and analyze the third reference detector. Figure 12.2 shows selected signals for each detector by determining the particle identification with the remaining ones. The spectra of electrons and pions of the Cherenkov 1 counter have been filled with electron and pion signals selected by Cherenkov 2 and Lead Glass, for Cherenkov 2 the particle identification of Chrenkov 1 and Lead Glass have been used and finally for the Lead Glass the information of Cherenkov 1 and 2 has been used.

With this selection clean spectra for electrons and pions for each reference detector were obtained, which allows the determination of the contamination of the selected samples at each cut position in the analysis requiring a particle identification. The clean spectra of electrons and pions have been scaled to fit the maximum of the raw spectra. The panels in the left column of figure 12.3 shows the scaled clean samples and the sum of both in green compared to the raw spectra in blue. The right part of figure 12.3 depicts the ratio of summed up scaled clean samples to the actual raw spectrum. At higher values the ratio suffers from low statistics which results in large errors. The dip at low values for the two

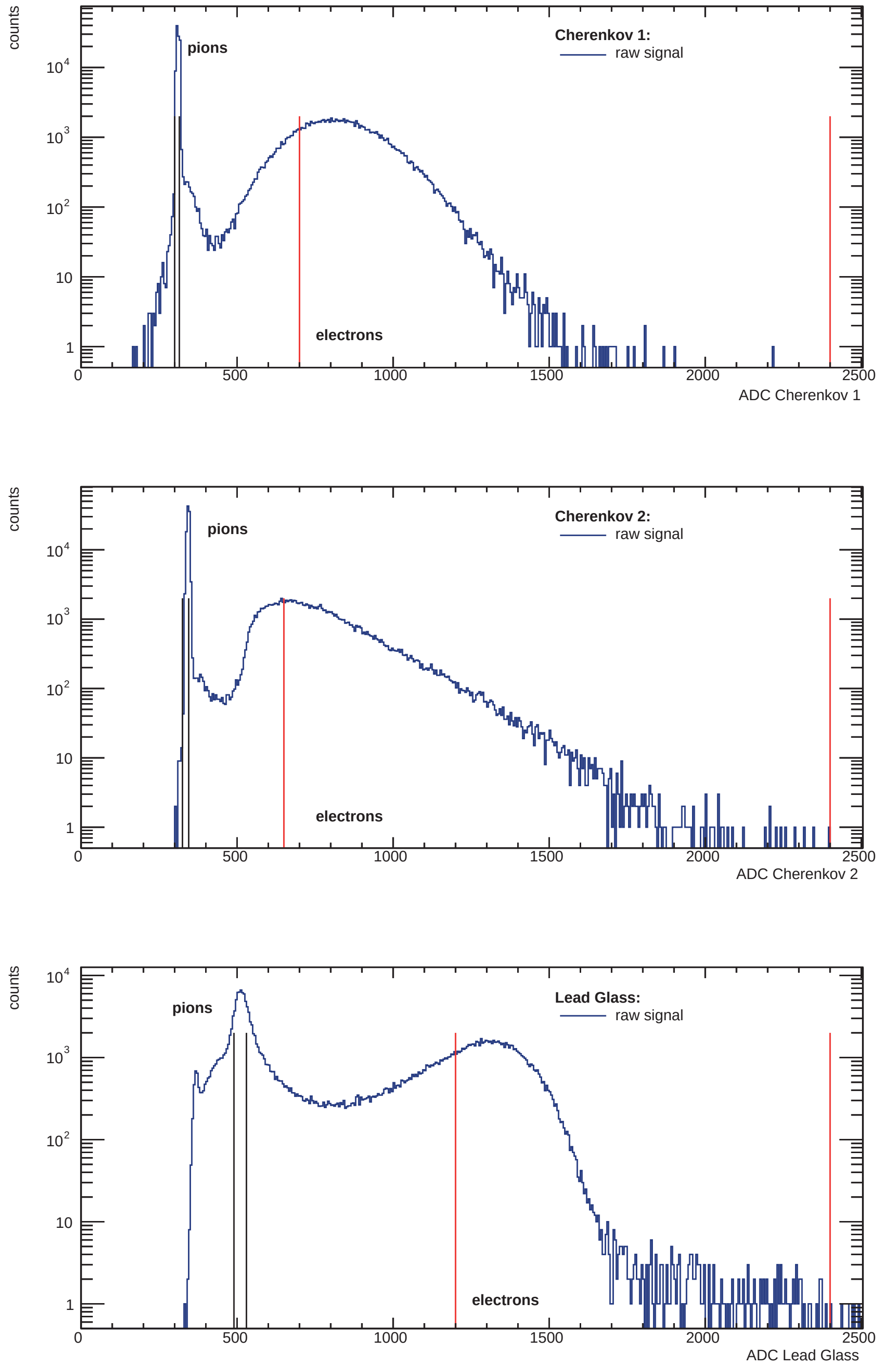

Figure 12.1: Raw spectra of the PiD reference detectors. The lines indicate the cuts used for electrons (red) and pions (black).

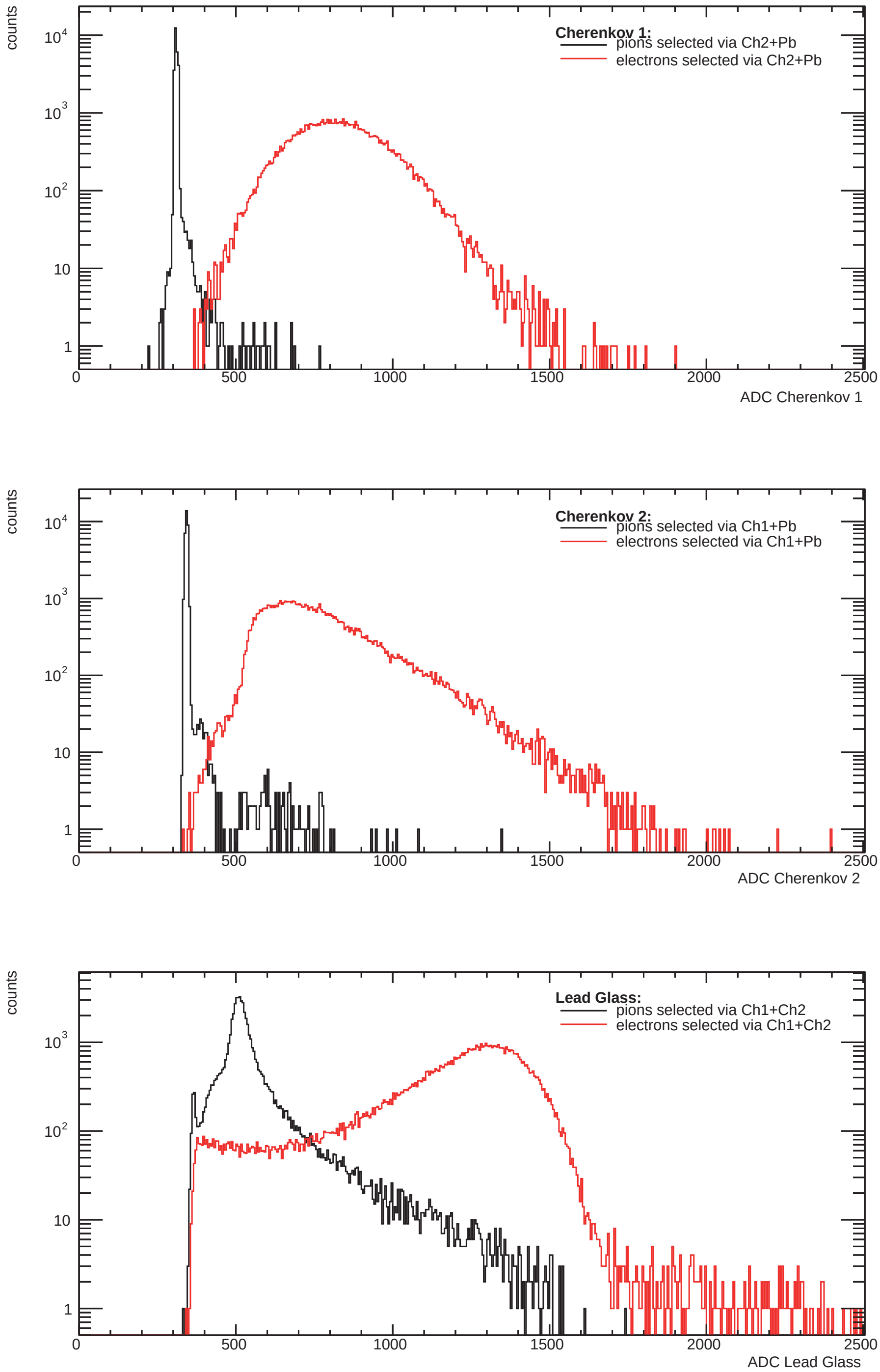

Figure 12.2: Spectra of selected signals for each detector with determined reference particle identification by the other two reference detectors, respectively.

Cherenkov counters is caused by the fact that muons could not be filtered out reliably. Besides this, the ratio shows that the scaled histograms of selected clean electrons and pions describe the raw spectra over a wide range and almost over the complete range.

With the knowledge of the composition of the raw spectra obtained with the reference particle identification detectors the running integral of the electron and pion component can be computed. For electrons, which show up at *high* values in the reference detectors, the integral starts from the upper edge of the spectra and sums up the content for every bin of the histogram going from high values to low values on the x-axis. This running integral is shown as solid red line in the upper panels of figure 12.4. For pions this calculation starts at low values and sums up bin by bin towards higher values on the x-axis. The resulting running integral is shown as a solid black line in figure 12.4 for pions. To determine the corresponding contamination the reverse running integral has also been computed: to obtain the contamination of the pion sample, the electron sample has been integrated from low values to high values, which is shown as dashed red line, and the pion sample from high to low values is shown as dashed black line. This reverse running integral represents the amount of wrong identified particles at a given position in the raw spectra. The right panels of figure 12.4 depict the ratio of correctly identified particles to wrong identified particles at a given cut position for electrons in red and pions in black. With this procedure, the purity of each reference detector used has been obtained.

Using the individual purities of the reference particle identification, two sets of cuts have been prepared for the later analysis of the test beam data. The first set is aimed for a very clean particle identification and only allows a contamination of 1% misidentified particles in each set disregarding the consequently following decreasing in event statistics. If the requested value could not be reached, the minimum in the regarded distribution has been selected. The combination of the individual purities results in an overall contamination of the electron and pion samples. A fraction of $\approx 1 \cdot 10^{-6}$ of the total electron spectra is generated by misidentified pions in the runs with a particle momentum of $3\,GeV/c$ at the 2011 test beam campaign. The pion sample is contaminated with a fraction of $\approx 5.25 \cdot 10^{-6}$ with misidentified electrons in this runs. The second set of *soft* particle identification cuts applies thresholds of maximal 10% misidentified particles and increases the event statistics. The resulting contamination is in the order of a fraction of $\approx 1 \cdot 10^{-3}$ of the total spectra for electrons and pions.

12.2 Signal extraction

The raw signals of the prototypes are digitized and read out with the SPADIC rev. 0.3. These signals are contaminated with noise. To quantify the performance of the prototypes and the raw signals of the prototypes have to be analyzed and a correction algorithm has been developed [Dil13]. Figure 12.5 shows a single event recorded with the SPADIC 0.3. The signal has been generated by an induced pulse on the foil based entrance window. The color code of the shown histograms represents the eight read-out channels of the SPADIC. The x-axis shows the corresponding time bin of the SPADIC read out cycle and the y-axis represents the ADC value of the digitized signal. According to the spread of the baselines and structures at higher time bins, comparing figure 12.5 left and right already reasons a noise correction algorithm.

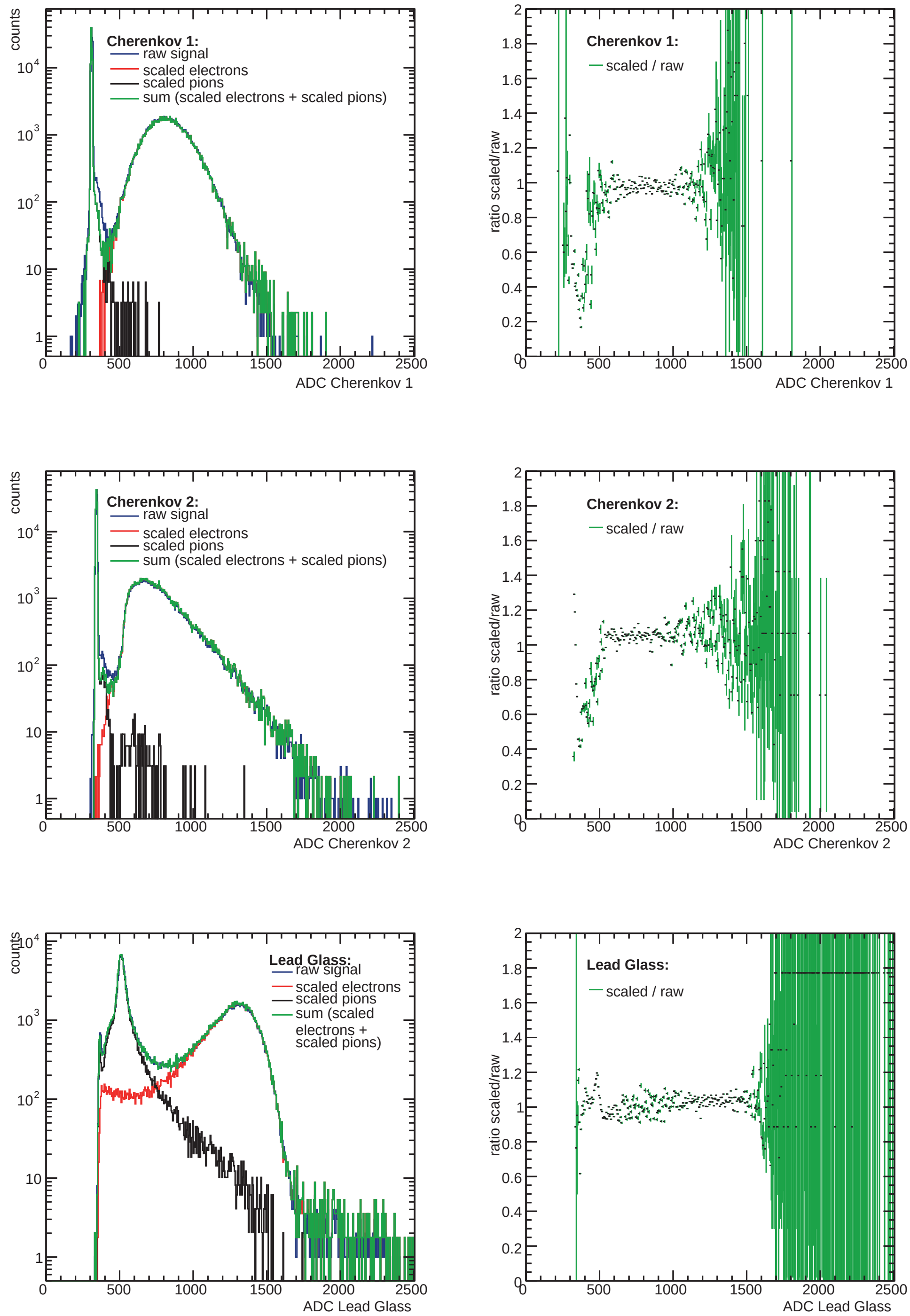

Figure 12.3: Scaled Signals (left) and ratio (right) to the raw spectra of the reference detectors.

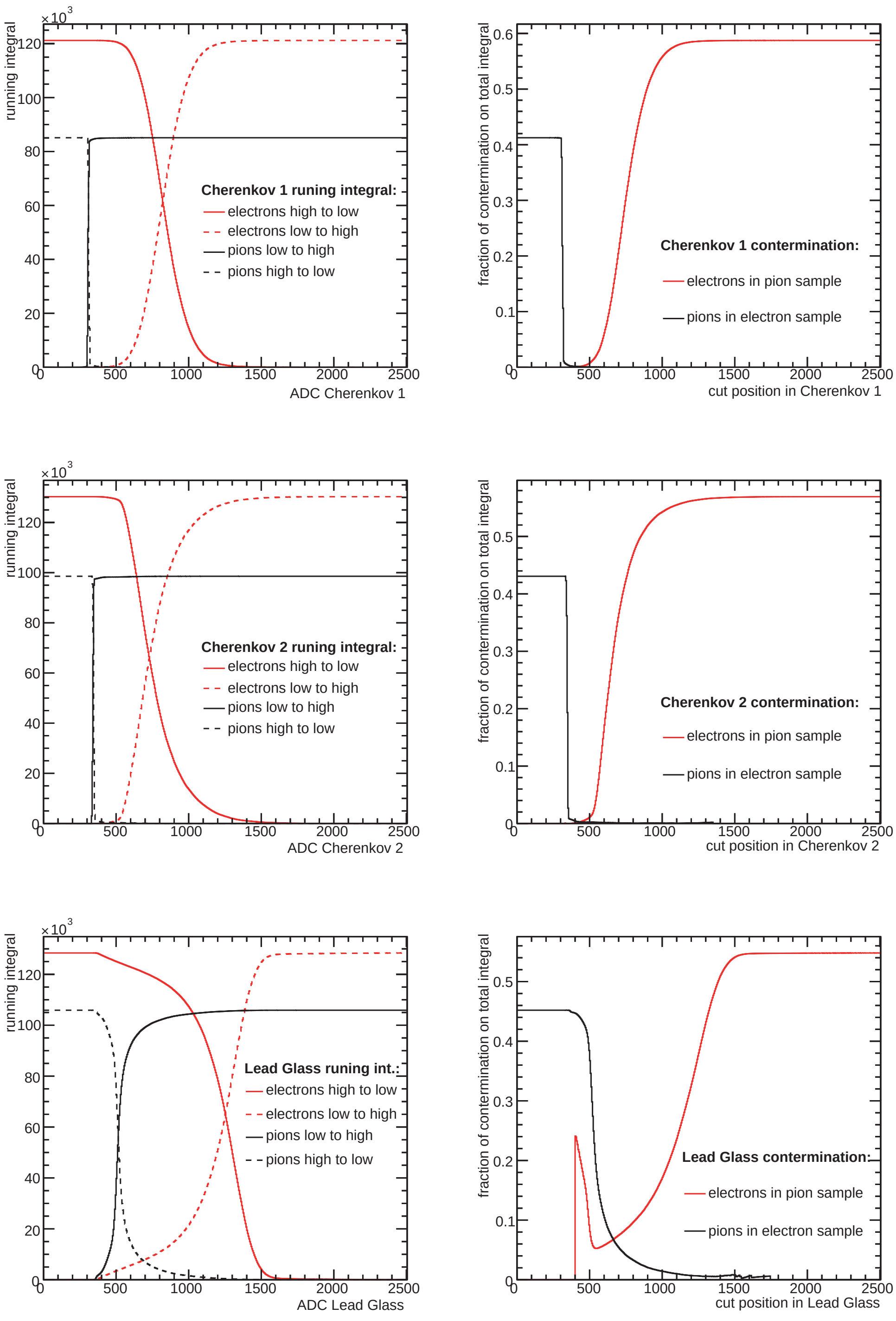

Figure 12.4: Running integrals of scaled signals and fraction of contamination depending on the cut position.

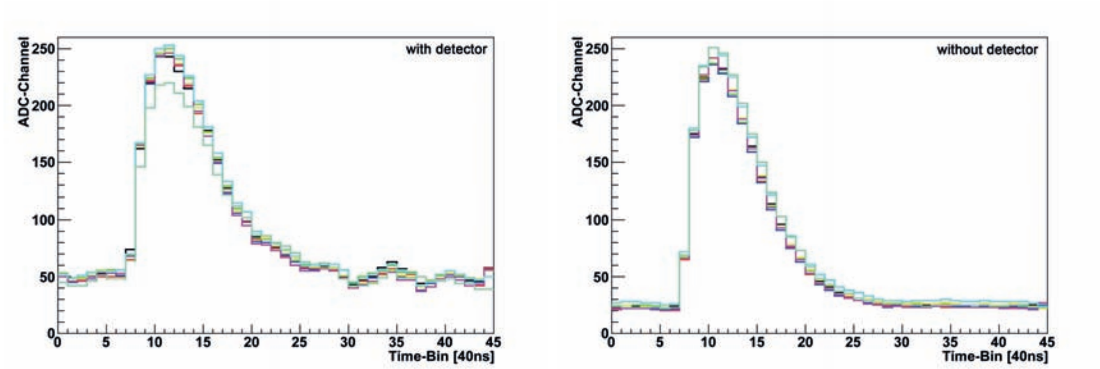

Figure 12.5: Raw signal recorded by the SPADIC. The signal has been generated via a test pulse on the entrance window to mimic a real signal including electronic noise of the prototype on the left, and a test pulse generated directly in the SPADIC without external distortions (compare to figure 8.2) on the right [Dil13].

For comparison figure 12.5 (right) shows a signal generated directly in the read-out electronics injected in the SPADIC read out chip. A marginal separation of the baseline is also visible but the general signal shape is without any disturbing structures. The spread of the baseline is explained with intrinsic differences in the components used for the amplification circuit [AFP09].

The distortions in the signal shape in figure 12.5 (left) all show a similar behavior, which leads to the assumption that this noise is correlated between all eight read out channels. This correlation enables a procedure to correct the signal carrying channels with the noise of the non-signal channels which is described in chapter 12.2.1.

To quantify the contamination of the read out signal with electronics noise, an overlay of 75,000 events injected via the cathode plane into a prototype is shown in figure 12.6. Each time bin of each channel in every event generates an entry in this two dimensional histogram, where the color code represents the yield. The width of the resulting band can be used to determine the spread generated by different baseline values and noise together. To determine the width of the band in figure 12.6 the fourth time bin has been projected on the y-axis. The time bin has been chose such that it is before the rising edge of the signal and so not influenced by the generated signal. The resulting projection is shown in figure 12.7 [Dil13].

The distribution in figure 12.7 has been fitted with a Gaussian distribution, it has a mean position at 50 ADC values and a σ of about 6. The width of this Gaussian distribution used already 5% of the dynamic range of the SPADIC 0.3, which underlines the need of an efficient noise cancellation algorithm. This value can be used to compare to a noise cancellation scheme and quantify its performance.

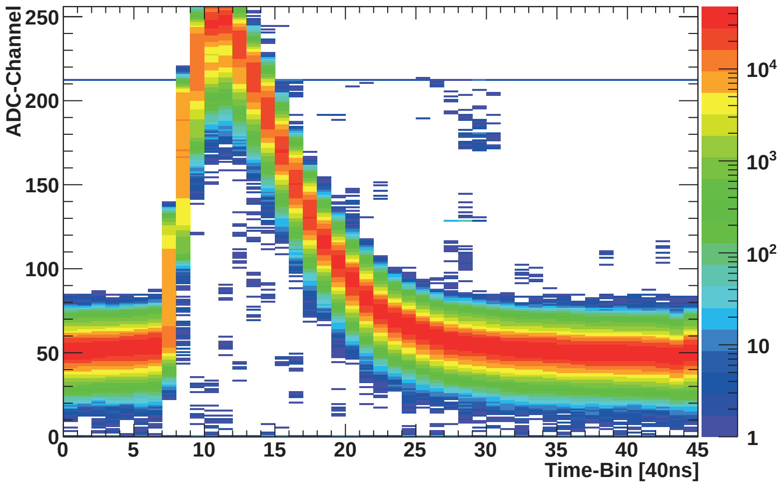

Figure 12.6: Overlay of the noise contaminated read out signal based on 75000 injected events [Dil13].

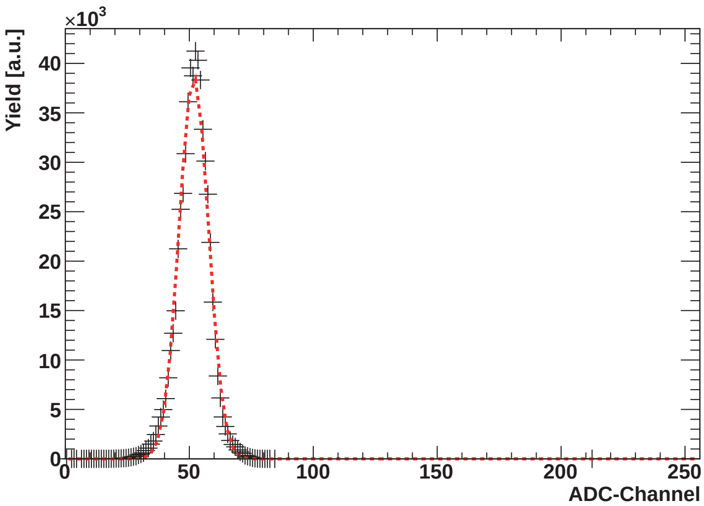

Figure 12.7: Projection of time bin four on the y-axis fitted with a Gaussian distribution [Dil13].

12.2.1 Noise Cancellation Algorithm

According to the considerations of signal extraction a step-wise noise correction algorithm has been developed, which uses steps to correct the spread of the baseline and a dedicated step to cancel correlated noise in the signal carrying channels. The overall sequence of the correction algorithm is shown in figure 12.8.

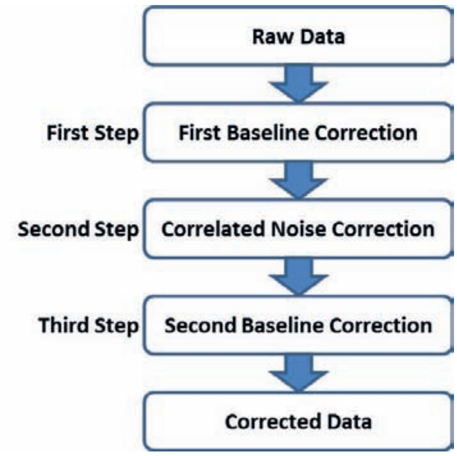

Figure 12.8: Subsequent procedure of noise cancellation [Dil13].

The first step is a correction of the baseline of each individual channel. According to the read-out delay adjustment of the SPADIC the first five to ten time bins of the signal are averaged. The resulting average offset is subtracted from every time bin of this channel. This value represents the offset of the separate channels to a zero value. By subtracting this offset also the spread among the channels is corrected. This first baseline correction may already be influenced by any noise contaminating the signal but it is absolutely necessary for the second correction step, because differences in the baseline lead to incorrect correlation values.

The second step in the noise cancellation scheme corrects for correlated noise in the signals. To identify this noise and to separate it from also correlated signal an approach based on a covariance matrix is used. This covariance matrix calculates the correlation of the signal of each channel to any other channel. The higher the correlation value, the more common in shape are the signals. The calculation of the correlation value is based on [Win72]:

$$\langle x_i \rangle^{(1)} = x_{i1} \tag{12.1}$$

$$\langle x_i \rangle^{(n)} = \langle x_i \rangle^{(n-1)} + \frac{1}{n}\left(x_{in} - \langle x_i \rangle^{(n-1)}\right) \tag{12.2}$$

$$C^1_{i,j} = 0 \tag{12.3}$$

$$C^{(n)}_{i,j} = C^{(n-1)}_{i,j} + \frac{1}{n-1}\left[\left(x_{in} - \langle x_i \rangle^{(n)}\right)\left(x_{jn} - \langle x_j \rangle^{(n)}\right)\right] - \frac{1}{n}C^{(n-1)}_{ij} \tag{12.4}$$

The deviation of the amplitude x_{in} of the regarded time bin n from the mean value of the amplitudes $\langle x_i \rangle$ of the corresponding channels i and j are compared to each other. It is assumed that the channel with the lowest maximal amplitude does not carry any signal (it was not hit by any particle in this event), the correlation of all other channels to this non-hit-channel is calculated. According to the resulting correlation values it is decided which channel was hit and carries signal, and which has not been hit and only contains noise. This threshold is used to separate signal carrying channels in the event-by-event noise correction. By calculating the mean value of all non-hit channels a common noise for all channels is obtained and subtracted from all channels. The averaging over all non-signal channels is used to minimize fluctuations in the noise determination by the lowest non-hit channel and to prevent an overcorrection of the signal carrying channels by excluding channels which carry signals with lower amplitudes. Simpler correction algorithms like the usage of only the two lowest channels in amplitude may lead to overcorrections or may be not efficient in the subtraction of unwanted electronic noise.

Within this event-by-event based noise correction the covariance matrix is calculated by using the ROOT class *TPrinciple* [R. 97]. The correlation value is defined to be 1 for maximal correlation. The *TPrinciple* class additionally normalizes the correlation values in the covariance matrix, so that the sum of the values on the principal diagonal add up to 1. This values represent the correlation values $C_{i,i}$ of the regarded vector with itself, which lead to a normalization a_{norm} and the maximum correlation value c_{max}:

$$\sum_{i}^{n} C_{i,i} = 1 \Rightarrow a_{norm} = \frac{1}{n} = C_{max} \tag{12.5}$$

where n represents the number of columns/rows in a symmetric $n \times n$ matrix, which is in this case the number of the considered read out channels.

Figure 12.9 shows the distribution of the correlation values of events taken in run 2410001 with the 4+4 mm prototype at CERN PS during the 2011 test beam campaign. By taking all eight channels of the SPADIC rev 0.3 into account, a maximal correlation value of

$$C_{max} = 0.125 \tag{12.6}$$

has been determined. The peak at $C > 0.112$ is the correlation of the reference channel (lowest amplitude) combined with itself. The shape of the distribution depicts a rise for values at around

$$C_{i,j} = C_{threshold} = 0.112 \tag{12.7}$$

For lower values the corresponding channels are considered to carry signal. For higher values the correlation of the signals are more likely to contain noise. The value of $C_{threshold}$ has to be specified for each running condition setting [Dil13].

The final step in the noise correction algorithm is an additional pedestal correction. This step is required due to slight over- or underestimations in the covariance based noise correction. It is technically identical to the first offset correction and wipes out deviations to zero in the baseline of the individual channels. This step terminates the noise correction procedure.

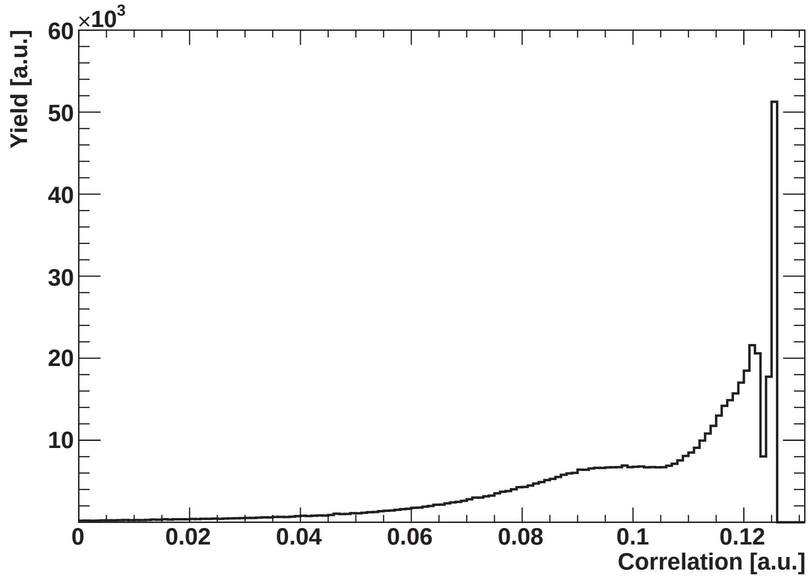

Figure 12.9: Distribution of the correlation value for SPADIC 17 in run 2410001 of the 2011 test beam campaign. The depicted values represent the correlation between the minimal amplitude channel and all remaining seven others to this channel [Dil13].

To illustrate the performance of the covariance-matrix-based noise cancellation algorithm figure 12.10 brings the not-corrected signal of an event face to face with the corrected signals of the same event. Figure 12.11 opposes an overlay of raw and corrected events taken in run 2210009 of the 2011 test beam campaign with SPADIC 17 attached to FFM006 (4+4 mm prototype). This overlay demonstrates the expected narrowing of the baseline band and emphasizes the efficient use of the dynamic range of the SPADIC rev 0.3 ADC.

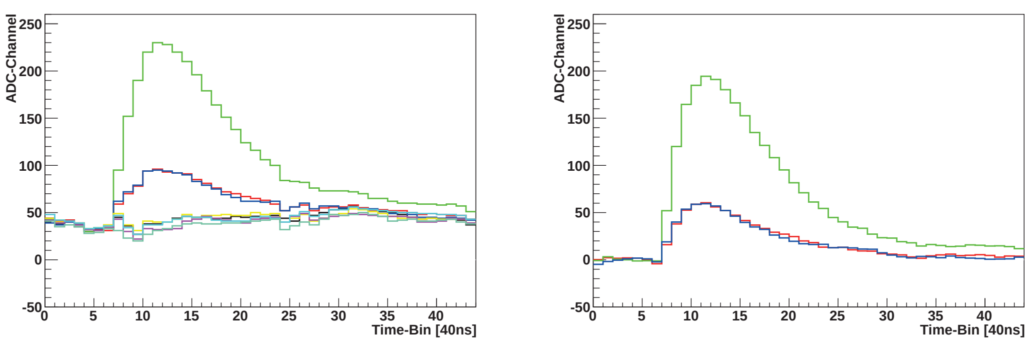

Figure 12.10: Raw signals for all eight SPADIC channels (left) and corrected signals only for channels carrying hit information (right) [Dil13].

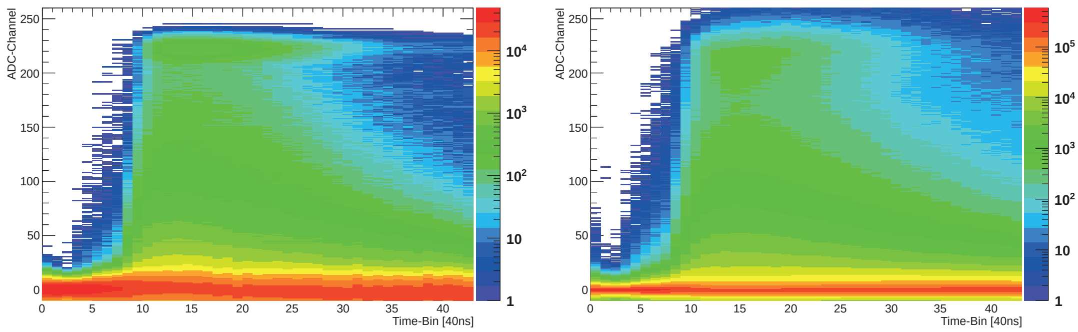

Figure 12.11: Overlay of the raw signals (left) and noise corrected signals (right) for all eight SPADIC channels [Dil13].

12.3 Cluster Finding Algorithm

The generated signals in the MWPC are split over the segmented pads connected to individual channels of the read-out electronics. The digitized and stored signals of the initial avalanche, referred as *cluster*, are reconstructed by the cluster finding algorithm. The reconstructed cluster contains all information (energy loss and potential generated transition radiation photon) of the deposited charge generated by the particle passing through.

The used cluster finding algorithm processes the noise corrected signals. For each individual channel a signal strength is obtained and filled in a histogram as shown in figure 12.12 for demonstration. The signal strength can be the signal amplitude of the given channel or the integral of the signal region in a given window of time bins.

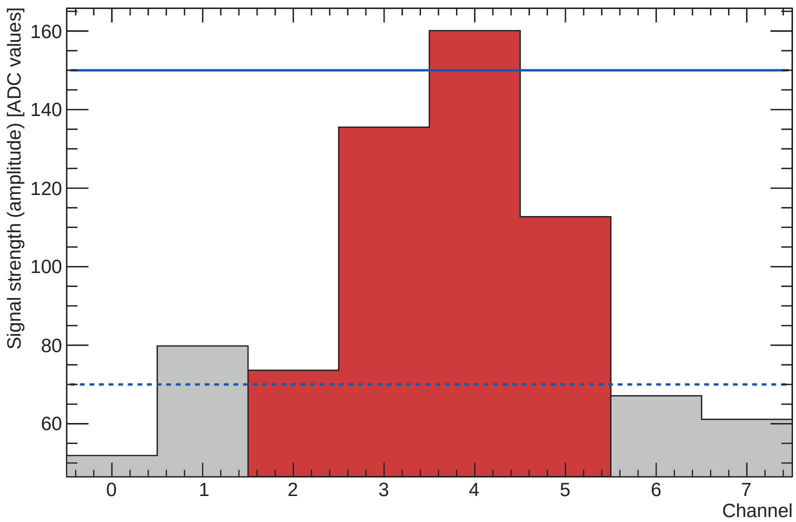

Figure 12.12: Demonstration of the cluster finding algorithm: Thresholds are indicated as blue lines, channels assigned to the cluster are shown as red bars, channels not counted are depicted in gray.

The used cluster finding algorithm employs two different thresholds to determine the cluster size and its contained deposited charge. The first threshold is used to decide if the analyzed event contains a sufficiently large signal for further processing. This threshold is set to a value of 5 in the demonstration in figure 12.12 and is depicted as solid blue line. If this value is exceeded, all channels over the second threshold are counted as signal carrying channels. This second threshold is set to a value of 3 in the demonstration in figure 12.12 and is depicted as dashed blue line. The cluster finding algorithm additionally applies constrains to the cluster shape. It is assumed, that the cluster evolves with monotonically decreasing signals from its maximum. If a signal in a channel is higher than the neighboring closer to the maximum value, this channel is rejected (see channel 1 in figure 12.12). The sum of the signal amplitudes, or the integrated signal respectively, of the individual channels contributing to the cluster is interpreted as the total deposited charge q_{tot} of this cluster. The distribution of the cluster size is shown in figure 12.13 for the generation III 5+5 mm prototype with ALICE-type radiator in run set 2 of the 2011 test beam campaign. The average cluster size calculated as the mean of the distributions is 4.48 based on the signal amplitude and 3.36 based on the integral of the signal region.

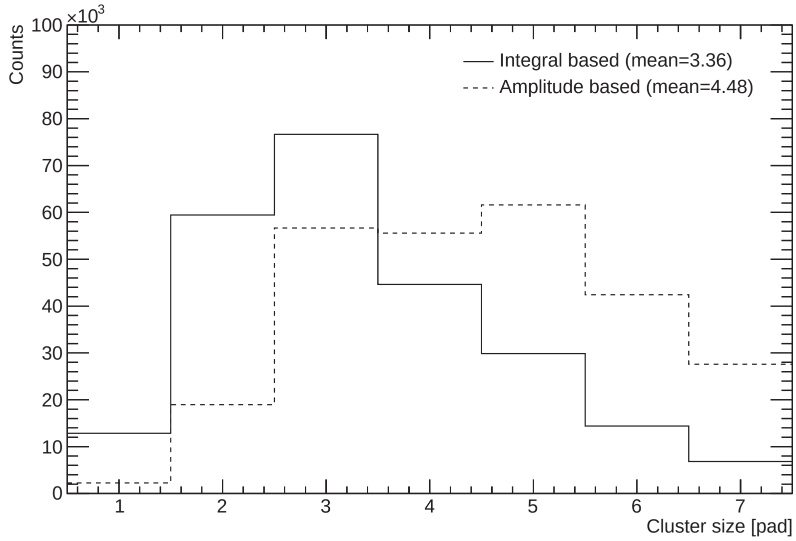

Figure 12.13: Average cluster size obtained with the described cluster finding algorithm based on the signal amplitude and the signal integrated over time.

12.4 Spectra of deposited charge

The calculated total deposited charge by the cluster finding algorithm is filled into a histogram. Based on the external particle identification the values for electrons and pions are separated. These spectra are normalized to an integral of one and shown in figure 12.14 for the generation III and IV 4+4 mm prototype with the ALICE-type reference radiator based on integrated signals in the cluster finding algorithm. The results for the amplitude based cluster finding is shown in figure 12.15

According to the energy loss inside the gas, the spectrum formed by the pions follows a Landau distribution. For the electrons additionally the emitted TR photon evolves a

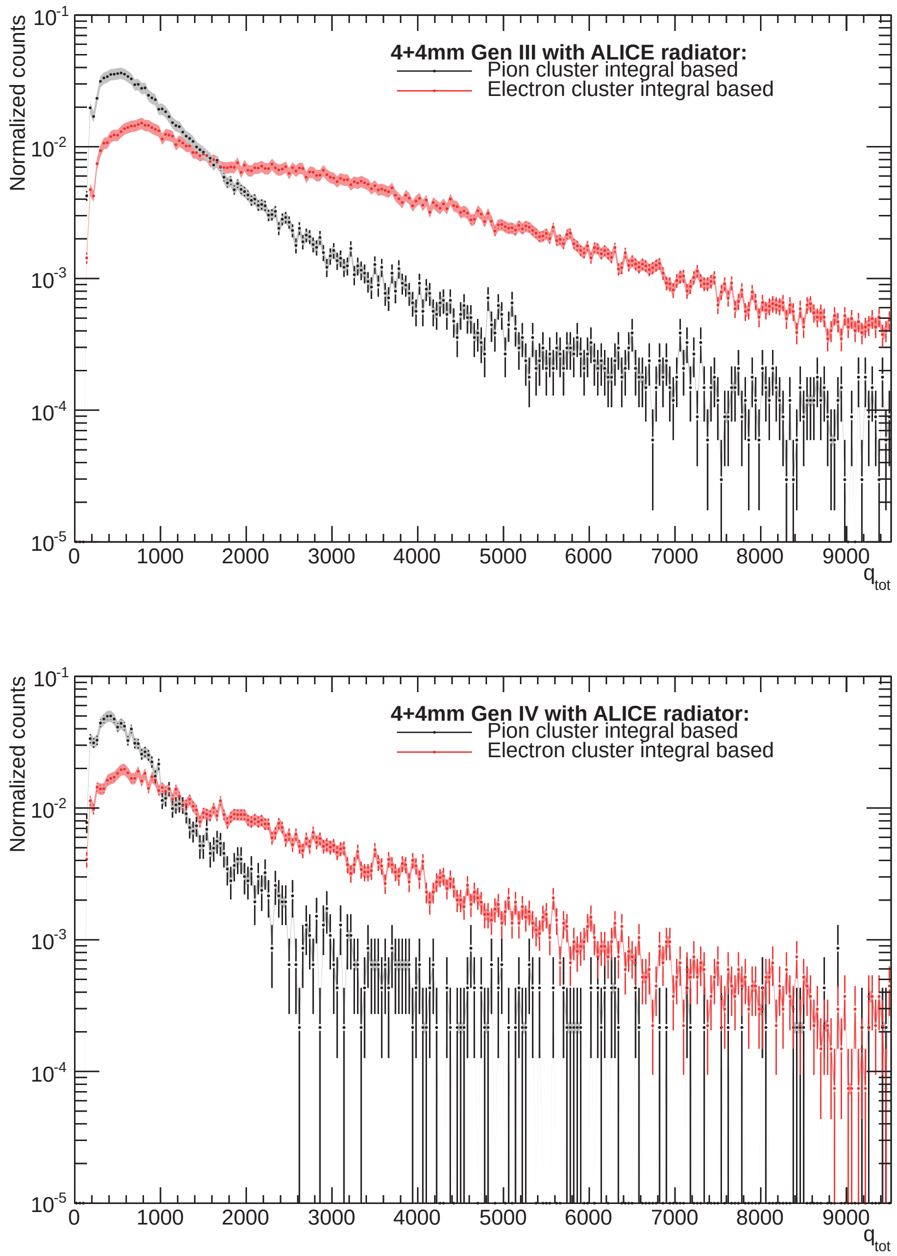

Figure 12.14: Top figure: Integrated ADC distribution for the 4+4 mm generation III prototype, run set 2/2011 with the ALICE type reference radiator. Bottom figure: 4+4 mm generation IV prototype, run set 1/2012 also with ALICE type reference radiator. The cluster finding algorithm is based on the integrated signal.

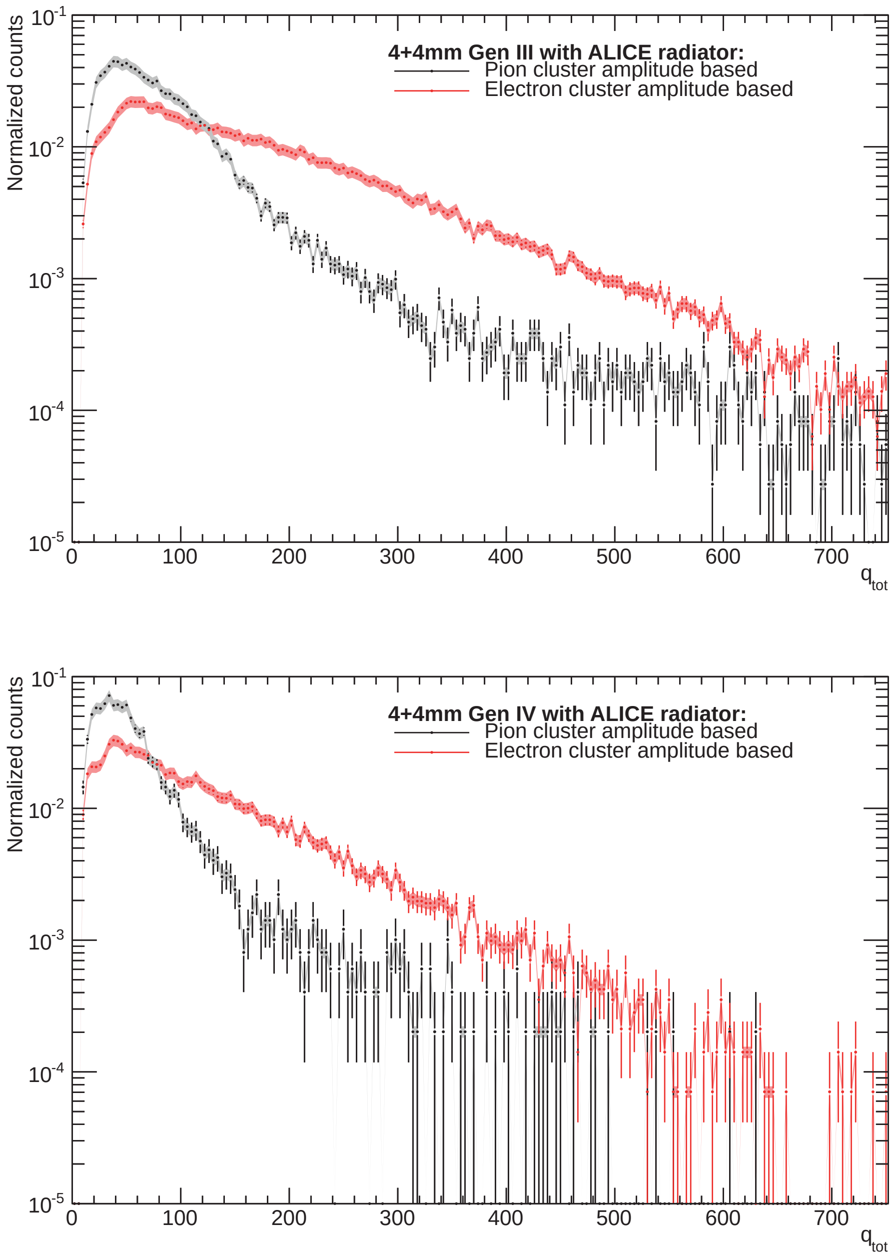

Figure 12.15: Top figure: Integrated ADC distribution for the 4+4 mm generation III prototype, run set 2/2011 with the ALICE type reference radiator. Bottom figure: 4+4 mm generation IV prototype, run set 1/2012 also with ALICE type reference radiator. The cluster finding algorithm is based on the signal amplitude.

bulge at higher values. The bottom part of figure 12.14 and 12.15 shows the spectra of the 4+4 mm Generation IV prototype with the same ALICE-type radiator. During the test beam campaign 2012 a significant gap between radiator and entrance window impaired the absorption of the TR photon inside the MWPC. This causes the lowering of the electron signal, whereas the pion spectra is comparable to the measurement with the generation III prototype of the same geometry.

12.4.1 Gain Calibration

To be able to compare measurements of different prototype geometries and generations a calibration on the gas gain is mandatory. During the test beam campaign 2012 the conditions for the gas system have been recorded and a variation on the differential overpressure causes changes in the gas gain and so in the signal generation (see chapter 11.2.1) and 9.2.1. To perform this calibration equally to the data of both test beam campaigns, a pure data driven approach has been followed.

The energy loss of pions is known to follow a Landau distribution. It has been fitted and the most probable value (MPV) is extracted. The gain calibration shifts this value to a fixed position. In this analysis the MPV has been chosen to be at a position of 500 a.u.. A gain calibration factor g_{cal} is obtained by

$$g_{cal} = \frac{500}{MPV} \tag{12.8}$$

This factor is multiplied to the q_{tot} value obtained by the cluster finding algorithm in a re-running of the analysis. With this procedure the resulting spectra are corrected for any variation in the gas gain of the used prototypes.

12.4.2 Electron-Pion-Separation based on one Detector Layer

To quantify the electron-pion separation capabilities of the tested radiator-MWPC-combinations the characteristic quantity $R_{e-\pi,p<90\%}$ is obtained. It is only based on the spectra of deposited charge.

$R_{e-\pi,p<90\%}$ is the fraction of the total pion spectrum, which would be wrongly counted as electrons when integrating the electron spectrum from the upper edge down to a certain threshold. This threshold is set to 90% according to the experimental requirement (see chapter 6.1). The integral of 90% in the electron spectrum defines the position p where the pion spectrum is divided, represented as green line in figure 12.16. $R_{e-\pi,p<90\%}$ is defined as:

$$R_{e-\pi,p<90\%} = \frac{I_{\pi,p<90\%e}}{I_{\pi,total}} \tag{12.9}$$

$R_{e-\pi,p<90\%}$ is shown for different radiator prototypes combined with both generation IV prototypes in figure 12.17.

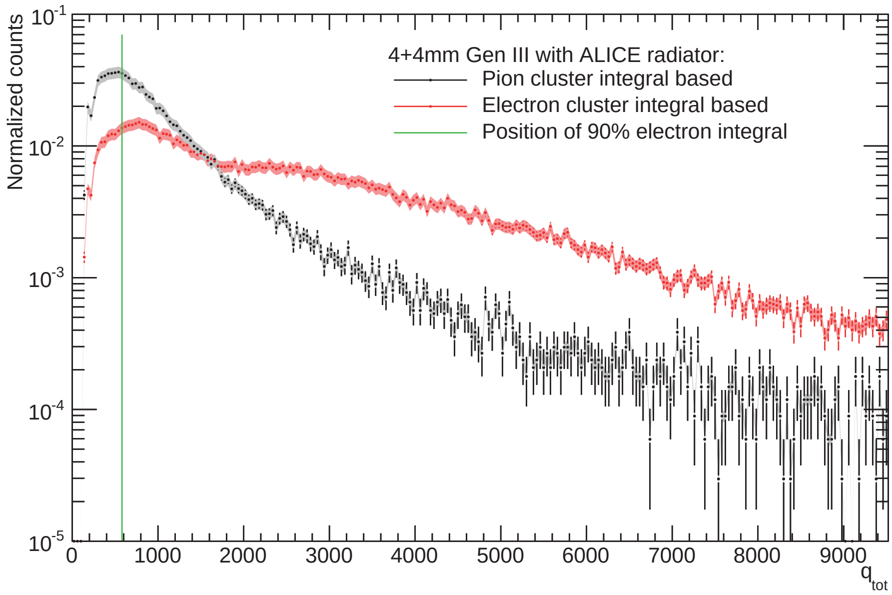

Figure 12.16: Illustration of the definition of misidentified pions. The green line represents the position of 90% integrated input spectra.

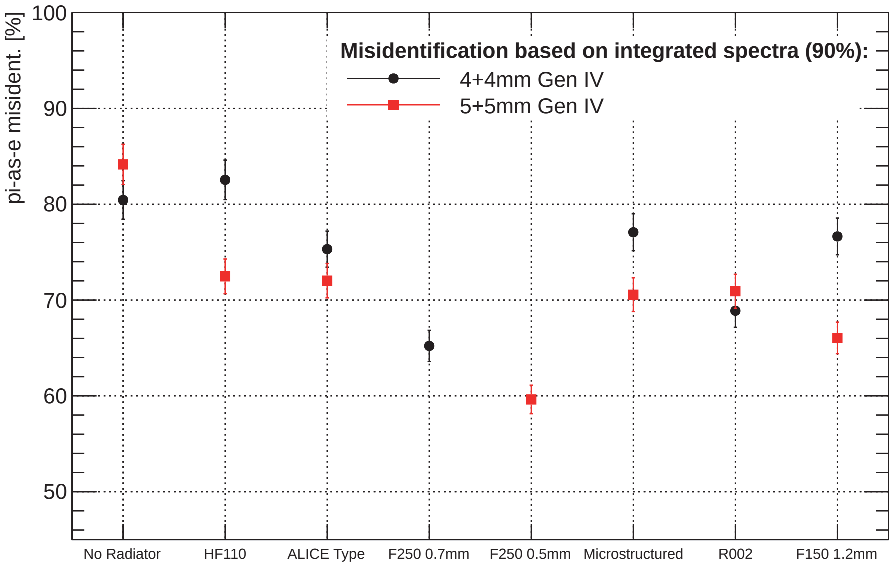

Figure 12.17: $R_{e-\pi,p<90\%}$ for different radiators with the generation IV prototypes.

12.5 Likelihood Extrapolation Method

The likelihood method is a statistical method to extrapolate the electron-pion-discrimination capabilities of a tested prototype to a number of multiple layers of subsequently following prototypes of these kind. These electron-pion-discrimination capability is one of the key characterizations of a TRD [AW11]. Two kinds of likelihood extrapolations are used, the classic likelihood and the logarithmic modification.

12.5.1 Classic Likelihood Extrapolation

The classic likelihood is constructed using the spectra of the deposited charge as input. Taking these measured and normalized spectra of one detector layer as probability distributions for electrons ($P(E_i|e)$) and pions ($(P(E_i|p))$) to produce a signal of the magnitude E_i (figure 12.16) the likelihood for an electron L_{el} and for a pion L_π are defined as [Wil06]:

$$L_{el} = \frac{P_e}{P_e + P_\pi} \tag{12.10}$$

$$L_\pi = \frac{P_\pi}{P_\pi + P_e} \tag{12.11}$$

with

$$P_e = \prod_{i=1}^{N} P(E_i|e) \quad and \quad P_\pi = \prod_{i=1}^{N} P(E_i|\pi) \tag{12.12}$$

where the product runs over the number of extrapolated detector layers.

The resulting likelihood spectra for the given input spectra extrapolating from one to twelve layers are shown in figure 12.18 as an overlay for three, six, nine and twelve layers. The functional form of the spectra is developing strongly to the characteristic shape with increasing number of layers. The likelihood spectra for small number of layers (< 3) is still deformed and shows minor binning effects. These effects are caused by the binning of the input spectra and the fact that only a finite number of values are available for the over pronounced dE/dx region. This effect vanishes to multiple layers due to the multiplicative construction of L.

The electron/pion capabilities for a TRD are quantified in the number of pions misidentified as electrons when requiring a given electron efficiency. According to the experimental requirements of less than 1% pions in the electron sample (see chapter 6.1) the *pion-as-electron-misidentification* is calculated. To determine the misidentified pions the likelihood for electrons and pions are integrated from high to low values until the sum reaches the required 90% for electrons. The fraction of the pion integral to the total integral is interpreted as the percentage of misidentified pions. The position of this 90% is represented with a green line for every layer in Figure 12.19. The pion-as-electron-misidentification depending on the number layers for one set of radiator and detector prototype is shown exemplary in Figure 12.20.

By calculating the pion-as-electron-misidentification as function of the requested fraction of all electrons the position where the border of less than 1% can be reached [ALI01]. Figure 12.21 shows this relation for a fixed number of layers of generation IV 5+5 mm prototype with attached radiator R002 at a particle momentum of $3\,GeV/c$ exemplary. In

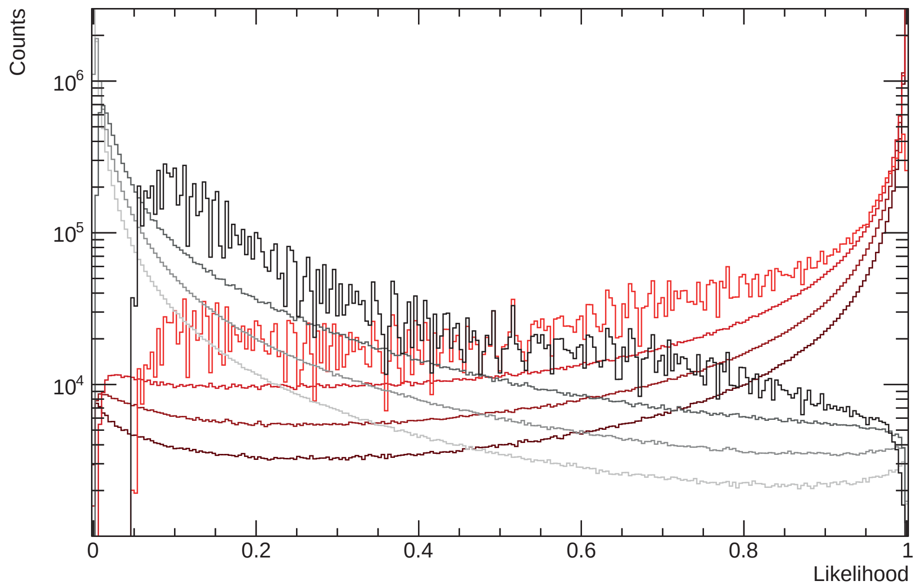

Figure 12.18: Overlay of the calculated likelihood spectra for three, six, nine and twelve extrapolated layers represented with gradual bleaching out colors for higher number of layers.

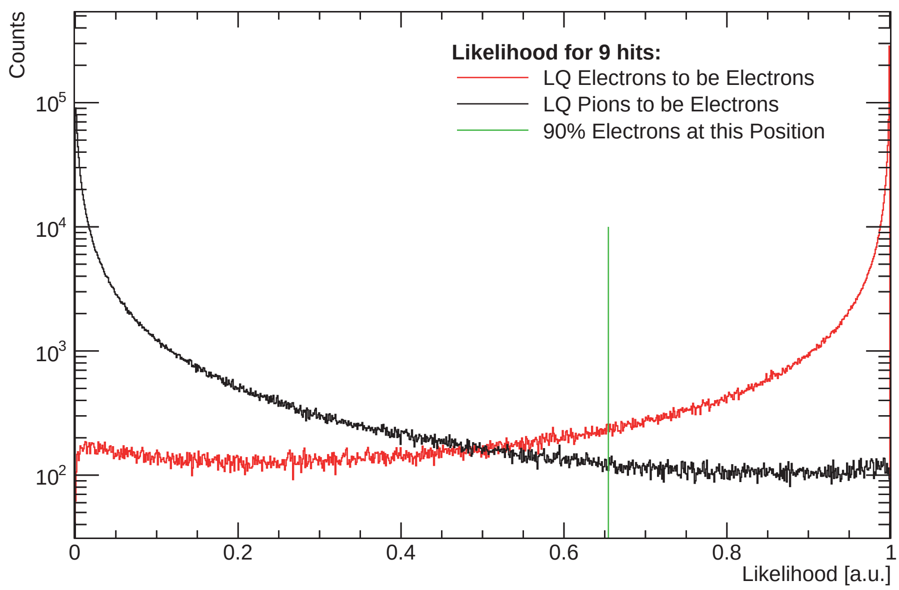

Figure 12.19: Illustration of the definition of misidentified pions. The green line represents the position of 90% integrated input spectra.

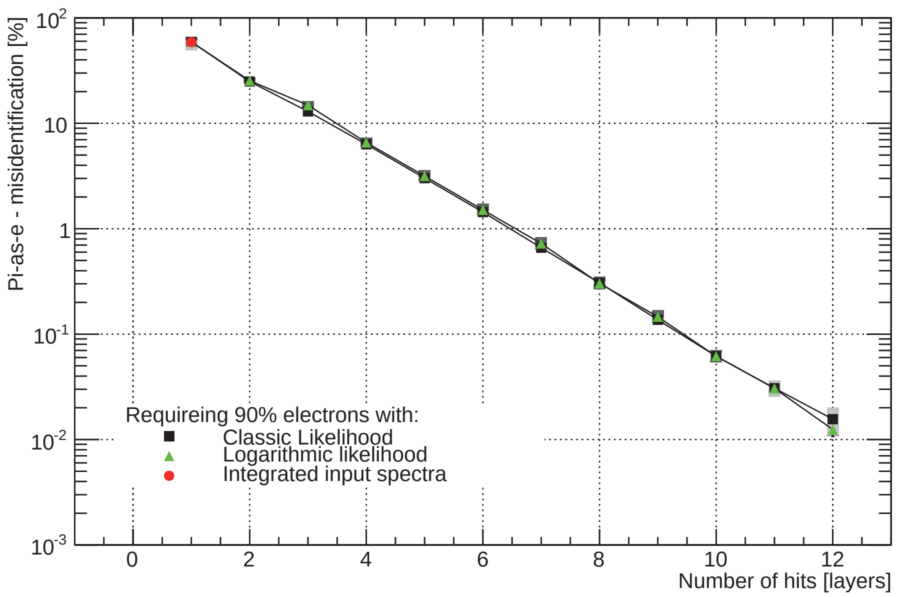

Figure 12.20: Resulting percentage of pions which are identified as electrons depending on the number of extrapolated layers. The point for one layer is calculated based on the input due to the binning effects in the over pronounced dE/dx-Region of the input spectra.

this case, with 6 detector layers and when requiring less than 60% of the electrons, an misidentification of 1% of the pions can be achieved.

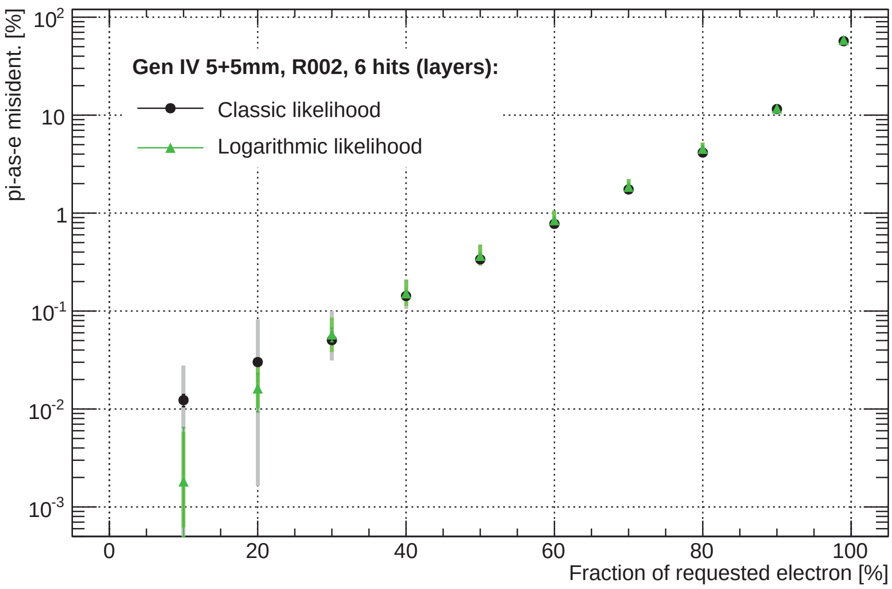

Figure 12.21: Calculated pion-as-electron-misidentification as function of requested fraction of electrons for 6 layers of generation IV 5+5 mm prototype with attached radiator R002 at a particle momentum of $3\,GeV/c$.

12.5.2 Logarithmic Likelihood Extrapolation

The logarithmic likelihood [Mor] extrapolation uses the same input spectra as the classic likelihood method and calculates the separate probabilities P_e and P_π.

$$L_{el} = \log \frac{P_e}{P_\pi} \tag{12.13}$$

$$L_\pi = \log \frac{P_\pi}{P_e} \tag{12.14}$$

Contrary to the classic likelihood, the range of possible values are $[-\infty, \infty]$ which allows a wider separation of the likelihood values. An overlay of the resulting spectra of logarithmic likelihood is shown in figure 12.23.

The logarithmic likelihood spectra are integrated to an electron identification of 90% equally to the classic likelihood method. Both methods are in very good agreement. The results for the logarithmic likelihood method are shown as green markers in figure 12.20 and 12.21.

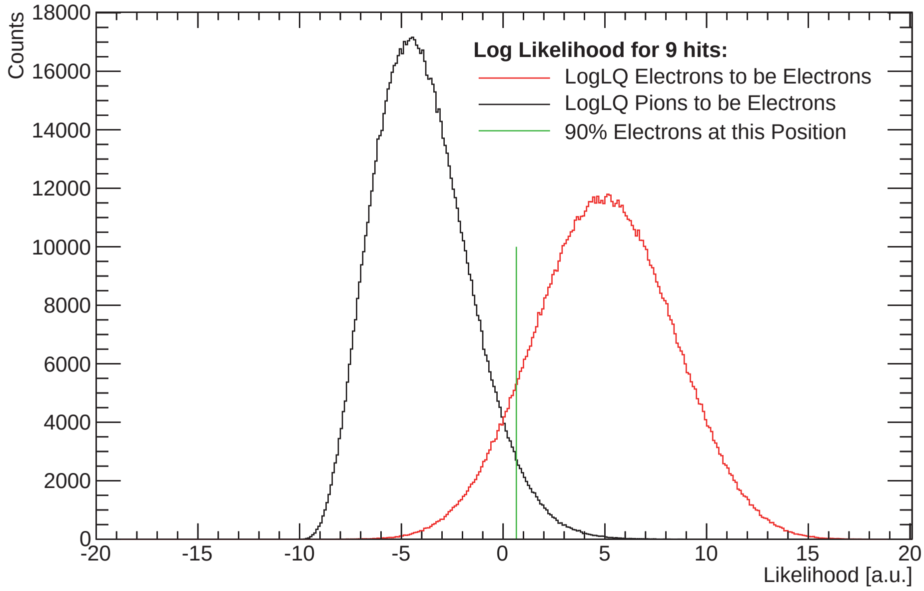

Figure 12.22: Illustration of the definition of misidentified pions. The green line represents the position of 90% integrated input spectra.

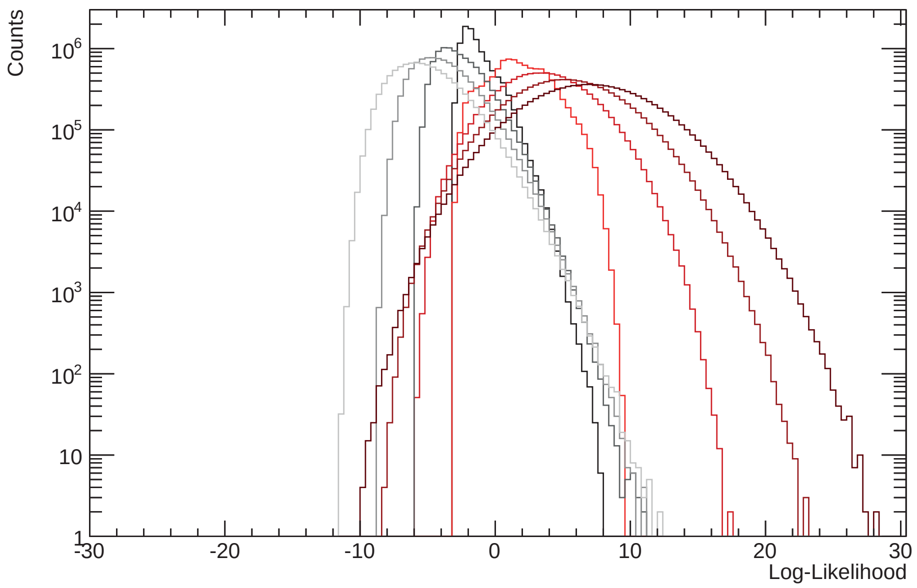

Figure 12.23: Overlay of the calculated logarithmic likelihood spectra for three, six, nine and twelve extrapolated layers represented with gradual bleaching out colors for higher number of layers.

12.5.3 Results of the Likelihood Extrapolation Methods

It has to be stressed, that the likelihood extrapolation assumes a sufficiently large signal in each detector layer to contribute to the q_{tot}-spectrum. This has to be folded with the detector efficiency which will lower the final performance.

During the 2011 test beam campaign the generation III prototypes have been tested only with a small number of radiator prototypes. Figure 12.24 depicts the results of the classic likelihood extrapolation for the 4+4 mm and 5+5 mm prototypes combined with the ALICE reference radiator and without radiator, where only differences in dE/dx cause a marginal decreasing of the pion-as-electron-misidentification. For the 4+4 mm MWPC also the results for a foil radiator and the radiator type N are shown. The radiator type N features ≈425 transitions and surpasses the performance of the regular foil radiator with 250 layers. The radiator type N achieves an pion-as-electron misidentification of 4.15%±0.11(stat.) $^{+0.02}_{-0.02}$(syst.) for 6 layers/hits and 0.40%±0.03(stat.) $^{+0.01}_{-0.01}$(syst.) for 10 layers/hits in the generation III 4+4 mm MWPC. The statistical errors are obtained by the pure statistical error on the corresponding likelihood spectra, the systematic error are originated in the finite binning of the likelihood spectra and the procedure of determining the 90% border line in this spectra.

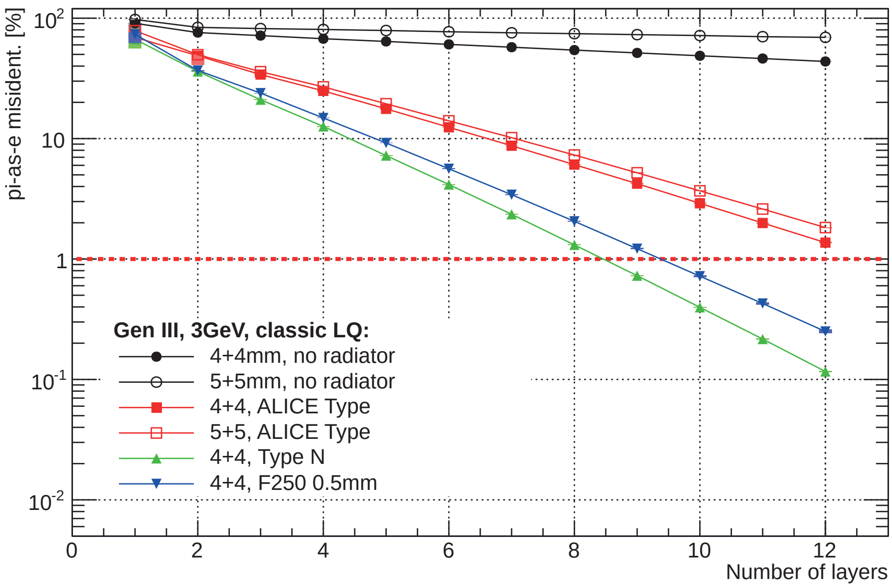

Figure 12.24: Pion-as-electron-misidentification when requiring 90% electron efficiency for different radiator prototypes combined with the generation III prototypes during the 2011 test beam campaign.

Figure 12.25 emphasizes the performances for a selected set of layers. Since the future CBM TRD will consists of three stations with 4+4+2 detector layers the extrapolated performances for all combinations can be obtained. The compatible low pion-as-electron-misidentification of the radiator type N lead to a further investigation on foam-based radiators during the 2012 test beam campaign.

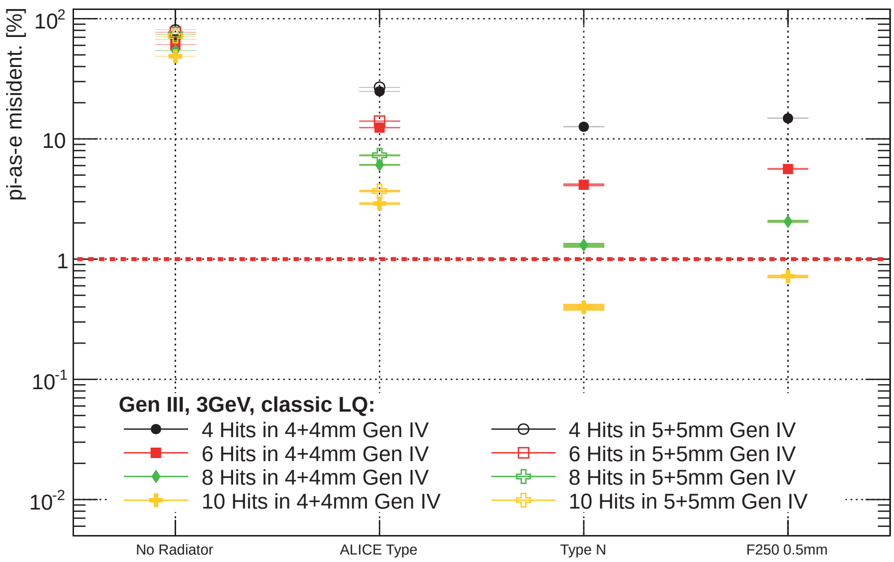

Figure 12.25: Comparison of radiators with the 4+4 mm and 4+4 mm generation III prototypes in the test beam campaign 2011.

During the test beam campaign 2012 a variety of radiators could be tested with the generation IV prototypes. As already stated during this campaign an unavoidable gap between radiator and entrance window caused modifications in the q_{tot}-spectra. Since this modification in the input spectra is the same for all runs, a comparison of radiator performance is still possible.

Figure 12.26 and 12.27 depict the results for the 4+4 mm and 5+5 mm MWPC prototype. In both cases the radiator prototype R002 features a performance comparable to the foil-based radiators. At ten extrapolated layers it achieves a pion-as-electron-misidentification of 0.81%±0.03(stat.) $^{+0.01}_{-0.01}$(syst.) with the 4+4 mm MWPC and 0.75% ±0.03(stat.) $^{+0.01}_{-0.01}$(syst.) with the 5+5 mm MWPC. Figure 12.28 summarizes the radiator performances.

During the 2012 test beam campaign a dedicated scan over the particle momentum has been conducted. The resulting pion-as-electron misidentification for both generation IV prototypes with the R002 and the regular foil radiator respectively are shown in figure 12.29.

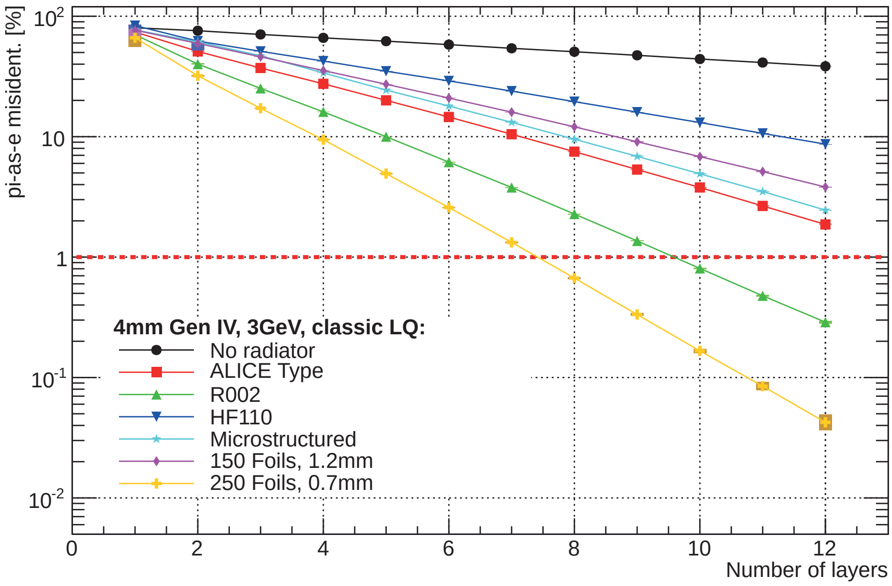

Figure 12.26: Pion-as-electron-misidentification when requiring 90% electron efficiency for different radiator prototypes combined with the generation IV 4+4 mm prototype during the 2012 test beam campaign.

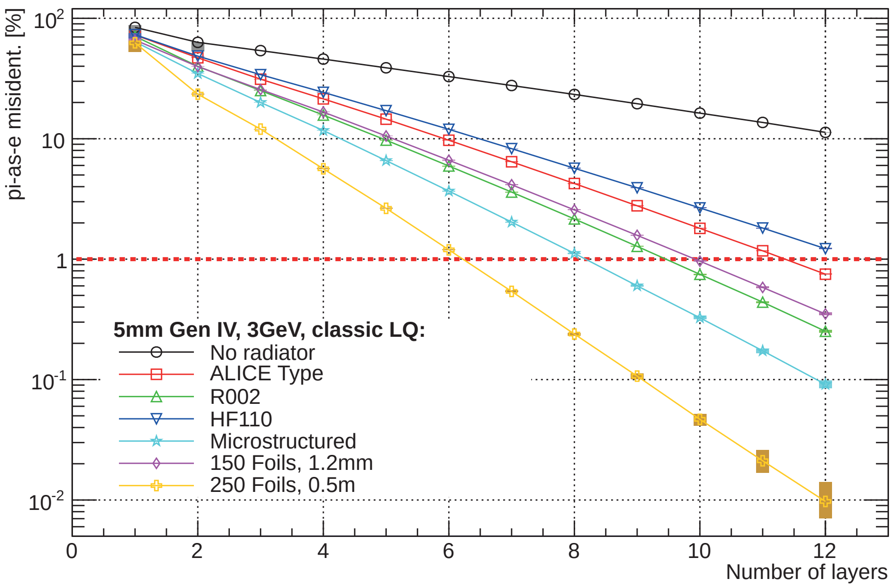

Figure 12.27: Pion-as-electron-misidentification when requiring 90% electron efficiency for different radiator prototypes combined with the generation IV 5+5 mm prototype during the 2012 test beam campaign.

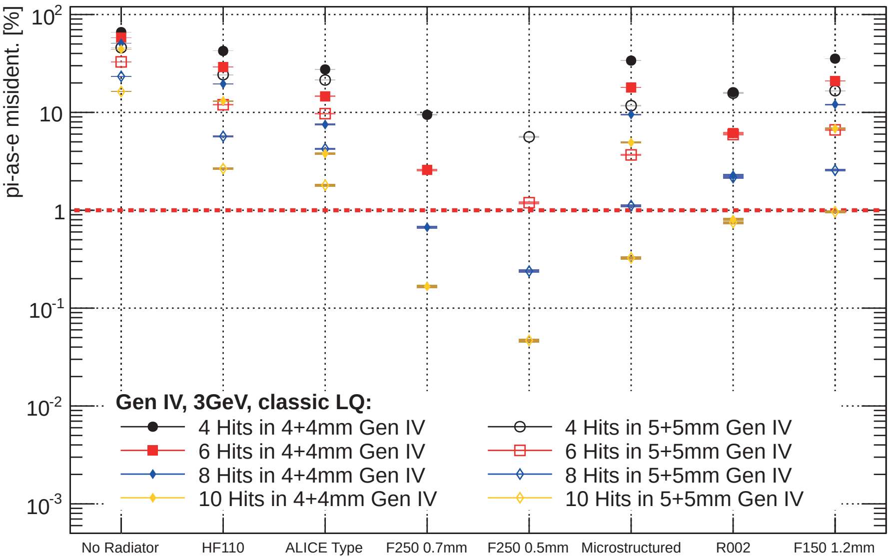

Figure 12.28: Comparison of radiators with the 4+4 mm and 5+5 mm generation IV prototypes in the test beam campaign 2012.

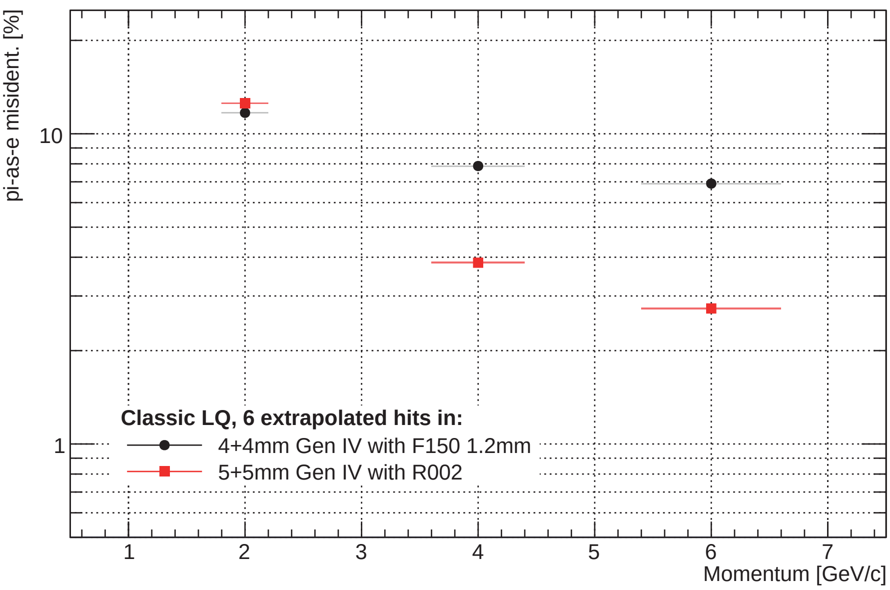

Figure 12.29: Pion-as-electron-misidentification when requiring 90% electron efficiency depending on particle momentum.

12.6 Pad Response Function

The pad response function characterizes the distribution of a generated cluster and its spread over the read out pads. The signal height of a given pad is plotted versus its reconstructed position with respect to the pad with the maximum signal. The position is obtained via a weighted mean. Figure 12.30 depicts the pad response function exemplary for the 4+4 mm (left) and 5+5 mm (right) generation IV prototype in run *Be_run29* during the 2012 test beam campaign. In this representation the obtained values are exclusively calculated for a cluster size of three.

The theoretical description of the pad response function is given by the Mathieson formula [BRR08] :

$$P_0 = \frac{K_1}{K_2\sqrt{K_3}}\left(\arctan\left[\sqrt{K_3}\tanh K_2(\lambda + \frac{w}{2})\right] - \arctan\left[\sqrt{K_3}\tanh K_2(\lambda - \frac{w}{2})\right]\right) \tag{12.15}$$

where

$$K_1 = \frac{K_2\sqrt{K_3}}{4\arctan\sqrt{K_3}} \ , \quad K_2 = \frac{\pi}{2}\left(1 - \frac{\sqrt{K_3}}{2}\right) \quad and \lambda \quad = \frac{x}{h} \tag{12.16}$$

with x as the reconstructed position, w as with of the read out pad and h as gap between anode and cathode plane. K_3 is an additional geometrical parameter taking the diameter $d = 20\,\mu$m and the anode wires pitch $s = 2.5$ mm into account. According to [E. 88] the parameter K_3 has been approximated with $K_{3,4+4mm}$= 0.3 and $K_{3,5+5mm}$= 0.217. The resulting theoretical pad response function is shown as full black line in figure 12.30. The discussed overpressure in the MWPC causes a bulging of the entrance windows and thus a increase of the distance of the anode wires to the entrance window. The resulting deformations in the electric field effects the generation of the signal. The deviation of the measured distribution to the calculated Mathieson distribution can be explained by this deformations.

12.7 Conclusions

The presented results prove that the proposed MWPCs fulfill the experimental requirements. In combination with regular foil radiators and with foam based radiators the 4+4 mm and 5+5 mm detector geometries can exceed the requested value of 1% in pion-as-electron-misidentification. However, since foil-based radiators are extremely difficult to construct, foam-based radiators are proposed. The performance of foam-based radiators is competitive to regular radiators with comparable specifications. Furthermore foam based radiators may serve as additional support for the foam based entrance window and, as the proposed foam is made out of polyethylene which is an industrial mass product, are cost efficient.

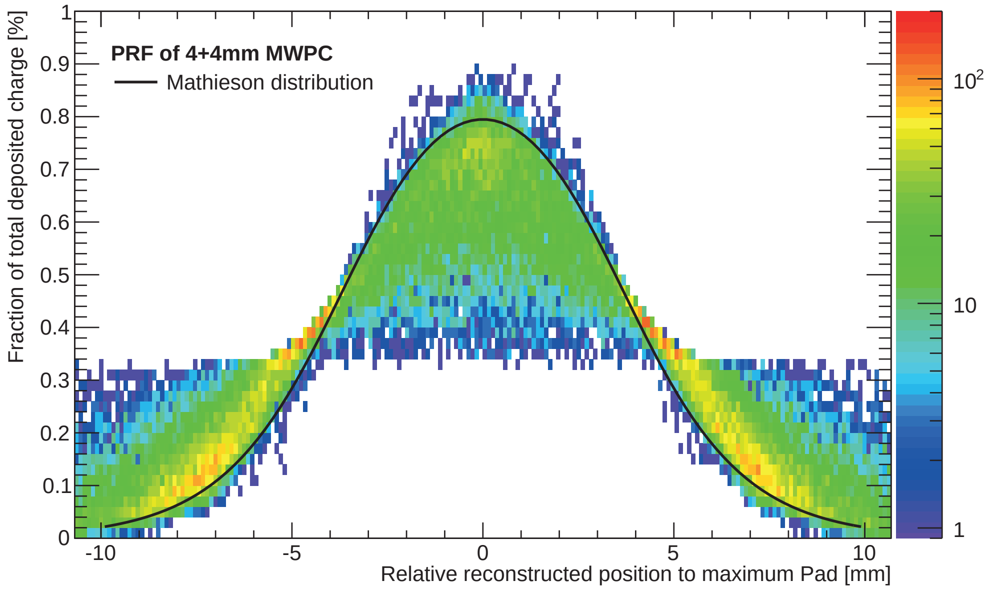

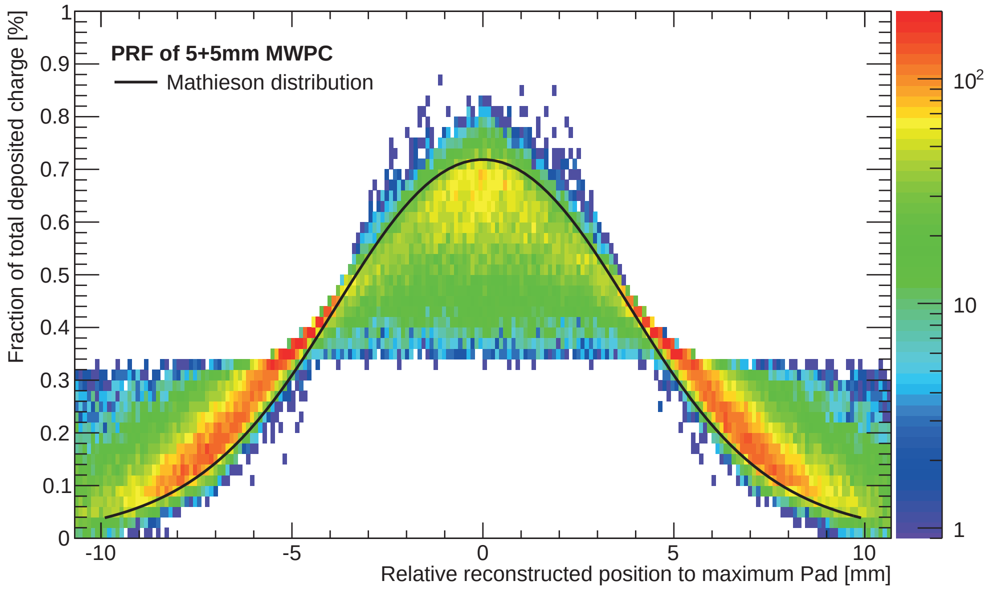

Figure 12.30: Pad response function for the 4+4 mm (top figure) and 5+5 mm (bottom figure) generation IV prototypes for fixed 3 pad cluster size. The theoretical Mathieson distribution is shown as black line.

13 Further Developments

The proposed generation III and IV prototypes have been proven to fulfill the requirements in terms of electron-as-pion misidentification. Further currently planned developments and required measurements are described in brief.

13.1 High Rate Tests

The required high rate test campaign is currently planed for all TRD prototypes of the involved institutions. It will take place in the FOPI cave at the GSI SIS18 experimental area. The TRD prototypes will be exposed to a high flux environment of secondary charged particles where the currents of the applied high voltage are monitored and the generated raw signals on the pad plane are recorded. A measurement scheme is under elaboration.

13.2 Front End Electronics

The SPADIC Chip has been designed to serve as the read out electronics for the future CBM TRD. The prototype of the SPADIC in its revision 0.3 has been used for three test beam campaigns. A first version of the revision 1.0 has been tested during the 2012 test beam campaign. The FASP read out chip has also demonstrated its functionality during the test campaigns. However, the TRB3, a FPGA based read out device, may be a third potential read out electronics device, which is currently under elaboration.

13.3 Stabilizing the Entrance Window

The variations in the gas gain have been simulated in chapter 9.2 and the unavoidable bulging of the entrance window have been shown in chapter 10.1. A simple possibility of stabilizing the entrance window is to make use of a stiff and stable radiator material to provide additional mechanical stability. By mounting the radiator directly in front of the entrance window a bulging can be reduced as shown in figure 13.1. Potential radiator materials have been tested with sufficiently low electron es pion misidentification. A case study on the feasibility of this setup is currently under investigation.

13.4 Alternative Wire Configuration: Anode and Field Wires

Another possibility to reduce the gas gain variation due to bulging is the usage of an alternating wire grid configuration [D. 11]. The anode wires are sequenced with wired connected to the high voltage and grounded wires. The resulting electric field is shown in figure 13.2. Due to the higher electric field focused in the inner part of the MWPC a

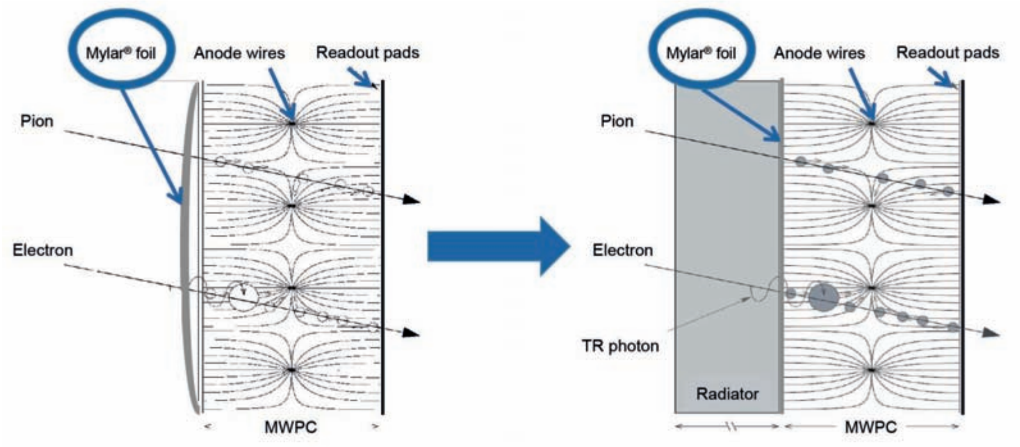

Figure 13.1: Conceptual idea of supporting and stabilizing the foil-based entrance window by the radiator material [Dil14].

distance variation at the outer areas has a smaller effect on the simulated gas gain, as for the classical wire geometry.

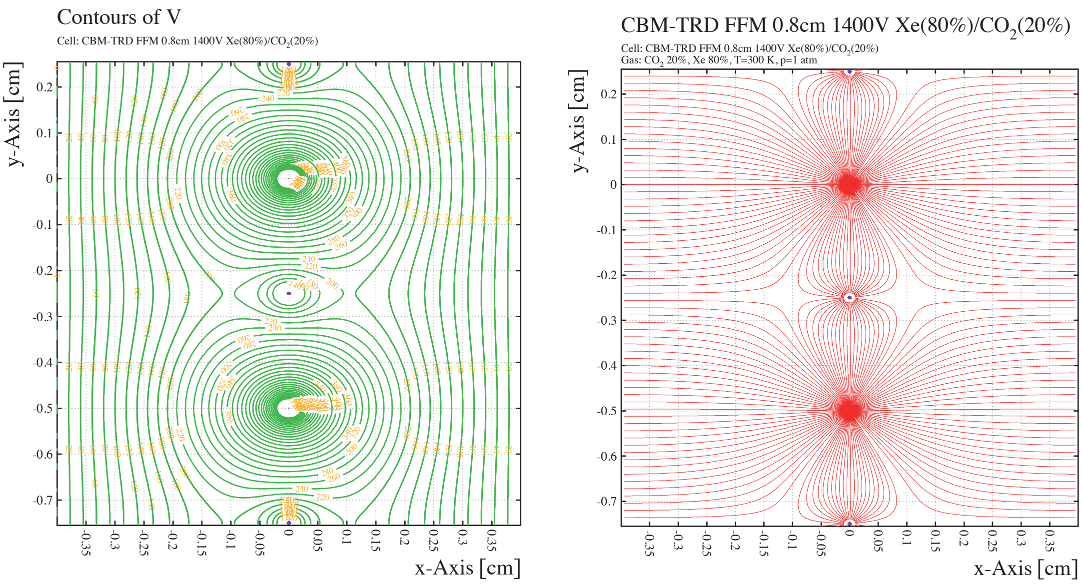

Figure 13.2: Field configuration (left) and electron drift lines (right) of alternating wire grid [Hel14].

The resulting gain variation depending on the expansion is shown in figure 13.3, which demonstrates the larger robustness of such configuration.

Prototypes based on the small generation III frame setup using this alternating wire grid configuration are currently being manufactured and to be tested in an upcoming test beam campaign.

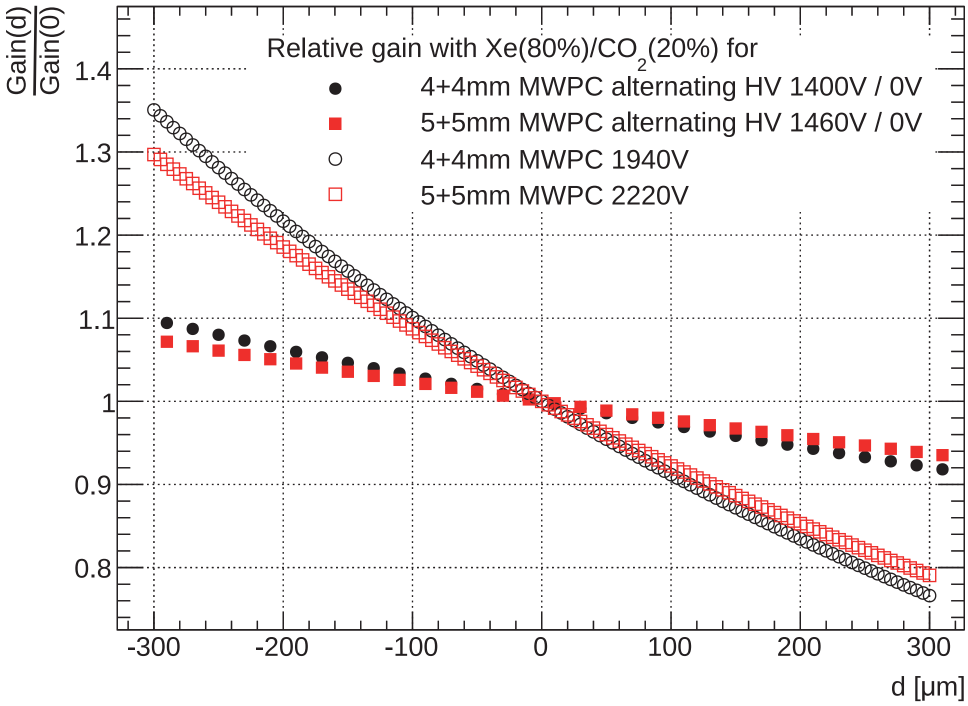

Figure 13.3: Gain variation depending on expansion of alternating wire grid configuration [Hel14].

14 Summary

The Compressed Baryonic Matter (CBM) experiment at the future FAIR facility will use collisions of heavy ions to explore the phase diagramm of QCD. A hot and dense state of nuclear matter will be generated. Rare probes and their reaction products will be reconstructed and analyzed using the detector setup of CBM.

The Transition Radiation Detector (TRD) of the CBM experiment has to provide electron-pion separation as well as charged-particle tracking. The intended measurements of rare probes in an environment of high particle rates define the experimental requirements of the TRD. The TRD has to suppress pions over electrons with a factor 100 at an electron efficiency of 90%. To integrate the TRD into the different measurement scenarios of CBM it is currently planned to build three stations with 4+4+2 detector layers, which allows the TRD to be integrated into the experimental setups in an optimal way. For the realization of a TRD different approaches are followed. Within this work, thin and symmetric Multi-Wire Proportional Chambers (MWPCs) without additional drift region were proposed. With respect to the expected high particle flux, thin MWPCs provide a faster signal generation compared to MWPCs with a dedicated drift region. The proposed prototypes feature a foil-based entrance window to minimize the material budget and to reduce the absorption probability of the generated TR photon.

Based on the conceptual design of thin and symmetric MWPCs without drift region, multiple prototypes were constructed and their performance presented within this thesis. The existing first generation served as proof-of-concept studies. With the constructed prototypes of generations II and III the geometries of the wire and cathode planes were determined to be 4+4 mm and 5+5 mm. Based on the results of a performed test beam campaign in 2011 with this prototypes new prototypes of generation IV were manufactured and tested in a subsequent test beam campaign in 2012. Generation IV prototypes feature real-size dimensions of a module in the inner area of the future TRD.

Prototypes of different radiators were developed together with the MWPC prototypes. Along with regular foil radiators, foam-based radiator types made of polyethylene foam were utilized. Also radiators constructed in a sandwich design, which used different fiber materials confined with solid foam sheets, were used.

For the prototypes without drift region, simulations of the electrostatic and mechanical properties were performed. The GARFIELD software package was used to simulate the electric field and to determine the resulting drift lines of the generated electrons. The mean gas amplification depending on the utilized gas and the applied anode voltage was simulated and the gas-gain homogeneity was verified. Since the thin foil-based entrance window experiences a deformation due to pressure differences inside and outside the MWPC, the variation on the gas gain depending on the deformation was simulated. The mechanical properties focusing on the stability of the entrance window was determined with a finite-element method to facilitate an approximation on the gas-gain variation.

The properties of the prototypes were verified with in-lab measurements. The simulated expansion of the foil-based entrance window was validated with overpressure tests. The absolute gas gain was measured in a setup using ionizing radiation of a ^{55}Fe source. The homogeneity of the relative gas gain of the generation IV prototypes at a given expansion of the entrance window as well as the energy resolution were also determined.

The objective of this work was the determination of the electron-pion separation capabilities of the MWPC prototypes combined with different radiator prototypes. In test beam campaigns 2011 and 2012 the prototypes of generation II, III and IV were exposed to a mixed electron-pion beam at the CERN PS. For these test beam campaigns, an online monitoring system based on the Go4 framework was developed for the employed SPADIC v0.3 read-out chain. The data read-out was integrated in the MBS and DABC based data acquisition system. During the test beam campaign 2012, ambient conditions and slow control parameters were collected additionally. To determine external particle identification two Cherenkov counters and a lead glass were used in combination. A separation procedure was used to determine the purity of the reference particle identification. The raw data obtained with the SPADIC v0.3 was noise corrected using a multi-step algorithm. This procedure used empty events to correct for the baseline offsets in the read-out electronics. Furthermore, the noise of the collected signals was canceled using a covariance matrix approach to distinguish between signal-carrying channels and channels only containing noise. The corrected data were used in a cluster finding algorithm based on the signal amplitude as well as on the integrated signal. With this information, in combination with the external particle identification, the spectra of total deposited charge for electrons and pions were measured. These spectra were corrected for variations in the gas gain using a multiplicative shifting procedure.

Based on the generated spectra of deposited charge, the electron-pion separation performance of MWPC prototypes combined with the utilized radiator prototypes were evaluated in this work. Therefore, a procedure for only one detector layer as well as an extrapolation method were employed. The extrapolation method was based on the calculation of a classical and a logarithmic likelihood. The electron-as-pion misidentification of combined radiator and MWPC prototypes were compared. The performance in electron-pion-separation of the foam-based radiators turned out to be compatible to the theoretically well understood regular foil-based radiators. Foam-based radiators represent an easy-to-handle and cost-efficient alternative to regular radiators. Additionally, they provide the possibility of a mechanical stabilization for the foil-based entrance window. The electron-pion separation was also analyzed depending on the momentum of the detected particle. Using the information of the employed cluster-finding algorithm the pad response functions were determined.

Concluding from the results of the analysis performed in this thesis, thin and symmetric Multi-Wire Proportional Chambers with amplification region only combined with a foam-based radiator fulfill the requirements for the Transition Radiation Detector of the CBM experiment in terms of electron-as-pion misidentification.

Bibliography

[AA] A. Andronic, P. Braun-Munzinger J. Cleymans K. Fukushima L.D. McLerran H. Oeschler R.D. Pisarski K. Redlich C. Sasaki H. Satz J. S. D. Blaschke B. D. Blaschke: Hadron Production in Ultra-relativistic Nuclear Collisions: Quarkyonic Matter and a Triple Point in the Phase Diagram of QCD. In: *arXiv:0911.4806*

[AC12] ATLAS ; Collaborations, CMS: *Higgs booklet : First observations of a new particle in the search for the Standard Model Higgs boson at the LHC*. Booklet, 2012

[AFP09] Armbruster, T. ; Fischer, P. ; Perić, I. ; Armbruster, T. (Hrsg.) ; Fischer, P. (Hrsg.) ; Perić, I. (Hrsg.): *A Self Triggered Amplifier/Digitizer Chip for CBM*. Proceedings TWEEP-09, 2009 (TWEEP-09)

[AK12] Armbruster, T. ; Krieger, M.: *SPADIC1.0 Data Sheet, Version 0.27*. http://spadic.uni-hd.de/spadic10/data/spadic10spec.pdf. `http://spadic.uni-hd.de/spadic10/data/spadic10spec.pdf`. Version: Oct. 2012

[ALI01] ALICE Collaboration: Technical Design Report of the Transition Radiation Detector / CERN/LHCC 2001-021. 2001. – Forschungsbericht

[AR09] Antiproton, FAIR F. ; Research, Ion: FAIR Green Paper - The Modularized Start Version - A stepwise approach to the realisation of the Facility for Antiproton and Ion Research in Europe. (October 2009)

[AW11] Andronic, A. ; Wessels, J. P.: Transition Radiation Detectors. (2011). `http://arxiv.org/abs/1111.4188`

[Bal13] Ballé, Tanita: *Studien zum Einfluss der Ausdehnung des Eingangsfensters auf die Gasverstärkung des CBM-TRD*. Bacherlor Thesis, December 2013

[Ber09] Bergmann, Cyrano: *Development and Test of a Transition Radiation Detector Prototype for CBM @ FAIR*, Westfälische Wilhelms-Universität Münster, Diplomarbeit, 2009

[Ber12] Bergmann, Cyrano: *Foto of the test beam setup 2012*. Private Communication, 12 2012

[Ber13] Bergmann, Cyrano: *Development, Simulation and Test of Transition Radiation Detector Prototypes for the Compressed Baryonic Matter Experiment at the Facility for Antiproton and Ion Research (TO BE SUBMITTED)*, Westfälische Wilhelms-Universität Münster, Diss., 2013

[BF11] Bengt Friman, Jörn Knoll-Stefan Leupold Jorgen Randrup Ralf R. Claudia Höhne H. Claudia Höhne: *The CBM Physics Book*. Springer, 2011

[BRR08] Blum, W ; Riegler, Werner ; Rolandi, L: *Particle detection with drift chambers*. Berlin; New York : Springer, 2008. – ISBN 9783540766841 3540766847

[Col97] Collaboration, NA50: Anomalous J/ψ suppression in $Pb + Pb$ interactions at 158 GeV/c per nucleon. In: *Physical Letters B* 410.38 (1997), S. 337 – 343

[col05] collaboration, CBM: Compressed Baryonic Matter Experiment Technical Status Report CBM experiment. 2005. – Forschungsbericht

[Col10] Collaboration, PHENIX: Detailed measurement of the e^+e^- pair continuum in $p + p$ and $Au + Au$ collisions at $\sqrt{s_{NN}} = 200GeV$ and implications for direct photon production. In: *Physical Review* C 81 (2010)

[CW75] C.W. FABJAN ; W. STRUCZINKSKI: COHERENT EMISSION OF TRANSITION RADIATION IN PERIODIC RADIATORS. In: *PHYSICS LETTERS* 57B (1975), S. 483 – 486

[D. 11] D. Varga, G.Hamar, G.Kiss: Asymmetric Multi-Wire Proportional Chamber with reduced requirements to mechanical precision. In: *Nuclear Instruments and Methods in Physics Research A* 648 (2011), S. 163–167

[Dah08] Dahms, Torsten: *Dilepton spectra in $p + p$ and $Au + Au$ collisions at RHIC*, Stony Brook University, Diss., 2008

[DFH+98] Durieu, L. ; Ferrando, O. ; Hemery, J. Y. ; Riunaud, J. P. ; Williams, B.: The CERN PS east area in the LHC era. In: *17th IEEE Particle Accelerator Conference*, 1998, S. 228–230

[Dil10] Dillenseger, Pascal: *Entwicklung eines Teststands zur Untersuchung von Transition-Radiation-Detektoren für das CBM-Experiment*. Bacherlor Thesis, November 2010

[Dil13] Dillenseger, Pascal: *Charakterisierung und Signalanalyse von TRD-Prototypen für das CBM Experiment*. Master Thesis, September 2013

[Dil14] Dillenseger, Pascal: *Entrance window flattening using a foam based radiator*. Private Communication, 01 2014

[E. 88] E. Mathieson: Cathode Charge Distributions in Multiwire Chambers: 4. Empirical formula for small anode-cathode separation. In: *Nuclear Instruments and Methods in Physics Research* A270 (1988), S. 602–603

[Ems13a] Emschermann, David: *CBM TRD geometries*. Private Communication. `http://cbm.uni-muenster.de/cbmroot/more/trd_rich_much_geo_v1.00/`. Version: 05.09.2013

[Ems13b] Emschermann, David: *Pad Plane Geometries for the full size CBM TRD Prototypes*. Webpage, private comunication. `http://cbm.uni-muenster.de/padplane/`. Version: 08.10.2013

[FAI] FAIR - Facility for Antiproton and Ion Research in Europe GmbH: *The FAIR complex*. `http://www.fair-center.eu/index.php?id=1`

[FEA] FEA, Abaqus: *Abaqus FEA software suite*. Software Package. `http://www.3ds.com/products-services/simulia/portfolio/abaqus/abaqus-portfolio/abaquscfd/`

[FS12] Friese, Volker (eds.) ; Sturm, Christian [.: CBM Progress Report 2011 / GSI Darmstadt. 2012. – Forschungsbericht

[FS13] Friese, Volker (eds.) ; Sturm, Christian [.: CBM Progress Report 2012 / GSI Darmstadt. 2013. – Forschungsbericht. – `https://www-alt.gsi.de/documents/DOC-2013-Mar-49.html`

[Gar] Garfield Help Pages: *Penning-Transferes*. Webpage. `http://consult.cern.ch/writeup/garfield/help/`

[GM64] Gell-Mann, M.: A schematic model of baryons and mesons. In: *Physical Letters* 8.3 (1964), S. 214–215

[Gro10] Group, Particle D.: *Particle Physics Booklet*. IOP Publishing, 2010

[GS08] Grupen, C. ; Shwartz, B.: *Particle detectors*. Bd. ISBN 978-0-521-18795-4. Cambridge University Press, 2008

[Hel13a] Hellbär, Ernst: *Absolute gas gain simulation for the generation III prototypes*. Private Communication, 2013

[Hel13b] Hellbär, Ernst: *Elektrostatische Simulationsstudien zum Übergangsstrahlungsdetektor des CBM-Experiments*. Bacherlor Thesis, 2013

[Hel13c] Hellbär, Ernst: *Ion Mobility and Signal Simulation for FFM Type CBM TRD Prototypes*. Private Communication, 09 2013

[Hel14] Hellbär, Ernst: *Field Configuration and Gas Gain Variation using the Alternating Wire Grid Configuration for the CBM TRD*. Private Communication, 2014

[J.A09] J.Adamczewski-Musch, S.Linev, H.G.Essel ; GSI (Hrsg.): *DABC: User Manual*. GSI, 2009

[J.A13] J.Adamczewski-Musch, M.Al-Turany, D.Bertini, H.G.Essel, S. Linev ; GSI (Hrsg.): *The Go4 Analysis Framework Reference Manual v4.6*. GSI, 2013

[Kle05] Kleinknecht, Konrad: *Detektoren für Teilchenstrahlung*. Teubner B.G, 2005

[Kön86] Königsmann, Kay: *Radiative Decays in the Psi Family*. North-Holland, 1986

[Kra06] Kramer, Frederick: *Studie zur Messung von Quarkonia mit dem ALICE-TRD und Aufbau eines Teststandes fur seine Auslesekammern*, Institut für Kernphysik Frankfurt, Diplomarbeit, 2006

[LB13] Linev, Sergey ; Bergmann, Cyrano: *The DAQ-Software Setup at CERN TestTest campaign 2012*. private communication, October 2013

[Leo94] Leo, William R.: *Techniques for Nuclear and Particle Physics Experiments: A How-to Approach*. Springer-Verlag New York Inc., 1994

[Lin12] Linev, Sergey: *CBM Online Software - Present State*. CBM Workshop on Online Data Processing. `https://indico.gsi.de/materialDisplay.py?contribId=0&sessionId=3&materialId=slides&confId=1838`. Version: September 2012

[MBG99] M. Bleicher, C. Spieles-S.A. Bass C. Ernst S. Soff L. Bravina M. Belkacem H. Weber H. S. E. Zabrodin Z. E. Zabrodin ; Greiner, W.: Relativistic Hadron-Hadron Collisions in the Ultra-Relativistic Quantum Molecular Dynamics Model. In: *J. Phys. G: Nucl. Part. Phys.* 25 (1999), S. 1859–1896

[Mic11] Michael Staib, et al: *Thermal Stretching of Large-Area GEM Foils Using an Infrared Heating Method*. March 2011

[Mor] Morino, Yuhei: *Study of Electron Identication Capability of ALICE TRD*, Department of Physics, Graduate School of Science, University of Tokyo, Diplomarbeit

[MS86] Matsui, T. ; Satz, H.: J/ψ suppression by quark-gluon plasma formation. In: *Physical Letters B* 178.17 (1986), S. 416 – 422

[Mue13] Mueller, Walter: *Summary of basic MUCH, RICH, TRD and ToF geometry parameters - v1.00*. CBM Tecnical Board, 24.06.2013

[Nie13] Niebur, Wolfgang: Geometrie of SIS-100 and SIS-300 Setup. In: *21st CBM Collaboration Meeting* (11.04.2013)

[Off14] http://www.fair-center.de/de/bau-konstruktion/wie-fair-gebaut-wird.html

[Para] Particle Data Group:The Center for X-Ray Optics: *Atomic Nuclear Properties and X-Ray Database*. Webpage. http://pdg.lbl.gov/AtomicNuclearProperties/

[Parb] Particle Data Group:The Center for X-Ray Optics: *Atomic Nuclear Properties and X-Ray Database*. Webpage. http://henke.lbl.gov/optical_constants/

[PRSZ08] Povh, Bogdan ; Rith, Klaus ; Scholz, Christoph ; Zetsche, Frank: *Teilchen und Kerne: Eine Einführung in die physikalischen Konzepte*. Berlin : Springer Berlin, 2008. – ISBN 9783540680758 3540680756 9783540680802 3540680802

[PSK13] Philip Stanley, Janet A. ; Kraimer, Marty ; GSI (Hrsg.): *EPICS Record Reference Manual*. GSI, 2013

[R. 97] R. Brun and F. Rademakers: ROOT - An Object Oriented Data Analysis Framework. In: *Nuclear Instruments and Methods* A 389 (1997), 81-86. http://root.cern.ch/

[R. 00] R. Barth, Yifei Du, H.G. Essel, R. Fritzsche, H . Güringer, J. Hoffmann, F. Humbert, N. Kurz, R.S. Mayer, W. Ott, D. Schall ; GSI (Hrsg.): *GSI Multi-Branch System Reference Manual*. GSI, 2000

[Rap11] Rapp, Ralf: Theory of Soft Electromagnetic Emission in Heavy-Ion Collisions. In: *Acta Phys.Polon* B42 (2011), S. 2823 – 2852

[Rei08] Reichelt, Patrick: *Bestimmung der Gasverstärkung der ALICE - TRD - Auslesekammern*. Bacherlor Thesis, 2008

[Rei11] Reichelt, Patrick: *Simulationsstudien zur Entwicklung des Übergangsstrahlungszählers für das CBM-Experiment*, Institut für Kernphysik Frankfurt, Diplomarbeit, 2011

[Reu13] Reuss, Kathrin: *Studien zur Ausdehnung des Eingangsfensters des CBM-TRDs*. Bacherlor Thesis, 2013

[RJ74] R. H. Millar ; J. R. Greening: Experimental X-ray mass attenuation coefficients for materials of low atomic number in the energy range 4 to 25 keV. In: *J. Phys. B: Atom. Molec. Phys* 7 (1974), S. 2332–2344

[ROS13] ROSNER, Günther: FAIR Progress. In: *21st CBM Collaboration Meeting* (08.04.2013)

[RT00] Rob Veenhof ; Tariq Mahmoud: *Mobility data for Xenon ions in Xenon*. Webpage. http://rjd.web.cern.ch/rjd/Alice/xenon_mobility.html. Version: 10 2000

[S. 03] S. Agostinelli et al.: Geant4 - a simulation toolkit. In: *Nuclear Instruments and Methods in Physics Research* 506 (2003), S. 250–303

[SBRR] Stefan B. Ruester, Michael Buballa Igor A. S. Verena Werth W. Verena Werth ; Rischke, Dirk H.: *The phase diagram of neutral quark matter: Self-consistent treatment of quark masses*. http://dx.doi.org/10.1103/PhysRevD.72.034004

[SMw] *File: Standard Model of Elementary Particles.svg (06.08.2013)*. http://en.wikipedia.org/wiki/File:Standard_Model_of_Elementary_Particles.svg

[Uni] University of Waikato: *The structure of the nucleus*. http://www.sciencelearn.org.nz/Contexts/Just-Elemental/Science-Ideas-and-Concepts/The-structure-of-the-nucleus

[Vee] Veenhof, Rob: *Garfield - simulation of gaseous detectors*. Software Package (Version 9 (7.36)). http://garfield.web.cern.ch/garfield/

[Vol] Voltaire: *Le dîner du comte de Boulainvilliers*

[Wil06] Wilk, Alexander: Analysis of the electron/pion separation capability with real size ALICE TRD prototypes using a neural network algorithm. In: *Nuclear Instruments and Methods in Physics Research A* (2006), S. 314–316

[Win72] Wind, H: *Function parametrization*. 1972

[WJ80] W. W. M. Allison ; J. H. Cobb: Relativistic charged particle identification by energy loss. In: *Ann. Rev. Nucl. Part. Sci.* 30 (1980), S. 253–98

[WV10] Walter F. J. Müller ; Volker Friese: CBM Progress Report 2009 / GSI Darmstadt. 2010. – Forschungsbericht

[WYH10] W. Yu, H. A. ; Hartig, M.: Performance studies on the CBM-TRD using J/Ψ. In: *CBM Progress Report 2010* (2010), S. 41

List of Runs 2011

								Position 1 FFM004		Position 2 FFM002		Position 3 FFM006		Position 4 FFM005		
Run #	Set	Date	Start	End	Beam	Trigger	Gas	Radiator	HV [V]	Radiator	HV [V]	Radiator	HV [V]	Radiator	HV [V]	Comment
Te_run6	-	18.10.					Argon	ALICE	2100	ALICE	2100	ALICE	1910	ALICE	2200	
Te_run1910000	-	19.10.					Argon	ALICE	2100	ALICE	2100	ALICE	1910	ALICE	2200	
Te_run1910001	-	19.10.					Argon	ALICE	2100	ALICE	2100	ALICE	1910	ALICE	2200	
Te_run1910002	-	19.10.					Argon	ALICE	2100	ALICE	2100	ALICE	1910	ALICE	2200	
Te_run1910004	-	19.10.					Argon	ALICE	2100	ALICE	2100	ALICE	1910	ALICE	2200	
Te_run1910005	-	19.10.				mu	Argon	ALICE	2100	ALICE	2100	ALICE	1910	ALICE	2200	
Te_run1910006	-	19.10.				mu	Argon	ALICE	2100	ALICE	2100	ALICE	1910	ALICE	2200	
Te_run1910007	-	19.10.	11:15	12:00		mu	Argon	ALICE	2100	ALICE	2100	ALICE	1910	ALICE	2200	
Te_run1910008	-	19.10.	12:10	12:15		mu	Argon	ALICE	2100	ALICE	2100	ALICE	1910	ALICE	2200	
Te_run1910009	-	19.10.	13:00	13:50		mu	Argon	ALICE	2100	ALICE	2100	ALICE	1910	ALICE	2200	
Te_run1910020	-	19.10.	14:04	14:10		mu	Argon	ALICE	2100	ALICE	2100	ALICE	1910	ALICE	2200	
Be_run1910021	-	19.10.	14:15		4 GeV/c	s1+s2	Argon	ALICE	2100	ALICE	2100	ALICE	1910	ALICE	2200	
Be_run1910022	-	19.10.			4 GeV/c	s1+s2	Argon	ALICE	2100	ALICE	2100	ALICE	1910	ALICE	2200	
Be_run1910023	-	19.10.			2 GeV/c	s1+s2	Argon	ALICE	2100	ALICE	2100	ALICE	1910	ALICE	2200	
Be_run1910030	-	19.10.	21:25	21:45	2 GeV/c	s1+s2	Argon	ALICE	2100	ALICE	2100	ALICE	1910	ALICE	2200	
Be_run1910031	-	19.10.	21:45	21:49	2 GeV/c	s1+s2	Argon	ALICE	2100	ALICE	2100	ALICE	1910	ALICE	2200	
Be_run1910032	-	19.10.	21:50	21:48	2 GeV/c	s1+s2	Argon	ALICE	2100	ALICE	2100	ALICE	1910	ALICE	2200	
Be_run1910042	-	19.10.	22:02	22:15	2 GeV/c	s1+s2	Argon	ALICE	2100	ALICE	2100	ALICE	1910	ALICE	2200	
Be_run1910043	-	19.10.	22:25	22:44	3 GeV/c	s1+s2	Argon	ALICE	2120	ALICE	2140	ALICE	1910	ALICE	2250	
Be_run1910044	-	19.10.	22:51	23:07	4 GeV/c	s1+s2	Argon	ALICE	2120	ALICE	2160	ALICE	1910	ALICE	2280	
Be_run1910045	-	19.10.	23:35	23:55	6 GeV/c	s1+s2	Argon	ALICE	2120	ALICE	2180	ALICE	1910	ALICE	2280	
Be_run1910046	-	20.10.	00:07	00:17	8 GeV/c	s1+s2	Argon	ALICE	2120	ALICE	2180	ALICE	1910	ALICE	2280	
Be_run1910047	-	20.10.	00:28	00:49	4 GeV/c	s1+s2	Argon	ALICE	2120	ALICE	2180	ALICE	1910	ALICE	2280	
Be_run1910048	-	20.10.	00:55	00:57	4 GeV/c	s1+s2	Argon	ALICE	2120	ALICE	2180	ALICE	1910	ALICE	2280	
Be_run1910049	-	20.10.	00:58	01:01	4 GeV/c	s1+s2	Argon	ALICE	2120	ALICE	2180	ALICE	1910	ALICE	2280	
Be_run1910050	-	20.10.	01:01	01:05	4 GeV/c	s1+s2	Argon	ALICE	2120	ALICE	2180	ALICE	1910	ALICE	2280	
Be_run1910052	-	20.10.	01:28	02:53	4 GeV/c	s1+s2	Argon	ALICE	2120	ALICE	2180	ALICE	1910	ALICE	2280	
Be_run2010000	-	20.10.	12:03	13:50	3 GeV/c	s1+s2	Argon	ALICE	2120	ALICE	2180	ALICE	1910	ALICE	2280	
Te_run2010000	-	20.10.	13:50	14:10	-	Dubna1	Argon	ALICE	2120	ALICE	2180	ALICE	1910	ALICE	2280	
Be_run2010001	-	20.10.	18:10	18:20	3 GeV/c	Ch2+Hod+S2	Argon	ALICE	2130	ALICE	2205	ALICE	1910	ALICE	2300	
Be_run2010002	1	20.10.	18:30	18:50	3 GeV/c	Ch2+Hod+S2	Argon	ALICE	2130	ALICE	2205	ALICE	1910	ALICE	2300	
Be_run2010003	1	20.10.	19:20	20:25	3 GeV/c	Ch2+Hod+S2	Argon	ALICE	2130	ALICE	2205	ALICE	1910	ALICE	2300	
Be_run2010004	1	20.10.	20:34	21:15	3 GeV/c	Ch2+Hod+S2	Argon	ALICE	2130	ALICE	2205	ALICE	1910	ALICE	2300	
Be_run2010005	1	20.10.	21:16	21:35	3 GeV/c	Ch2+Hod+S2	Argon	ALICE	2130	ALICE	2205	ALICE	1910	ALICE	2300	
Be_run2010006	1	20.10.	21:35	22:00	3 GeV/c	Ch2+Hod+S2	Argon	ALICE	2130	ALICE	2205	ALICE	1910	ALICE	2300	
Be_run2010007	-	21.10.	00:10	00:25	3 GeV/c	Ch2+Hod+S2	Ar+Xe	ALICE	2130	ALICE	2205	ALICE	1910	ALICE	2300	Changes from Ar to Xe
Be_run2010008	-	21.10.	00:35	00:58	3 GeV/c	Ch2+Hod+S2	Ar+Xe	ALICE	2130	ALICE	2205	ALICE	1910	ALICE	2300	
Be_run2110000	2	21.10.	11:05	11:12	3 GeV/c	Ch2+Hod+S2	Xenon	ALICE	2130	ALICE	2205	ALICE	1910	ALICE	2325	
Be_run2110001	2	21.10.	11:48	12:32	3 GeV/c	Ch2+Hod+S2	Xenon	ALICE	2130	ALICE	2205	ALICE	1910	ALICE	2325	
Be_run2110002	2	21.10.	12:36	12:46	3 GeV/c	Ch2+Hod+S2	Xenon	ALICE	2130	ALICE	2205	ALICE	1910	ALICE	2325	
Be_run2110003	2	21.10.	12:47	12:53	3 GeV/c	Ch2+Hod+S2	Xenon	ALICE	2130	ALICE	2205	ALICE	1910	ALICE	2325	
Be_run2110004	2	21.10.	12:53		3 GeV/c	Ch2+Hod+S2	Xenon	ALICE	2130	ALICE	2205	ALICE	1910	ALICE	2325	RICH tests, maybe bad data

Run #	Set	Date	Start	End	Beam	Trigger	Gas	Position 1 FFM004 Radiator	HV [V]	Position 2 FFM002 Radiator	HV [V]	Position 3 FFM006 Radiator	HV [V]	Position 4 FFM005 Radiator	HV [V]	Comment
Be_run2110009	2	21.10.	13:40		$3\,GeV/c$	Ch2+Hod+S2	Xenon	ALICE	2130	ALICE	2205	ALICE	1910	ALICE	2325	Powercut in front area (RICH), Problems with EPICS on recu-very
Be_run2110010	-	21.10.	15:10	15:36	$3\,GeV/c$	Ch2+Hod+S2	Xenon	ALICE	2130	ALICE	2205	ALICE	1910	ALICE	2325	TTree corrupted due to power cut?
Be_run2110011	2	21.10.	15:57	16:01	$3\,GeV/c$	Ch2+Hod+S2	Xenon	ALICE	2130	ALICE	2205	ALICE	1910	ALICE	2325	
Be_run2110012	2	21.10.	16:01	16:05	$3\,GeV/c$	Ch2+Hod+S2	Xenon	ALICE	2130	ALICE	2205	ALICE	1910	ALICE	2325	
Be_run2110012	2	21.10.	16:08	16:13	$3\,GeV/c$	Ch2+Hod+S2	Xenon	ALICE	2130	ALICE	2205	ALICE	1910	ALICE	2325	
Be_run2110013	2	21.10.	16:14	16:15	$3\,GeV/c$	Ch2+Hod+S2	Xenon	ALICE	2130	ALICE	2205	ALICE	1910	ALICE	2325	
Te_run2110014	2	21.10.	16:15	16:18	$3\,GeV/c$	Ch2+Hod+S2	Xenon	ALICE	2130	ALICE	2205	ALICE	1910	ALICE	2325	
Be_run2110015	2	21.10.	16:18	18:00	$3\,GeV/c$	Ch2+Hod+S2	Xenon	ALICE	2130	ALICE	2205	ALICE	1910	ALICE	2325	Run stopped due to SP problems
Te_run2110016	2	21.10.	18:14	18:16	-	Ch2+Hod+S2	Xenon	ALICE	2130	ALICE	2205	ALICE	1910	ALICE	2325	
Be_run2110017	3	21.10.	20:58	21:24	$3\,GeV/c$	Ch2+Hod+S2	Xenon	NO	2130	NO	2205	NO	1910	NO	2325	
Be_run2110018	3	21.10.	21:26	22:21	$3\,GeV/c$	Ch2+Hod+S2	Xenon	NO	2130	NO	2205	NO	1910	NO	2325	
Be_run2110019	3	21.10.	22:27	22:50	$3\,GeV/c$	Ch2+Hod+S2	Xenon	NO	2130	NO	2205	NO	1910	NO	2325	
Be_run2110020	3	21.10.	22:52	23:59	$3\,GeV/c$	Ch2+Hod+S2	Xenon	NO	2130	NO	2205	NO	1910	NO	2325	
Be_run2110021	4	22.10.	00:29	02:32	$3\,GeV/c$	Ch2+Hod+S2	Xenon	ALICE	2150	ALICE	2230	ALICE	1910	F300	2325	
Be_run2110022	4	22.10.	02:47	03:08	$3\,GeV/c$	Ch2+Hod+S2	Xenon	ALICE	2150	ALICE	2230	ALICE	1910	F300	2325	
Be_run2110023	5	22.10.	03:26	05:26	$3\,GeV/c$	Ch2+Hod+S2	Xenon	ALICE	2150	ALICE	2230	ALICE	1910	F250	2325	
Be_run2110024	6	22.10.	05:36	08:05	$3\,GeV/c$	Ch2+Hod+S2	Xenon	ALICE	2150	ALICE	2230	ALICE	1910	F200	2325	
Be_run2110026	7	22.10.	08:28	09:51	$3\,GeV/c$	Ch2+Hod+S2	Xenon	ALICE	2150	ALICE	2230	ALICE	1910	F150	2325	
Be_run2210000	8	22.10.	10:52	12:30	$3\,GeV/c$	Ch2+Hod+S2	Xenon	ALICE	2150	ALICE	2230	ALICE	1910	F350	2325	
Be_run2210001	-	22.10.	13:00	14:45	$3\,GeV/c$	Ch2+Hod+S2	Xenon	ALICE	2150	ALICE	0	ALICE	1910	F350	2325	Problems with Baseline: FFM002 OFF!
Be_run2210002	8	22.10.	16:20	17:06	$3\,GeV/c$	Ch2+Hod+S2	Xenon	ALICE	2150	ALICE	2230	ALICE	1910	F350	2325	
Be_run2210003	8	22.10.	17:07	18:14	$3\,GeV/c$	Ch2+Hod+S2	Xenon	ALICE	2150	ALICE	2230	ALICE	1910	F350	2325	
Be_run2210004	-	22.10.	18:44	18:50	$3\,GeV/c$	Ch2+Hod+S2	Xenon	ALICE	0	ALICE	0	ALICE	0	F350	0	ALL FFM ROC's OFF
Be_run2210005	-	22.10.	18:51	20:00	$3\,GeV/c$	Ch2+Hod+S2	Xenon	ALICE	0	ALICE	0	ALICE	0	F350	0	ALL FFM ROC's OFF
Be_run2210006	9	22.10.	20:01	20:15	$3\,GeV/c$	Ch2+Hod+S2	Xenon	ALICE	2150	ALICE	2230	ALICE	1910	F350	2325	
Be_run2210007	10	22.10.	21:32	22:19	$3\,GeV/c$	Ch2+Hod+S2	Xenon	ALICE	2150	ALICE	2230	F250	1910	ALICE	2325	
Be_run2210008	10	22.10.	22:20	23:05	$3\,GeV/c$	Ch2+Hod+S2	Xenon	ALICE	2150	ALICE	2230	F250	1910	ALICE	2325	
Be_run2210009	10	22.10.	23:05	23:50	$3\,GeV/c$	Ch2+Hod+S2	Xenon	ALICE	2150	ALICE	2230	F250	1910	ALICE	2350	
Be_run2210010	11	23.10.	00:02	00:50	$3\,GeV/c$	Ch2+Hod+S2	Xenon	ALICE	2150	ALICE	2230	F350	1860	ALICE	2375	
Be_run2210011	11	23.10.	00:51	02:31	$3\,GeV/c$	Ch2+Hod+S2	Xenon	ALICE	2150	ALICE	2230	F350	1860	ALICE	2375	
Be_run2210012	12	23.10.	02:40	04:50	$3\,GeV/c$	Ch2+Hod+S2	Xenon	ALICE	2170	ALICE	2230	F300	1860	ALICE	2400	Run Stopped due to MBS Problem
Be_run2310000	13	23.10.	09:05	09:15	$3\,GeV/c$	Ch2+Hod+S2	Xenon	ALICE	2185	ALICE	2230	F200	1910	ALICE	2400	
Be_run2310001	-	23.10.	09:22	11:59	$3\,GeV/c$	Ch2+Hod+S2	Xenon	ALICE	2185	ALICE	2230	F200	1910	ALICE	2400	
Be_run2310002	14	23.10.	12:36	12:38	$3\,GeV/c$	Ch2+Hod+S2	Xenon	ALICE	2200	ALICE	2230	F150	1910	ALICE	2400	
Be_run2310003	14	23.10.	12:39	14:34	$3\,GeV/c$	Ch2+Hod+S2	Xenon	ALICE	2200	ALICE	2230	F150	1910	ALICE	2425	
Be_run2310004	14	23.10.	15:12	17:39	$3\,GeV/c$	Ch2+Hod+S2	Xenon	ALICE	2220	ALICE	2230	F150	1910	ALICE	2450	
Be_run2310005	15	23.10.	18:24	19:05	$3\,GeV/c$	Ch2+Hod+S2	Xenon	ALICE	2220	ALICE	2230	Type N	1910	ALICE	2450	
Be_run2310006	15	23.10.	19:06	19:17	$3\,GeV/c$	Ch2+Hod+S2	Xenon	ALICE	2220	ALICE	2230	Type N	1910	ALICE	2450	
Be_run2310007	15	23.10.	19:20	19:59	$3\,GeV/c$	Ch2+Hod+S2	Xenon	ALICE	2220	ALICE	2230	Type N	1910	ALICE	2450	
Be_run2310008	15	23.10.	20:00	20:41	$3\,GeV/c$	Ch2+Hod+S2	Xenon	ALICE	2220	ALICE	2230	Type N	1910	ALICE	2450	
Be_run2310009	15	23.10.	20:42	21:05	$3\,GeV/c$	Ch2+Hod+S2	Xenon	ALICE	2220	ALICE	2230	Type N	1910	ALICE	2450	
Be_run2310010	-	23.10.	22:11	23:15	$3\,GeV/c$	Ch2+Hod+S2	Xenon	ALICE	2220	ALICE	1620-1800	F250	1885	ALICE	2500	HV tuning FFM001
Be_run2310011	-	23.10.	23:15	00:01	$3\,GeV/c$	Ch2+Hod+S2	Xenon	ALICE	2220	ALICE	1620	F250	1885	ALICE	2500	
Be_run2310012	16	24.10.	00:08	00:20	$3\,GeV/c$	Ch2+Hod+S2	Xenon	ALICE	2220	ALICE	1600	F250	1950	ALICE	2500	
Be_run2310013	16	24.10.	00:21	01:05	$3\,GeV/c$	Ch2+Hod+S2	Xenon	ALICE	2220	ALICE	1600	F250	1950	ALICE	2500	
Be_run2310014	16	24.10.	01:08	02:00	$3\,GeV/c$	Ch2+Hod+S2	Xenon	ALICE	2220	ALICE	1600	F250	1950	ALICE	2500	
Be_run2310015	16	24.10.	02:01	02:33	$3\,GeV/c$	Ch2+Hod+S2	Xenon	ALICE	2220	ALICE	1600	F250	1950	ALICE	2500	

Run #	Set	Date	Start	End	Beam	Trigger	Gas	Position 1 FFM004 Radiator	Position 1 FFM004 HV [V]	Position 2 FFM002 Radiator	Position 2 FFM002 HV [V]	Position 3 FFM006 Radiator	Position 3 FFM006 HV [V]	Position 4 FFM005 Radiator	Position 4 FFM005 HV [V]	Comment
Be_run2310016	16	24.10.	02:34	03:00	$3\,GeV/c$	Ch2+Hod+S2	Xenon	ALICE	2220	ALICE	1600	F250	1950	ALICE	2500	
Be_run2310017	16	24.10.	03:01	03:28	$3\,GeV/c$	Ch2+Hod+S2	Xenon	ALICE	2220	ALICE	1600	F250	1800	ALICE	2500	
Be_run2310018	16	24.10.	03:28	03:40	$3\,GeV/c$	Ch2+Hod+S2	Xenon	ALICE	2220	ALICE	1600	F250	1800	ALICE	2500	
Be_run2310019	16	24.10.	03:59	04:07	$3\,GeV/c$	Ch2+Hod+S2	Xenon	ALICE	2220	ALICE	1600	F250	1800	ALICE	2500	
Be_run2310021	16	24.10.	04:10	04:32	$3\,GeV/c$	Ch2+Hod+S2	Xenon	ALICE	2220	ALICE	1600	F250	1800	ALICE	2500	
Be_run2310023	16	24.10.	04:42	04:50	$3\,GeV/c$	Ch2+Hod+S2	Xenon	ALICE	2220	ALICE	1600	F250	1800	ALICE	2500	
Be_run2310024	16	24.10.	04:52	05:11	$3\,GeV/c$	Ch2+Hod+S2	Xenon	ALICE	2220	ALICE	1600	F250	1800	ALICE	2500	
Be_run2310025	16	24.10.	05:11	05:36	$3\,GeV/c$	Ch2+Hod+S2	Xenon	ALICE	2220	ALICE	1600	F250	1800	ALICE	2500	
Be_run2310026	16	24.10.	05:36	06:19	$3\,GeV/c$	Ch2+Hod+S2	Xenon	ALICE	2220	ALICE	1600	F250	1800	ALICE	2500	
Be_run2310027	16	24.10.	06:19	06:44	$3\,GeV/c$	Ch2+Hod+S2	Xenon	ALICE	2220	ALICE	1600	F250	1800	ALICE	2500	
Be_run2310028	16	24.10.	06:45	07:31	$3\,GeV/c$	Ch2+Hod+S2	Xenon	ALICE	2220	ALICE	1600	F250	1800	ALICE	2500	
Be_run2310029	16	24.10.	07:32	07:55	$3\,GeV/c$	Ch2+Hod+S2	Xenon	ALICE	2220	ALICE	1600	F250	1800	ALICE	2500	
Be_run2410000	16	24.10.	07:58	08:23	$3\,GeV/c$	Ch2+Hod+S2	Xenon	ALICE	2220	ALICE	1600	F250	1800	ALICE	2500	
Be_run2410001	16	24.10.	08:25	09:10	$3\,GeV/c$	Ch2+Hod+S2	Xenon	ALICE	2220	ALICE	1600	F250	1800	ALICE	2500	
Be_run2410002	16	24.10.	09:15	10:12	$3\,GeV/c$	Ch2+Hod+S2	Xenon	ALICE	2220	ALICE	1600	F250	1800	ALICE	2500	
Be_run2410003	16	24.10.	10:21	10:50	$3\,GeV/c$	Ch2+Hod+S2	Xenon	ALICE	2220	ALICE	1600	F250	1800	ALICE	2500	
Be_run2410004	16	24.10.	10:51	11:03	$3\,GeV/c$	Ch2+Hod+S2	Xenon	ALICE	2220	ALICE	1600	F250	1800	ALICE	2500	
Be_run2410005	16	24.10.	11:05	11:30	$3\,GeV/c$	Ch2+Hod+S2	Xenon	ALICE	2220	ALICE	1600	F250	1800	ALICE	2500	
Be_run2410006	16	24.10.	11:32	12:01	$3\,GeV/c$	Ch2+Hod+S2	Xenon	ALICE	2220	ALICE	1600	F250	1800	ALICE	2500	
Be_run2410007	16	24.10.	12:03	12:14	$3\,GeV/c$	Ch2+Hod+S2	Xenon	ALICE	2220	ALICE	1600	F250	1800	ALICE	2500	
Be_run2410008	16	24.10.	12:15	12:30	$3\,GeV/c$	Ch2+Hod+S2	Xenon	ALICE	2220	ALICE	1600	F250	1800	ALICE	2500	
Be_run2410009	16	24.10.	12:32	13:20	$3\,GeV/c$	Ch2+Hod+S2	Xenon	ALICE	2220	ALICE	1600	F250	1800	ALICE	2500	
Be_run2410010	16	24.10.	13:22	13:58	$3\,GeV/c$	Ch2+Hod+S2	Xenon	ALICE	2220	ALICE	1600	F250	1800	ALICE	2500	
Be_run2410011	-	24.10.	16:30	16:44	$2\,GeV/c$	Ch2+Hod+S2	Xenon	ALICE	2220	ALICE	1600	F250	1800	ALICE	2220	FFM001 shows no data
Be_run2410012	17	24.10.	16:45	17:41	$2\,GeV/c$	Ch2+Hod+S2	Xenon	ALICE	2220	ALICE	1600	F250	1800	ALICE	2220	
Be_run2410013	17	24.10.	17:48	18:16	$2\,GeV/c$	Ch2+Hod+S2	Xenon	ALICE	2220	ALICE	1600	F250	1800	ALICE	2220	
Be_run2410014	17	24.10.	18:18	18:35	$2\,GeV/c$	Ch2+Hod+S2	Xenon	ALICE	2220	ALICE	1600	F250	1800	ALICE	2220	
Be_run2410015	17	24.10.	18:36	18:52	$2\,GeV/c$	Ch2+Hod+S2	Xenon	ALICE	2220	ALICE	1600	F250	1800	ALICE	2220	
Be_run2410016	17	24.10.	18:53	19:00	$2\,GeV/c$	Ch2+Hod+S2	Xenon	ALICE	2220	ALICE	1600	F250	1800	ALICE	2220	
Be_run2410017	17	24.10.	19:10	20:19	$2\,GeV/c$	Ch2+Hod+S2	Xenon	ALICE	2220	ALICE	1600	F250	1800	ALICE	2220	
Be_run2410018	17	24.10.	20:35	21:40	$2\,GeV/c$	Ch2+Hod+S2	Xenon	ALICE	2220	ALICE	1600	F250	1800	ALICE	2220	
Be_run2410019	17	24.10.	21:43	21:49	$2\,GeV/c$	Ch2+Hod+S2	Xenon	ALICE	2220	ALICE	1600	F300	1800	ALICE	2220	
Be_run2410020	17	24.10.	21:49	22:00	$2\,GeV/c$	Ch2+Hod+S2	Xenon	ALICE	2220	ALICE	1600	F300	1800	ALICE	2220	
Be_run2410021	18	24.10.	23:00	23:25	$4\,GeV/c$	Ch2+Hod+S2	Xenon	ALICE	2220	ALICE	1600	F300	1800	ALICE	2220	
Be_run2410022	18	24.10.	23:45	04:51	$4\,GeV/c$	Ch2+Hod+S2	Xenon	ALICE	2220	ALICE	1600	F300	1800	ALICE	2220	
Be_run2410023	18	25.10.	04:52	07:27	$4\,GeV/c$	Ch2+Hod+S2	Xenon	ALICE	2220	ALICE	1600	F300	1800	ALICE	2240	
Be_run2410024	18	25.10.	07:31	08:02	$4\,GeV/c$	Ch2+Hod+S2	Xenon	ALICE	2220	ALICE	1600	F300	1800	ALICE	2240	
Be_run2410025	18	25.10.	08:08		$4\,GeV/c$	Ch2+Hod+S2	Xenon	ALICE	2220	ALICE	1600	F300	1800	ALICE	2240	
Be_run2510001	18	25.10.	08:53	09:00	$4\,GeV/c$	Ch2+Hod+S2	Xenon	ALICE	2220	ALICE	1600	F300	1800	ALICE	2240	
Be_run2510002	18	25.10.	09:03	09:08	$4\,GeV/c$	Ch2+Hod+S2	Xenon	ALICE	2220	ALICE	1600	F300	1800	ALICE	2240	
Be_run2510003	18	25.10.	09:11	10:05	$4\,GeV/c$	Ch2+Hod+S2	Xenon	ALICE	2220	ALICE	1600	F300	1800	ALICE	2240	
Be_run2510004	19	25.10.	10:50	11:44	$6\,GeV/c$	Ch2+Hod+S2	Xenon	ALICE	2220	ALICE	1600	F300	1800	ALICE	2240	
Be_run2510005	19	25.10.	13:11	13:12	$6\,GeV/c$	Ch2+Hod+S2	Xenon	ALICE	2220	ALICE	1600	F300	1800	ALICE	2240	
Be_run2510006	19	25.10.	13:15	13:35	$6\,GeV/c$	Ch2+Hod+S2	Xenon	ALICE	2220	ALICE	1600	F300	1800	ALICE	2240	
Be_run2510007	19	25.10.	13:57	14:04	$6\,GeV/c$	Ch2+Hod+S2	Xenon	ALICE	2220	ALICE	1600	F300	1800	ALICE	2240	
Be_run2510008	19	25.10.	14:05	14:50	$6\,GeV/c$	Ch2+Hod+S2	Xenon	ALICE	2220	ALICE	1600	F300	1800	ALICE	2240	
Be_run2510009	19	25.10.	15:08	16:12	$6\,GeV/c$	Ch2+Hod+S2	Xenon	ALICE	2220	ALICE	1600	F300	1800	ALICE	2240	
Be_run2510010	19	25.10.	16:17	16:35	$6\,GeV/c$	Ch2+Hod+S2	Xenon	ALICE	2220	ALICE	1600	F300	1800	ALICE	2240	
Be_run2510011	19	25.10.	16:40	17:30	$6\,GeV/c$	Ch2+Hod+S2	Xenon	ALICE	2220	ALICE	1600	F300	1800	ALICE	2240	
Be_run2510012	19	25.10.	17:45	18:45	$6\,GeV/c$	Ch2+Hod+S2	Xenon	ALICE	2220	ALICE	1600	F300	1800	ALICE	2240	
Be_run2510013	20	25.10.	19:10	20:36	$10\,GeV/c$	Ch2+Hod+S2	Xenon	ALICE	2220	ALICE	1600	F300	1800	ALICE	2240	
Be_run2510014	21	25.10.	21:20	00:48	$8\,GeV/c$	Ch2+Hod+S2	Xenon	ALICE	2220	ALICE	1600	F300	1800	ALICE	2240	
Be_run2610001	21	26.10.	01:21	04:30	$8\,GeV/c$	Ch2+Hod+S2	Xenon	ALICE	2220	ALICE	1600	F300	1800	ALICE	2240	
Be_run2610002	21	26.10.	04:50	08:00	$8\,GeV/c$	Ch2+Hod+S2	Xenon	ALICE	2220	ALICE	1600	F300	1800	ALICE	2240	
Te_run2610003	21	26.10.	09:50	09:57	$8\,GeV/c$	Bucharest0	Xenon	ALICE	2220	ALICE	1600	F300	1800	ALICE	2240	
Te_run2610004	21	26.10.	10:02	10:13	$8\,GeV/c$	Bucharest0	Xenon	ALICE	2220	ALICE	1600	F300	1800	ALICE	2240	
Te_run2610005	21	26.10.	10:15	10:25	$8\,GeV/c$	Bucharest1	Xenon	ALICE	2220	ALICE	1600	F300	1800	ALICE	2240	

Run #	Set	Date	Start	End	Beam	Trigger	Gas	Position 1 FFM004 Radiator	Position 1 FFM004 HV [V]	Position 2 FFM002 Radiator	Position 2 FFM002 HV [V]	Position 3 FFM006 Radiator	Position 3 FFM006 HV [V]	Position 4 FFM005 Radiator	Position 4 FFM005 HV [V]	Comment
Be_run2610006	22	26.10.	22:15	22:40	$4\,GeV/c$	Ch2+Hod+S2	Xenon	F350	2200	ALICE	1600	ALICE	1800	ALICE	2240	Segmented Scintilator between FFM001 and FFM006
Be_run2610007	22	26.10.	22:48	23:25	$4\,GeV/c$	Ch2+Hod+S2	Xenon	F350	2200	ALICE	1700	ALICE	1800	ALICE	2240	
Be_run2610008	22	26.10.	23:26	00:09	$4\,GeV/c$	Ch2+Hod+S2	Xenon	F350	2200	ALICE	1700	ALICE	1800	ALICE	2240	
Be_run2610009	22	26.10.	23:26	00:09	$4\,GeV/c$	Ch2+Hod+S2	Xenon	F350	2200	ALICE	1700	ALICE	1800	ALICE	2240	Double counted run?
Be_run2610010	22	27.10.	00:10	01:00	$4\,GeV/c$	Ch2+Hod+S2	Xenon	F350	2200	ALICE	1700	ALICE	1800	ALICE	2240	
Be_run2710001	22	27.10.	01:10	03:02	$4\,GeV/c$	Ch2+Hod+S2	Xenon	F350	2200	ALICE	1700	ALICE	1800	ALICE	2240	
Be_run2710002	22	27.10.	03:18	04:30	$4\,GeV/c$	Ch2+Hod+S2	Xenon	F350	2200	ALICE	1700	ALICE	1800	ALICE	2240	
Be_run2710003	22	27.10.	04:32	06:46	$4\,GeV/c$	Ch2+Hod+S2	Xenon	F350	2200	ALICE	1700	ALICE	1800	ALICE	2240	
Be_run2710004	22	27.10.	06:54	08:13	$4\,GeV/c$	Ch2+Hod+S2	Xenon	F350	2200	ALICE	1700	ALICE	1800	ALICE	2240	
Be_run2710005	22	27.10.	08:15	09:11	$4\,GeV/c$	Ch2+Hod+S2	Xenon	F350	2200	ALICE	1700	ALICE	1800	ALICE	2240	
Be_run2710006	22	27.10.	09:20	10:26	$4\,GeV/c$	Ch2+Hod+S2	Xenon	F350	2200	ALICE	1700	ALICE	1800	ALICE	2240	
Be_run2710007	22	27.10.	11:20	11:23	$4\,GeV/c$	Ch2+Hod+S2	Xenon	F350	2200	ALICE	1700	ALICE	1800	ALICE	2240	
Be_run2710008	23	27.10.	11:28	12:44	$4\,GeV/c$	Ch2+Hod+S2	Xenon	F300	2200	ALICE	1750	ALICE	1800	ALICE	2400	
Be_run2710009	23	27.10.	12:50	13:30	$4\,GeV/c$	Ch2+Hod+S2	Xenon	F300	2200	ALICE	1650	ALICE	1800	ALICE	2400	
Be_run2710010	23	27.10.	14:25	15:08	$4\,GeV/c$	Ch2+Hod+S2	Xenon	F300	2200	ALICE	1650	ALICE	1800	ALICE	2400	
Te_run2710011	23	27.10.	15:30	15:38	$4\,GeV/c$	Ch2+Hod+S2	Xenon	F300	2200	ALICE	1650	ALICE	1800	ALICE	2400	
Te_run2710012	23	27.10.	15:50	16:37	$4\,GeV/c$	Ch2+Hod+S2	Xenon	F300	2200	ALICE	1650	ALICE	1800	ALICE	2400	
Be_run2710013	23	27.10.	16:57	17:37	$4\,GeV/c$	Ch2+Hod+S2	Xenon	F300	2200	ALICE	1650	ALICE	1800	ALICE	2400	RICH moved, Aluminium profile in beam
Be_run2710014	23	27.10.	17:51	18:00	$4\,GeV/c$	Ch2+Hod+S2	Xenon	F300	2200	ALICE	1650	ALICE	1800	ALICE	2400	
Be_run2710015	23	27.10.	18:07	18:20	$4\,GeV/c$	Ch2+Hod+S2	Xenon	F300	2200	ALICE	1650	ALICE	1800	ALICE	2400	
Be_run2710016	23	27.10.	18:21	18:26	$4\,GeV/c$	Ch2+Hod+S2	Xenon	F300	2200	ALICE	1650	ALICE	1800	ALICE	2400	
Be_run2710017	23	27.10.	18:41	20:41	$4\,GeV/c$	Ch2+Hod+S2	Xenon	F300	2200	ALICE	1650	ALICE	1800	ALICE	2400	
Be_run2710018	23	27.10.	20:44	20:49	$4\,GeV/c$	Ch2+Hod+S2	Xenon	F300	2200	ALICE	1650	ALICE	1800	ALICE	2400	
Be_run2710019	23	27.10.	21:38	21:40	$4\,GeV/c$	Ch2+Hod+S2	Xenon	F300	2200	ALICE	1650	ALICE	1800	ALICE	2400	
Be_run2710020	-	27.10.	21:50	22:36	$2\,GeV/c$	Ch2+Hod+S2	Xenon	F300	2200	ALICE	1650	ALICE	1800	ALICE	2400	
Be_run2710021	-	27.10.	22:39	22:39	$2\,GeV/c$	Hod+S2	Xenon	F300	2200	ALICE	1650	ALICE	1800	ALICE	2400	
Be_run2710022	23	27.10.	22:40	22:41	$2\,GeV/c$	Hod+S2	Xenon	F300	2200	ALICE	1650	ALICE	1800	ALICE	2400	
Be_run2710023	23	27.10.	23:00	23:13	$2\,GeV/c$	Hod+S2	Xenon	F300	2200	ALICE	1650	ALICE	1800	ALICE	2400	
Be_run2710025	23	27.10.	23:56	00:27	$2\,GeV/c$	Hod+S2	Xenon	F300	2200	ALICE	1650	ALICE	1800	ALICE	2400	
Be_run2710026	23	27.10.	00:37	01:23	$2\,GeV/c$	Hod+S2	Xenon	F300	2200	ALICE	1650	ALICE	1800	ALICE	2400	
Be_run2710028	23	28.10.	01:27	08:14	$2\,GeV/c$	Hod+S2	Xenon	F300	2200	ALICE	1650	ALICE	1800	ALICE	2400	
Be_run2810001	23	28.10.	08:45	09:30	$2\,GeV/c$	Hod+S2	Xenon	F300	2200	ALICE	1650	ALICE	1800	ALICE	2400	
Be_run2810002	-	28.10.	09:30	09:35	$2\,GeV/c$	Hod+S2	Xenon	F300	2200	ALICE	1650	ALICE	1800	ALICE	2400	
Be_run2810003	23	28.10.	09:35	09:50	$2\,GeV/c$	Hod+S2	Xenon	F300	2200	ALICE	1650	ALICE	1800	ALICE	2400	
Be_run2810005	24	28.10.	11:07	13:00	$4\,GeV/c$	Ch2+Hod+S2	Xenon	F250	2200	ALICE	1650	ALICE	1800	NO	2400	
Be_run2810006	24	28.10.	13:03	13:21	$4\,GeV/c$	Ch2+Hod+S2	Xenon	F200	2200	ALICE	1650	ALICE	1800	NO	2400	
Be_run2810007	24	28.10.	13:25	13:56	$4\,GeV/c$	Ch2+Hod+S2	Xenon	F200	2200	ALICE	1650	ALICE	1800	NO	2400	
Be_run2810008	24	28.10.	13:58	14:02	$4\,GeV/c$	Ch2+Hod+S2	Xenon	F200	2200	ALICE	1650	ALICE	1800	NO	2400	
Be_run2810009	24	28.10.	14:03	14:05	$4\,GeV/c$	Ch2+Hod+S2	Xenon	F200	2200	ALICE	1650	ALICE	1800	NO	2400	
Be_run2810010	25	28.10.	15:30	15:45	$4\,GeV/c$	Ch2+Hod+S2	Xenon	F200	2245	ALICE	1650	ALICE	1800	ALICE	2400	
Be_run2810011	25	28.10.	16:11	17:38	$4\,GeV/c$	Ch2+Hod+S2	Xenon	F200	2195	ALICE	1650	ALICE	1800	ALICE	2400	
Be_run2810012	25	28.10.	17:41	18:45	$4\,GeV/c$	Ch2+Hod+S2	Xenon	F200	2195	ALICE	1650	ALICE	1800	ALICE	2400	
Be_run2810013	25	28.10.	19:21	19:50	$4\,GeV/c$	Ch2+Hod+S2	Xenon	F200	2195	ALICE	1650	ALICE	1800	ALICE	2400	Powercut in whole experimental area!
Be_run2910001	26	29.10.	11:20	11:54	$4\,GeV/c$	Ch2+Hod+S2	Xenon	F150	2220	ALICE	1650	ALICE	1920	ALICE	2220	
Be_run2910002	26	29.10.	11:56	11:59	$4\,GeV/c$	Ch2+Hod+S2	Xenon	F150	2220	ALICE	1650	ALICE	1920	ALICE	2220	
Be_run2910003	26	29.10.	12:02	12:21	$4\,GeV/c$	Ch2+Hod+S2	Xenon	F150	2220	ALICE	1650	ALICE	1920	ALICE	2220	
Be_run2910004	27	29.10.	13:11	13:15	$4\,GeV/c$	Ch2+Hod+S2	Xenon	F250+1xAlu	2220	ALICE	1650	ALICE	1920	ALICE	2220	
Be_run2910005	27	29.10.	13:17	13:48	$4\,GeV/c$	Ch2+Hod+S2	Xenon	F250+1xAlu	2220	ALICE	1650	ALICE	1920	ALICE	2220	
Be_run2910006	27	29.10.	15:20	16:09	$4\,GeV/c$	Ch2+Hod+S2	Xenon	F250+1xAlu	2220	ALICE	1650	ALICE	1920	ALICE	2220	
Be_run2910007	28	29.10.	16:15	17:04	$4\,GeV/c$	Ch2+Hod+S2	Xenon	F250+2xAlu	2220	ALICE	1650	ALICE	1920	ALICE	2220	
Be_run2910008	28	29.10.	17:18	17:24	$4\,GeV/c$	Ch2+Hod+S2	Xenon	F250+2xAlu	2220	ALICE	1650	ALICE	1920	ALICE	2220	

Run #	Set	Date	Start	End	Beam	Trigger	Gas	Position 1 FFM004		Position 2 FFM002		Position 3 FFM006		Position 4 FFM005		Comment
								Radiator	HV [V]	Radiator	HV [V]	Radiator	HV [V]	Radiator	HV [V]	
Be_run2910009	28	29.10.	17:25	18:10	$4\,GeV/c$	Ch2+Hod+S2	Xenon	F250+2xAlu	2220	ALICE	1650	ALICE	1920	ALICE	2220	
Be_run2910010	28	29.10.	18:37	19:28	$4\,GeV/c$	Ch2+Hod+S2	Xenon	F250+2xAlu	2220	ALICE	1650	ALICE	1920	ALICE	2220	
Be_run2910012	29	29.10.	19:32	20:34	$4\,GeV/c$	Ch2+Hod+S2	Xenon	F250	2220	ALICE	1650	ALICE	1920	ALICE	2220	
Be_run2910013	-	29.10.	20:36	20:46	$4\,GeV/c$	Ch2+Hod+S2	Xenon	F250	2220	ALICE	1650	ALICE	1920	ALICE	2220	Xenon totaly empty
Be_run2910014	-	29.10.	21:00	21:30	$5\,GeV/c$	Ch2+Hod+S2	Ar+Xe	F250	2220	ALICE	1650	ALICE	1920	ALICE	2220	Switch to Argon
Be_run2910015	-	29.10.	21:45	22:31	$7\,GeV/c$	Ch2+Hod+S2	Ar+Xe	F250	2220	ALICE	1650	ALICE	1920	ALICE	2220	
Be_run2910016	-	29.10.	22:41	23:30	$9\,GeV/c$	Ch2+Hod+S2	Ar+Xe	F250	2220	ALICE	1650	ALICE	1920	ALICE	2220	
Be_run2910017	-	29.10.	23:52	09:37	$2\,GeV/c$	Ch2+Hod+S2	Ar+Xe	F250	2220	ALICE	1650	ALICE	1920	ALICE	2220	
Be_run3010001	-	30.10.	10:14	10:34	$2\,GeV/c$	Ch2+Hod+S2	Argon	F250	2220	ALICE	1650	ALICE	1920	ALICE	2220	
Be_run3010002	-	30.10.	10:37	11:05	$2\,GeV/c$	Ch2+Hod+S2	Argon	F250	2220	ALICE	1650	ALICE	1920	ALICE	2220	
Be_run3010003	-	30.10.	11:08	11:27	$2\,GeV/c$	Ch2+Hod+S2	Argon	F250	2220	ALICE	1650	ALICE	1920	ALICE	2220	
Be_run3010004	-	30.10.	11:34	11:43	$2\,GeV/c$	Ch2+Hod+S2	Argon	F250	2220	ALICE	1650	ALICE	1920	ALICE	2220	
Be_run3010005	-	30.10.	11:46	12:07	$2\,GeV/c$	Ch2+Hod+S2	Argon	F250	2220	ALICE	1650	ALICE	1920	ALICE	2220	
Be_run3010006	-	30.10.	12:29	12:46	$2\,GeV/c$	Ch2+Hod+S2	Argon	F250	2220	ALICE	1650	ALICE	1920	ALICE	2220	
Be_run3010008	-	30.10.	13:06	13:34	$2\,GeV/c$	Ch2+Hod+S2	Argon	F250	2220	ALICE	1650	ALICE	1920	ALICE	2220	
Be_run3010009	-	30.10.	13:39	14:00	$2\,GeV/c$	Ch2+Hod+S2	Argon	F250	2220	ALICE	1650	ALICE	1920	ALICE	2220	
Be_run3010010	-	30.10.	14:07	14:25	$2\,GeV/c$	Ch2+Hod+S2	Argon	F250	2220	ALICE	1650	ALICE	1920	ALICE	2220	
Be_run3010011	-	30.10.	14:30	14:50	$2\,GeV/c$	Ch2+Hod+S2	Argon	F250	2220	ALICE	1650	ALICE	1920	ALICE	2220	
Be_run3010012	-	30.10.	14:55	14:57	$2\,GeV/c$	Ch2+Hod+S2	Argon	F250	2220	ALICE	1650	ALICE	1920	ALICE	2220	
Be_run3010013	-	30.10.	15:02	15:14	$2\,GeV/c$	Ch2+Hod+S2	Argon	F250	2220	ALICE	1650	ALICE	1920	ALICE	2220	
Be_run3010014	-	30.10.	15:18	15:39	$2\,GeV/c$	Ch2+Hod+S2	Argon	F250	2220	ALICE	1650	ALICE	1920	ALICE	2220	
Be_run3010015	-	30.10.	15:39	16:00	$2\,GeV/c$	Ch2+Hod+S2	Argon	F250	2220	ALICE	1650	ALICE	1920	ALICE	2220	

List of Runs 2012

Run	Set	DAQ Date	DAQ Start	DAQ Stop	DAQ Beam	Pos. 1 FFM011 Radiator	Pos. 1 FFM011 HV [V]	Pos. 2 FFM010 Radiator	Pos. 2 FFM010 HV [V]	Conditions Pressure MWPC [mbar]	Conditions Pressure absolute [mbar]	Conditions Temp. [°C]	Conditions Humidity [%]	Comments
1		28.10.2012			$4\,GeV/c$	ALICE Type	2100	ALICE Type	1900					
2		28.10.2012			$4\,GeV/c$	ALICE Type	2100	ALICE Type	1900					
3		28.10.2012			$4\,GeV/c$	ALICE Type	2100	ALICE Type	1900					
4		28.10.2012			$4\,GeV/c$	ALICE Type	2100	ALICE Type	1900					
5		29.10.2012			$4\,GeV/c$	ALICE Type	2100	ALICE Type	1900					
6		29.10.2012			$4\,GeV/c$	ALICE Type	2100	ALICE Type	1900					
7		29.10.2012			$4\,GeV/c$	ALICE Type	2100	ALICE Type	1900					
8		29.10.2012			$4\,GeV/c$	ALICE Type	2100	ALICE Type	1900					
9		29.10.2012			$4\,GeV/c$	ALICE Type	2100	ALICE Type	1900					
10		29.10.2012			$4\,GeV/c$	ALICE Type	2100	ALICE Type	1900					
11		29.10.2012			$4\,GeV/c$	ALICE Type	2100	ALICE Type	1900					In Logbook HV for FFM011 is listed as 2200 V
12		29.10.2012			$4\,GeV/c$	ALICE Type	2250	ALICE Type	1950			15,7	34	HV Adjustment for both MWPCs
13		29.10.2012	11:00	11:34	$4\,GeV/c$	ALICE Type	2250	ALICE Type	1950			15,7	34	
14		29.10.2012	11:52	12:35	$3\,GeV/c$	ALICE Type	2250	ALICE Type	1950			16	33,9	Position adjusted before run
15		29.10.2012	13:00	13:40	$3\,GeV/c$	ALICE Type	2250	ALICE Type	1950			17	33	Position adjusted before run
16		29.10.2012	13:48	13:58	$3\,GeV/c$	ALICE Type	2250	ALICE Type	1950			17,8	32,2	
17		29.10.2012			$3\,GeV/c$	ALICE Type	2275	ALICE Type	1975			18	32,2	
18		29.10.2012			$3\,GeV/c$	ALICE Type	2275	ALICE Type	1975					
19		29.10.2012			$3\,GeV/c$	ALICE Type	2275	ALICE Type	1975	0,755	967,3	18,6	30,9	HV Adjusting after this run
20		29.10.2012	16:30	16:57	$3\,GeV/c$	ALICE Type	2295	ALICE Type	1995	0,757	967,3	18,6	31,1	Run after short no beam in PS
21		29.10.2012	17:15	18:10	$3\,GeV/c$	ALICE Type	2295	ALICE Type	1995	0,283	967,2	18,5	31,2	Adjusting of PbGlass-HV, removed Bubbler from FFM gas line
22		29.10.2012	18:20	19:25	$3\,GeV/c$	ALICE Type	2270	ALICE Type	1970	0,281	967,3	17,9	32,8	HV Adjusted: after bubbler was removed, preasure droped–¿ foil closer to wires
23		29.10.2012	19:29	19:30	$3\,GeV/c$	ALICE Type	2250	ALICE Type	1950	0,281	967,3	17,9	32,8	HV Adjutment / RPC Allignment (Access)
24	1	29.10.2012	19:48	???	$3\,GeV/c$	ALICE Type	2250	ALICE Type	1950	0,282	968,1	17,2	33,5	RPC Allignment (Access)

Run	Set	DAQ Date	Start	Stop	Beam	Pos. 1 FFM011 Radiator	HV [V]	Pos. 2 FFM010 Radiator	HV [V]	Conditions Pressure MWPC [mbar]	Pressure absolute [mbar]	Temp. [°C]	Humidity [%]	Comments
25	1	29.10.2012	20:24	20:35	$3\,GeV/c$	ALICE Type	2250	ALICE Type	1950	0,282	968,1	17,2	33,5	RPC Allignment (Access)
26	1	29.10.2012	20:38	21:06	$3\,GeV/c$	ALICE Type	2250	ALICE Type	1950	0,288	968,3	17,1	33,7	RICH changes mirror Position
27	1	29.10.2012	20:07	21:35	$3\,GeV/c$	ALICE Type	2250	ALICE Type	1950	0,288	968,3	17,1	33,7	Changes in preasure of Cherenkov
28	1	29.10.2012	21:40	21:53	$3\,GeV/c$	ALICE Type	2250	ALICE Type	1950	0,286	968,2	16,9	33,7	Stopped for DAQ-Test (Implementation of Spadic-Reinitializion works now)
29	1	29.10.2012	21:55	23:55	$3\,GeV/c$	ALICE Type	2250	ALICE Type	1950	0,286	968,2	16,7	33,8	
30	2	30.10.2012	0:20	0:40	$3\,GeV/c$	F250 0.7mm	2240	FFM R002	1940	0,293	967,7	16,1	34	New RICH Mirror Position
31	2	30.10.2012	0:45	3:00	$3\,GeV/c$	F250 0.7mm	2240	FFM R002	1940	0,294	967,7	15,9	34	New RICH Mirror Position
32	2	30.10.2012	3:06	6:07	$3\,GeV/c$	F250 0.7mm	2240	FFM R002	1940	0,292	966,7	15,6	34,7	New RICH Mirror Position
33	2	30.10.2012	6:07	7:00	$3\,GeV/c$	F250 0.7mm	2240	FFM R002	1940	0,296	966	15,1	34,7	changed FFM 10 + 11 to no radiators adjusted baseline of susibo 5 via proti, tried it via susibo voltage made no difference
34	3	30.10.2012	7:34	7:35	$3\,GeV/c$	no Radiator	2240	No Radiator	1940	0,296	966,4	14,9	34,8	
35	3	30.10.2012	7:40	7:53	$3\,GeV/c$	no Radiator	2240	No Radiator	1940	0,296	966,4	14,9	34,8	stopped for Bucharest to change radiators
36	3	30.10.2012	7:59	9:54	$3\,GeV/c$	no Radiator	2240	No Radiator	1940	0,295	966,5	15	34,8	RICH moved Mirror
37	3	30.10.2012			$3\,GeV/c$	no Radiator	2240	No Radiator	1940	0,286	965,6	15,7	35,6	MS connected Bubbler to their gas line (expect sligthly higer preasure in our MWPCs

Run	Set	DAQ				Pos. 1 FFM011		Pos. 2 FFM010		Conditions				Comments
		Date	Start	Stop	Beam	Radiator	HV [V]	Radiator	HV [V]	Pressure MWPC [mbar]	Pressure absolute [mbar]	Temp. [°C]	Humidity [%]	
38	3	30.10.2012			$3\,GeV/c$	no Radiator	0	No Radiator	0					Befor this run: large oxigen contermination in compleat gas system (more than 1% O2 content). Leakage search started. Gas line partialy opend. HV turned OFF for safety for both MWPCs Flow reduced to 8l/h FFM011 showes large increase in Current... 2240V @rising Current (1nA per minute). It started at 2nA after ramping, than continuusly ingreasing.
39	3	30.10.2012			$3\,GeV/c$	no Radiator	0	No Radiator	0					RICH LED run, no TRD in
40		30.10.2012	14:15		$3\,GeV/c$	no Radiator	0	No Radiator	0					RICH LED run, no TRD in
41	3	30.10.2012	15:25	16:11	$3\,GeV/c$	no Radiator	2240	No Radiator	1940	0,286	959,9	20,1	31,2	1st run after problems with gas systrm. O2 content should be around 0, exhaust line of our MWPCs was extended–¿higher preasure in mwpc –¿ lower gain. Preasure at beginning of run: 0.309mbar, after 20min back to 0.286mbar (seems to be stable). Stopped for MS for HV adjusting
42	3	30.10.2012	16:12	16:42	$3\,GeV/c$	no Radiator	2240	No Radiator	1940	0,282	959,4	20,6	30,8	Stopped for short access for Bucharest
43	3	30.10.2012	16:54	17:45	$3\,GeV/c$	no Radiator	2240	No Radiator	1940	0,278	959,3	20,6	30,7	Pressure continues to drop... 10minutes after start of run: 0.263mbar
44	4	30.10.2012			$3\,GeV/c$	F150 1.2mm	2240	FFM R003	1940			19,5	31,3	

Run	Set	DAQ Date	DAQ Start	DAQ Stop	DAQ Beam	Pos. 1 FFM011 Radiator	Pos. 1 FFM011 HV [V]	Pos. 2 FFM010 Radiator	Pos. 2 FFM010 HV [V]	Conditions Pressure MWPC [mbar]	Conditions Pressure absolute [mbar]	Conditions Temp. [°C]	Conditions Humidity [%]	Comments
45	4	30.10.2012	20:18	21:00	$3\,GeV/c$	F150 1.2mm	2240	FFM R003	1940	0,126	960,6	18,5	32,5	many overflows in MWPC due to very low pressure (−¿high Gain) reduced HV to 2200/1890V
46	4	30.10.2012	21:04	21:30	$3\,GeV/c$	F150 1.2mm	2200	FFM R003	1890	0,117	960,9	18,1	34,5	
47	4	30.10.2012	21:39	22:05	$3\,GeV/c$	F150 1.2mm	2200	FFM R003	1890	0.139	960,8	17,6	35,3	added red pigtail flow adjusted
48	4	30.10.2012	22:12	22:29	$3\,GeV/c$	F150 1.2mm	2200	FFM R003	1890	0.170	960,9	17,3	35,4	
49	4	30.10.2012	23:12	0:25	$3\,GeV/c$	F150 1.2mm	2200	FFM R003	1900	0.250 =¿ 0.200	960,9	17,2	35,1	added blue (longer) pigtail - back 2 red pigtail / flow adjusted
50	4	31.10.2012	0:31	2:05	$3\,GeV/c$	F150 1.2mm	2200	FFM R003	1900	0.200 =¿ 0.302 (1:37)	960,9	16,5	35,7	added shorted blue one
51	4													pigtail slighly adjusted
52	4	31.10.2012	2:45	2:58	$3\,GeV/c$	F150 1.2mm	2200	FFM R003	1900	0,245	960,1	15,9	36,2	
53	4	31.10.2012	2:59	4:31	$3\,GeV/c$	F150 1.2mm	2200	FFM R003	1900	0,24	960,1	15,8	36,3	
54	4	31.10.2012	4:32	5:38	$3\,GeV/c$	F150 1.2mm	2200	FFM R003	1900	0,235	959,7	15,5	36,2	
55	5	31.10.2012	5:58	7:07	$3\,GeV/c$	F150 0.7mm	2200	FFM R007	1900	0,236	959,5	15,3	36,3	RUN with Beam-stopper
56	5	31.10.2012	7:07	7:50	$3\,GeV/c$	F150 0.7mm	2200	FFM R007	1900	0,24	959,5	15,2	36,5	
57	5	31.10.2012	7:50	8:16	$3\,GeV/c$	F150 0.7mm	2200	FFM R007	1900	0,239	959,2	15,1	38,3	
58	5	31.10.2012	9:40	9:47	$3\,GeV/c$	F150 0.7mm	2200	FFM R007	1900	0,216	959	15,1	38,3	Preasure dropes, outside world preasure drops also
59	5	31.10.2012	10:01	13:01	$3\,GeV/c$	F150 0.7mm	2200	FFM R007	1900	0,213	958,6	15,9	39,4	
60	6	31.10.2012	14:09	14:38	$3\,GeV/c$	F250 0.5mm	2200	FFM R005	1900	0,19	953,8	17,2	41,5	Bucuresti reconected Detector again / Orbisphere MS shows some peaks to 1000ppmV and max 2200ppmVb
61	6	31.10.2012	14:39		$3\,GeV/c$	F250 0.5mm	2200	FFM R005	1900	0,192	953,2	17,3	41,1	Restart MS Spadic 03
62	6	31.10.2012	15:05	15:10	$3\,GeV/c$	F250 0.5mm	2200	FFM R005	1900	0,189	952,9	17,3	42	
63	6	31.10.2012	15:12	16:07	$3\,GeV/c$	F250 0.5mm	2200	FFM R005	1900	0,21	952,8	17,4	42,7	
64	7	31.10.2012	17:00	17:20	$3\,GeV/c$	F250 0.5mm	2200	F150 1.2mm	1900	0,2	952,1	17,7	43,2	
65	7	31.10.2012	17:50	18:20	$3\,GeV/c$	F250 0.5mm	2200	F150 1.2mm	1900					Fracam offline
66	7	31.10.2012	18:43		$3\,GeV/c$	F250 0.5mm	2200	F150 1.2mm	1900					
67	7	31.10.2012	20:15	23:38	$3\,GeV/c$	F250 0.5mm	2200	F150 1.2mm	1900					
68	8	31.10.2012	23:52	0:44	$3\,GeV/c$	MS Rohacell HF 110	2200	MS Rohacell HF 110	1900	0,211		17,4	47	
69	8	01.11.2012	0:52	5:24	$3\,GeV/c$	MS Rohacell HF 110	2200	MS Rohacell HF 110	1900	0,209	948,6	17,4	47,6	
70	9	01.11.2012	5:35	7:37	$3\,GeV/c$	FFM R07	2200	Foil 0.7 250Layer	1900	0,216	948	17,4	46,1	
71	9	01.11.2012	7:47	8:44	$3\,GeV/c$	FFM R07	2200	Foil 0.7 250Layer	1900	0,214	948	17,4	46,1	RICH pruges gas PRF of FFM010 seems to be symetric now. TO BE CHECKED offline
72	9	01.11.2012	8:45	10:09	$3\,GeV/c$	FFM R07	2200	Foil 0.7 250Layer	1900					

Run	Set	DAQ Date	Start	Stop	Beam	Pos. 1 FFM011 Radiator	HV [V]	Pos. 2 FFM010 Radiator	HV [V]	Conditions Pressure MWPC [mbar]	Pressure absolute [mbar]	Temp. [°C]	Humidity [%]	Comments
73	9	01.11.2012	11:29	11:38	$3\,GeV/c$	FFM R07	2200	Foil 0.7 250Layer	1900	0,262	948,7	17,5	43,5	New Electron trigger set up, should be 50% Electrons, 50 others. Run stopped because of no beam from PS
74	9	01.11.2012	12:57	13:14	$3\,GeV/c$	FFM R07	2200	Foil 0.7 250Layer	1900	0,218	947,5	19,1	40,5	Run stopped due to no beam from PS
75	9	01.11.2012	13:30	13:40	$3\,GeV/c$	FFM R07	2200	Foil 0.7 250Layer	1900	0,214	947,5	19,3	40,4	Agian problems in PS
76	9	01.11.2012	14:11	15:18	$3\,GeV/c$	FFM R07	2200	Foil 0.7 250Layer	1900	0,223	948,1	19,9	40,9	Agian no beam
77	9	01.11.2012	16:16	18:25	$3\,GeV/c$	FFM R07	2200	Foil 0.7 250Layer	1900	0,215	948	19,4	39,4	low statistics
78	9	01.11.2012	18:26	21:25	$3\,GeV/c$	FFM R07	2200	Foil 0.7 250Layer	1900	0,217	950,2	19,9	41,2	low statistics
79	9	01.11.2012	21:26	22:02	$3\,GeV/c$	FFM R07	2200	Foil 0.7 250Layer	1900	0,212	952,5	18,2	45,5	low statistics
80	9	01.11.2012	22:03	23:43	$3\,GeV/c$	FFM R07	2200	Foil 0.7 250Layer	1900	0,206	953,6	18,1	46,5	low statistics
81	10	01.11.2012	23:55	0:40	$3\,GeV/c$	FFM R02	2200	MS Unreg Foil 250 layers	1900	0,217	954,6	17,9	48,5	
82	10	02.11.2012	0:45	2:22	$3\,GeV/c$	FFM R02	2200	MS Unreg Foil 250 layers	1900					
83	10	02.11.2012	2:24	4:10	$3\,GeV/c$	FFM R02	2200	MS Unreg Foil 250 layers	1900					
84	10	02.11.2012	4:11	5:10	$3\,GeV/c$	FFM R02	2200	MS Unreg Foil 250 layers	1900					Full beam (3Spills) back
85	10	02.11.2012	5:15	6:50	$3\,GeV/c$	FFM R02	2200	MS Unreg Foil 250 layers	1900					
86	10	02.11.2012	6:50	6:51	$3\,GeV/c$	FFM R02	2200	MS Unreg Foil 250 layers	1900					
87	10	02.11.2012	6:53	7:27	$3\,GeV/c$	FFM R02	2200	MS Unreg Foil 250 layers	1900					
88	10	02.11.2012	7:43	8:19	$3\,GeV/c$	FFM R02	2200	MS Unreg Foil 250 layers	1900	0,208	959,9	19,8	41,1	
89	10	02.11.2012	8:21	9:02	$3\,GeV/c$	FFM R02	2200	MS Unreg Foil 250 layers	1900	0,209	959,9	19,8	41,3	Preasure at 8:52 was 0.227
90	10	02.11.2012	9:05	10:23	$3\,GeV/c$	FFM R02	2200	MS Unreg Foil 250 layers	1900	0,229	960,1	19	41,7	
91	11	02.11.2012	11:13	12:35	$3\,GeV/c$	MS Unreg Foil 250 layers	2200	Foil 0.5 150Layer	1900	0,234	959,8	20	40	FFM011 has 12.1nA current, MS removed MWPC wirh Sus18, preasure at 12:09 was 0.209
92	11	02.11.2012	12:36	13:28	$3\,GeV/c$	MS Unreg Foil 250 layers	2200	Foil 0.5 150Layer	1900	0,204	950,2	20,9	35,7	New RICH mirror position
93	11	02.11.2012	13:30	14:30	$3\,GeV/c$	MS Unreg Foil 250 layers	2200	Foil 0.5 150Layer	1900	0,206	957,8	21	35,2	New RICH mirror position, Preasure at 14:10 was 0.190mBar
94	11	02.11.2012	14:37	16:28	$3\,GeV/c$	MS Unreg Foil 250 layers	2200	Foil 0.5 150Layer	1900	0,202	957,1	21,5	34,1	New bukarest radiators, stopped for bucharest for access
95	11	02.11.2012	16:56	19:02	$3\,GeV/c$	MS Unreg Foil 250 layers	2200	Foil 0.5 150Layer	1900	0,2	958,4	20,6	34,3	
96	11	02.11.2012	19:22	21:08	$3\,GeV/c$	MS Unreg Foil 250 layers	2200	Foil 0.5 150Layer	1900	0,216	960,7	19,6	40,5	
97	12	02.11.2012	22:10	22:34	$3\,GeV/c$	Foil 1,2 150 layers	2200	FFM R02	1900	0,203	961,7	19,3	42	
98	12	02.11.2012	22:43	22:44	$3\,GeV/c$	Foil 1,2 150 layers	2200	FFM R02	1900	0,203	961,7			pedestals run Te_run98
99	12	02.11.2012	22:45	23:00	$3\,GeV/c$	Foil 1,2 150 layers	2200	FFM R02	1900	0,203	961,7			
100	12	02.11.2012	23:00	23:50	$3\,GeV/c$	Foil 1,2 150 layers	2200	FFM R02	1900	0,203	961,7			
101	12	02.11.2012	23:55	0:50	$3\,GeV/c$	Foil 1,2 150 layers	2200	FFM R02	1900	0,203	961,7			
102	12	03.11.2012	0:52	1:44	$3\,GeV/c$	Foil 1,2 150 layers	2200	FFM R02	1900	0,203	961,7			
103	12	03.11.2012	1:50	2:11	$3\,GeV/c$	Foil 1,2 150 layers	2200	FFM R02	1900	0,203	961,7			

		DAQ				Pos. 1 FFM011		Pos. 2 FFM010		Conditions				
Run	Set	Date	Start	Stop	Beam	Radiator	HV [V]	Radiator	HV [V]	Pressure MWPC [mbar]	Pressure absolute [mbar]	Temp. [°C]	Humidity [%]	Comments
104	12	03.11.2012	2:13	3:06	$3\,GeV/c$	Foil 1,2 150 layers	2200	FFM R02	1900	0,203	961,7			
105	12	03.11.2012	3:09	4:00	$3\,GeV/c$	Foil 1,2 150 layers	2200	FFM R02	1900	0,201	961,3	20,7	38,5	
106	12	03.11.2012	4:02	4:55	$3\,GeV/c$	Foil 1,2 150 layers	2200	FFM R02	1900	0,201	961	20,8	38	
107	12	03.11.2012	4:58	5:19	$3\,GeV/c$	Foil 1,2 150 layers	2200	FFM R02	1900	0,196	960,9	20,8	37,8	
108	12	03.11.2012	5:21	6:00	$3\,GeV/c$	Foil 1,2 150 layers	2200	FFM R02	1900	0,2	960,9	20,7	38	at 5:53 No Beam, Main Power Supply tripped
109	12	03.11.2012	7:36	8:02	$3\,GeV/c$	Foil 1,2 150 layers	2200	FFM R02	1900	0,204	960	20,4	38,4	
110	12	03.11.2012	8:03	9:15	$3\,GeV/c$	Foil 1,2 150 layers	2200	FFM R02	1900					
111	12	03.11.2012	9:17	10:10	$3\,GeV/c$	Foil 1,2 150 layers	2200	FFM R02	1900					
112	12	03.11.2012	10:14	10:30	$3\,GeV/c$	Foil 1,2 150 layers	2200	FFM R02	1900					
113	12	03.11.2012	10:36	10:51	$3\,GeV/c$	Foil 1,2 150 layers	2200	FFM R02	1900					
114	13	03.11.2012	11:00	11:42	$3\,GeV/c$	none	2200	none	1900					
115	13	03.11.2012	11:44	12:50	$3\,GeV/c$	none	2200	none	1900					
116	13	3.11.2012	12:51	13:42	$3\,GeV/c$	none	2200	none	1900					
117	13	3.11.2012	13:46	14:10	$3\,GeV/c$	none	2200	none	1900		960	20,4	38,4	
118	13	3.11.2012	14:12	15:02	$3\,GeV/c$	none	2200	none	1900					
119	13	3.11.2012	15:05	15:40	$3\,GeV/c$	none	2200	none	1900					
120	13	3.11.2012	15:42	16:22	$3\,GeV/c$	none	2200	none	1900					
121	13	3.11.2012	16:25	16:49	$3\,GeV/c$	none	2200	none	1900	0,191	958,1	21,7	37,2	
122	13	3.11.2012	16:51	17:25	$3\,GeV/c$	none	2200	none	1900	0,194	958,1	21,6	37,3	
123	13	3.11.2012	17:28	18:17	$3\,GeV/c$	none	2200	none	1900	0,2	957,8	21,6	37,1	
124	13	3.11.2012	18:22	21:08	$3\,GeV/c$	none	2200	none	1900	0,198	958,2	21,5	37,2	preasure dropped to 0.192 during the run; stopped due to no beam (last minute running with beam stopper)!
125	14	3.11.2012	21:23	21:38	$3\,GeV/c$	FFM R02	2200	Foil 150 1.2mm	1900	0,195	958,3	21,6	40,6	RICH test run, but no beam
126	14	3.11.2012	23:00	23:40	$8\,GeV/c$	FFM R02	2200	Foil 150 1.2mm	1900	0,198	958,5	21,8	44,3	Cerenkov1+2: changed gas mixture from N2/CO2 to pure CO2 and pressure
127	14	3.11.2012	23:41	1:25	$8\,GeV/c$	FFM R02	2200	Foil 150 1.2mm	1900	0,203	958,5	21,8	45,8	
128	14	4.11.2012	1:27	1:53	$8\,GeV/c$	FFM R02	2200	Foil 150 1.2mm	1900					
129	14	4.11.2012	1:54	2:22	$8\,GeV/c$	FFM R02	2200	Foil 150 1.2mm	1900					
130	14	4.11.2012	2:23	2:53	$8\,GeV/c$	FFM R02	2200	Foil 150 1.2mm	1900					
131	14	4.11.2012	2:56	3:39	$8\,GeV/c$	FFM R02	2200	Foil 150 1.2mm	1900					
132	14	4.11.2012	3:40	4:00	$8\,GeV/c$	FFM R02	2200	Foil 150 1.2mm	1900					
133	14	4.11.2012	4:04	5:21	$8\,GeV/c$	FFM R02	2200	Foil 150 1.2mm	1900					
134	14	4.11.2012	5:22	6:13	$8\,GeV/c$	FFM R02	2200	Foil 150 1.2mm	1900					
135	14	4.11.2012	6:14	7:09	$8\,GeV/c$	FFM R02	2200	Foil 150 1.2mm	1900					
136	14	4.11.2012	7:10	7:55	$8\,GeV/c$	FFM R02	2200	Foil 150 1.2mm	1900					
137	14	4.11.2012	7:56	8:43	$8\,GeV/c$	FFM R02	2200	Foil 150 1.2mm	1900					
138	14	4.11.2012	8:48	9:20	$8\,GeV/c$	FFM R02	2200	Foil 150 1.2mm	1900	0,199	956,3	21,7	45,9	
139	14	4.11.2012	9:23	10:55	$8\,GeV/c$	FFM R02	2200	Foil 150 1.2mm	1900					
140	14	4.11.2012	10:56	11:30	$8\,GeV/c$	FFM R02	2200	Foil 150 1.2mm	1900					
141	14	4.11.2012	11:32	12:00	$8\,GeV/c$	FFM R02	2200	Foil 150 1.2mm	1900					
142	14	4.11.2012	12:03	12:47	$8\,GeV/c$	FFM R02	2200	Foil 150 1.2mm	1900	0,195	954,8	22,1	47,7	
143	14	4.11.2012	12:55	13:25	$8\,GeV/c$	FFM R02	2200	Foil 150 1.2mm	1900					
144	14	4.11.2012	13:30	14:23	$8\,GeV/c$	FFM R02	2200	Foil 150 1.2mm	1900	0,196	953,9	22,2	49,3	no beam, trouble with booster
145	14	4.11.2012	14:51	15:11	$8\,GeV/c$	FFM R02	2200	Foil 150 1.2mm	1900	0,196	953	22,3	50,9	

		DAQ				Pos. 1 FFM011		Pos. 2 FFM010		Conditions				
Run	Set	Date	Start	Stop	Beam	Radiator	HV [V]	Radiator	HV [V]	Pressure MWPC [mbar]	Pressure absolute [mbar]	Temp. [°C]	Humidity [%]	Comments
146	14	4.11.2012	15:14	17:06	$8\,GeV/c$	FFM R02	2200	Foil 150 1.2mm	1900	0,197	952,9	22,3	51,7	PR1 rised to 0.21 during run
147	15	4.11.2012	17:10	19:48	$6\,GeV/c$	FFM R02	2200	Foil 150 1.2mm	1900					
148	15	4.11.2012	19:53	20:43	$6\,GeV/c$	FFM R02	2200	Foil 150 1.2mm	1900					
149	15	4.11.2012	20:44	21:10	$6\,GeV/c$	FFM R02	2200	Foil 150 1.2mm	1900					
150	15	4.11.2012	21:18	21:26	$6\,GeV/c$	FFM R02	2200	Foil 150 1.2mm	1900	0,253	956,9	21,1	51,4	
151	15	4.11.2012	21:28	22:01	$6\,GeV/c$	FFM R02	2200	Foil 150 1.2mm	1900					
152	15	4.11.2012	22:02	22:43	$6\,GeV/c$	FFM R02	2200	Foil 150 1.2mm	1900					
153	15	4.11.2012	22:50	23:37	$6\,GeV/c$	FFM R02	2200	Foil 150 1.2mm	1900	0,257	957,5	20,6	50,6	RICH changes something (Mirror,HV, whatever)
154	15	4.11.2012	23:39	0:28	$6\,GeV/c$	FFM R02	2200	Foil 150 1.2mm	1900	0,258	957,7	20,6	50,4	RICH changed mirror position
155	15	5.11.2012	0:30	1:11	$6\,GeV/c$	FFM R02	2200	Foil 150 1.2mm	1900	0,264	957,9	20,5	49,9	RICH changed mirror position
156	15	5.11.2012	1:15	1:31	$6\,GeV/c$	FFM R02	2200	Foil 150 1.2mm	1900	0,268	958,2	20,4	49,9	RICH changed mirror position
157	15	5.11.2012	1:32	3:53	$6\,GeV/c$	FFM R02	2200	Foil 150 1.2mm	1900	0,269	958,1	20,4	49,5	stopped: no beam ("Central Timing has problems")
158	15	5.11.2012	4:54	6:54	$6\,GeV/c$	FFM R02	2200	Foil 150 1.2mm	1900	0,264	957,9	20,1	48,5	RICH changed mirror position
159	15	5.11.2012	6:55	8:51	$6\,GeV/c$	FFM R02	2200	Foil 150 1.2mm	1900	0,268	958,9	19,8	48,1	shortly no beam at end of run
160	15	5.11.2012	9:01	9:40	$6\,GeV/c$	FFM R02	2200	Foil 150 1.2mm	1900	0,272	960,3	19,7	45,7	Low intensity beam
161	15	5.11.2012	9:44	10:09	$6\,GeV/c$	FFM R02	2200	Foil 150 1.2mm	1900	0,245	961	19	46,5	access for DAQ
162	15	5.11.2012	10:15	11:16	$6\,GeV/c$	FFM R02	2200	Foil 150 1.2mm	1900	0,215	960,8	19,6	45,2	PR1 drops to 0.193 at 10:45
163	15	5.11.2012	11:24	11:55	$6\,GeV/c$	FFM R02	2200	Foil 150 1.2mm	1900	0,203	960,9	20,2	43,4	
164	15	5.11.2012	11:57	12:11	$6\,GeV/c$	FFM R02	2200	Foil 150 1.2mm	1900	0,186	961	20,4	42,9	
165	15	5.11.2012	12:16		$6\,GeV/c$	FFM R02	2200	Foil 150 1.2mm	1900					
166	15	5.11.2012		13:31	$6\,GeV/c$	FFM R02	2200	Foil 150 1.2mm	1900					
167	16	5.11.2012			$4\,GeV/c$	FFM R02	2200	Foil 150 1.2mm	1900	0,232	961,1	20,7	41,6	Beam at $4\,GeV/c$, Adjustin Cherenkovs (100V lower), Pb-Glass 100V higer
168	16	5.11.2012	13:56	14:26	$4\,GeV/c$	FFM R02	2200	Foil 150 1.2mm	1900	0,236	961,2	20,6	42,1	DAQ restarted
169	16	5.11.2012	14:33	15:05	$4\,GeV/c$	FFM R02	2200	Foil 150 1.2mm	1900	0,241	961,5	20,4	43,7	FASP included in DAQ
170	16	5.11.2012	15:07	16:26	$4\,GeV/c$	FFM R02	2200	Foil 150 1.2mm	1900	0,238	961,6	20,4	44,5	Access for Rich mirror position
171	16	5.11.2012	17:03	17:40	$4\,GeV/c$	FFM R02	2200	Foil 150 1.2mm	1900	0,265	962,3	20,3	46,3	
172	16	5.11.2012	17:44	18:08	$4\,GeV/c$	FFM R02	2200	Foil 150 1.2mm	1900	0,204	963,4	20,3	42,5	
173	16	5.11.2012	18:09	18:30	$4\,GeV/c$	FFM R02	2200	Foil 150 1.2mm	1900	0,23		20,3		
174	16	5.11.2012	18:33	18:50	$4\,GeV/c$	FFM R02	2200	Foil 150 1.2mm	1900	0,231		20,3		
175	16	5.11.2012	18:51	19:10	$4\,GeV/c$	FFM R02	2200	Foil 150 1.2mm	1900	0,232	964,8	20,3	42	Rich access
176	16	5.11.2012	19:17	19:35	$4\,GeV/c$	FFM R02	2200	Foil 150 1.2mm	1900	0,23	965,3	20,2	42,1	
177	16	5.11.2012	19:37	19:57	$4\,GeV/c$	FFM R02	2200	Foil 150 1.2mm	1900	0,23	965,5	20,2	42	
178	16	5.11.2012	19:58	20:17	$4\,GeV/c$	FFM R02	2200	Foil 150 1.2mm	1900	0,232	965,8	20,1	41,9	
179	16	5.11.2012	20:18	20:36	$4\,GeV/c$	FFM R02	2200	Foil 150 1.2mm	1900					
180	16	5.11.2012	21:00	21:20	$4\,GeV/c$	FFM R02	2200	Foil 150 1.2mm	1900	0,251	966,4	19,9	42,8	
181	16	5.11.2012	21:21	21:43	$4\,GeV/c$	FFM R02	2200	Foil 150 1.2mm	1900	0,247	966,5	19,9	43,4	
182	16	5.11.2012	21:45	22:07	$4\,GeV/c$	FFM R02	2200	Foil 150 1.2mm	1900	0,247	966,6	19,8	44,3	
183	16	5.11.2012	22:08	22:30	$4\,GeV/c$	FFM R02	2200	Foil 150 1.2mm	1900	0,244	966,6	19,8	44,7	

		DAQ				Pos. 1 FFM011		Pos. 2 FFM010		Conditions				
Run	Set	Date	Start	Stop	Beam	Radiator	HV [V]	Radiator	HV [V]	Pressure MWPC [mbar]	Pressure absolute [mbar]	Temp. [°C]	Humidity [%]	Comments
184	16	5.11.2012	22:31	23:06	$4\,GeV/c$	FFM R02	2200	Foil 150 1.2mm	1900	0,242	966,5	19,7	45,2	
185	16	5.11.2012	23:08	23:29	$4\,GeV/c$	FFM R02	2200	Foil 150 1.2mm	1900	0,244	966,6	19,6	45,1	
186	16	5.11.2012	23:30	23:49	$4\,GeV/c$	FFM R02	2200	Foil 150 1.2mm	1900					
187	16	5.11.2012	23:50	0:08	$4\,GeV/c$	FFM R02	2200	Foil 150 1.2mm	1900					
188	16	6.11.2012	0:10	0:27	$4\,GeV/c$	FFM R02	2200	Foil 150 1.2mm	1900					
189	16	6.11.2012	0:28	0:41	$4\,GeV/c$	FFM R02	2200	Foil 150 1.2mm	1900	0,246	966,9	19,6	45	
190	16	6.11.2012	0:43	0:57	$4\,GeV/c$	FFM R02	2200	Foil 150 1.2mm	1900					
191	16	6.11.2012	0:58	1:13	$4\,GeV/c$	FFM R02	2200	Foil 150 1.2mm	1900					
192	16	6.11.2012	1:18	1:34	$4\,GeV/c$	FFM R02	2200	Foil 150 1.2mm	1900	0,241	966,9	19,6	43,5	
193	16	6.11.2012	1:36	1:53	$4\,GeV/c$	FFM R02	2200	Foil 150 1.2mm	1900					
194	16	6.11.2012	1:55	2:11	$4\,GeV/c$	FFM R02	2200	Foil 150 1.2mm	1900					
195	16	6.11.2012	2:19	2:36	$4\,GeV/c$	FFM R02	2200	Foil 150 1.2mm	1900					
196	16	6.11.2012	2:37	2:57	$4\,GeV/c$	FFM R02	2200	Foil 150 1.2mm	1900					
197	16	6.11.2012	3:03	3:50	$4\,GeV/c$	FFM R02	2200	Foil 150 1.2mm	1900					
198	16	6.11.2012	3:53	4:16	$4\,GeV/c$	FFM R02	2200	Foil 150 1.2mm	1900	0,239	967,1	19,3	43,1	
199	16	6.11.2012	4:17	4:33	$4\,GeV/c$	FFM R02	2200	Foil 150 1.2mm	1900	0,24	967,2	19,4	43,1	
200	16	6.11.2012	4:36	5:00	$4\,GeV/c$	FFM R02	2200	Foil 150 1.2mm	1900	0,24	967,4	19,3	43,3	From 5:00 on: No Beam - Technical Stop 8-18 Interventions, 18-20 restart, 20 Beams back (announced)
201	16	6.11.2012	11:07	11:18	$4\,GeV/c$	FFM R02	2200	Foil 150 1.2mm	1900					Testrun, RICH electronic
202	16	6.11.2012	11:20	11:34	$4\,GeV/c$	FFM R02	2200	Foil 150 1.2mm	1900					Test run for RICH/DAQ
203	16	6.11.2012	11:37	11:54	$4\,GeV/c$	FFM R02	2200	Foil 150 1.2mm	1900					Test run for RICH/DAQ
204	16	6.11.2012	11:56	12:14	$4\,GeV/c$	FFM R02	2200	Foil 150 1.2mm	1900					Test run for RICH/DAQ
205		6.11.2012	12:14	12:40		FFM R02	2200	Foil 150 1.2mm	1900					Test run for RICH/DAQ
206		6.11.2012	12:41	12:57		FFM R02	2200	Foil 150 1.2mm	1900					Test run for RICH/DAQ
207		6.11.2012	13:05	14:08		FFM R02	2200	Foil 150 1.2mm	1900					Test run for RICH/DAQ
208	17	7.11.2012	8:06	8:40	$2\,GeV/c$	FFM R02	2200	Foil 150 1.2mm	1900	0,204	983,9	16,7	42	First run after technal stop (still low intensity beam)
209	17	7.11.2012	9:10	9:47	$2\,GeV/c$	FFM R02	2200	Foil 150 1.2mm	1900	0,213	985,2	15,2	45,3	
210	17	7.11.2012	12:41	12:54	$2\,GeV/c$	FFM R02	2200	Foil 150 1.2mm	1900	0,227	982,7	19,2	37,1	
211	17	7.11.2012	13:51	14:21	$2\,GeV/c$	FFM R02	2200	Foil 150 1.2mm	1900	0,236	983,4	16,2	37,4	gas flow 9.5l/h
212	17	7.11.2012	14:27	14:33	$2\,GeV/c$	FFM R02	2200	Foil 150 1.2mm	1900	0,236	983,3	16,1	38,7	
213	17	7.11.2012	14:34	14:48	$2\,GeV/c$	FFM R02	2200	Foil 150 1.2mm	1900	0,231	983	16,8	38,1	
214	17	7.11.2012	15:05	15:35	$2\,GeV/c$	FFM R02	2200	Foil 150 1.2mm	1900	0,19	981,9	19,2	34,1	
215	17	7.11.2012	16:54	17:15	$2\,GeV/c$	FFM R02	2200	Foil 150 1.2mm	1900	0,171	980,2	20,6	32,7	
216	17	7.11.2012	17:24	17:51	$2\,GeV/c$	FFM R02	2200	Foil 150 1.2mm	1900	0,171	980,1	20,6	33,2	
217	17	7.11.2012	17:57		$2\,GeV/c$	FFM R02	2200	Foil 150 1.2mm	1900	0,17	980,3	20,4	35,1	
218	17	7.11.2012	19:47	20:39	$2\,GeV/c$	FFM R02	2200	Foil 150 1.2mm	1900					
219	17	7.11.2012	20:40	21:40	$2\,GeV/c$	FFM R02	2200	Foil 150 1.2mm	1900					
220	17	7.11.2012	21:41	21:52	$2\,GeV/c$	FFM R02	2200	Foil 150 1.2mm	1900					
221	17	7.11.2012	21:53	22:13	$2\,GeV/c$	FFM R02	2200	Foil 150 1.2mm	1900					FRA001 died in this run
222	17	7.11.2012	22:19	23:09	$2\,GeV/c$	FFM R02	2200	Foil 150 1.2mm	1900					

Run	Set	DAQ Date	DAQ Start	DAQ Stop	DAQ Beam	Pos. 1 FFM011 Radiator	Pos. 1 FFM011 HV [V]	Pos. 2 FFM010 Radiator	Pos. 2 FFM010 HV [V]	Conditions Pressure MWPC [mbar]	Conditions Pressure absolute [mbar]	Conditions Temp. [°C]	Conditions Humidity [%]	Comments
223	17	7.11.2012	23:53	0:20	$2\,GeV/c$	FFM R02	2200	Foil 150 1.2mm	1900	0,182	980,9	18,8	37,9	FFM R002 rotated, 3mm additional air btween radiator and MWPC
224	17	8.11.2012	0:24	0:51	$2\,GeV/c$	FFM R02	2200	Foil 150 1.2mm	1900	0,181	980,8	18,6	38	DAQ crashed
225	17	8.11.2012	0:52	1:37	$2\,GeV/c$	FFM R02	2200	Foil 150 1.2mm	1900	0,184	981	18,5	38	PR1 dropped to 0.165 @ 1:35am
226	17	8.11.2012	1:38	2:23	$2\,GeV/c$	FFM R02	2200	Foil 150 1.2mm	1900	0,165	980,5	18,4	37,4	PR1 dropped to 0.156 @ 2:05am
227	17	8.11.2012	2:24	3:09	$2\,GeV/c$	FFM R02	2200	Foil 150 1.2mm	1900	0,154	980,2	18,2	37	
228	17	8.11.2012	3:10	3:55	$2\,GeV/c$	FFM R02	2200	Foil 150 1.2mm	1900	0,152	979,8	18	36,6	
229	17	8.11.2012	5:45	6:30	$2\,GeV/c$	FFM R02	2200	Foil 150 1.2mm	1900	0,159	978,7	17,6	36,1	
230	17	8.11.2012	6:35	7:22	$2\,GeV/c$	FFM R02	2200	Foil 150 1.2mm	1900	0,158	978,3	17,6	35,8	
231	17	8.11.2012	7:44	8:48	$2\,GeV/c$	FFM R02	2200	Foil 150 1.2mm	1900					
232	17	8.11.2012	8:49	9:42	$2\,GeV/c$	FFM R02	2200	Foil 150 1.2mm	1900	0,171	978,7	17,8	35,5	
233	17	8.11.2012	9:43	10:29	$2\,GeV/c$	FFM R02	2200	Foil 150 1.2mm	1900	0,142	978,1	18,7	36,8	Stopped for RICH (TRB thresholds)
234	17	8.11.2012	10:32	10:57	$2\,GeV/c$	FFM R02	2200	Foil 150 1.2mm	1900	0,13	977,5	19,4	37,3	Stopped for RICH
235	17	8.11.2012	11:10	11:28	$2\,GeV/c$	FFM R02	2200	Foil 150 1.2mm	1900	0,12	976,8	19,9	37,5	very low preasure, Xe flow at only 7.5l/h!!! (bottle empty?) current in FFM011 at 16.1nA!
236	17	8.11.2012	11:36	12:00	$2\,GeV/c$	FFM R02	2200	Foil 150 1.2mm	1900	0,119	976			FFM011 at 24nA! but now dropping
237	17	8.11.2012	12:11	12:34	$2\,GeV/c$	FFM R02	2200	Foil 150 1.2mm	1900					
238	17	8.11.2012	12:35	12:55	$2\,GeV/c$	FFM R02	2200	Foil 150 1.2mm	1900					
239	17	8.11.2012	12:56	13:14	$2\,GeV/c$	FFM R02	2200	Foil 150 1.2mm	1900					
240	18	8.11.2012	14:46	15:04	$3\,GeV/c$	MS Cell Air 2mm	2200	MS Cell Air 2mm	1900	0,14	973,8	20	39	Same Radiator for all TRD, 2mm of Cell Air sheats, 25sheats in total, 75 to 100 transitions
241	18	8.11.2012	15:06	15:55	$3\,GeV/c$	MS Cell Air 2mm	2200	MS Cell Air 2mm	1900	0,121	973,1	21,1	36,8	Preasure still dropping: 0.113 @ 15:22, 0.109 @15:32
242	18	8.11.2012	15:56	17:07	$3\,GeV/c$	MS Cell Air 2mm	2200	MS Cell Air 2mm	1900	0,101	972,4	21,9	35,3	Xe preasure dropes (bottle empty?) Flow constand below 8l/h but high preasure variations (0.025mbar/min)
243	18	8.11.2012	17:08	18:00	$3\,GeV/c$	MS Cell Air 2mm	2200	MS Cell Air 2mm	1900	0,112	972,4	22,2	34,5	
244	18	8.11.2012	18:01	18:39	$3\,GeV/c$	MS Cell Air 2mm	2200	MS Cell Air 2mm	1900	0,13	972,3	22,3	33,6	Preasure rising again
245	18	8.11.2012	18:41	19:20	$3\,GeV/c$	MS Cell Air 2mm	2200	MS Cell Air 2mm	1900	0,132	972,2	22,3	33,7	
246	18	8.11.2012	19:20	19:55	$3\,GeV/c$	MS Cell Air 2mm	2200	MS Cell Air 2mm	1900	0,132	972,2	22,3	33,7	
247	19	8.11.2012	21:08	21:09	$3\,GeV/c$	FFM R009 Type B	2200	Foil 0.5 250L	1900	0,132	972,2	22,4	33,8	DAQ chrashed

Run	Set	DAQ Date	Start	Stop	Beam	Pos. 1 FFM011 Radiator	HV [V]	Pos. 2 FFM010 Radiator	HV [V]	Conditions Pressure MWPC [mbar]	Pressure absolute [mbar]	Temp. [°C]	Humidity [%]	Comments
248	19	8.11.2012	21:58	22:34	$3\,GeV/c$	FFM R009 Type B	2200	Foil 0.5 250L	1900	0,131	972,3	22,4	34,6	DAQ back
249	19	8.11.2012	22:40	23:24	$3\,GeV/c$	FFM R009 Type B	2200	Foil 0.5 250L	1900					
250	19	8.11.2012	23:36	0:02	$3\,GeV/c$	FFM R009 Type B	2200	Foil 0.5 250L	1900	0,13	972,1	22,3	35,8	
251	19	9.11.2012	0:04	0:36	$3\,GeV/c$	FFM R009 Type B	2200	Foil 0.5 250L	1900	0,131	972,1	22,3	36,2	
252	19	9.11.2012	1:15	1:30	$3\,GeV/c$	FFM R009 Type B	2200	Foil 0.5 250L	1900	0,134	971,1	22,4	36,6	
253	19	9.11.2012	1:47	2:28	$3\,GeV/c$	FFM R009 Type B	2200	Foil 0.5 250L	1900	0,132	970,6	22,4	36,5	
254	19	9.11.2012	2:48	3:23	$3\,GeV/c$	FFM R009 Type B	2200	Foil 0.5 250L	1900	0,132	970,4	22,2	37,2	
255	19	9.11.2012	3:30	4:08	$3\,GeV/c$	FFM R009 Type B	2200	Foil 0.5 250L	1900	0,134	970,5	21,9	37,4	
256	19	9.11.2012	4:27	5:00	$3\,GeV/c$	FFM R009 Type B	2200	Foil 0.5 250L	1900	0,14	970,3	21,7	37,4	
257	19	9.11.2012	5:03	5:47	$3\,GeV/c$	FFM R009 Type B	2200	Foil 0.5 250L	1900	0,14	970,3	21,4	37	
258	19	9.11.2012	5:51	6:49	$3\,GeV/c$	FFM R009 Type B	2200	Foil 0.5 250L	1900	0,147	970,4	21,2	36,4	
259	19	9.11.2012	6:53	7:22	$3\,GeV/c$	FFM R009 Type B	2200	Foil 0.5 250L	1900	0,152	970,5	21,1	35,5	
260	19	9.11.2012	7:26	7:59	$3\,GeV/c$	FFM R009 Type B	2200	Foil 0.5 250L	1900	0,153	970,7	20,9	35,2	
261	19	9.11.2012	8:10	8:53	$3\,GeV/c$	FFM R009 Type B	2200	Foil 0.5 250L	1900	0,16	970,7	20,8	35,2	
262	19	9.11.2012	8:58	9:30	$3\,GeV/c$	FFM R009 Type B	2200	Foil 0.5 250L	1900	0,159	970,6	20,8	35,6	
263	19	9.11.2012	9:35	10:13	$3\,GeV/c$	FFM R009 Type B	2200	Foil 0.5 250L	1900	0,154	970,1	21,4	36,1	
264	20	9.11.2012	10:26	11:07	$3\,GeV/c$	FFM R02	2200	FFM R03	1900	0,181	970,2	20,8	39,7	MBS crashed
265	20	9.11.2012	11:21	11:31	$3\,GeV/c$	FFM R02	2200	FFM R03	1900	0,144	968,7	22,1	38,4	Current in FFM011 at 24.5nA (11:54)
266	20	9.11.2012	11:35	12:12	$3\,GeV/c$	FFM R02	2200	FFM R03	1900	0,129	968,2	22,6	37,7	
267	20	9.11.2012	12:27	13:03	$3\,GeV/c$	FFM R02	2200	FFM R03	1900					Current in FFM011 at 31nA (13:03)
268	20	9.11.2012	13:05	13:08	$3\,GeV/c$	FFM R02	2200	FFM R03	1900	0,112	966,5	23,4	35,5	
269	20	9.11.2012	13:10	14:04	$3\,GeV/c$	FFM R02	2200	FFM R03	1900	0,112	966,6	23,4	35,4	Current in FFM011 at 21nA (13:14)
270	20	9.11.2012	14:05	14:45	$3\,GeV/c$	FFM R02	2200	FFM R03	1900	0,115	966,5	23,2	35,1	
271	20	9.11.2012	14:49	15:27	$3\,GeV/c$	FFM R02	2200	FFM R03	1900					
272	20	9.11.2012	15:27	15:40	$3\,GeV/c$	FFM R02	2200	FFM R03	1900					
273	20	9.11.2012	15:51	16:02	$3\,GeV/c$	FFM R02	2200	FFM R03	1900					
274	20	9.11.2012	16:04	16:12	$3\,GeV/c$	FFM R02	2200	FFM R03	1900					
275	20	9.11.2012	17:22	17:33	$3\,GeV/c$	FFM R02	2200	FFM R03	1900					Power Cut at 16:30
276	20	9.11.2012	18:19	18:42	$3\,GeV/c$	FFM R02	2200	FFM R03	1900					Spadic 5 crashed moved from CAVE / tested with external power supply / installed again / after changing LV u2 from 3,5V to 3,315V running again
277	20	9.11.2012	18:48	19:13	$3\,GeV/c$	FFM R02	2200	FFM R03	1900					
277	20	9.11.2012	18:48	19:13										
278	20	9.11.2012	20:02	21:00	$3\,GeV/c$	FFM R02	2200	FFM R03	1900					
279	20	9.11.2012	21:02	21:50	$3\,GeV/c$	FFM R02	2200	FFM R03	1900					
280	20	9.11.2012	21:51	2:002	$3\,GeV/c$	FFM R02	2200	FFM R03	1900					
281	20	9.11.2012		23:52	$3\,GeV/c$	FFM R02	2200	FFM R03	1900					
282	20	9.11.2012	23:55	0:22	$3\,GeV/c$	FFM R02	2200	FFM R03	1900					
283	20	10.11.2012	0:25	0:50	$3\,GeV/c$	FFM R02	2200	FFM R03	1900	0,11	963,3	22,8	42,3	
284	20	10.11.2012	2:30	3:00	$3\,GeV/c$	FFM R02	2200	FFM R03	1900					
285	20	10.11.2012	3:05	3:31	$3\,GeV/c$	FFM R02	2200	FFM R03	1900					
286	20	10.11.2012	3:32	4:06	$3\,GeV/c$	FFM R02	2200	FFM R03	1900	0,11	961,7	22,7	44	
287	20	10.11.2012	4:06	4:35	$3\,GeV/c$	FFM R02	2200	FFM R03	1900	0,11	961,4	22,7	44,5	

		DAQ				Pos. 1 FFM011		Pos. 2 FFM010		Conditions				
Run	Set	Date	Start	Stop	Beam	Radiator	HV [V]	Radiator	HV [V]	Pressure MWPC [mbar]	Pressure absolute [mbar]	Temp. [°C]	Humidity [%]	Comments
288	20	10.11.2012	4:35	5:07	$3\,GeV/c$	FFM R02	2200	FFM R03	1900	0,111	961,1	22,6	45,1	
289	20	10.11.2012	5:07	5:36	$3\,GeV/c$	FFM R02	2200	FFM R03	1900	0,111	960,5	22,4	45,8	
290	20	10.11.2012	5:36	5:57	$3\,GeV/c$	FFM R02	2200	FFM R03	1900	0,111	960,2	22,4	46,1	
291	20	10.11.2012	7:35	8:31	$3\,GeV/c$	FFM R02	2200	FFM R03	1900	0,111	958,8	22,5	47,1	
292	20	10.11.2012	9:28	10:04	$3\,GeV/c$	FFM R02	2200	FFM R03	1900	0,107	959,3	22,6	47,3	
293	20	10.11.2012	10:11	10:45	$3\,GeV/c$	FFM R02	2200	FFM R03	1900					
294	20	10.11.2012	10:47	11:13	$3\,GeV/c$	FFM R02	2200	FFM R03	1900	0,109	958,6	22,6	47,5	
295	21	10.11.2012	11:30	11:55	$3\,GeV/c$	FFM R03	2200	Foil 0,7 150L	1900	0,109	958,3	22,7	47,4	
296	21	10.11.2012	12:00	12:26	$3\,GeV/c$	FFM R03	2200	Foil 0,7 150L	1900	0,109	957,9	22,9	47	
297	21	10.11.2012	12:27	12:48	$3\,GeV/c$	FFM R03	2200	Foil 0,7 150L	1900	0,108	957,6	23	46,8	
298	21	10.11.2012	15:16	15:40	$3\,GeV/c$	FFM R03	2200	Foil 0,7 150L	1900	0,104	955,7	23,5	46,8	
299	21	10.11.2012	15:42	16:10	$3\,GeV/c$	FFM R03	2200	Foil 0,7 150L	1900					
300	21	10.11.2012	16:15	16:34	$3\,GeV/c$	FFM R03	2200	Foil 0,7 150L	1900					
301	21	10.11.2012	16:36	16:56	$3\,GeV/c$	FFM R03	2200	Foil 0,7 150L	1900	0,103	955,3	23,5	48,2	
302	21	10.11.2012	16:57	17:20	$3\,GeV/c$	FFM R03	2200	Foil 0,7 150L	1900	0,104	955,3	23,4	48,6	
303	21	10.11.2012	17:21	17:35	$3\,GeV/c$	FFM R03	2200	Foil 0,7 150L	1900					
304	21	10.11.2012	17:39	17:44	$3\,GeV/c$	FFM R03	2200	Foil 0,7 150L	1900					
305	21	10.11.2012	17:46	18:09	$3\,GeV/c$	FFM R03	2200	Foil 0,7 150L	1900					
306	21	10.11.2012	21:35	22:34	$3\,GeV/c$	FFM R03	2200	Foil 0,7 150L	1900	0,104	957,6	22,9	50,4	
307	21	10.11.2012	22:35	23:05	$3\,GeV/c$	FFM R03	2200	Foil 0,7 150L	1900	0,102	958,5	22,8	50,3	
308	21	10.11.2012	23:06	23:37	$3\,GeV/c$	FFM R03	2200	Foil 0,7 150L	1900					
309	21	10.11.2012	23:38	0:08	$3\,GeV/c$	FFM R03	2200	Foil 0,7 150L	1900					
310	21	11.11.2012	0:09	0:10	$3\,GeV/c$	FFM R03	2200	Foil 0,7 150L	1900	0,102	958,1	23	50,2	
311	21	11.11.2012	0:20	0:48	$3\,GeV/c$	FFM R03	2200	Foil 0,7 150L	1900	0,102	958	23	50,3	
312	21	11.11.2012	0:49	1:17	$3\,GeV/c$	FFM R03	2200	Foil 0,7 150L	1900	0,102	958,1	23,1	49,9	
313	21	11.11.2012	1:18	1:43	$3\,GeV/c$	FFM R03	2200	Foil 0,7 150L	1900	0,102	958,1	23,1	49,4	
314	21	11.11.2012	1:45	2:00	$3\,GeV/c$	FFM R03	2200	Foil 0,7 150L	1900	0,101	958	23,1	48,7	
315	21	11.11.2012	2:16	2:45	$3\,GeV/c$	FFM R03	2200	Foil 0,7 150L	1900	0,103	957,8	23,1	48,1	
316	21	11.11.2012	2:45	3:01	$3\,GeV/c$	FFM R03	2200	Foil 0,7 150L	1900	0,102	957,6	23,2	47	
317	21	11.11.2012	3:01	3:30	$3\,GeV/c$	FFM R03	2200	Foil 0,7 150L	1900	0,098	957,9	23,2	46,6	
318	21	11.11.2012	3:30	3:55	$3\,GeV/c$	FFM R03	2200	Foil 0,7 150L	1900	0,099	957,7	23,2	45,9	
319	21	11.11.2012	4:31	4:56	$3\,GeV/c$	FFM R03	2200	Foil 0,7 150L	1900	0,101	957,5	22,9	46,4	
320	21	11.11.2012	5:38	5:40	$3\,GeV/c$	FFM R03	2200	Foil 0,7 150L	1900	0,1	958,2	22,7	46,9	
321	21	11.11.2012	6:25	6:31	$3\,GeV/c$	FFM R03	2200	Foil 0,7 150L	1900					
322	21	11.11.2012	6:39	7:04	$3\,GeV/c$	FFM R03	2200	Foil 0,7 150L	1900					
323	21	11.11.2012	7:05	7:55	$3\,GeV/c$	FFM R03	2200	Foil 0,7 150L	1900	0,1	958,4	22,7	46,3	
324	21	11.11.2012	7:56	8:20	$3\,GeV/c$	FFM R03	2200	Foil 0,7 150L	1900	0,1	959	22,6	46,4	
325	21	11.11.2012	8:24	9:05	$3\,GeV/c$	FFM R03	2200	Foil 0,7 150L	1900	0,102	959,2	22,7	46,3	
326	22	11.11.2012	9:25	10:44	$3\,GeV/c$	Foil 0,7 150L	2200	Foil 0,7 150L	1900	0,097	959,9	22,8	46,6	
327	22	11.11.2012	10:51	11:25	$3\,GeV/c$	Foil 0,7 150L	2200	Foil 0,7 150L	1900	0,096	961,3	23	46,9	
328	22	11.11.2012	12:12	13:22	$3\,GeV/c$	Foil 0,7 150L	2200	Foil 0,7 150L	1900	0,094	961,5	23,2	46,5	
329	22	11.11.2012	14:46	14:50	$3\,GeV/c$	Foil 0,7 150L	2200	Foil 0,7 150L	1900	0,086	962,8	23,5	45,7	
330	22	11.11.2012	14:53	15:29	$3\,GeV/c$	Foil 0,7 150L	2200	Foil 0,7 150L	1900	0,088	962,9	23,5	45,9	
331	22	11.11.2012	15:31	16:18	$3\,GeV/c$	Foil 0,7 150L	2200	Foil 0,7 150L	1900					
332	22	11.11.2012	16:19	16:40	$3\,GeV/c$	Foil 0,7 150L	2200	Foil 0,7 150L	1900					
333	22	11.11.2012	16:41	17:03	$3\,GeV/c$	Foil 0,7 150L	2200	Foil 0,7 150L	1900					
334	22	11.11.2012	17:04	17:37	$3\,GeV/c$	Foil 0,7 150L	2200	Foil 0,7 150L	1900					
335	22	11.11.2012	17:38	18:06	$3\,GeV/c$	Foil 0,7 150L	2200	Foil 0,7 150L	1900					
336	22	11.11.2012	18:15	18:23	$3\,GeV/c$	Foil 0,7 150L	2200	Foil 0,7 150L	1900					
337		11.11.2012	18:32	19:15	$3\,GeV/c$	Foil 0.5 350L	2200	no Radiator	1900	0,088	966,7	23,3	46,3	
338		11.11.2012	19:32	19:44	$3\,GeV/c$	Foil 0.5 350L	2200	no Radiator	1900					
339		11.11.2012	19:50		$3\,GeV/c$	Foil 0.5 350L	2200	no Radiator	1900					
340		11.11.2012			$3\,GeV/c$	Foil 0.5 350L	2200	no Radiator	1900					
341		11.11.2012	21:02		$3\,GeV/c$	Foil 0.5 350L	2200	no Radiator	1900					
342		11.11.2012			$3\,GeV/c$	Foil 0.5 350L	2200	no Radiator	1900					